PARTICLE PRODUCTION STUDIES IN Au+Au and U+U COLLISIONS USING THE STAR DETECTOR AT RHIC AND UNDERSTANDING THE FREEZE-OUT DYNAMICS

By

DEBADEEPTI MISHRA

(Enrollment No. : PHYS11201304011)

National Institute of Science Education and Research, HBNI,

Jatani - 752050, INDIA

A thesis submitted to the

Board of Studies in Physical Sciences

In partial fulfillment of requirements

For the Degree of
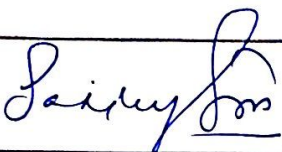
DOCTOR OF PHILOSOPHY
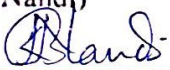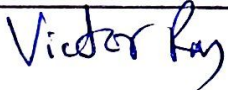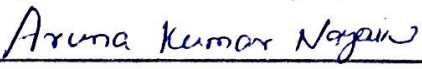
of

HOMI BHABHA NATIONAL INSTITUTE

November, 2019

Homi Bhabha National Institute

Recommendations of the Viva Voce Board

As members of the Viva Voce Board, we certify that we have read the dissertation prepared by Debadeepti Mishra entitled PARTICLE PRODUCTION STUDIES IN Au+Au and U+U COLLISIONS USING THE STAR DETECTOR AT RHIC AND UNDERSTANDING THE FREEZE-OUT DYNAMICS and recommend that it maybe accepted as fulfilling the dissertation requirement for the Degree of Doctor of Philosophy.
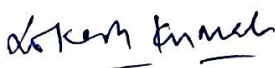
Chair - (Dr. Sanjay Swain)		Date: 22/11/2019
Guide/Convener - (Dr. Bedangadas Mohanty)		Date: 22/11/2019
Co-guide - (Dr. Lokesh Kumar)		Date: 22·11·2019
Examiner - (Dr. Basanta Kumar Nandi)		Date: 22/11/2019
Member 1 - (Dr. Prolay Mal)		Date: Nov 22, 2019
Member 2 - (Dr. Victor Roy)		Date: 22·11·19
External Member - (Dr. Aruna Kumar Nayak)		Date: 22/11/2019

Final approval and acceptance of this dissertation is contingent upon the candidate's submission of the final copies of the dissertation to HBNI.

I hereby certify that I have read this dissertation prepared under my direction and recommend that it may be accepted as fulfilling the dissertation requirement.

Date: 22/11/2019

Place: NISER

Dr. Lokesh Kumar

(Co-Guide)

Dr. Bedangadas Mohanty

(Guide)

STATEMENT BY AUTHOR

This dissertation has been submitted in partial fulfillment of requirements for an advanced degree at Homi Bhabha National Institute (HBNI) and is deposited in the Library to be made available to borrowers under rules of the HBNI.

Brief quotations from this dissertation are allowable without special permission, provided that accurate acknowledgment of source is made. Requests for permission for extended quotation from or reproduction of this manuscript whole or in part may be granted by the Competent Authority of HBNI when in his or her judgment the proposed use of the material is in the interests of scholarship. In all other instances, however, permission must be obtained from the author.

Debadeepti Mishra

Debadeepti Mishra

DECLARATION

I, hereby declare that the investigation presented in the thesis has been carried out by me. The work is original and has not been submitted earlier as a whole or in part for a degree / diploma at this or any other Institution / University.

Debadeepti Mishra

4

This is for my lovely **Mother**

and heartily dedicated to my **Family**

ACKNOWLEDGMENTS

building of my personality, career and this Ph.D too. Now the time comes to admire the angel of my life - my sweet younger sister Swayamsidha. Her love, care, support and presence for the last 27 years of my life including the Ph.D carrier are most price worthy for me.

Also, mention worthy are the encouragement and belief on my potentiality of my Babu Mamu, Suresh Mamu, Kuni Mausi, Mini Mausi, Buli Mausi and other relatives.

Above all, the thesis writing time of my life has been blessed by the Almighty, with the little greatest gift to hold a life within me. Medically this is the time when an expecting mother nourishes her baby. But for me, my baby within me is the one who filled me and flourished me throughout my thesis writing period. My baby is undoubtedly the un-detachable part of this thesis and the key to make it complete.

I can never forget to "Pranam" at the feet of the Almighty for fulfilling me with the strength and inspiration to move forward and to defeat the worst situations of life. All His blessing enlightens my life and I surrender myself at His feet for his secure shelter to shade me.

Debadeepti Mishra
(Debadeepti Mishra)

SUMMARY

In this thesis the data from the STAR detector at RHIC for Au+Au collisions at $\sqrt{s_{NN}} = 14.5$ GeV and U+U collisions at $\sqrt{s_{NN}} = 193$ GeV are extensively analyzed.

We have measured the transverse momentum (p_T) spectra of $\pi^\pm$, $K^\pm$ and $p(\bar{p})$ in Au+Au collisions at $\sqrt{s_{NN}} = 14.5$ GeV in mid-rapidity ($|y| < 0.1$) in nine different collision centrality classes. We have extracted dN/dy, $\langle p_T \rangle$, particle ratios, chemical and kinetic freeze-out parameters in nine centralities in Au+Au collisions at $\sqrt{s_{NN}} = 14.5$ GeV and are compared with the corresponding published results of STAR from $7.7 - 200$ GeV. The values of dN/dy for $\pi^\pm$, $K^\pm$ and p have a slight centrality dependence and for $\bar{p}$ it is almost flat with centrality. $\langle p_T \rangle$ increases from peripheral to central collision for $\pi^\pm$, $k^\pm$ and $p(\bar{p})$ indicating stronger radial flow effects in central collisions. π^-/π^+ and K^-/K^+ ratios have almost no centrality dependence, whereas $\bar{p}/p$ ratio increases with centrality. An increase in K^+/π^+, K^-/π^- and p/π^+ ratio with increasing centrality and no significant centrality dependence for $\bar{p}/\pi^-$ ratio is observed. The chemical freeze-out temperature T_{ch} has no significant centrality dependence, while the baryon chemical potential has a weak centrality dependence. The kinetic freeze-out temperature T_k decreases, while average flow velocity $\langle \beta \rangle$ increases from peripheral to central collisions. The results in Au+Au collisions at $\sqrt{s_{NN}} = 14.5$ GeV are further compared with models like AMPT and UrQMD to investigate the partonic and hadronic contributions to the particle production. The prediction from AMPT model is in better agreement with STAR results, whereas UrQMD calculations are in poor agreement in Au+Au collisions at $\sqrt{s_{NN}} = 14.5$ GeV.

Uranium is a prolate shaped nucleus in contrast to the nearly spherical shaped Gold nucleus and hence can have different initial stage orientations of the colliding nuclei. This might have its effect on the finally measured bulk properties of the system. In this context, we have measured the p_T spectra of $\pi^\pm$, $K^\pm$ and $p(\bar{p})$ in mid-rapidity ($|y| < 0.1$) in U+U collisions at $\sqrt{s_{NN}} = 193$ GeV for nine collision centrality classes. We have extracted dN/dy, $\langle p_T \rangle$, particle ratios and kinetic freeze-out parameters of the particles for the nine centralies. We have observed the values of dN/dy increases with an increase in centrality for $\pi^\pm$, $K^\pm$ and p, whereas $\bar{p}$ remain constant to this. This is due to contributions from soft and hard processes in-

volving nucleon-nucleon binary collisions. $\langle p_T \rangle$ increases from peripheral to central collisions indicating stronger radial flow effects in central collisions. All the results are compared with the published results of Au+Au collisions at $\sqrt{s_{NN}} = 200$ GeV. We have observed that in spite of different geometrical shapes, the results in U+U collisions at $\sqrt{s_{NN}} = 193$ GeV are consistent with the published results in Au+Au collisions at $\sqrt{s_{NN}} = 200$ GeV within systematic uncertainty. A comparison with the calculations from AMPT model modified to include the deformation of Uranium nucleus is also carried out in U+U collisions at $\sqrt{s_{NN}} = 193$ GeV. AMPT model calculation with 10 mb cross-section describes the STAR results upto a good extent than AMPT model with 1.5 mb cross-section, in U+U collisions at $\sqrt{s_{NN}} = 193$ GeV.

We have applied the statistical thermodynamic model to the small system of p+p collisions producing less number of particles which is very successful in predicting the yields in heavy-ion collisions producing a huge number of particles. The p+p collisions at $\sqrt{s} = 17.3, 200, 900$ and 7000 GeV are analyzed in two freeze-out schemes: single freeze-out (1CFO) assuming all hadrons to freeze-out at a single time and double freeze-out (2CFO) taking two different freeze-out times for strange and non-strange hadrons. At lower energies, freeze-out T_{ch} is found to be higher than A+A collisions, whereas at higher energy it is in agreement with heavy-ion collisions. We observed the value of radius is remarkably smaller for the p+p collisions in comparison with A+A collisions at the same energy, as expected. Additionally, the strangeness saturation factor is found to be lower in p+p than A+A collisions.

The systematics of the Hadron Resonance Gas (HRG) model in explaining mean hadron yields and higher moments of conserved charges (Baryon number (B), Strangeness (S) and Charge (Q)) with the inclusion of the theoretically predicted resonances waiting for their full experimental confirmation is studied in this thesis. The data are analyzed in two different freeze-out schemes (1CFO and 2CFO). We have calculated one dimensioned parameter T and two suitably chosen dimensionless parameters μ_B/T and VT^3. We found that the freeze-out T is mostly influenced by the systematics of the hadron spectrum, whereas μ_B/T and VT^3 are almost unaffected. A lowering of T is observed upon addition of extra resonances. The flavor hierarchy is also supported resulting in the difference of strange and non-strange T upon addition of extra resonances.

PUBLICATIONS

∗1. "Freezeout systematics due to the Hadron Spectrum"

Sandeep Chatterjee, Debadeepti Mishra, Bedangadas Mohanty, Subhasis Samanta

Phys Rev. **C 96**, 054907, (2017)

∗2. "Freeze-out conditions in proton-proton Collisions at the Highest Energies Available at the BNL Relativistic Heavy Ion Collider and the CERN Large Hadron Collider"

Sabita Das, Debadeepti Mishra, Sandeep Chatterjee, and Bedangadas Mohanty

Phys Rev. **C 95**, 014912, (2017)

3. "Freeze out Parameters in Heavy-ion Collisions at AGS, SPS, RHIC and LHC Energies"

Sandeep Chatterjee, Sabita Das, Lokesh Kumar, D. Mishra, Bedangadas Mohanty, Raghunath Sahoo and Natasha Sharma

Advances in High Energy Physics, **349013** (2015)

∗4. "Bulk Properties of the System Formed Au+Au collisions at $\sqrt{s_{NN}} = 14.5$ GeV Using the STAR Detector at RHIC"

J. Adam *et al.* (STAR Collaboration)

(Primary authors : Debadeepti Mishra, Vipul Bairathi, Subhash Sinha, Md. Nasim, Lokesh Kumar, Bedangadas Mohanty, Declan Keane)

arXiv:**1908.03585** [nucl-ex], (2019)

(Accepted in Phys. Rev. **C**)

∗5. "Pion, Kaon and (Anti)Proton Production in U+U Collisions at $\sqrt{s_{NN}} = 193$ GeV in STAR"

J. Adam *et al.* (STAR Collaboration)

(Primary authors : Debadeepti Mishra, Lokesh Kumar and Bedangadas Mohanty)

STAR Note : **PSN0711**

Target Journal: Phys. Rev. **C** (Under final stage of review within STAR Collaboration)

List of Conference Proceedings

1. "Freeze-out Parameters in Heavy-ion Collisions at AGS, SPS, RHIC and LHC Energies"

   Sandeep Chatterjee, Sabita Das, Lokesh Kumar, D. Mishra *et al.*

   Proceeding of DAE Symp. on Nucl, Phys. **59** (2014) 714-715

∗2. "Identified Particle Production in Au+Au Collisions at $\sqrt{s_{NN}} = 14.5$ GeV in STAR"

   Debadeepti Mishra (For the STAR Collaboration)

   Proceedings of DAE Symp. on Nucl. Phys. **60** (2015) 764-765

∗3. "Identified Particle Production in Au+Au Collisions at $\sqrt{s_{NN}} = 14.5$ GeV in STAR"

   Debadeepti Mishra (For the STAR Collaboration)

   Proceedings of Asian Triangle Heavy Ion Conference (ATHIC) **59** (2016)

∗4. "Freeze-out Conditions in proton-proton Collisions from SPS to LHC Energies"

   Sabita Das, Debadeepti Mishra, Sandeep Chatterjee, and Bedangadas Mohanty

   Proceedings of DAE Symp. on Nucl. Phys. **61** (2016) 782-783

∗5. "Identified Particle Production in U+U Collisions at $\sqrt{s_{NN}} = 193$ GeV in STAR"

   Debadeepti Mishra (For the STAR Collaboration)

   Proceedings of XXII DAE Symposium on High Energy Physics, Springer Proc. Phys. **203** (2018) 247-249

∗6. "Freeze-out Systematics due to the Hadron Spectrum"

   Sandeep Chatterjee, Debadeepti Mishra, Bedangadas Mohanty, Subhasis Samanta

   Proceedings of DAE Symp. on Nucl. Phys. **62** (2017) 920-921

Selected List of Publications as a Part of STAR Collaboration

1. Measurement of the longitudinal spin asymmetries for weak boson production in proton-proton collisions at $\sqrt{s_{NN}} = 510$ GeV.

   J. Adam *et al.* (STAR Collaboration), Phys. Rev. **D 99** (2019) 51102

2. Transverse spin transfer to Lambda and anti-Lambda hyperons in polarized proton-proton collisions at $\sqrt{s_{NN}} = 200$ GeV,

   J. Adam *et al.* (STAR Collaboration) Phys. Rev. **D 98** (2018) 91103

3. The Proton-Omega correlation function in Au+Au collisions at $\sqrt{s_{NN}} = 200$ GeV,

   J. Adam *et al.* (STAR Collaboration), Phys. Lett. **B 790** (2019) 490

4. Low p_T $e + + e^-$ Pair Production in Au+Au Collisions at $\sqrt{s_{NN}} = 200$ GeV and U+U Collisions at $\sqrt{s_{NN}} = 193$ GeV at STAR,

   J. Adam *et al.* (STAR Collaboration), Phys. Rev. Lett. **121** (2018) 132301

5. Longitudinal Double-Spin Asymmetries for Dijet Production at Intermediate Pseudorapidity in Polarized pp Collisions at $\sqrt{s_{NN}} = 200$ GeV,

   J. Adam *et al.* (STAR Collaboration), Phys. Rev. **D 98** (2018) 32011

6. Longitudinal double-spin asymmetries for π^0s in the forward direction for 510 GeV polarized pp collisions,

   J. Adam *et al.* (STAR Collaboration), Phys. Rev. **D 98** (2018) 32013

7. Global polarization of Lambda hyperons in Au+Au collisions at $\sqrt{s_{NN}} = 200$ GeV,

   J. Adam *et al.* (STAR Collaboration), Phys. Rev. **C 98** (2018) 14910

8. J/ψ production cross section and its dependence on charged-particle multiplicity in p+p collisions at $\sqrt{s_{NN}} = 200$ GeV,

   J. Adam *et al.* (STAR Collaboration), Phys. Lett. **B 786** (2018) 87

9. Global polarization of Lambda hyperons in Au+Au collisions at $\sqrt{s_{NN}} = 200$ GeV,

   J. Adam *et al.* (STAR Collaboration), Phys. Rev. **C 98** (2018) 14910

10. Beam energy dependence of rapidity-even dipolar flow in Au+Au collisions,

    J. Adam *et al.* (STAR Collaboration), Phys. Lett. **B 784** (2018) 26

11. Correlation Measurements Between Flow Harmonics in Au+Au Collisions at RHIC,

    J. Adam *et al.* (STAR Collaboration), Phys. Lett. **B 783** (2018) 459

12. Azimuthal anisotropy in Cu+Au collisions at $\sqrt{s_{NN}} = 200$ GeV ,

    L. Adamczyk *et al.* (STAR Collaboration), Phys. Rev. **C 98** (2018) 14915

13. Transverse spin-dependent azimuthal correlations of charged pion pairs measured in $p^\uparrow$+p collisions at $\sqrt{s} = 500$ GeV,

    L. Adamczyk *et al.* (STAR Collaboration), Phys. Lett. **B 780** (2018) 332

14. Measurement of hyper triton lifetime in Au+Au collisions at the Relativistic Heavy-Ion Collider,

    L. Adamczyk *et al.* (STAR Collaboration), Phys. Rev. **C 97** (2018) 54909

15. Collision Energy Dependence of Moments of Net-Kaon Multiplicity Distributions at RHIC,

    L. Adamczyk *et al.* (STAR Collaboration), Phys. Lett. **B 785** (2018) 551

16. Beam-Energy Dependence of Directed Flow of Λ, $\bar{\Lambda}$, K^+, K^-, K_s^0 and ϕ in Au+Au Collisions,

    L. Adamczyk *et al.* (STAR Collaboration), Phys. Rev. Lett. **120** (2018) 62301

17. Azimuthal transverse single-spin asymmetries of inclusive jets and charged pions within jets from polarized-proton collisions at $\sqrt{s_{NN}} = 500$ GeV,

    L. Adamczyk *et al.* (STAR Collaboration), Phys. Rev. **D 97** (2018) 32004

18. Beam Energy Dependence of Jet-Quenching Effects in Au+Au Collisions at $\sqrt{s_{NN}} =$ 7.7, 11.5, 14.5, 19.6, 27, 39, and 62.4 GeV,

    L. Adamczyk *et al.* (STAR Collaboration), Phys. Rev. Lett. **121** (2018) 32301

19. Coherent diffractive photoproduction of rho0 mesons on gold nuclei at 200 GeV/nucleon-pair at the Relativistic Heavy Ion Collider,

L. Adamczyk *et al*. (STAR Collaboration), Phys. Rev. **C 96** (2017) 54904

20. Measurements of jet quenching with semi-inclusive hadron+jet distributions in Au+Au collisions at $\sqrt{s_{NN}} = 200$ GeV,

   L. Adamczyk *et al*. (STAR Collaboration), Phys. Rev. **C 96** (2017) 24905

21. Bulk Properties of the Medium Produced in Relativistic Heavy-Ion Collisions from the Beam Energy Scan Program,

   L. Adamczyk *et al*. (STAR Collaboration), Phys. Rev. **C 96** (2017) 44904

22. Harmonic decomposition of three-particle azimuthal correlations at RHIC,

   L. Adamczyk *et al*. (STAR Collaboration), Phys. Rev. **C 98** (2018) 34918

23. Measurement of D^0 azimuthal anisotropy at mid-rapidity in Au+Au collisions at $\sqrt{s_{NN}} = 200$ GeV,

   L. Adamczyk *et al*. (STAR Collaboration), Phys. Rev. Lett. **118** (2017) 212301

24. Constraining the initial conditions and temperature dependent transport with three-particle correlations in Au+Au collisions,

   L. Adamczyk *et al*. (STAR Collaboration), Phys. Lett. **B 790** (2019) 81

25. Global Lambda hyperon polarization in nuclear collisions: evidence for the most vortical fluid,

   L. Adamczyk *et al*. (STAR Collaboration), Nature **548** (2017) 62

26. Measurement of the cross section and longitudinal double-spin asymmetry for di-jet production in polarized pp collisions at $\sqrt{s_{NN}} = 200$ GeV,

   L. Adamczyk *et al*. (STAR Collaboration), Phys. Rev. **D 95** (2017) 71103

27. Di-Jet Imbalance Measurements at $\sqrt{s_{NN}} = 200$ GeV at STAR,

   L. Adamczyk *et al*. (STAR Collaboration), Phys. Rev. Lett. **119** (2017) 62301

28. Upsilon production in U+U collisions at sqrt(sNN)=193 GeV with the STAR experiment,

   L. Adamczyk *et al*. (STAR Collaboration), Phys. Rev. **C 94** (2016) 64904

29. Charge-dependent directed flow in Cu+Au collisions at $\sqrt{s_{NN}} = 200$ GeV,

L. Adamczyk *et al.* (STAR Collaboration), Phys. Rev. Lett. **118** (2017) 12301

30. Energy dependence of J/psi production in Au+Au collisions at $\sqrt{s_{NN}} = 39$, 62.4 and 200 GeV,

L. Adamczyk *et al.* (STAR Collaboration), Phys. Lett. **B 771** (2017) 13

31. Direct virtual photon production in Au+Au collisions at $\sqrt{s_{NN}} = 200$ GeV,

L. Adamczyk *et al.* (STAR Collaboration), Phys. Lett. **B 770** (2017) 451

32. Jet-like Correlations with Direct-Photon and Neutral-Pion Triggers at $\sqrt{s_{NN}} = 200$ GeV,

L. Adamczyk *et al.* (STAR Collaboration), Phys. Lett. **B 760** (2016) 689

33. Near-side azimuthal and pseudorapidity correlations using neutral strange baryons and mesons in d+Au, Cu+Cu and Au+Au collisions at $\sqrt{s_{NN}} = 200$ GeV,

B. Abelev *et al.* (STAR Collaboration), Phys. Rev. **C 94** (2016) 14910

$*$ indicates the paper on which the thesis is build up.

Debadeepti Mishra
(Debadeepti Mishra)

Contents

4 Pion, Kaon and (Anti-)Proton Production in U+U Collisions at $\sqrt{s_{NN}} = 193$ GeV in STAR   **156**

List of Figures

24

29

31

List of Tables

Chapter 1

Introduction

The thirst for knowledge always adds up the perfect spice to the cooking of new science. A little contribution serves a lot for a bigger field to emerge. The work presented in this thesis may prove to be little meaningful in this sense. So, on the standard frame of analysis, a trial for some new impressions has been attempted throughout this thesis chapters.

1.1   The Standard Model

As the name clearly justifies, the Standard Model (SM) [1] of particle physics establishes a standardized platform to study the properties of elementary particles and the interactions among them. It is the unique theory proposed by Glashow, Salam and Weinberg unifying and characterizing the three fundamental forces of nature (weak, electromagnetic and strong) except gravity. It explains the physics at the fundamental level through the classification of ultimate constituents of matter as quarks and leptons. Again to structure matter, some binding force is necessary to hold the nucleons to form atoms. So, the gauge bosons are proposed as the mediator particles to exchange force or interaction among the so called elementary particles. Briefly in SM, quarks and leptons along with the gauge bosons are the fundamental building blocks of matter.

Based on the theoretical considerations of quantum field theory and supportive experimental evidences, 3 generations of quarks and 3 generations of leptons have been proposed. Each of the three generations of quarks contains two quarks. Those are up (u) and down (d); charm (c)

and strange (s); top (t) and bottom (b), generation wise respectively. The three generations of leptons known as electron (e), muon (μ) and tau (τ) come with their corresponding neutrino partners (ν_e, ν_μ, ν_τ). Each of these elementary particles has its own anti-particles with exactly the same mass and opposite quantum numbers.
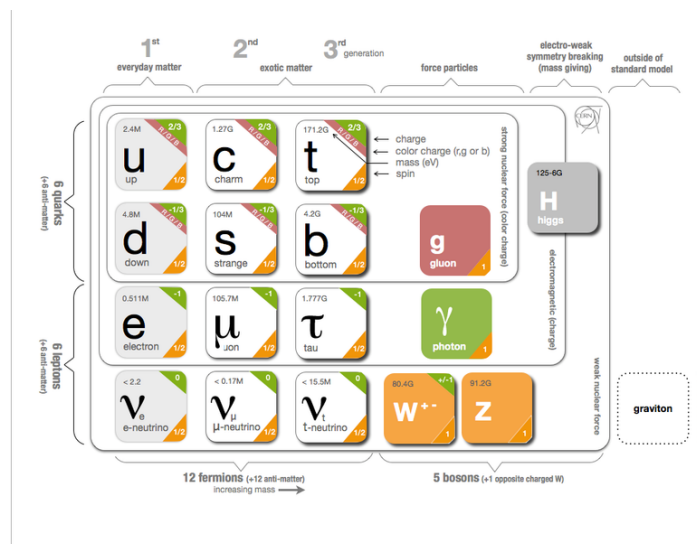
Figure 1.1: Pictorial view of elementary particles of Standard Model and force exchanging gauge bosons along with Higgs [5].

The standard model has nomenclature for three sets of different force carriers for each one of the three basic forces of nature : strong, electromagnetic and weak. Gluons for the strong, photons for the electromagnetic and $W^\pm$ and Z bosons for the weak force. Further, the graviton has been hypothesized as the mediator of the force of gravity in respect of a parallel argument but has not been included in SM. In the standard model, the exciting physics has been added by the inclusion of Higgs boson [2] by P. W Higgs, F. Englert and R. Brout in 1964. The experimental confirmation of this new particle by ATLAS [3] and CMS [4] experiments have given us the complete picture of elementary particles. This Higgs boson plays a vital role in the generation of mass of fundamental particles. A pictorial diagram showing the fundamental complete set of building blocks of matter is shown in Figure 1.1 [5].

The standard model description considers spin, iso-spin, baryon number, strangeness, hypercharge, charge, color quantum numbers and their conservation laws to explain the physics of the world of composite particle called as Hadrons. These hadrons are made up of quarks

and are sub-divided into baryons and mesons. The baryons are fermions containing 3 quarks, whereas mesons are bosons containing a quark and an anti-quark.

There are two prescribed theories dedicated to strong and electromagnetic interactions as Quantum Chromodynamics (QCD) [6] and Quantum Electrodynamics (QED) [7] respectively. The weak force along with electromagnetic interaction is described by electro-weak theory [8]. All these theories are then combined together to completely describe the features of particle physics world in SM.

1.2   The Quantum Chromodynamics (QCD)

The interacting physics of quark-quark, quark-gluon and gluon-gluon are characterized by the theory of quantum chromodynamics. The quantum mechanical arguments of QED are generalized to QCD by considering the color charge of quarks and gluons instead of electron charge in QED. In view of Pauli's exclusion principle, three different color charges are associated with quarks replacing the single electronic charge in QED. This results in the construction of a non-abelian group satisfying local gauge invariance in the case of QCD. The group theoretical representation satisfies the algebra of $SU_c(3)$ unitary group, where the subscript 'c' is for color quantum number. The gluons emerge from the color-potential introduction to the Hamiltonian of the theory. The $SU_c(3)$ group algebra provides us 8 color gauge fields to represent gluons. These 8 number of color force carriers known as gluons along with three generations of quark flavors form the backbone of the QCD theory.

1.2.1   Quark Confinement and Asymptotic Freedom

The strong force being associated with 3 color quantum numbers exhibits two interesting phenomena. Those are quark confinement and asymptotic freedom [9]. The length scale of the strong force is characterized by the strong coupling constant (α_S), which has the mathematical expression of the form,

$$\alpha_S(\mu^2) \approx \frac{12\pi}{(11n_c - 2n_f)\ln(|\mu^2|/\Lambda_{\text{QCD}}^2)}, \tag{1.1}$$

41
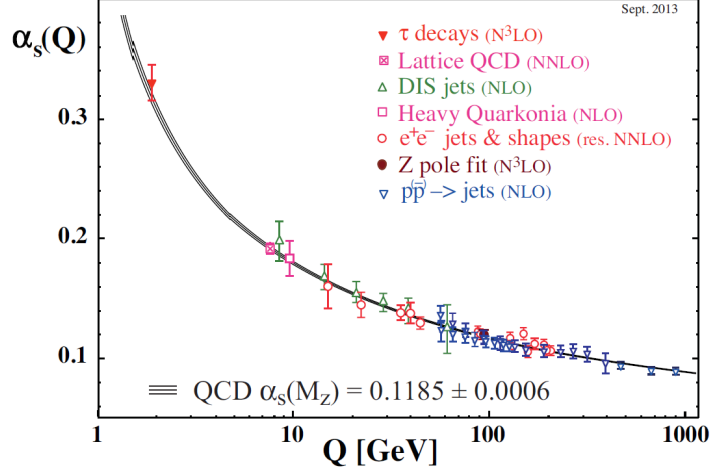
Figure 1.2: Individual measurements for the strong coupling constant $\alpha_s(Q)$ as a function of energy scale Q. The Figure is taken from ref [10].

where the scale parameter μ has the dimension of mass and can be conveniently chosen to effectively mimic the momentum transfer in the perturbative QCD (pQCD) approximation. The number of colors $n_c = 3$ enters in the gluon loop diagram and n_f is the number of active quark flavors. The strength of the interaction at a given momentum scale is determined by the measurable dimensionful parameter Λ_{QCD}^2. The theoretically allowed window for the value of Λ_{QCD}^2 lies in the range of $100 - 500$ MeV in the absence of precise experimental measurement. The experimentally extracted value of α_S from different experiments being compared with pQCD calculations is shown in Fig. 1.2 [10]. We can see that the effective coupling constant is finite at large distances, i.e. for small momentum transfer, and it increases with the distance between the quarks. As a result of which a very tight binding force acts between the quarks and couples them inside the hadrons. This property is popularly known as quark confinement. On the other hand, for large momentum transfer or as the distance between the quarks are very small, α_S values are quite small enough. This results in the quarks to behave like free particles within the scale of the QCD parameter. This behavior is termed as Asymptotic freedom of quarks.

1.2.2 A New Phase of Matter : Quark-Gluon-Plasma (QGP)

The asymptotic freedom nature of quarks has invoked the idea of a new phase known as the Quark-Gluon-Plasma (QGP) by T.D Lee in the year 1974 [11]. He suggested that at sufficiently

very high temperature or energy density over a relatively large volume, a deconfined state of quarks and gluons would exist as they behave as asymptotically free particles. The available degrees of freedom in this state are the color degrees of freedom. This deconfined state of matter is the quark-gluon-plasma state suspected to exist after few microseconds of Big-Bang in the early stage of the universe. This is a strongly interacting state of matter and behaves as an almost perfect fluid [12]. Owing to its strongly interacting nature, the QGP state sometimes has also been termed as sQGP.

Experimentally this condition can be achieved by high-energy heavy-ion collisions. Dedicated man made environment to create such a medium is provided by the experimental setup of Relativistic Heavy-Ion Collider (RHIC) at the Brookhaven National Laboratory and A Large Ion Collider Experiment (ALICE) by the Large Hadron Collider (LHC) at CERN.

1.2.3   QCD Phase Transition

With arguments in the QCD framework, we have ended up with two scenarios; one in which quarks are bound within hadrons and the other in which quarks and gluons behave like free particles within the volume of QGP. There are also Lattice QCD calculations supporting the existence of these two phases termed as hadron gas and the QGP. A probable phase transition
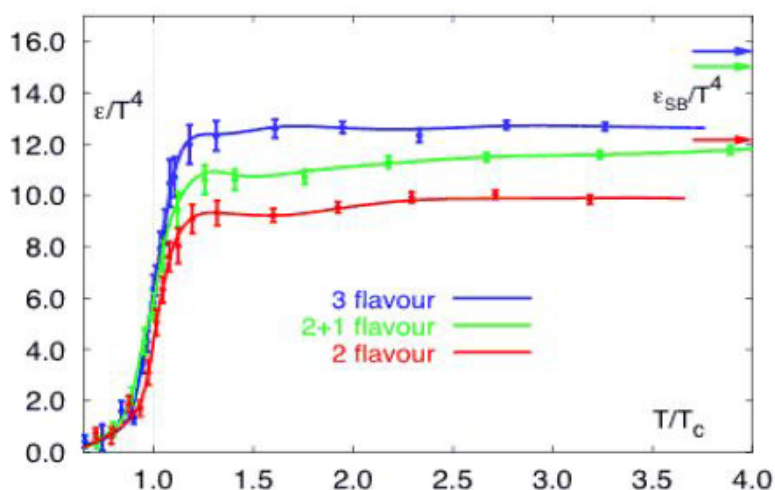
Figure 1.3: Calculations for the energy density $/T^4$ from lattice QCD as a function of temperature scaled by the critical temperature (T_c). The Stefan-Boltzmann limits are also shown as arrows on right side [13].

between these two phases has also been predicted. Figure 1.3 shows the energy density $/T^4$ as a function of temperature scaled by critical temperature (T_c) from lattice QCD calculations [13]. The right hand side arrows indicate the Stefan-Boltzmann limit. The mathematical expression for the energy density for a gas of massless hadrons from thermodynamical calculations is given as

$$\epsilon = g \frac{\pi^2}{30} T^4,$$

(1.2)

where g is the number of degree of freedom. For the hadron gas (HG) consisting of only massless pions which are found in 3 states, we have

$$\epsilon_{HG} = 3 \frac{\pi^2}{30} T^4$$

(1.3)

For the QGP medium of quarks and gluons, the expression for energy density can be rewritten as

$$
\begin{aligned}
\epsilon_{\text{QGP}} &= 2_{\text{spin}} \times 8_{\text{colors}} \times \frac{\pi^2}{30} T^4 + 2_{q-\bar{q}} \times 2_{\text{spin}} \times 3_{\text{colors}} \times n_f \times \frac{7}{8} \frac{\pi^2}{30} T^4 \\
\epsilon_{\text{QGP}} &= \left(16 + \frac{21}{2} \times n_f \right) \frac{\pi^2}{30} T^4
\end{aligned}
$$

(1.4)

Now, we can clearly observe that the number of degrees of freedom is considerably high for the QGP medium than the hadron gas. This explains a sudden rise in energy density in Figure 1.3 as there occurs a transition from hadron gas to QGP phase at a critical temperature of $T_c \sim 154$ MeV [14]. So, the divergence of the QCD order parameter confirms the hadron gas and liquid QGP phase transition.

1.2.4 The QCD Phase diagram

The observation of the phase transition from hadron gas to QGP and vice-versa, theorizes the unique phase diagram of QCD. This conjectured phase diagram as shown in Fig. 1.4 [15] is the relationship between temperature and baryon chemical potential. The line separating the
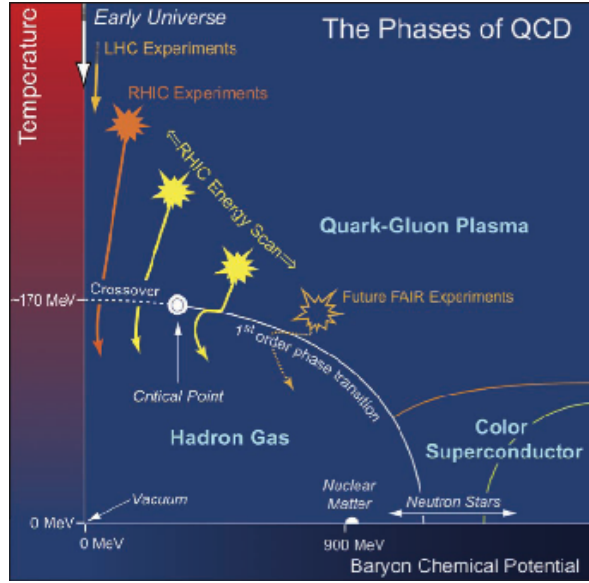
Figure 1.4: The contemplated phase diagram of QCD for strong interactions of nuclear matter.

hadron phase and QGP phase predicted from lattice QCD and QCD based model calculations is a first order phase transition line [16] and is known as the QCD phase boundary. At a very small value of baryon chemical potential (i.e. $\mu_B \approx 0$) represented by a dotted line, a rapid crossover with no real transition has been suspected between the hadron phase and QGP [17, 18]. The point at which the first order phase transition line terminates is suspected to be a second order phase transition. The corresponding temperature to this point is the famous, most hunted critical point (T_c) in the QCD phase diagram. QCD calculations also give a suggestive color-superconducting phase for the QCD matter at a higher value of baryon chemical potential [19].

The interest of the exploration of the QCD phase diagram and the search for the QCD critical point are the main notion of designated experiments like RHIC and ALICE. The experimental observables provided by lattice QCD calculations are the higher moments of conserved charges (Baryon number, Strangeness and charge). The correlation length of the QCD matter being associated with the moments gives important information about the QCD phase transition and critical point [20–24].

1.3 Heavy-ion Collisions

The experimental approach to create the hot and dense QGP medium is achieved by nucleus-nucleus collisions. The desired facilities for this being provided by experiments like RHIC and
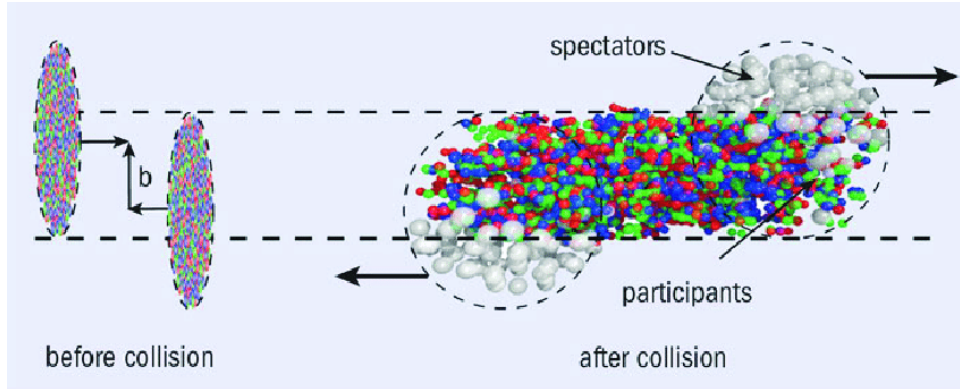
Figure 1.5: A schematic diagram depicting the before and after scenario of nucleus-nucleus collision. The concept of participant and spectator nucleons are also picturized [25].

LHC. The scenario which happens in such an experiment can be explained as follows.

In the center of mass frame, two bare nuclei are accelerated at a very high velocity approaching the speed of light. As a result of which they appear to be Lorentz contracted along the direction of the beam axis as depicted in Fig. 1.5 [25]. The region of overlap between the two colliding nuclei is parameterized by the impact parameter b. This is defined as the perpendicular distance between the centers of two incoming nuclei. The nucleons present within the overlapped region only take part in the collision and are termed as "participant" nucleons. The other nucleons outside the overlapped region remaining unaffected during the collision process are termed as "spectator" nucleons. The impact parameter scale is used to classify the centrality of the collision. The collisions having small impact parameter or larger overlapping area are classified as central collisions. On the other hand, the collisions with large impact parameter or smaller overlapping area are classified as peripheral collisions. The collisions having impact parameter between the two extremities are assigned with a centrality class in between them.

As the nucleus-nucleus collision occurs, a medium with very high energy density and temperature is created in a small volume. This medium rapidly thermalizes and the system is popularly called as a *"fireball"*. Next, the evolution of the system can proceed through two different circumstances as represented in the space-time diagram in Fig. 1.6 [26]. If the energy density is not high enough for the creation of a QGP medium, then a medium consisting of a gas of hadrons forms as manifested on the left hand side of Fig. 1.6. On the other hand if the energy density over shoots the critical value for the formation of QGP, a deconfined phase of QGP forms represented on the right hand side of Fig. 1.6 [27]. This highly interacting system

Figure 1.6: A schematic diagram manifesting the space-time evolution of the system formed in high-energy heavy-ion collision experiments [26, 27].

undergoes a rapid expansion as it evolves and cools down. The phase transition from the QGP phase to the hadron phase occurs. As this process takes a little time, there is supposed to be the presence of a mixed phase containing both QGP and Hadron gas. After further expansion, this mixed phase ends up with the existence of only the phase of hadron gas. This hadron gas expands and interaction among the particles continues to happen with decay and formation of new particles. After a certain time or temperature, the expanding system cools down enough that the energy for any such inelastic process to occur drops below the threshold. This stage is known as "*chemical freeze-out*" and is parameterized by the chemical freeze-out temperature T_{ch}. The particle abundance and type get fixed after this stage. Next, only elastic collision between the particles happens, which results in the change of momentum of various particles. The expanding medium at a certain point becomes so dilute that the particles cease to collide even elastically. This temperature/time is the stage of "*kinetic freeze-out*" characterized by the temperature T_{fo}. After this stage, the momentum of particles are fixed and the particles free flow towards the detector, where they are finally detected.

1.4 The Scientific Out Look of RHIC Program

The Relativistic Heavy Ion Collider (RHIC) experiment functioning at the Brookhaven National Laboratory is a dedicated scientific program to high-energy heavy-ion collisions. The study of the properties of the medium, the exploration of the QCD phase diagram, the hunt for the QCD critical point and of course a thirst for some new physics motivates the research program at RHIC.

From the early days of its set up it took data for Au+Au collisions at $\sqrt{s_{NN}} = 200$ GeV and provided many key physical features of the medium formed in heavy-ion collisions. The indications for the formation of the QGP medium has also been found out. Then, the plan went to address the next step questions about the structure of the phase diagram, phase properties and critical phenomena.

In order to explore the QCD phase diagram and to find signs of QCD critical point, RHIC has performed the first phase of its Beam Energy Scan Program (BES-I) in the years 2011-2012. It took Au+Au data at various center of mass energies $\sqrt{s_{NN}} = 7.7, 11.5, 19.6, 27$ and 39 GeV. Later, in the year 2014, Au+Au collisions at $\sqrt{s_{NN}} = 14.5$ GeV has been added to BES-I program. Bulk properties of the system like constituent quark scaling, suppression of high momentum hadron yields in central collisions, local parity violation and many have been featured [28]. The investigations for any critical behavior in the observables such as fluctuation in the conserved charged susceptibilities, directed flow of identified hadrons and azimuthally sensitive femtoscopy are carried out [29–36]. Most importantly, it scanned the $T - \mu_B$ plane of the QCD phase diagram near the suggested critical point [37]. To add more statistics to the observables or for more precise measurement the phase-II of the BES program has also been commissioned [38].

In addition to taking data in Au+Au collisions, RHIC has also made a flavor to add data from different systems. This is in order to investigate the system size and shape sensitiveness of the bulk properties of the system. Keeping this in view, RHIC has taken data for different systems like p+p, d+Au, He+Au, Au+Au, U+U, Cu+Cu and Cu+Au. Where, there is difference not only on the size of the colliding nuclei but also on the shape of the nuclei. For example, the Gold nucleus has nearly a spherical shape, but the Uranium nucleus has a prolate shape. This

geometrical difference of the nuclei size may strive a little new observation.

Gathering data from a vast area of energies and systems has added up the one-to-one competitive and interesting physics research goal to the RHIC program and is still ongoing.

1.5   Signatures of QGP Phase

The huge experiments designed to perform the high-energy heavy-ion collisions only delivers us pulses of electronic signal, which gives an impression of produced particles. The highly energetic fireball formed in the experiment being so short lived is out of direct human outreach. However, the finally observed particles carry the impression of the environment through which they have passed. So, even we have only the final products to deal with, but we can back interpolate the information about the medium. So, the careful investigation of the final observables as a bulk helps us to have a picture of the whole process through which the system has evolved. The various stages in high-energy heavy-ion collisions such as the QGP phase, the phase transition, the hadronic phase and the subsequent freeze-out of hadrons are thus back traced from their signatures on the final by products. In the succeeding sub-sections, we will briefly summarize some of the unique indications of the very interesting QGP medium formed in high-energy heavy-ion collisions.

1.5.1   Strangeness Enhancement

One observable concerned with the formation of the phase consisting of a dissolved sea of quarks and gluons is the production of a new quark flavor, which is strangeness. The initially colliding nuclei have only the stable valance 'u' and 'd' quarks bound within the nucleons. The only mechanism through which the final state can contain strange quarks within hadrons that, it has to originate from the medium. The enhancement of strange particles is one of the first proposed sign of the deconfined phase of quarks and gluons [39]. The mass of strange quarks and anti-quarks is of similar magnitude as that of the energy at which nucleons melts into quarks and gluons. This implies that the abundance of strange quarks is sensitive to the condition, structure and dynamics of the deconfined QGP phase. The dominant channel for the
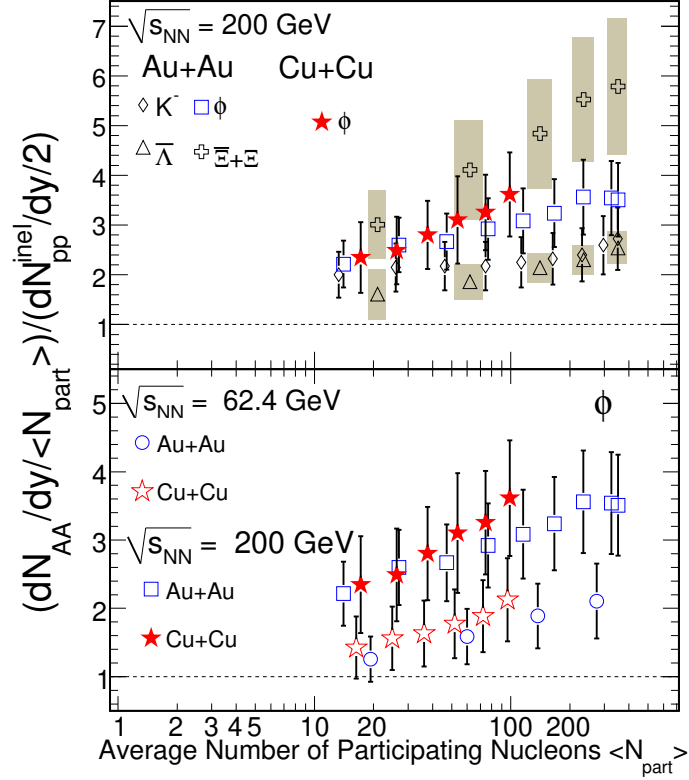
Figure 1.7: Upper panel : The fraction of yields of K^-, ϕ, $\bar{\Lambda}$, $\Xi + \bar{\Xi}$ in Au+Au and Cu+Cu collision at $\sqrt{s_{NN}} = 200\text{GeV}$ scaled by average number of participant nucleons ($\langle N_{\text{part}} \rangle$) w.r.t the corresponding yields in p+p collisions. Lower panel : It represents the same observable but for collision energy of $\sqrt{s_{NN}} = 62.4$ GeV

generation of strange quark flavor in the hot dense fluid of quarks and gluons is the gluon-fusion reaction $g\bar{g} \to s\bar{s}$ [39, 40].

The excitation function of strangeness is qualitatively investigated by calculating the ratio of kaon (K^+) yield to that of pion (π^+) yield. This ratio characterizes the relative abundance of strangeness over hadron multiplicity. The SPS experiment at CERN and STAR experiment at RHIC has observed the excessive production of kaons relative to pions upto three times the value in p+p collisions at the same energy [41–46].

The measured strangeness enhancement of a particular species of particle is experimentally evaluated as the ratio of strange hadron yield per participant nucleons in nucleus-nucleus collision to that of a small reference system like p+p collisions. The measurements from the STAR experiment for strangeness enhancement of K^-, ϕ, $\bar{\Lambda}$, $\Xi + \bar{\Xi}$ in Au+Au and Cu+Cu collisions with respect to p+p collisions as a function of the average number of participant nucleons is shown in Fig. 1.7. It is found that the ratio is greater than one and increases with centrality

as well as energy. Thus, the experimental observation indicates the formation of a deconfined phase with enhanced production of strange quarks.

1.5.2 Quarkonia Suppression

The charm quark (c) (or bottom quark (b)) is ten (or forty) times heavier than the strange quark. Hence the threshold of energy needed for the production of charm quarks can only be available at a very initial stage of the collision. If QGP forms, the $c\bar{c}$ pair or $b\bar{b}$ pair so produced will be submerged in the sea of various other quarks and gluons. The other lighter quarks and gluons in the surrounding of a charm or anti-charm quark (bottom or anti-bottom quark) will thus weaken the binding between charm and anti-charm pair. This effect is known as Debye's color screening [47]. There are various bound states of c and $\bar{c}$ or b and $\bar{b}$ which are nomenclatured as Quarkonia particles such as J/Ψ, Υ, Υ', Υ''. The strong suppression of Quarkonia production in heavy-ion collisions was first predicted by Matsui and Satz and is one of the prominent indications to the QGP medium known as Quarkonia suppression [48]. The significance of suppression depends on the binding energy of Quarkonia particles and the temperature of the
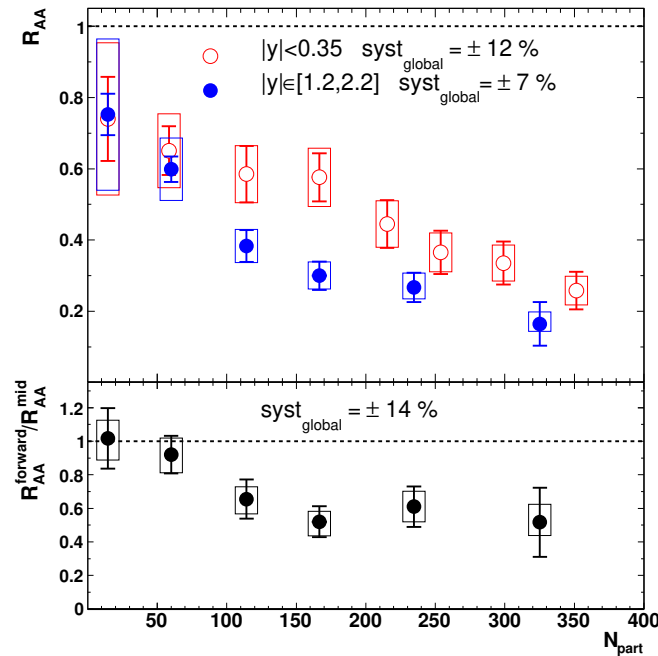
Figure 1.8: Upper panel : R_{AA} of J/Ψ in Au+Au collisions at $\sqrt{s_{NN}} = 200$ GeV as a function of N_{part}. The mid rapidity and forward rapidity data are respectively shown in open and solid symbols. Lower panel : Ratio of J/Ψ R_{AA} in forward rapidity to mid-rapidity as a function of N_{part} [52].

QGP medium. This suppression leads to the occurrence of open charm or open bottom quarks combined with other light quarks instead of bound states of c$\bar{\text{c}}$ pair or b$\bar{\text{b}}$ pair at the final stage.

The yield of the bound state of c$\bar{\text{c}}$ known as J/Ψ is extensively studied at the CERN SPS in Pb+Pb and In+In collisions [49, 50] and at RHIC experiment in Au+Au collisions [51, 52]. The J/Ψ suppression is expressed by the nuclear modification factor R_{AA} as a function of the number of participant nucleons N_{part}. This is the yield of J/Ψ in Au+Au collisions relative to p+p collisions as shown in Fig. 1.8 for Au+Au collisions at $\sqrt{s_{NN}} = 200$ GeV [51, 52]. A significant suppression of J/Ψ yield in Au+Au collisions relative to p+p collision is observed for central collisions.

Another proposed effect to study the presence of QGP medium by the J/Ψ production is known as J/Ψ regeneration [53]. Depending on the absolute abundance of open charm, there is a possibility of in-plasma production of J/Ψ. Observation of this new mechanism of formation of J/Ψ would contribute to the proof of mobility of the charmed quarks in the hot dense medium. The R_{AA} of J/Ψ can also be investigated through this regeneration mechanism [54].

1.5.3   Jet Quenching

The disappearance of jets of hadrons produced form the interaction of hard quarks and gluons during initial interaction in heavy-ion collisions is known as *jet quenching*. The jets consist of highly energetic clutch of particles within a narrow cone from hard scattering. Obeying the momentum conservation, the hadron jets are produced back to back as pictorially depicted in Fig. 1.9 for a A+A collision known as dijets. The in-medium effects of the hot dense quark gluon plasma are due to both elastic [56] and non-elastic processes such as gluon radiation [57]. The high momentum partons are more strongly subjected to this high gluon density inside QGP [58]. As a result of this interaction, the sub-leading jets gets absorbed in the QGP medium in A+A collision termed as the "quenched jet". In, small systems like p+p or d+Au, where there is no QGP, such an in-medium interruption is absent and hence no "jet quenching" is expected.

This interesting dissolution of jets in heavy-ion collision can be experimentally captured from the measurement of dihadron azimuthal correlations for high p_T particles. This quantity is measured for hadrons with $p_T > 2$ GeV/c in reference to a triggered hadron with
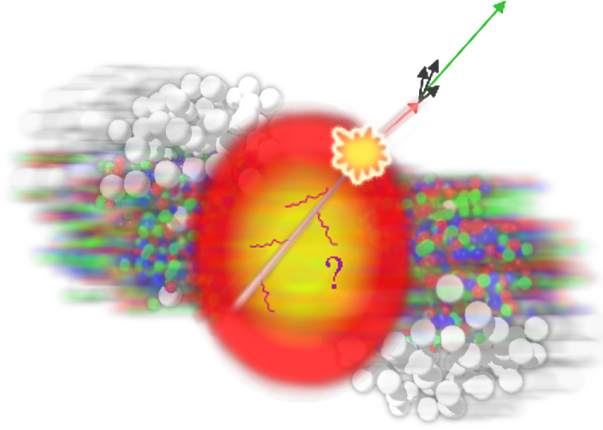
Figure 1.9: The two back-to-back jets produced initially in heavy-ion collision traveling in opposite directions. One of the two leading jets survives, whereas as the other sub-leading jet disappears in the medium being suffered from strong interaction in the colored charge plasma [55].

$p_T^{trig} > 4$ GeV/c by the STAR collaboration in p+p, d+Au and Au+Au collisions shown in Fig. 1.10 [59]. As can be seen from the Fig. 1.10, the away side jet in Au+Au collision is absent demonstrating the jet quenching effect in heavy-ion collision. In contrary to it, this away side jet is present in p+p and d+Au collisions, where there is no QGP.
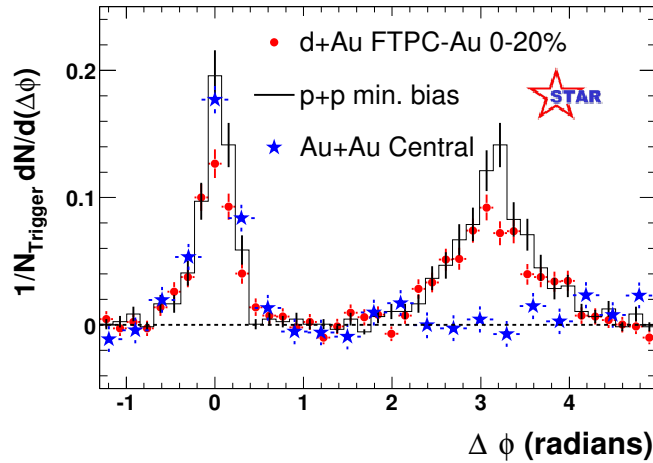
Figure 1.10: Measured dihadron azimuthal correlation in p+p, central d+Au and central Au+Au at $\sqrt{s_{NN}} = 200$ GeV by the STAR experiment at RHIC [59].

Another way to quantify the jet quenching effect is the nuclear modification factor (R_{AA}) which is defined as the ratio of a specific hadron yield in nucleon-nucleon collision to the corresponding p+p collision
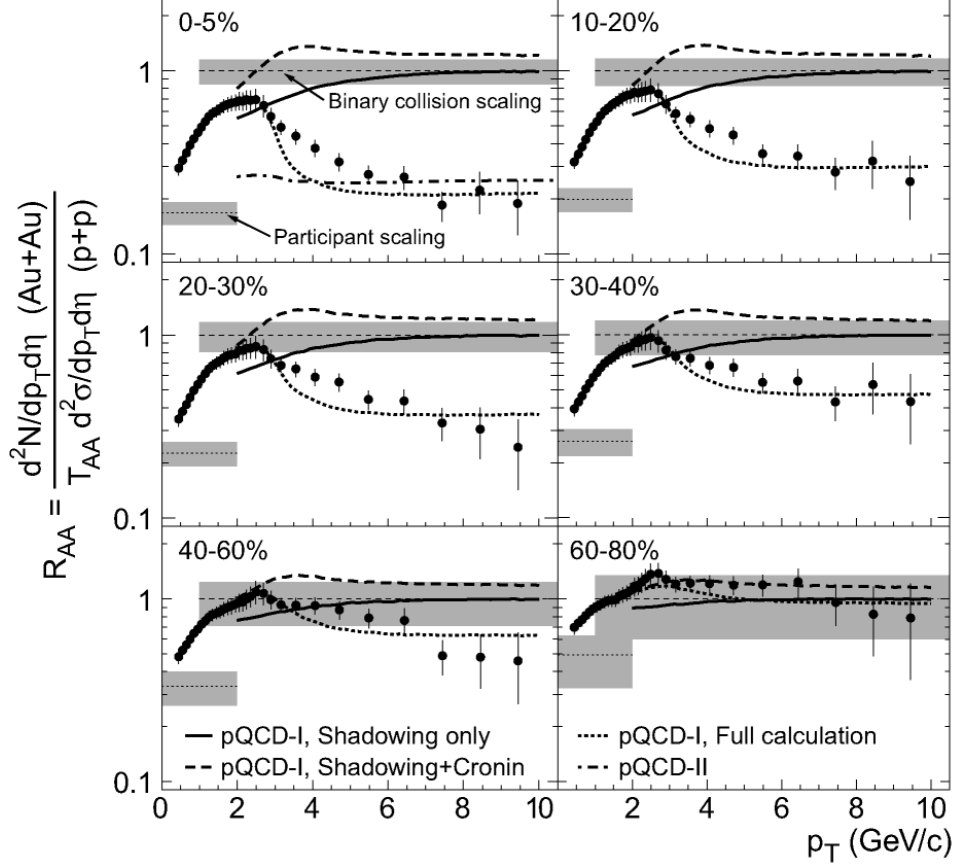
Figure 1.11: R_{AA} of charged hadron pairs in mid-rapidity ($|y| < 0.5$) in different centrality classes in Au+Au collisions relative to p+p collisions [60].

$$R_{AA} = \frac{1}{\langle N_{\text{coll}} \rangle} \frac{Yield_{AA}}{Yield_{pp}} \tag{1.5}$$

$\langle N_{\text{coll}} \rangle$ is the average number of nucleon-nucleon binary collisions. In the absence of any in-medium effect, R_{AA} in AA collisions is expected to be a multiplicative of pp collision with a value near unity at high p_T, where hard scattering predominantly occurs. R_{AA} is observed by the STAR experiment with respect to p_T in Au+Au collisions relative to p+p collisions at $\sqrt{s_{NN}} = 200$ GeV is shown in Fig. 1.11 [60]. As can be clearly seen, the value of R_{AA} is significantly lower than unity above $p_T > 6$ GeV/c for each collision centrality. The suppression is more visible for central collision where the in-medium effects were assumed to be most prominent. The results from Cronin enhancement and shadowing demonstrating the parton energy loss in the dense plasma medium alone can not explain this suppression. Moreover, observations at LHC [61] have found more suppression than RHIC. The suppression of R_{AA} of high p_T particles in central collisions is taken as one of the trademark of the deconfined phase [57, 62].

1.5.4 Direct Photons

Direct photons usually come out from the electromagnetic decay through gluonic channels :$q\bar{q} \to \gamma g$, $gq \to \gamma q$, $q\bar{q} \to \gamma\bar{q}$ in the quark-gluon-plasma. They are at first sight considered as a promising probe to the deconfined phase [63]. Photons interact electromagnetically as a result of which it will not be subjected to the strong interaction in the QGP medium. So, the final state primary spectra of direct photons is expected to remain unaltered. Hence, it carries most of the information about the initial stage and of the medium through which it passes.

The difficulty arises from the experimental side since a huge background is associated with the measurement of direct photons. Especially, the photon coming from the decay of π^0 forms the huge background. If the background could be subtracted out, the direct photon will act as the information carrier of the dynamics of the hot dense plasma and the evolution of the system.
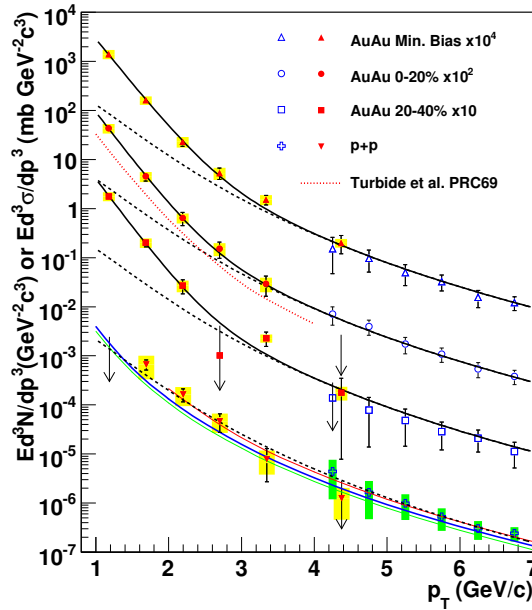
Figure 1.12: The invariant cross-section and yield of direct photon in p+p collisions and Au+Au collisions at $\sqrt{s_{NN}} = 200$ GeV as a function of p_T reported by the PHENIX experiment [64].

Direct photon measurements were carried out by the PHENIX experiment in Au+Au collisions at $\sqrt{s_{NN}} = 200$ GeV as shown in Fig. 1.12 [64]. The next to leading order pQCD (NLO pQCD) is also plotted [65]. The theoretical calculations from pQCD within uncertainty explains the direct photon yield in p+p collisions for $p_T > 2$ GeV/c. The results from Au+Au collisions are higher than p+p and scaled by T_{AA} for $p_T < 2.5$ GeV/c. This indicates that at
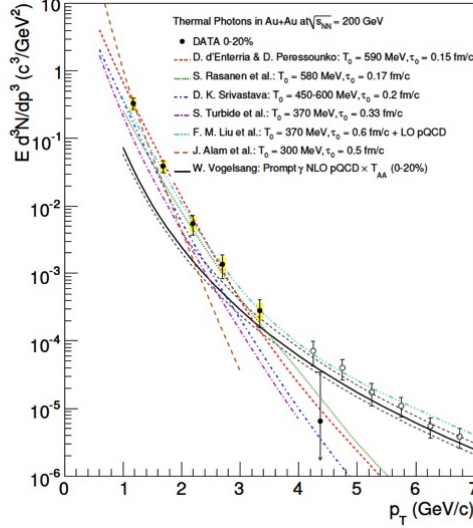
Figure 1.13: A comparison of theoretical calculations of thermal photon emission with the direct photon data in $0-20\%$ centrality from Au+Au collisions at $\sqrt{s_{NN}} = 200$ GeV [67].

low p_T, the direct photon yield increases substantially faster in A+A collisions than in p+p collisions scaled by p+p cross-section. The thermal photon spectrum calculated with initial temperature $T_{init} = 370$ MeV in Au+Au collisions is shown by red dotted curve [66]. A comparison of direct photon data in $0-20\%$ centrality from Au+Au collisions at $\sqrt{s_{NN}} = 200$ GeV and theoretical calculations of thermal photon emission is shown in Fig. 1.13 [67]. These models assume a chemically thermalized medium of hot dense QGP medium. The thermallization time being in the range $\tau_0 = 0.6$ fm/c to 0.15 fm/c corresponding to temperature range $T_{init} = 300$ MeV to 600 MeV. So, the measured direct photon spectra qualitatively justify the presence of a deconfined phase of quark-gluon-plasma.

1.5.5 Azimuthal Anisotropy or Flow

Situations are not always simple, symmetric and isotropic in nature. Rather its complex, asymmetric and anisotropic behavior fills up the research with more enthusiasm as the case of heavy-ion collision. The anisotropic flow of produced particles in non-central heavy-ion collision adds up a flavor to the study of the hydrodynamic evolution of the system.

The overlapped region in a non-central heavy-ion collision appears to be oval shaped after the collision as depicted in Fig. 1.14. As a result of which a spatial anisotropy is developed. This means particles along the short axis are subjected to more force than those along the
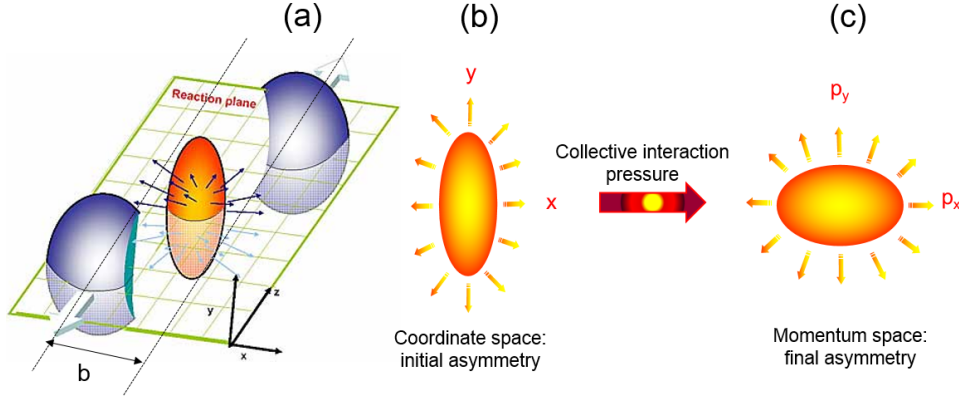
Figure 1.14: A pictorial representation showing the conversion of initial stage spatial anisotropy to final state momentum anisotropy.

long axis. This difference in pressure gradient resulting from the initial spatial dynamics is converted into the final state momentum dynamics [68, 69]. Hence, the collective expansion or *flow* of particles is expected to provide some valuable information about the formation of the deconfined phase of QGP in non-central heavy-ion collisions. The quantitative formulation of the azimuthal anisotropy can be written by viewing the azimuthal distribution of produced particles with respect to the *reaction plane*. Where the reaction plane is defined as the plane containing the beam axis and the direction of impact parameter. Thus, mathematically the azimuthal distribution of particles can be written by a Fourier series as

$$E\frac{d^3N}{d^3p} = \frac{1}{2\pi}\frac{d^3N}{p_T dp_T dy}\left(1 + \sum_{n=1}^{\infty} 2v_n \cos(n[\phi - \psi_r])\right),\qquad(1.6)$$

where ψ_r is the reaction plane angle and v_n is the nth order harmonic of flow coefficient. The first term characterizes the "isotropic flow", the first harmonic v_1 is known as the "directed flow" and the second harmonic is named as "elliptic flow".

1.5.5.1 Directed Flow

The pressure developed during the overlap of the colliding nuclei affects mostly the particles in forward and backward rapidities. It is a very early time phenomena in high-energy heavy-ion collisions. Directed flow is the measure of such side wise motion of the produced particles and acts as the messenger of the early time of collision [70]. The presence of a "softest point" in the equation of state is correlated with the first order phase transition and of course, the impulse of
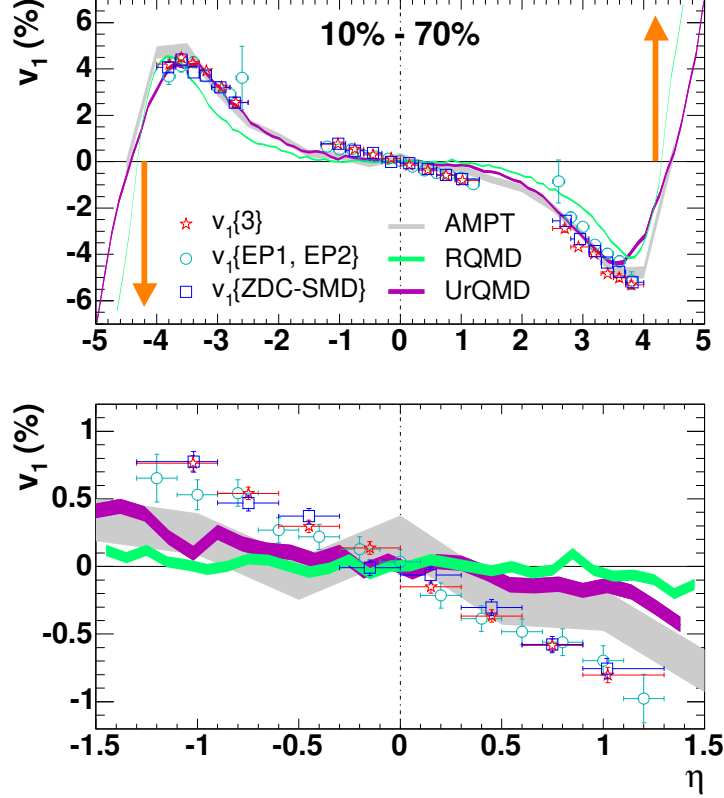
Figure 1.15: Upper panel : Directed flow of charged hadrons as a function of rapidity measured by the STAR experiment [77]. Bottom panel : The zoomed version of upper panel in the mid-rapidity region.

expansion of matter during the transition becomes substantially weak [71, 72]. It is advocated that a minimum in the directed flow as a function of beam energy is the experimental measure of the softening of the equation of state [73, 74]. And it is suggested as a distinct sign of the QGP phase [75].

Assuming the QGP, hydrodynamic calculations have demonstrated that, directed flow as a function of rapidity crosses "0" three times around mid-rapidity near central collisions showing a zig-zag nature. This zig-zag feature of $v_1(y)$ is characterized by an inclined ellipsoidal expansion of the fluid with QGP [76].

The measurements of charged particle v_1 in Au+Au collisions at $\sqrt{s_{NN}} = 62.4$ GeV in $10 - 70\%$ centrality as a function of rapidity y is shown in Fig. 1.15 [77]. Results are obtained from three different methods as shown in Figure 1.15, which are consistent with each other. Model calculation from AMPT [78], RQMD [70] and UrQMD [79] for the same beam energy, system and centrality are also shown for comparison purposes. As can be inferred from the

Fig. 1.15, the models under predicts the data in mid-rapidity, but are in agreement with the data at higher rapidity. The measurements in Fig. 1.15 does not show a prominent zig-zag nature as discussed before.

1.5.5.2 Elliptic Flow

The non-uniformity in the flow of particle in all directions in heavy-ion collision is measured by the observable "elliptic flow". Since the spatial anisotropy is maximum at the very beginning of the collision, elliptic flow is essentially sensitive to the early stage dynamics. So, the elliptic flow represents a very early stage phenomenon carrying the information of the journey from partonic to hadronic level [80]. v_2 is a powerful tool to peer into the QGP medium since it can be easily measured experimentally for a wide range of particles.

The experimental technique to calculate v_2 is from transverse momentum and azimuthal angle of the detected particles

$$v_2(p_T) = \langle \cos(2(\phi - \Psi_2)) \rangle_{p_T} \tag{1.7}$$

The STAR experiment has measured the v_2 of identified hadrons in Au+Au collisions at $\sqrt{s_{NN}} = 200$ GeV [81] as shown in Fig. 1.16 with the results from hydrodynamic model [82]. As can be observed from the figure for $p_T > 2$ GeV/c, the value of v_2 remains almost constant at dif-
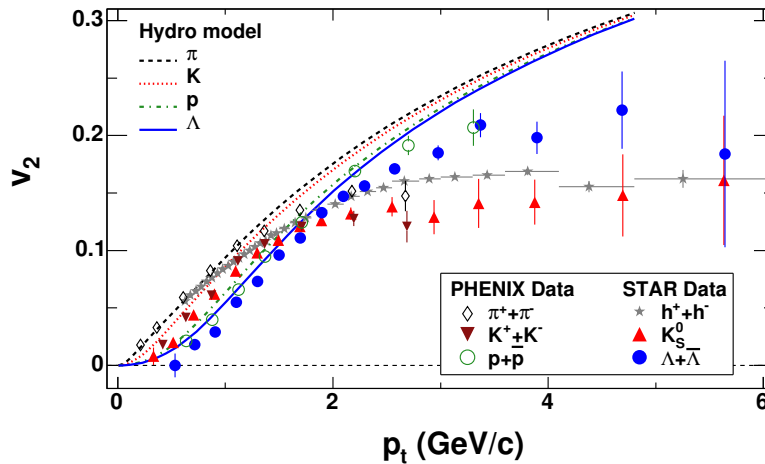
Figure 1.16: Elliptic flow v_2 as a function of p_T for minimum bias Au+Au collisions at $\sqrt{s_{NN}} = 200$ GeV measured in STAR [81]. The dotted and solid lines represents the model calculations for the same system and energy [82].

ferent values for mesons and separately for baryons. This splitting in the level of saturation in v_2 of mesons and baryons gives useful information about the flow of baryons and mesons. To understand more about this, an idea of "constituent quark scaling" (NCQ scaling) has been
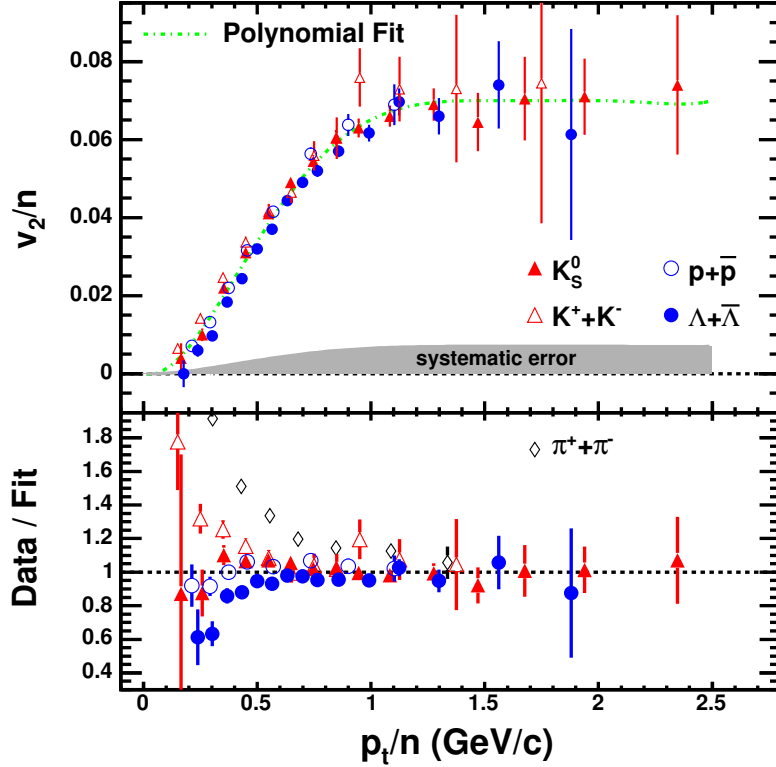
Figure 1.17: Top panel : v_2/n as a function of p_T/n measured by the STAR experiment for various identified hadrons [82]. n is the number of constituent quark which is 3 for baryons and 2 for mesons. The dashed-line represents the polynomial fit to the data. Bottom panel : The ratio of measured data in top panel to the polynomial fit as a function of p_T/n.

developed. i.e. the value of v_2 for a particle is divided by the number of constituent quarks (n) of that particle. For baryons, n = 3 as there are three quarks inside a baryon and for mesons n comes out to be 2 being composed a quark and anti-quark pair. This scaling has been represented by Fig. 1.17 from the results of STAR in Au+Au collisions at $\sqrt{s_{NN}} = 200$ GeV along with polynomial fit by dashed-line. To view the scaling, the data has been normalized by the fit function and is plotted in the bottom panel. As can be clearly inferred from the figure, except the v_2 of pion, the v_2 of all other particles respects the constituent quark scaling. The deviation of pion v_2 from NCQ scaling could be attributed to the large contamination to pion yield from resonance decays [83]. This NCQ scaling is an indication of the QGP medium and supports the idea of generation of hadrons via coalescence of constituent quarks [84]. This means that,

v_2 is associated at the quark level and gets added up at the hadronic level.

1.6   Identified Particle Production

The huge experiments built for the study of the medium in high-energy heavy-ion collisions give only electronic pulses as the output. This electric current is the impression of a hit of a produced particle on the detector. The history of the particle is then back traced by the application of tools and techniques. So, the first measurement is to count the number of particles falling on the detector and thereafter identification of their type and species. A particle is associated with the basic physical observables like charge, mass, energy and momentum. The charge and mass of the particle distinguishes various particle species. The particle after its identification from its physical property is called as an "identified particle". This is the first step in the backward tracing of the history of the processes in high-energy heavy-ion collisions. Thereafter all the calculations of the bulk properties of the system and understanding the collision dynamics follows.

Some of the physical observables concerned with this thesis work are transverse momentum spectra, average transverse momenta, particle yields and ratios. The extraction of chemical and kinetic freeze-out parameters from the yields of the particles is included as a primary part of the analysis in this thesis. The selected species of particles for the analysis are particularly $\pi^{\pm}$, $K^{\pm}$ and $p(\bar{p})$.

1.6.1   Transverse Momentum Spectra

For a particular species, then the number of particles counted exhibits a momentum distribution in a wide momentum range. So at first, the particle is analyzed through its dependence on the momentum. Due to this, the yield of the identified particles is generally observed as a function of the transverse momentum p_T. The generally accepted way for the expression of transverse momentum spectra is by calculating the invariant yield (Lorentz invariant yield) given by

$$E\frac{d^3N}{dp^3} = \frac{1}{2\pi p_T}\frac{d^2N}{dp_T dy},$$

(1.8)

where E is the energy of the particle and $d^2N/(dp_T dy)$ represents the particle event averaged yield. The transverse momentum spectra are characterized by evaluating particle yield (dN/dy) and average transverse momentum ($\langle p_T \rangle$). This spectra hides within it all the information of the system.

1.6.2 Particle Yields and Ratios

The step-by-step processes of calculation of bulk properties of the system includes at the very next step the extraction of particle yield within a particular rapidity window forms the measured transverse momentum spectra. Usually, the yields are summed up in the measured p_T region and then extrapolated to unmeasured regions of p_T through a suitable functional fitting. Particle yields serve as a beautiful probe to understand the collision dynamics of the system. Here, we
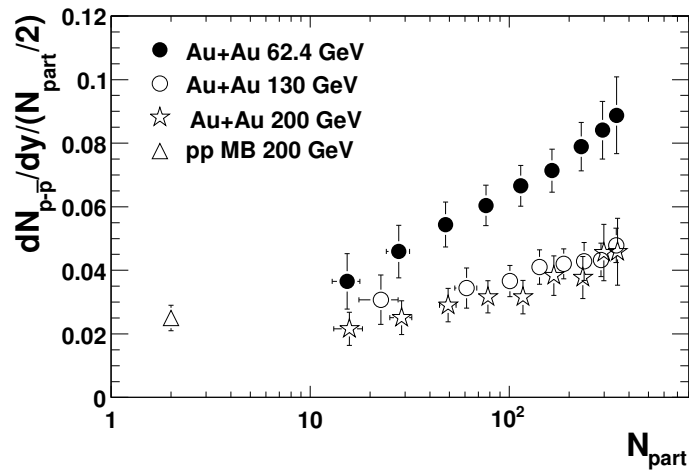
Figure 1.18: The net proton yield ($p - \bar{p}$) scaled by ($N_{\text{part}}/2$) as a function of N_{part} for p+p collisions at $\sqrt{s_{NN}} = 200$ GeV and Au+Au collisions at $\sqrt{s_{NN}} = 62.4$, 130 and 200 GeV measured by the STAR experiment at RHIC [85].

will look at the beam energy dependence of particle yields like protons. It is seen that in low energy heavy-ion collision the incoming nuclei experience a significant stopping during collisions. The increase of the energy of the colliding nuclei reduces this effect and the nuclei become more permeable. This phenomenon can be visualized from the dependence of net proton yield ($p-\bar{p}$) scaled by ($N_{\text{part}}/2$) as a function of N_{part} at different center of mass energies as shown in Fig. 1.18 [85]. This clearly demonstrates the dependence of stopping and baryon transport varies with collision energy.
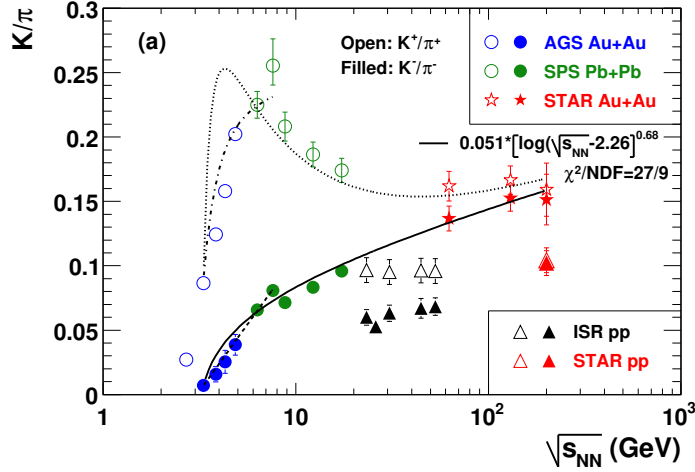
Figure 1.19: The K^+/π^+ and K^-/π^- ratios as a function of collision energy measured by various experiments at AGS, SPS, RHIC and LHC energies [85]. The curves passing through the data are from calculations from phenomenological fits.

The calculated particle yields are then used to obtain the ratios. Particle ratios with similar flavors as well as with different flavors are constructed. A very interesting behavior is captured in the K/π ratio as a function of collision energy measured at various experiments like AGS, SPS, RHIC and LHC shown in Fig. 1.19 [85]. A sharp increase of K^+/π^+ ratio is observed at lower energy where the particle production is mainly governed by associated production. Then this ratio falls up again after reaching a maximum with energy around 8 GeV. At higher energies, particle production mechanism is mainly governed by pair production. The peak at ~ 8 GeV is referred as the "horn" of the K^+/π^+ ratio. This weird behavior of K^+/π^+ ratio can be attributed to the phase transition between hadrons and QGP [86].

1.6.3 Average Transverse Momentum

Average transverse momentum ($\langle p_T \rangle$) of a particular particle species calculated from its p_T spectra qualitatively describes its shape or sharpness of fall with p_T. The predictive measurements in this context are carried out by various experiments involving various systems of collision at a wide range of energy. Fig. 1.20 is a representative plot for such a $\langle p_T \rangle$ measurement by the STAR experiment at RHIC [85] for π^-, K^- and $\bar{p}$. The dependence of $\langle p_T \rangle$ on particle species, centrality with a little dependence on beam energy can be inferred from the figure. Mainly speaking the dependency of $\langle p_T \rangle$ with $dN_{ch}/d\eta$ manifests the effects of multiple

scattering, transverse radial flow and also (semi)hard scattering [85].
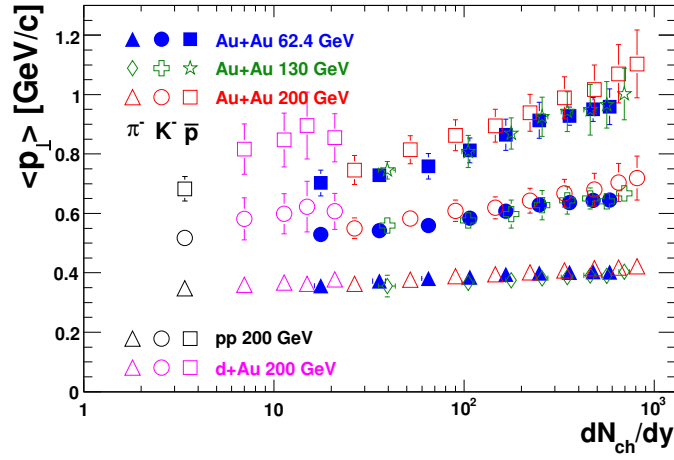
Figure 1.20: Mean-p_T as a function of centrality in p+p and d+Au collisions at $\sqrt{s_{NN}} = 200$ GeV and in Au+Au collisions at $\sqrt{s_{NN}} = 62.4, 130, 200$ GeV [85].

The observables like transverse momentum spectra, particle yields, average transverse momentum and particle ratios will be discussed in this theses in subsequent chapters.

1.7 Freeze-out Conditions

The evolution of the system in high-energy heavy-ion collisions is associated with two different experimentally accessible states known as chemical and kinetic freeze-out stages. With the passage of time the later stage follows the former. Experimental tools and techniques are quite developed in the study of the stages of freeze-out conditions in heavy-ion collisions. These studies generically improve our understanding of particle dynamics after hadronization. It is also identified that the chemical freeze-out occurs very close to the phase transition line. Hence, it may inform about some useful characteristic of the phase transition. A brief discussion about these two freeze-out stages and a summary of the past results in this context are discussed below. This provides the basic motivation for the presented analysis of the thesis in the later chapters.

1.7.1 Chemical Freeze-out

This chemical freeze-out stage in high-energy heavy-ion collision represents the point of the expansion after which the abundance of particles of the system freezes. i.e. inelastic processes happening in the hadronic phase stops due to a significant fall of temperature needed for such processes to occur. The surface is mainly characterized by the chemical freeze-out temperature T_{ch} and the baryon chemical potential μ_B. Where the μ_B represents the energy content of the baryons in the medium.

To explain the stage of chemical freeze-out, various thermodynamical models have been designed assuming a thermally and chemically equilibrated system of hadrons. These models use the information of particle yields or ratios as the input to extract the chemical freeze-out parameters [87]. In addition to the chemical freeze-out temperature T_{ch} and baryon chemical potential μ_B, another two parameters μ_S and μ_Q respectively defined as the strangeness chemical potential and charge chemical potential are also incorporated in the statistical models. Another parameter γ_s known as the strangeness saturation factor counting for any non-equilibrium production of strangeness is also included in some of the thermodynamical models.

The statistical thermal model proves to be very successful in describing the measured hadron yields including non-strange, strange and multi-strange hadrons [88]. The results of T_{ch} and μ_B from the thermal model fits to the measured hadron yields at SIS, AGS, SPS, top
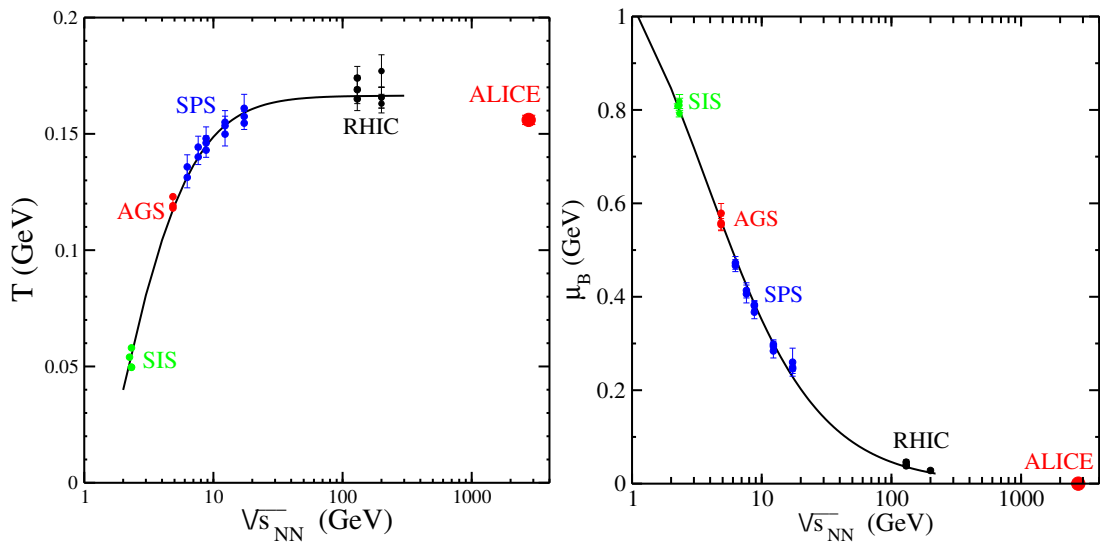
Figure 1.21: The variation of T and μ_B as a function of beam energy with the solid curves representing theoretical predictions [89].

65
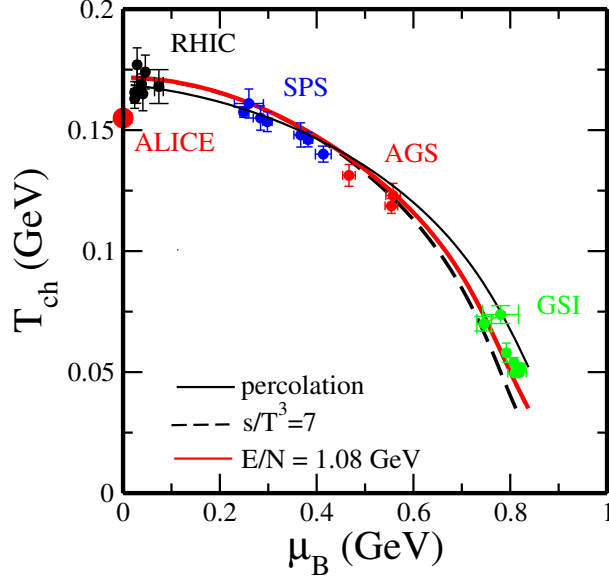
Figure 1.22: The correlated plot of T_{ch} and μ_B along various beam energies AGS-LHC [89]. The curves represents the theoretical calculation from various thermodynamical models [90].

RHIC and LHC energies as a function of collision energy is shown in Fig. 1.21 [89]. From the left plot of Fig. 1.21, it is observed that T_{ch} attains approximately a saturated value above SPS energies, which could be due to the fact that freeze-out is happening very close to the phase transition temperature. However, at lower energies it is predicted that the equilibrium time after phase transition is probably longer. The right plot of Fig. 1.21 shows the behavior of μ_B showing a fall off with collision energy. This is due to the fact that nuclear stopping decreases with increasing collision energy leading to net-baryon density to approach zero. The obtained values of T_{ch} and μ_B can be viewed as a correlated plot in the $T_{ch} - \mu_B$ plane as shown in Fig. 1.23. As can be seen, there are experimental measurements available covering a wide range of phase space of the $T_{ch} - \mu_B$ plane. Measurements are still ongoing to cover the remaining gap, also a part of this thesis analysis.

1.7.2   Kinetic Freeze-out

The progressive expansion of the fireball stages the medium to the kinetic freeze-out stage. At this stage, the system becomes so dilute that any elastic collision among the particles becomes impossible. As a result of this, the momentum of each particle ceases, after which the particles free flow to the detector. This stage called the kinetic freeze-out stage and is characterized
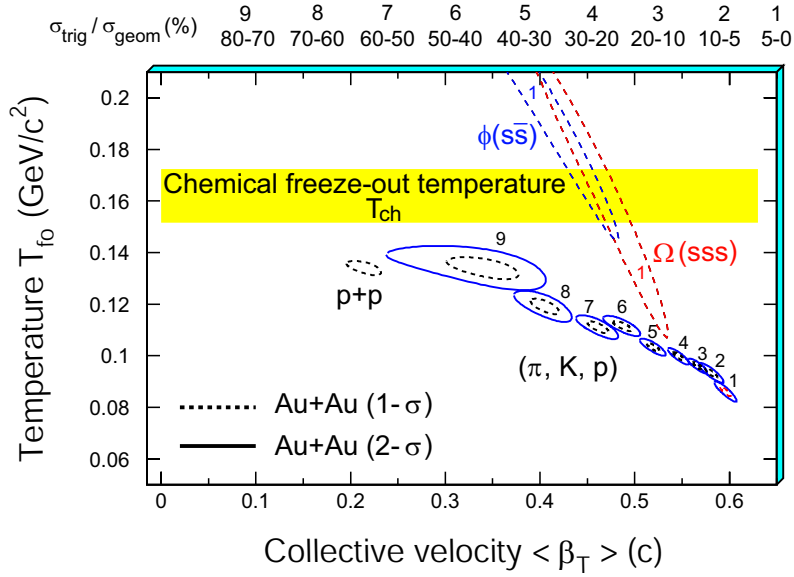
Figure 1.23: The χ^2 contours of T_{fo} and β obtained from thermal and radial flow fits for a variety of hadron species produced in Au+Au collisions at $\sqrt{s_{NN}} = 200$ GeV [59].

by the kinetic freeze-out temperature T_{fo} and the average flow velocity $\langle\beta\rangle$. β represents the radial flow velocity of the measured particles, demanding the system to be in hydrodynamic equilibrium. The transverse momentum spectra of the particles carry information about this stage and are used to extract the kinetic freeze-out parameters. Hydrodynamics based Blast-wave model is usually used to fit the particle p_T spectra to extract the values of T_{fo} and $\langle\beta\rangle$ [68, 91]. An earlier thermal and radial flow fit result for Au+Au collisions at $\sqrt{s_{NN}} = 200$ GeV is shown in Fig. 1.23 [59], which represents the χ^2 contours of T_{fo} and $\langle\beta\rangle$. The calculations including non-strange hadrons π^+, K^+, p and their anti-particles in the fitting gives higher values of flow velocity, whereas the inclusion of strange hadrons ϕ and Ω gives a relatively lower value of $\langle\beta\rangle$. This is a suggestive of the fact that, a rapid expansion of the medium is inferred after chemical freeze-out for the particles like π, K and p, whereas for Ω and ϕ this effect is reduced.

In the previous two sections, so far we have discussed some selected signatures of the QGP and status of observables directly related to the thesis. Most of the examples chosen are from STAR experiment at RHIC and PHENIX at RHIC. Similar results and newer results exists for other experiments and for the LHC experiments. Those we have not discussed in this chapter.

1.8 Thesis Layout

The thesis proceeds further with the motivation that, till now physics is not saturated, though it appears to the unscientific look. There is a lot to find out and investigate. Moreover, there always is a demand for the broadening of the framework of research for better understanding of the observations/theoretical predictions.

The thesis chapters hereafter are coordinated as follows. Chapter 2 summarizes the experimental platform used for the analysis in subsequent chapters 3 and chapter 4. i.e., it deals with the specification of the details of the STAR detector at RHIC. The subsequent two chapters hold the results of analysis on identified particle production and freeze-out dynamics in Au+Au collisions at $\sqrt{s_{NN}} = 14.5$ GeV and U+U collisions at $\sqrt{s_{NN}} = 193$ GeV respectively. A study of the thermal models in extracting the chemical freeze-out conditions in small systems like p+p collisions is presented in chapter 5. Chapter 6 is concerned with the observation of changes in the extraction of chemical freeze-out parameters by adding the unconfirmed resonances from PDG into the hadron resonance gas model. Finally, the last chapter summarizes all the results with a conclusion derived from the analysis carried out in this thesis work.

Bibliography

[1] S. L. Glashow, Nucl. Phys. **22**, 579 (1961); A. Salam and J. C. Ward, Phys. Lett. **13**, 168 (1964); S. Weinberg, Phys. Rev. Lett. **19**, 1264 (1967).

[2] P. W. Higgs, Phys. Lett. **12**, 132 (1964); Phys. Rev. Lett. **13**, 508 (1964); F. Englert and R. Brout, Phys. Rev. Lett. **13**, 321 (1964).

[3] G. Aad *et al*. (ATLAS Collaboration), Phys. Lett. B **716**, 1 (2012).

[4] W. Adam *et al*. (CMS Collaboration), Phys. Lett. B **716**, 30 (2012).

[5] http://united-states.cern/physics/standard-model-and-beyond.

[6] H. Kastrup, P. Zerwas, eds., QCD 20 yrs later World Scientific, Singapore (1993); D. J. Gross and F. Wilczek, Phys. Rev. Lett. **30**, 1343 (1973); H. Politzer, Phys. Rev. Lett. **30**, 1346 (1973).

[7] J. Schwinger, Phys. Rev. Lett. **73**, 416 (1948); J. Schwinger, Phys. Rev. Lett **74**, 1439 (1948); R. P. Feynman, Phys. Rev. Lett **76**, 769 (1949); R. P. Feynman, Phys. Rev. Lett **80**, 440 (1950); F. Dyson, Phys. Rev. Lett. **75**, 1736 (1949).

[8] S. L. Glashow, Nucl. Phys. **22**, 579 (1961); A. Salam and J. C. Ward, Phys. Lett. **13**, 168 (1964); S. Weinberg, Phys. Rev. Lett. **19**, 1264 (1967).

[9] D. Gross and F. Wilczek, Phys. Rev. Lett. **30**, 1343 (1973); Phys. Rev **D 8**, 3633 (1973).

[10] G. Dissertori, [Hep-Ex], arXiv:**1506.05407**, (2015).

[11] G. Baym, Nucl. Phys. **A 698, XXIII** (2002).

[12] Barbar Jack and Peter Steinberg, Physics Today **63**, 5, 39 (2010).

[13] F. Karsch, Nucl. Phys. **A 698**, 199 (2002).

[14] A. Bazavov *et al.*, Phys. Rev. **D 85**, 054503 (2012).

[15] M. M. Aggarwal *et al.* (STAR Collaboration), arXiv:**1007.2613** (2010).

[16] Y. Hatta and T. Ikeda, Phys. Rev. **D 67**, 014028 (2003) and references therein.

[17] F. R. Brown *et al.*, Phys. Rev. Lett. **65**, 2491 (1990).

[18] Y. Aoki, G. Endrődi, Z. Fodor, S. D. Katz and K. K. Szabo, Nature **443**, 675 (2006)

[19] Mark G. Alford, Krishna Rajagopal, Thomas Schaefer, Andreas Schmitt, Rev. Mod. Phys. **80**, 1455 (2008).

[20] Sourendu Gupta, Xiaofeng Luo, Bedangadas Mohanty, Hans Georg Ritter and Nu Xu, Science **332**(6037), 1525 (2011).

[21] Y. Hatta and M. A. Stephanov, Phys. Rev. Lett. **91**, 129901 (2003).

[22] M. A. Stephanov, Phys. Rev. Lett. **102**, 032301 (2009).

[23] M. A. Stephanov, Phys. Rev. Lett. **107**, 052301 (2011).

[24] L. Adamczyk et al. (STAR Collaboration), Phys. Rev. Lett. **112**, 032302 (2014).

[25] https://cerncourier.com/participants-and-spectators-at-the-heavy-ion-fireball/.

[26] https://particlesandfriends.wordpress.com/2016/10/14/evolution-of-collisions-and-qgp/.

[27] J. D. Bjorken, Phys. Rev. **D 27**, 140 (1983).

[28] Zebo Tang, Li Yi, Lijuan Ruan, Ming Shao, Hongfang Chen, Cheng Li, Bedangadas Mohanty, Paul Sorensen, Aihong Tang, Zhangbu Xu, Chin.Phys.Lett. **30**, 031201 (2013).

[29] J. Adams *et al.* (STAR Collaboration), Nucl. Phys. **A 757**, 102 (2005).

[30] L. Adamczyk *et al.* (STAR Collaboration), Phys. Rev. Lett. **120**, 062301 (2018).

[31] L. Adamczyk *et al.* (STAR Collaboration), Phys. Rev. Lett. **121**, 032301 (2018).

[32] L. Adamczyk *et al*. (STAR Collaboration), Phys. Rev. Lett. **116**, 112302 (2016).

[33] L. Adamczyk *et al*. (STAR Collaboration), Phys. Rev. Lett. **113**, 052302 (2014).

[34] L. Adamczyk *et al*. (STAR Collaboration), Phys. Rev. Lett. **112**, 162301 (2014).

[35] L. Adamczyk *et al*. (STAR Collaboration), Phys. Rev. Lett. **112**, 032302 (2014).

[36] L. Adamczyk *et al*. (STAR Collaboration), Phys. Rev. Lett. **110**, 142301 (2013).

[37] L. Adamczyk *et al*. (STAR Collaboration), Phys. Rev. **C 96**, 044904 (2017).

[38] STAR Internal Note, **SN0598** (2014).

[39] J. Rafelski and B. Muller, Phys. Rev. Lett. **48**, 1066 (1982).

[40] J. Rafelski and B. Muller, Phys. Rev. Lett. **56**, 2334E (1986).

[41] T. Alber *et al*. (NA49 Collaboration), Z. Phys. C **64**, 195 (1994).

[42] P. G. Jones (NA49 Collaboration), Nucl. Phys. **A 610**, 188c (1996).

[43] F. Sikler (NA49 Collaboration), Nucl. Phys. **A 611**, 45c (1996).

[44] C. Hohne (NA49 Collaboration), Nucl. Phys. **A 611**, 485c (1996).

[45] C. Adler *et al*. (STAR Collaboration) Phys. Lett. **B 595**, 143 (2004); J. Adams *et al*. (STAR Collaboration), Phys. Lett. **B s567**, 167 (2003).

[46] J. Adams *et al*. (STAR Collaboration), Phys. Rev. Lett. **92**, 182301 (2004); C. Adler *et al*. (STAR Collaboration), Phys. Rev. Lett. **89**, 092301 (2002).

[47] M. Gao, Phys. Rev. **D 41**, 626 (1990); H. Satz, Nucl. Phys. **A 418**, 447c (1984).

[48] T. Matsui and H. Satz, Phys. Lett. B **178**, 416 (1986).

[49] B. Alessandro *et al*. (NA50 Collaboration), Euro. Phys. J. **C 39**, 335 (2005); Eur. Phys. J. **C 48**, 329 (2006).

[50] R. Arnaldi *et al*. (NA60 Collaboration), Phys. Rev. Lett. **99**, 132302 (2007).

[51] A. Adare *et al*. (PHENIX Collaboration), Phys. Rev. Lett. **98**, 232002 (2007); Phys. Rev. Lett. **98**, 232301 (2007).

[52] A. Adare *et al*. (PHENIX Collaboration), Phys. Rev. Lett. **101**, 122301 (2008); Phys. Rev. Lett. **96**, 012304 (2006).

[53] A. Andronic *et al*., Nucl. Phys. **A 789** (2007) 334.

[54] L. Yan, P. Zhuang, and N. Xu, Phys. Rev. Lett. **97**, 232301 (2006).

[55] https://www2.lbl.gov/publicinfo/newscenter/features/2008/sabl_jets.html.

[56] J. D. Bjorken. Energy loss of energetic partons in quark-gluon plasma: Possible extinction of high momentum jets in hadron - hadron collisions. FERMILABPUB-82-059-THY.

[57] M. Gyulassy and M. Plumer, Phys. Lett. **B 243**, 432 (1990); R. Baier *et al*., Nucl. Phys. **B 483**, 291 (1997).

[58] X. N. Wang and M. Gyulassy, Phys. Rev. Lett. **68**, 1480 (1992).

[59] J. Adams *et al*. (STAR Collaboration), Nucl. Phys. **A 757**, 102 (2005).

[60] J. Adams *et al*., Phys. Rev. Lett. **91**, 172302 (2003).

[61] K. Aamodt *et al*. (ALICE Collaboration), Phys. Lett. **B 696**, 30, (2011); B. Abelev, *et al*. (ALICE Collaboration), Phys. Rev. Lett. **110**, 082302 (2013).

[62] X. N. Wang, Nucl. Phys. **A 715**, 775 (2003).

[63] E. V Shuryak, Phys. Lett. **B 78**, 150, (1978).

[64] A. Adare *et al*. (PHENIX Collaboration), Phys. Rev. Lett. **104**, 132301 (2010).

[65] L. E. Gordon and W. Vogelsang, Phys. Rev. **D 48**, 3136 (1993).

[66] S. Turbide, R. Rapp, and C. Gale, Phys. Rev. **C 69**, 014903 (2004).

[67] A. Adare *et al*. (PHENIX Collaboration), Phys. Rev. **C 81**, 034911 (2010).

[68] P. Huovinen, P. F. Kolb, U. W. Heinz, P. V. Ruuskanen and S. A. Voloshin, Phys. Lett. **B 503**, 58 (2001).

[69] D. Teaney, J. Lauret and E. V. Shuryak, arXiv:nucl-th/**0110037**.

[70] H. Sorge, Phys. Rev. Lett. **78**, 2309 (1997).

[71] E. Shuryak and O. V. Zhirov, Phys. Lett. **B 89**, 253 (1979).

[72] L. Van Hove, Z. Phys. **C 21**, 93 (1983); K. Kajantie, M. Kataja, L. McLerran and P. V. Ruuskanen, Phys. Rev. **D 34**, 2746 (1986); S. Chakrabarty, J. Alam, D. K. Srivastava and B. Sinha, Phys. Rev. **D 46**, 3802 (1992).

[73] L. V. Bravina, N. S. Amelin, L. P. Csernai, P. Levai and D. Strottman, Nucl. Phys. **A 566**, 461c (1994); L. V. Bravina, L. P. Csernai, P. Levai and D. Strottman, Phys. Rev. C **50**, 2161 (1994).

[74] D. H. Rischke, Y. Pursun, J. A. Maruhn, H. Stoecker and W. Greiner, Heavy Ion Phys. **1**, 309 (1995) [arXiv:nucl-th/**9505014**].

[75] L. P. Csernai and D. Rohrich, Phys. Lett. **B 458**, 454 (1999).

[76] A. Nyiri *et al.*, J. Phys. **G 31**, S1045 (2005).

[77] J. Adams *et al.* (STAR Collaboration), Phys. Rev. **C 73**, 34903 (2006).

[78] Z. W. Lin and C. M. Ko, Phys. Rev. **C 65**, 034904 (2002); L. W. Chen and C. M. Ko, J. Phys. **G 31**, S49 (2005); L. W. Chen, private communication (2005).

[79] S. A. Bass *et al.*, Prog. Part. Nucl. Phys. **41**, 225 (1998); M. Bleicher *et al.*, J. Phys. **G 25**, 1859 (1999); X. L. Zhu, private communication (2005).

[80] P. F. Kolb and U. W. Heinz, arXiv:nucl-th/**0305084v2**.

[81] J. Adams *et al.* (STAR Collaboration), Phys. Rev. **C 72**, 014904 (2005).

[82] P. Huovinen **et al.**, Phys. Lett. **B 503**, 58 (2001); U. Heinz and P. Kolb, Nucl. Phys. **A 702**, 269 (2002); F. Retiere and M. A. Lisa, Phys. Rev. **C 70**, 044907 (2004).

[83] X. Dong *et al.*, Phys. Lett. **B 597**, 328 (2004).

[84] D. Molnar and S. A. Voloshin, Phys. Rev. Lett. **91**, 092301 (2003); S. A. Voloshin, Nucl. Phys. **A 715**, 379 (2003).

[85] B. I. Abelev *et al.* (STAR Collaboration), Phys. Rev. **C 79**, 034909 (2009).

[86] S. V. Afanasiev *et al.* (NA49 Collaboration), Phys. Rev. **C 66**, 054902 (2002).

[87] J. Cleymans and K. Redlich, Phys. Rev. **C 60**, 054908 (1999); P. Braun- Munzinger *et al.*, Phys. Lett. **B 518**, 41 (2001); N. Xu and M. Kaneta, Nucl. Phys. **A 698**, 306 (2002).

[88] S. Chatterjee *et al.*, Adv. in High Eng. Phys., **2015**, 349013 (2015).

[89] J. Cleymans, arXiv:**1412.7045**.

[90] J. Randrup and J. Cleymans, Phys. Rev. **C 74**, 047901 (2006).

[91] E. Schnedermann, J. Sollfrank, and U. Heinz, Phys. Rev. **C 48**, 2462 (1993); D. Teaney, J. Lauret and E. V. Shuryak, Phys. Rev. Lett. **86**, 4783 (2002); P. Kolb *et al.*, Nucl. Phys. **A 696**, 197 (2001).

Chapter 2

Experimental Details

Any experimental discovery needs its explanation in a strong theoretical language. In the similar sense, a theoretical prediction has to be testified in an experimental laboratory for its genuineness. In the current focus of this thesis, for any supportive evidences of the predictions of QCD, there is the requirement of very huge experimental facilities. In terms of budget, area, technology, computing, risks, manpower and many more, these experiments are really big. And its bigness frames the opportunity of a vast area of research, examining at each point of time, the human intellect. It some times appears funny speaking that, for the search of tiny, invisible objects to human eye, huge experiments were built, which is also beyond the capture capacity of human vision.

This chapter of this thesis dedicatedly discusses about the Solenoidal Tracker At RHIC (STAR) experiment. The data of this experiment are primarily analyzed in the subsequent chapters of this thesis.

2.1 The Relativistic Heavy Ion Collider

The experimental platform required to test the predictions of QCD, took a lot of years of dedicated efforts to come into picture. The first-ever built successful collider experiment performing high-energy nucleus-nucleus collision is the Relativistic Heavy Ion Collider located at Brookhaven National Laboratory in Upton, New York. It is also unique in the sense that, it is the single facility till now for the spin-polarized proton collider.

The RHIC experiment has led its platform through an evolution from small fixed target experiments. Now a days, it is the second high-energy heavy-ion collider in the world, the Large Hadron Collider (LHC) being the biggest one. It started functioning in the year 2000, and till date taking data with a remarkable journey of 19 years. It was primarily designed to run p+p collisions at $\sqrt{s} = 500$ GeV and Au+Au collisions at $\sqrt{s_{NN}} = 200$ GeV. However, it successfully provided data in a wide range of center of mass energy ($\sqrt{s_{NN}} = 7.7\text{-}200$ GeV) and in addition also exploited various nuclei collision systems (p+p, p+Al, p+Au, d+Au, He+Au, Cu+Cu, Cu+Au, Zr+Zr, Ru+Ru, Au+Au and U+U).

The RHIC is a big quasi-circular superconducting storage ring particle accelerator. It individually consists of two concentric rings termed as "blue" and "yellow" rings to accelerate heavy-ions in opposite directions. It thus allows a virtually free choice of colliding positively charged nuclei in addition to protons. Both the rings share a common horizontal plane inside the RHIC tunnel having their own bending and focusing magnets and radio frequency source to deflect particles. The RHIC tunnel has a perimeter of 3.8 Km. Like a clock, the RHIC ring has six interaction points, where the two beams are allowed to cross each other. There are four experiments at 2 O' clock, 6 O' clock, 8 O' clock and 10 O' clock positions of the RHIC clock respectively named as BRAHMS, STAR, PHENIX and PHOBOS. Out of which PHOBOS and BRAHMS have completed their operation in the years 2005 and 2006, respectively. The experimental set up the RHIC experiment along with the accelerating steps of the beam is shown in Fig. 2.1 [1].

For a particular collision system, the beams undergo through various acceleration steps as mentioned below.

1. **Tandem Van de Graff :** The production of billions of ions and thereafter giving them an energy boost is the primary job of this Tandem Van de Graff [2]. It functions as an electrostatic accelerator. It can provide ions by stripping up their electrons ranging from Hydrogen to Iron in atomic numbers.

2. **Tandem-to-Booster (TtB) Line :** The ions generated at the Tandem Van de Graff are then passed to travel through an 850 m long tunnel called as the Tandem-To-Booster Line. It carries the ions through a vacuum via a magnetic field to a Booster synchrotron.
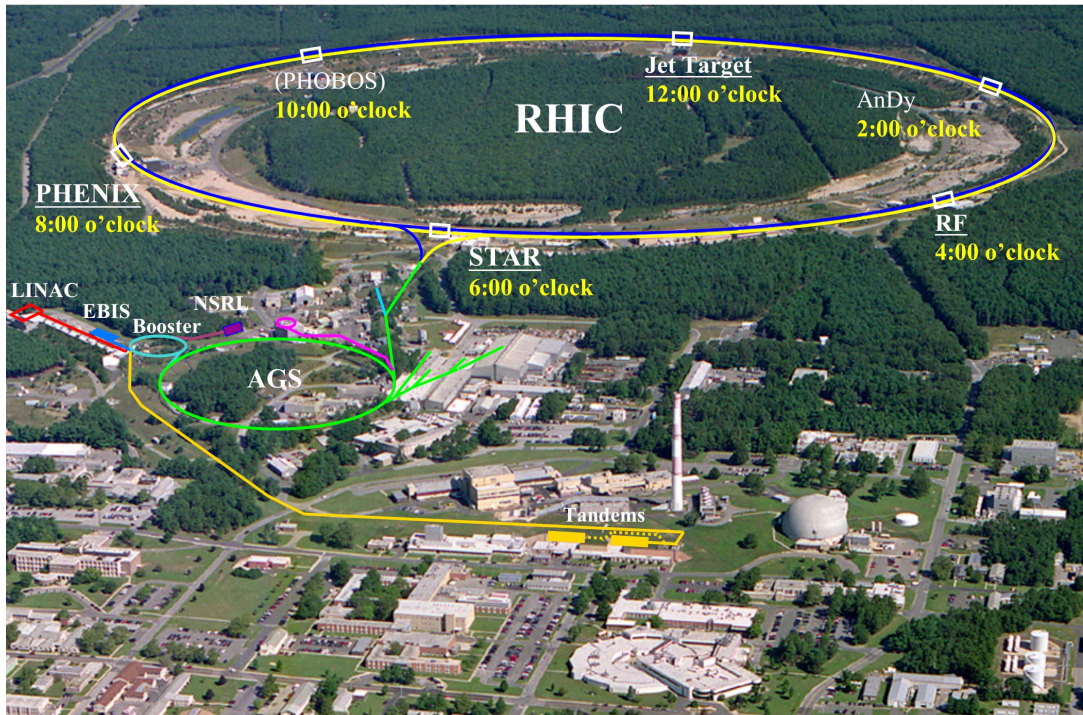
Figure 2.1: The RHIC ring complex showing its two colliding rings, beam injection point, the six interaction points or four major experiments and the various stages of acceleration of ions [1].

This TTB line consists of a series of bends arranged in pairs from which one selects the ions with the desired momentum. While the other two pairs are so adjusted that the ions with different momenta would emerge in the same direction [3]. At this stage the ions attain about 5% of the speed of light.

3. **Linear Accelerator (Linac) :** The Linac is a type of particle accelerator, that accelerates the ions along a linear beam line by the application of a series of oscillating electric potential. At RHIC for proton-proton collisions, the Linac supplies 200 MeV energetic protons. Which are transferred from the Linac to Booster.

4. **Booster Synchrotron :** The Booster synchrotron is a circular accelerator having a circumference of 201.8 m. It provides the ions more energy by rolling them on the downward sloping of the radio frequency electromagnetic waves. A parallel magnetic field inside the synchrotron and electric field do the job of acceleration of ions. The ions are put in bunches of six inside the synchrotron and accelerated upto 37% of the speed of light. It also does the job of electron stripping from the ions and finally, the beam is

transferred to the Alternating Gradient Synchrotron (AGS) via Booster to AGS line.

5. **Alternating Gradient Synchrotron (AGS) :** The ions are further accelerated like a circular booster inside the Alternating Gradient Synchrotron. The AGS further strips the electron from the ions along with it boosts them with more energy to accelerate upto a speed equivalent to 99.7% the speed of light.

6. **AGS-to-RHIC (AtR) Line :** From the AGS the beams are transferred to the AGS-to-RHIC line to finally reach the RHIC ring. Before the RHIC ring, the beams along its path meet a "Y" shape road divider. At this point, a switching magnet alternately directs the beam either to the clockwise RHIC ring or to the counter-clockwise ring.

The two independent beams after entering the RHIC ring makes many many rotations inside the ring and accelerated to the desired center of mass energy. The typical speed of the projectiles in the RHIC ring approaches 99.995% of the speed of light. Then they are allowed to collide only at the six interaction point to finally observe the most awaiting collision of ions.
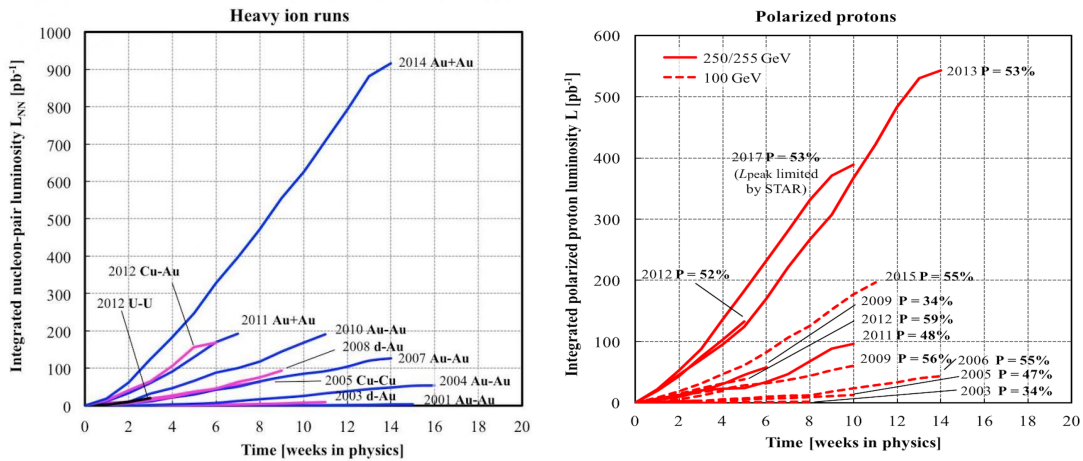
Figure 2.2: The time evolution of nucleon-nucleon pair luminosity in heavy-ions (left) and proton-proton (right) collisions achieved at RHIC [4].

RHIC is able to provide very high luminous beams making the task of very rare processes with smaller cross-section possible to recognize. The average luminosity achieved at RHIC for various systems of collision is depicted in Figure 2.2 [4]. The interaction rate (R) of the colliding particles are directly related with the luminosity ($\mathcal{L}$) and collision cross-section (σ) through the mathematical expression; $R = \mathcal{L} \times \sigma$. In an experiment, we have only the flexibility

to control and optimize the luminosity, but not the cross-section. Consider the Blue beam has N_B number of particles and the Yellow beam has N_Y number of particles per bunch. If each beam with n bunches per revolution is circling the RHIC ring at a revolution frequency f, then the luminosity is given by [5]

$$\mathcal{L} \simeq fn\frac{N_B N_Y}{A}, \tag{2.1}$$

where A denotes the overlapping cross-sectional area of the two colliding beams of particles. On its way of journey, the RHIC has now achieved the average luminosity value of 87×10^{26} cm^{2}s^{-1} for Au+Au collisions, which is 44 times the design value. A detailed summary of RHIC runs, systems of collisions and average luminosity values can be found at refs. [4].

2.2 The STAR Detector

The STAR detector stands for the Solenoidal Tracker At RHIC is one of the current running big experiments at RHIC. It is a dedicated heavy-ion collision experiment with a vast area of research program. To have a close look at the space-time evolution of the system formed in high-energy heavy-ion collision experiments, STAR provides a wide acceptance coverage in pseudo-rapidity(η) as well as full azimuthal coverage. In addition to physics research in heavy-ion physics, STAR is also carrying out spin physics program. Thus it offers space to both heavy-ion collisions as well as proton-proton collisions.

An overview of the STAR detector showing its major detector subsystems is shown in Figure 2.3 in three dimensions [6]. Figure 2.4 [7] depicts the cross-sectional view of the STAR experiment. Though appears complex, but the combined technology of all the detector subsystems provides high precision tracking, momentum analysis and excellent particle identification to STAR.

The STAR detector is enclosed within a huge solenoidal magnet providing a uniform magnet field along the beam direction. The STAR detector operates at the magnetic field of maximum 0.5 Tesla. The uniform magnetic field ensures the momentum measurement of the charged particles. The location of the STAR detector is defined in terms of the local right-
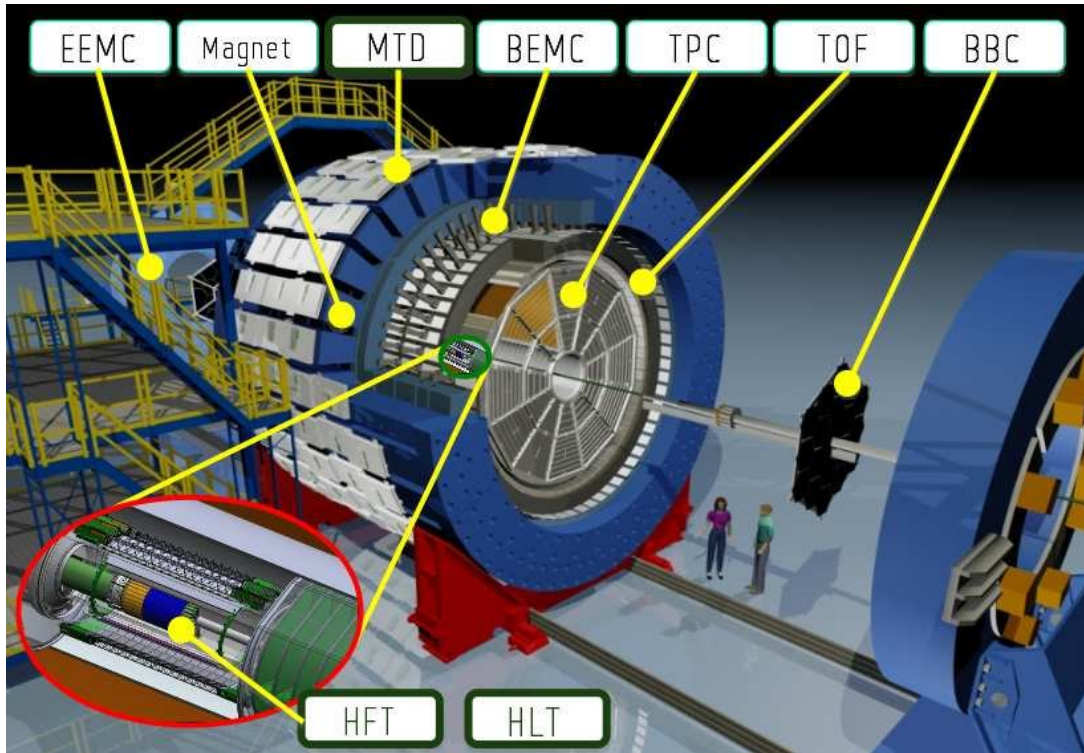
Figure 2.3: An overview of the Solenoidal Tracker At RHIC (STAR) detector [6]. The major sub-detectors displayed are the STAR magnet, BEMC/EEMC, MTD, TPC, TOF, BBC, HFT and HLT out of eighteen subsystems.
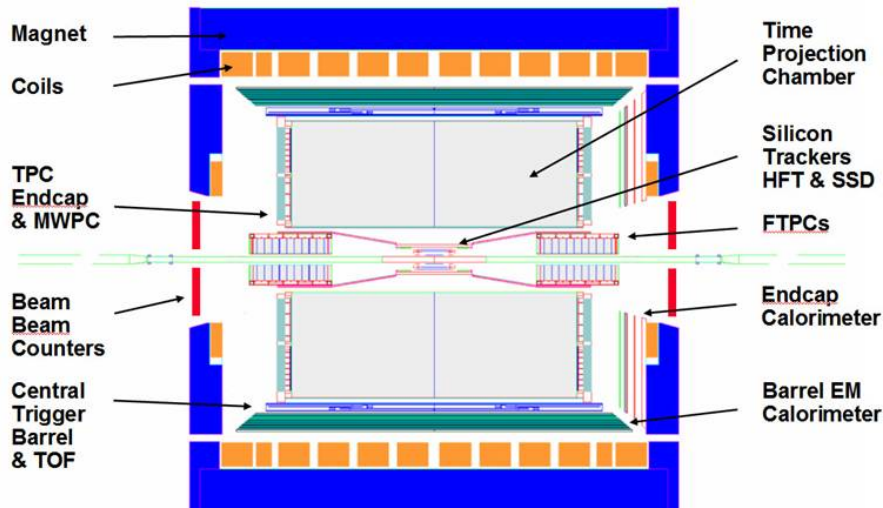
Figure 2.4: A side view of the Solenoidal Tracker At RHIC (STAR) experiment [7].

handed Cartesian co-ordinate system [8]. In this frame, the x-axis is parallel to the ground and away from the center of RHIC, the y-axis is perpendicular to the ground and the z-axis points to the west at STAR. The main detector used for particle tracking and identification is the Time Projection Chamber (TPC) [9]. It is 4.2 m long and has a pseudo-rapidity coverage of

$|\eta| \leq 1.8$ with a full 2π azimuthal geometrical symmetry. Two Forward Time Projection Chambers (FTPC) [10] were located on either side of TPC. It provides coverage in either forward or backward rapidity of $2.5 < |\eta| < 4$ covering the full azimuthal direction. The photon detection capability of the STAR detector is achieved by the Photon Multiplicity Detector (PMD) [11,12]. The PMD has pseudo-rapidity coverage in the forward region in the range 2.3-3.5, behind the FTPC. For the data analyzed in this thesis, these detectors were not there at the time of data taking. The particle identification capability of STAR is extended to higher momentum range with the Time Of Flight (TOF) [13] detector operating on Multi Resistive Plate Chamber technology [14]. TOF delivers full 2π azimuthal coverage with a pseudo-rapidity acceptance of $|\eta| \leq 0.9$. The functionality of TOF borrows information from another two twin sub detectors called as the pseudo Vertex Position Detector (pVPD) [13]. These are situated on both sides of TPC, each 5.7 m away from the center of the beam line. These detectors provide the start time information to the TOF. The detection of electromagnetically active particles is ensured through the inclusion of Electromagnetic Calorimeters. One Barrel Electromagnetic Calorimeter (BEMC) [15] covering $|\eta| < 1$ and Endcap Electromagnetic Calorimeter (EEMC) [16] covering $1 < |\eta| \leq 2$ does this job. These Electromagnetic Calorimeters contains Shower Maximum Detector (SMD), which distinguishes the amount of energy deposited by a single photon or a photon shower coming from neutral π^0 or η meson decays. The STAR particle identification capability is further enhanced in the heavy flavor sector by the inclusion of the Heavy Flavor Tracker (HFT) [17], which was partially installed at the center of the STAR TPC in the year 2014. The trigger detector system of STAR mainly comprises of three sub detectors. These are Zero Degree Calorimeters (ZDCs), Beam-Beam Counters (BBCs) and pseudo Vertex Position Detectors (pVPDs). All these are twin detectors situated on both sides of STAR TPC.

In the subsequent subsections, we will thoroughly discuss the main detector subsystems of STAR. Which includes TPC, TOF and trigger detectors relevant to the scope of this thesis.

2.2.1 Time Projection Chamber

The principle of operation for a typical Time Projection Chamber makes use of a combination of the electric and magnetic fields together with a sensitive volume of gas or liquid to give a

3-dimensional imaging of the particle track. The TPC was originally invented by an American physicist David R. Nygren, at Lawrence Berkeley Laboratory in the late 1970's. Its first major application was found in PEP-4 detector at the PEP storage ring at SLAC, which studied 29 GeV electron-positron collisions [18]. After this, the TPC continued its successful journey through technical evolution and proved its benefits of application from elementary particle collisions to heavy-ion collisions. The TPC delivers two important information about the track. Those are momentum associated with the particle and the energy deposited by the particle in TPC, which are used for the identification of a particle.

The STAR experiment uses the TPC [9] detector as its primary tracking device. It provides a pseudo-rapidity coverage of $|\eta| < 1.8$ with a full 2π azimuthal coverage. The STAR TPC can measure particle momenta from 100 MeV/c to 30 GeV/c. It has an excellent particle identification capability typically in the range of 100 MeV/c to 1 GeV/c.

2.2.1.1 Technical Design of TPC

The schematic 3-dimensional view of the STAR TPC is shown in Figure 2.5. It is enclosed within a solenoidal magnet field of strength 0.5 Tesla. It is a concentric cylindrical shaped detector with the beam line, which is 4.2 m long and 4 m in diameter. The inner and outer radii of the active volume of the TPC are 0.5 m and 2.0 m respectively. The TPC consists of a well defined outer field cage (OFC), one inner field cage (IFC) and two end caps. The OFC and IFC are combinely used to provide an approximate perfect electric field giving the space for the electrons to drift to the anode plane. It also ensures the recorded tracks to remain undistorted as well as its design favors to hold the TPC gas uncontaminated. The end caps are leveled at ground potential serves as the readout system.

A thin conductive Central Membrane (CM) at the center of the TPC in the xy-plan divides the TPC into equal east and west parts as depicted in Figure 2.5. It is a 70 μm membrane made up of carbon coated kapton forming the center of TPC. It is maintained at a voltage of $\sim$ 28 kV with respect to the detection planes and acts as the TPC cathode. An uniform electric field of $\approx$ 135 V/cm along the beam direction is defined in between the CM, concentric field-cage cylinders and the readout end caps. The field cage cylinders gives a sequence of equi-potential
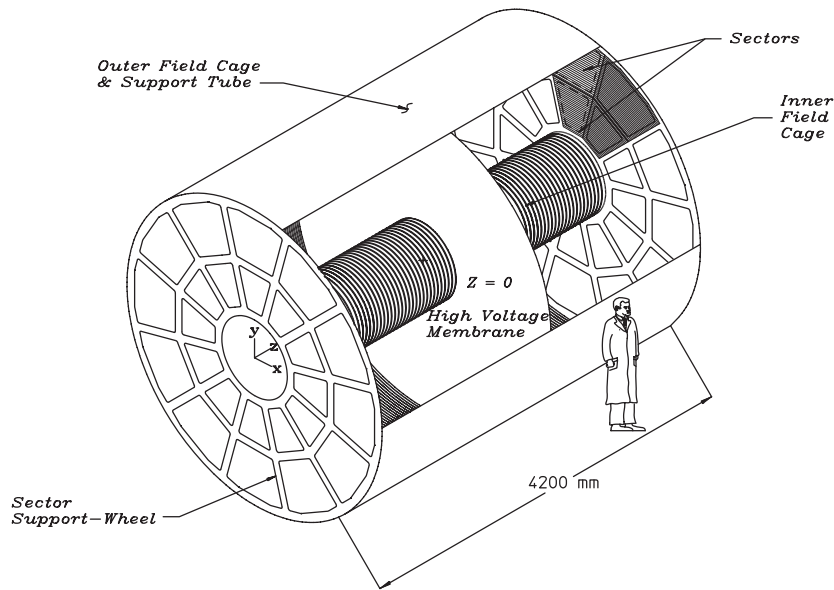
Figure 2.5: The three dimensional schematic view of the STAR TPC [9].

rings, which divides the space between the CM and anode planes into 182 equivalently spaced segments. It is very sensitive since track reconstruction and electron drift paths are closely related [9]. All the connection between the CM, IFC and OFC are designed to minimize the material budget and maintains a flat surface within 0.5 mm. The laser calibration system makes use of low work function material as a target which is provided by 36 Aluminum strips attached to each side of the CM.

The TPC is filled up with P10 gas which is a gas mixture of Argon (90%) and Methane (10%) and kept above 2 mbar atmospheric pressure. Its virtue is the fast drift velocity of electrons which peaks up at low electric field. The design technology of the TPC though simple makes it versatile, sensitive and more practically beneficial.

Multi-Wire Proportional Chambers (MWPC) forms the readout system of the TPC with readout pads. It consists of four components: a pad plane and three wire planes. The total TPC readout system is sub-divided into 24 sectors each having 12 readout sectors for each end cap. Subsequently, each sector is divided into inner and outer sectors with different pad row geometry as shown in Figure 2.6. A single inner sector comprises of small, widely spaced 13 pad rows. Its benefit is to maximize two-track resolution in a region of high particle density. On the other side, the outer sector is composed of large, densely packed 32 pad rows. It optimizes

Outer Pads
6.2 mm x 19.5 mm
Total of 3,942 Pads

6.7 x 20 mm Centers

Inner Pads
2.85 mm x 11.5 mm
Total of 1,750 Pads
Row 1 thru 8 on 48 mm Centers
Row 8 thru 13 on 52 mm Centers
Cross Spacing 3.35 mm

600.00 mm from DETECTOR CENTER

143 x 6.7 = 958.10 mm

97 x 6.7 = 649.90 mm

183 x 3.35 = 613.05 mm

87 x 3.35 = 291.45 mm

3.35 mm CROSS SPACING

48.00 mm RADIAL SPACING

52.00 mm

6.70 mm CROSS SPACING
(7 x 48) + (5 x 52) = 596.00 mm

20 mm RADIAL SPACING
31 x 20 = 620.00 mm

1271.95 mm from DETECTOR CENTER

Figure 2.6: One sector of the TPC anode plane. The inner and outer sub sectors with respectively small widely spaced pad rows and large densely spaced pad rows [9].

the ionization energy loss in a region with smaller particle population [19]. Hence, for a track at maximum 45 number of hits are possible if it traverses through all the pad rows.

2.2.1.2   Track Reconstruction

The STAR TPC is widely appreciated for its good track reconstruction capability. Generally, a track can be viewed as a 3-dimensional image by the specification of its x,y,z - co-ordinates at each point of the path of the track. Primarily, inside TPC volume, a charged particle traveling through the TPC gas ionizes the gas atoms and molecules producing an array of electrons. The x and y - position of each array of electrons are obtained from the adjacent pads along a single pad row. The information of the z-position of each array of electrons involves the measurement of the drift time from the origin of the array to the end cap. This drift time divided by the average drift velocity of the electrons calculates the z-position of the array of electrons. After finding the x, y, z co-ordinates of all the array of electrons, the TPC track reconstruction algorithm performs a helical fit to obtain the trajectory of a single particle. Practically, there can be a deviation from the helical shape of a particle track due to energy loss and multiple Coulomb scattering. Hence, a global track is obtained by adding tracking information from other inner detectors and performing a refit by the application of the Kalman fit method [20]. Back extrapolating the information of each global track to the origin, the z-position of the

84

primary collision vertex is determined. If a global track has the Distance of Closest Approach (DCA) less than 3 cm, then the track is refitted by including the primary vertex as an additional space point and is termed as a primary track. Nevertheless, the reconstruction efficiency of a track depends for sure on particle type, track quality cuts and track density.

2.2.1.3 Particle Identification

TPC definitely proves its excellence in charged particle identification by the measurement of ionization energy loss of a particle inside TPC. As described previously, a particle track at maximum will have 45 dE/dx points on the 45 pad rows of TPC. However, the limitations associated with large ionization fluctuation and shorter length of the particle trajectory over which dE/dx measured, the most probable value of dE/dx is necessarily used in calculation purpose instead of the average dE/dx value. This is obtained by calculating the truncated mean of the 75% cluster of electrons and discarding the 30% of the remaining large ionization clusters. The ionization energy loss of a particle traversing through the TPC volume can be mathematically expressed by the Bichsel function [21], which is an extension of the Bethe-Block formula [22]. For a particular particle with a given mass and definite track momentum, it is given by

$$-\frac{dE}{dx} = Kz^2\frac{Z}{A}\frac{1}{\beta^2}\left[\frac{1}{2}\ln\left(\frac{2m_ec^2\beta^2\gamma^2T_{max}}{I}\right) - \beta^2 - \frac{\delta^2}{2}\right],\qquad(2.2)$$

where K is a constant, z is the charge of the particle in integers, Z is the atomic number of the absorbing material, A is the atomic mass of the absorber, m_e is the mass of the electron, c is the speed of light in vacuum, I is the average ionization energy loss of the material, T_{max} is the maximum kinetic energy that can be achieved by a free electron in an interaction, δ is the correction based on the energy density and $\beta\gamma = p/mc$, where p and m being the momentum and mass of the charged particle. The formula clearly informs the mass dependence of dE/dx and hence can be used to identify the particle type. The ionization energy loss of primary and secondary charged particles inside TPC in STAR as a function of p_T is displayed in Figure 2.7 [9]. The dense bands measured in the experiment are the ionization energy loss of the charged particles. The red curves represent the theoretical prediction from the Bichsel
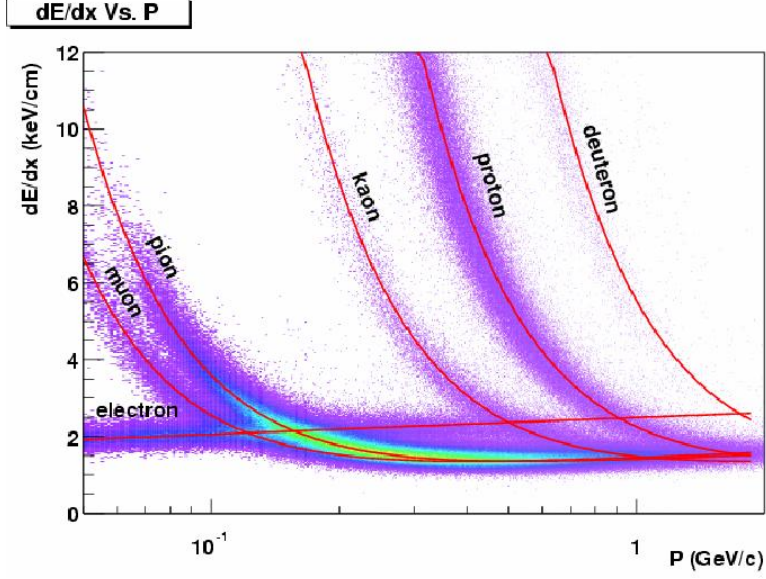
Figure 2.7: The ionization energy loss of primary and secondary particles inside TPC in STAR as a function of momentum P [9].

function for a particular choice of particle type. The dE/dx resolution capability of the STAR TPC is around 6-8%. Pions, kaons and (anti-)protons typically can be identified using only TPC upto transverse momentum range of 0.75, 0.75 and 1.0 GeV/c.

Qualitatively, a more reliable variable for particle identification is the $n\sigma$ variable, which measures the standard deviation of a Gaussian track from its measured value to the expected value and is defined as

$$n\sigma_i = \frac{1}{R} \log \frac{\langle dE/dx \rangle|_{measured}}{\langle dE/dx \rangle_i|_{expected}}, \tag{2.3}$$

where i is the particle type under consideration (e.g. e, π, K, p, d), $\langle dE/dx \rangle|_{measured}$ is the measured energy loss of the particle, $\langle dE/dx \rangle_i|_{expected}$ is the mean energy loss of that particle obtained from the Bichsel function [21] and R is the dE/dx resolution of TPC which is typically of the order of 6% to 8% [9, 24]. Similarly, another more suitable variable for particle identification is the z variable defined as

$$z_i = \ln \left(\frac{\langle dE/dx \rangle|_{measured}}{\langle dE/dx \rangle_i|_{expected}} \right), \tag{2.4}$$

all the variables have the same meaning as described above. In the context of this thesis, our choice will be the z variable for particle identification using TPC.

2.2.2 Time Of Flight and Pseudo Vertex Position Detector

The particle identification capability of the STAR experiment is pushed to a higher momentum range beyond the range of TPC by the TOF detector [13]. The complete particle identification action is fulfilled through the combination of two sub-detectors: the Time Of Flight and the pseudo Vertex Position detector. The schematic view of the TOF detector subsystem with the TOF tray and two pVPD's are shown in Figure 2.8. The TOF detector placed just above TPC surrounds it with a little less pseudo-rapidity acceptance of $|\eta| < 0.9$ with full azimuth. It consists of total 120 trays equally distributed in numbers of 60 on east and west sides. STAR has performed the upgrade to a full barrel TOF detector in the year 2010 implementing the Multi Resistive Plate Chamber (MRPC) [14] technology. Each tray of TOF has 32 MRPC modules covering 6 degrees in azimuthal direction around TPC. MRPC is basically a stack of resistive plates with a gas gap between two adjacent plates. High voltage is applied on both sides of the outer plates, which produces a strong electric field in the vicinity of the sub gaps between the plates. The plates being resistive to an avalanche of signal, the signal induced on the collecting plate is the sum of signals from all the gaps. A cross-sectional view of the MRPC module with long side and short side are separately shown in Figure 2.9 [14]. The individual dimension of each side of the module is also displayed. All these technologies at last delivers the stop time of an event.

There are two identical pVPDs situated on both sides equidistantly from the center of the beam pipe at 5.7 m away. Its pseudo-rapidity coverage lies within the range of $4.24 \leq \eta \leq 5.1$
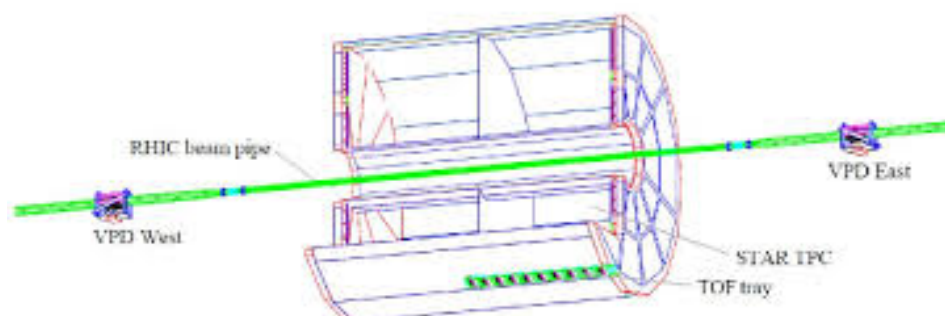
Figure 2.8: The schematic diagram of TOF system displaying the TOF tray and the two pVPD's. For clear visibility, the TPC is cut away and the STAR magnet and other subsystem are not displayed [13].
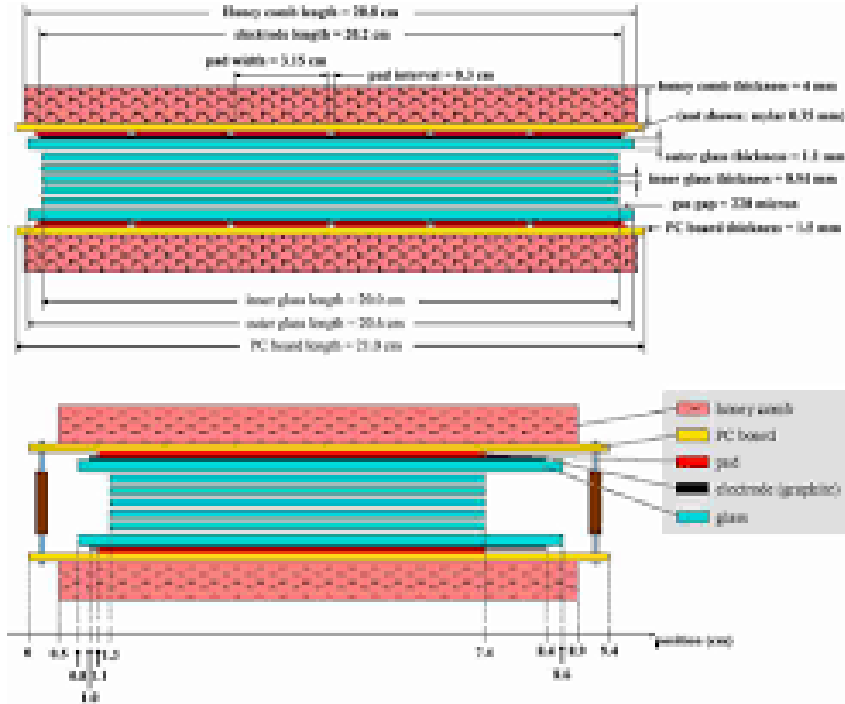
Figure 2.9: Two side views of the MRPC used in STAR TOF. The top is for long side view and the bottom is for short side. The scales of both sides are not in equal futting [14].

with 19 channels on each side. It does the important job of giving the start time information of an event to the TOF. Additionally, it gives independently the z-component of the collision vertex.

As such the combined information received from TOF and pVPDs are taken together to calculate the time interval Δt. For particle identification purpose, the path length (l) and mo-
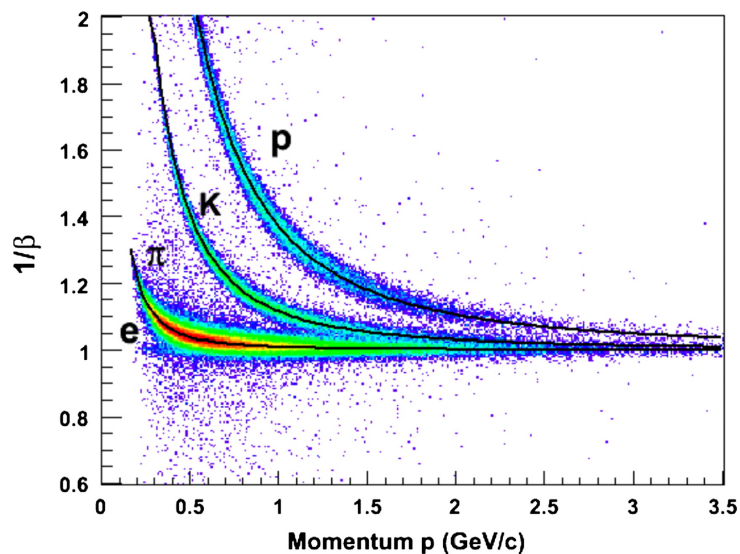
Figure 2.10: $1/\beta$ as a function momentum from TOF in p+p collisions at $\sqrt{s_{NN}} = 200$ GeV in STAR [23].

mentum p information provided by TPC completes the procedure. The inverse of velocity is then determined by $1/\beta = c\Delta t/l$, where c is the speed of light. The particle identification in TOF is usually estimated from the m^2 variable given as

$$m^2 = p^2 \left(\frac{1}{\beta} - 1 \right).$$
(2.5)

A representative figure showing $1/\beta$ as a function of momentum in p+p collisions at $\sqrt{s_{NN}} = 200$ GeV in STAR [23] is depicted in Figure 2.10. As can be inferred from Figure 2.10 that $1/\beta$ bands are now clearly separated upto momentum 2 GeV/c. This TOF information is successfully used to identify pions, kaons and proton upto transverse momentum range of 2 GeV/c.

2.2.3 Trigger Detectors

The main utility of the trigger system is to quickly select a useful event in a particle detector from all the events occurring. Its relevance lies in the management of computing power, data storage as well as selection of data with required physics interest.

The STAR detector is practically designed to detect charged as well as neutral particles. The data acquisition system (DAQ) [25] of STAR is very fast, flexible and records data simultaneously from multiple detectors falling in a wide range of readout rates. The main sub-detectors of STAR used for particle identification (e.g. TPC, FTPC, TOF etc) are comparatively slow
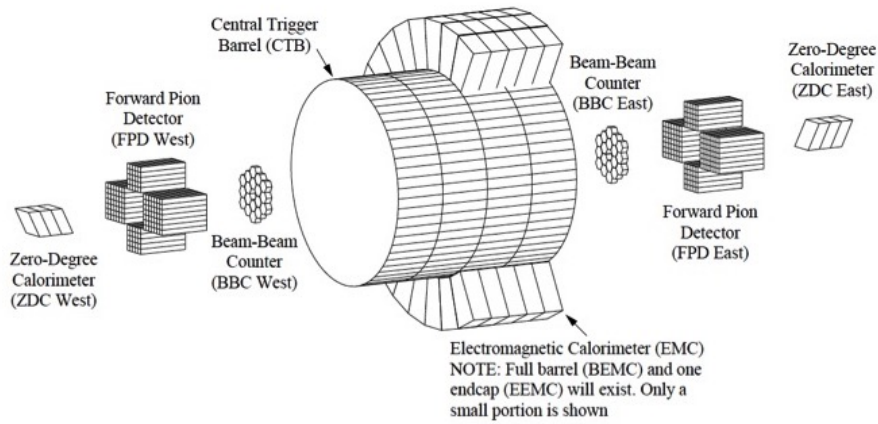
Figure 2.11: The schematic diagram of all the trigger detectors of STAR packed together [27]. Now a days, central trigger barrel is replaced by the TOF system and Forward Pion Detector (FPD) anticipated by Forward Meson Spectrometer (FMS) in STAR.

and typically has a rate of the order of $\sim$ 100 Hz. Whereas the interaction rate for the highest luminosity beam at RHIC is $\sim$ 10 MHz. So. in order to ensure, the smooth recording of every useful event, a fast detector is required to counteract this 5 order magnitude difference. This is achieved in STAR by the application of Trigger Detectors which are super fast in their job of selection of good events for physics analysis. The STAR trigger system [26] prompts other sub-detectors to record useful data followed by its fast selection of events. There are also triggers to select and group very rare, specific events to enhance their statistics. Some of the main trigger detector systems of STAR are the ZDC, BBC, VPD, BEMC and EEMC described briefly below. A schematic diagram of all the trigger system used in STAR is depicted in Figure 2.11 [27].

2.2.3.1   Zero Degree Calorimeter

The Zero Degree Calorimeters (ZDCs) [28] are common to all the four experiments at RHIC. The ZDCs are small transverse area hadron calorimeters and appear in pairs on each side at the same distances from the center of a detector. These are located next to the DX dipole magnets of each heavy-ion experiment at RHIC. The ZDCs measure the neutral particle energy within a solid angle of 2 mrad about the beam direction as the DX magnet sweeps out the charged particles. The ZDCs are located at a distance of $\sim$18 m away from the interaction point on both sides having a horizontal acceptance of $\pm$5 cms. The ZDCs solves the dual purpose by counting the number of free spectator neutrons [29] as well as the coincident signal from either side of the interaction region is used for luminosity monitoring. Additionally, the ZDCs do a useful job of determining the collision vertex by measuring time difference between the coincidence. The time resolution of the ZDC is typically of the order of 100 psec. There are two Shower Maximum Detectors (SMDs) sandwiched between the first and second module of ZDC which are sensitive to positions. Their application lies in the study of the spatial distribution of the neutron hits on the transverse plane of ZDCs. The installation of ZDC-SMD in STAR spreads its area of research to a more wide range including anisotropic flow, ultra-peripheral collisions and spin physics [30].

2.2.3.2 Beam-Beam Counter

The specific design of ZDCs are suitable for triggering Au+Au collisions with high particle multiplicity events. On the other side, for relatively low multiplicity events of p+p collisions, a different trigger subsystem proves to be more reliable, which is the Beam-Beam Counter.
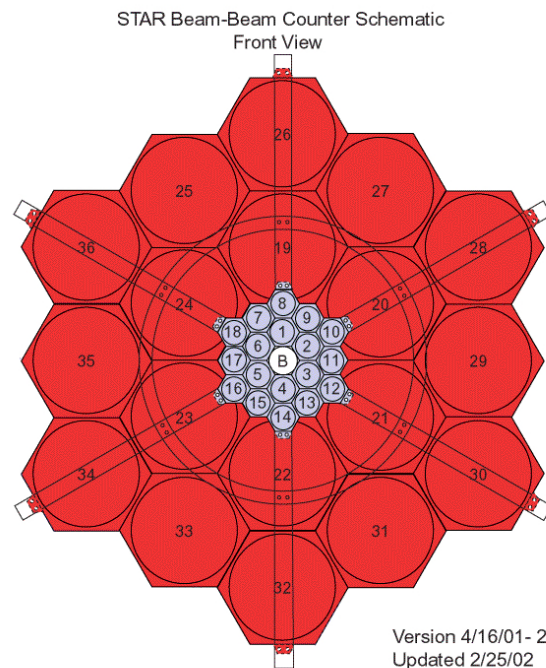
Figure 2.12: The schematic picture of the Beam-Beam Counter showing small (blue) and large (red) tiles with the beam pipe crossing it at the center represented by the symbol 'B' [27].

There are a pair of Beam-Beam Counter surrounding the beam pipe at a distance of 3.75 m away from the center of the nominal interaction point (IP) at east and west pole tips of the STAR magnet. Each BBC consists of two rings of hexagonal scintillator tiles as shown in Figure 2.12 [27]. The outer ring is composed of large tiles and the inner ring is composed of small tiles. The small inner ring has inner and outer diameter of 9.6 cm and 48 cm consisting of 2×18 array of small hexagonal tiles. It corresponds to pseudo-rapidity coverage of $3.4 < \eta < 5.0$. The large outer ring consists of 2×18 array large tiles with inner and outer diameter of 38 cm and 193 cm. Thus corresponding to the pseudo-rapidity coverage of $2.1 < \eta < 3.6$. A charged particle traversing through the BBCs produce light in the scintillator tiles. The BBCs coincidence rate provides minimum trigger required for the p+p collisions.

In addition to the triggering action of BBCs for p+p collisions, it measures the absolute luminosity $\mathcal{L}$ with 15% precision and relative luminosity R for different proton spin orientations with high precision. The small tiles of BBCs are also used to reconstruct the first-order event plane in the directed flow analysis. The timing difference between the two counters of BBC gives the location of the primary vertex position.

2.2.3.3 Vertex Position Detector

Since 2009, the two Vertex Position Detectors (VPDs) [13] are also employed in the triggering of events in high-energy heavy-ion collisions. The VPD pairs are situated on both sides of STAR at a distance of 5.7 m away from the center of the interaction point (IP) with a pseudo-rapidity range of coverage $4.24 < |\eta| < 5.1$. Each VPD is composed of 19 Lead converters and plastic scintillators with photo multiplier tube readout. The east and west VPD coincidence rate provides the minimum biased triggered events. Additionally, the time difference between the coincidence of east and west VPD delivers the location of the primary vertex position. Much better timing resolution than BBCs is achieved from VPDs.

2.2.3.4 Electromagnetic Calorimeters

The basic operation of electromagnetic calorimeters is to measure the energy of the particle that primarily interacts via electromagnetic interactions. The STAR detector makes use of Electromagnetic calorimeters to trigger rare and high p_T processes such as jets, leading hadrons, direct photon and heavy quarks. It also provides wide acceptance for photons, electrons (from J/Ψ and Υ decays), π^0 and η mesons in polarized p+p collisions through Au+Au collisions. Technically STAR employs two electromagnetic calorimeters: Barrel Electromagnetic Calorimeter (BEMC) and Endcap Electromagnetic Calorimeter (EEMC) to be discussed below. The schematic diagram of the side view of BEMC and end view of EEMC is shown in Figure 2.13 [15, 31].

Barrel Electromagnetic Calorimeter (BEMC) :

As the name clearly justifies, the basic design of the Barrel Electromagnetic Calorimeter (BEMC) [15] completely covers the STAR TPC with an area of nearly 60 m^2. Thus it exhibits full az-
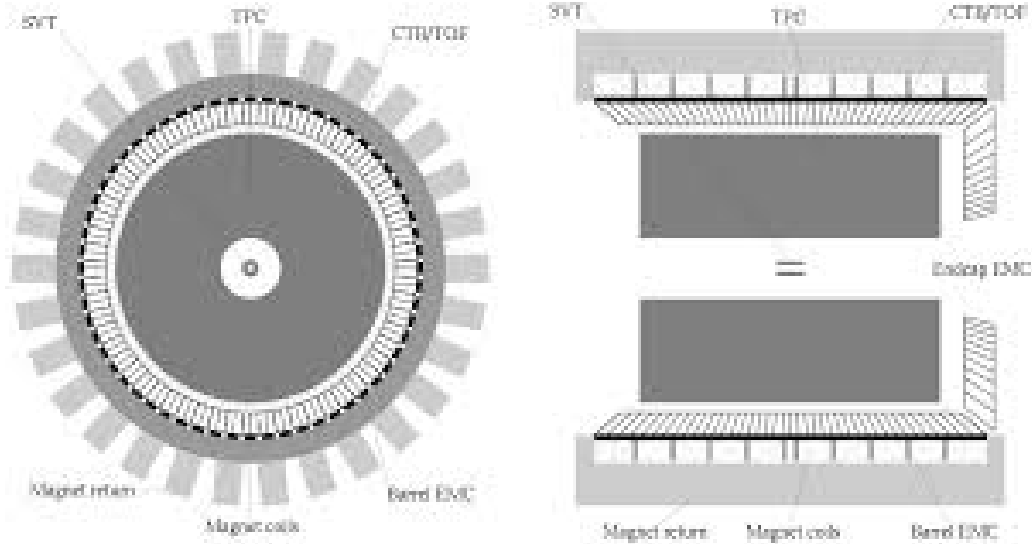
Figure 2.13: The schematic end view of Barrel EMC and side view of Endcap EMC of STAR [15, 31].

imuthal coverage and pseudo-rapidity acceptance of $|\eta| < 1$. The Barrel EMC consists of alternate layers of lead and scintillator planes and falls on the category of sampling calorimeter type. It contains 20 layers of lead plates and 20 layers of scintillator plates. The full BEMC is subdivided into 120 modules with 60 on the east side and 60 on the west side. Each module has a coverage of 6 degree in $\Delta\phi$ and 1.0 unit in $\Delta\eta$. Further, each module is segmented into 40 towers, 2 in ϕ and 20 in η direction. Thus each tower has a span in $\eta - \phi$ space of 0.05×0.05. For triggering purpose, the towers are grouped in sets of 16 to give 300 trigger patches with $\eta - \phi$ coverage of 0.2×0.2. Thus in total, the BEMC is composed of 4800 towers projecting back to the center of the interaction region. Each individual tower is composed of an assemblage of lead-scintillators and an SMD located at a distance of about ~ 5 radiation length (X_0) from the front of the lead-scintillator bundle. The primary purpose of the SMD is to provide fine spatial resolution in a calorimeter.

The BEMC measures the neutral energy in the form of produced photons by detecting the cascade of particles, when those photons interact with the calorimeter. The energy deposited in an individual tower or sum of towers can be used to trigger high p_T events [15]. The use of BEMC makes it possible to reconstruct π^0 at relatively high p_T (25-30 GeV/c) and also the identification of single electrons and pairs in a region of dense hadron backgrounds coming from the W and Z boson decays.

Endcap Electromagnetic Calorimeter (EEMC) :

As suggesting the name of EEMC, it is mounted inside the west STAR magnet pole tip and covers the pseudo-rapidity region of $1 \leq \eta \leq 2$ with full azimuthal angle. It extends the rapidity coverage of BEMC and also supplements it. The EEMC is also a lead-scintillator of sampling electromagnetic calorimeter type. Similar to BEMC it has 720 individual towers with a size of either 0.05×0.1 or 0.1×0.1 in the $\eta - \phi$ plane. These are further grouped together to form 90 trigger patches each having a coverage of 0.3×0.2 in $\eta - \phi$ plane. The SMD is also included in the design of EEMC optimizing its capability to discriminate between photon and π^0 or η^0 over an energy region of 10-40 GeV. Pre-shower and post-shower layer technology implemented in EEMC is used to discriminate between electrons and hadrons. The acceptance of EEMC improves STAR's capacity to detect photons, π^0, η, to discriminate electrons, positrons and to trigger high p_T particles and jets.

Bibliography

[1] M. J. Tannenbaum, arXiv:**1201.5900** [nucl-ex], (2012)

[2] J. Benjamin *et al*., IEEE Particle Accelerator Conference (PAC99).

[3] L. Ahrens *et al*., IEEE Particle Accelerator Conference (PAC2001).

[4] http://www.agsrhichome.bnl.gov/RHIC/Runs/

[5] R. Fernow, Introduction to Experimental Particle Physics (Cambridge University Press, Cambridge, 1986).

[6] D Arkhipkin, J Lauret, IOP Conf. Series: Journal of Physics: Conf. Series **898** (2017) 032023.

[7] http://rnc.lbl.gov/ jhthomas/public/HeavyFlavorTracker/

[8] https://drupal.star.bnl.gov/STAR/starnotes/public/csn0121 (1996).

[9] M. Anderson *et al*., Nucl. Instr. Meth. **A 499**, 659 (2003); H. Wieman *et al*., IEEE Trans. Nuc. Sci. **44**, 671 (1997); J. Thomas *et al*., Nucl. Instr. Meth. **A 478**, 166 (2002).

[10] K. H. Ackermann *et al*., Nucl. Instr. Meth. **A 499**, 713 (2003).

[11] M. M. Aggarwal *et al*., Nucl. Instr. Meth. **A 499**, 751 (2003).

[12] M. M. Aggarwal *et al*., Nucl. Instr. Meth. **A 488**, 131 (2002).

[13] W. Llope *et al*., Nucl. Instr. Meth. **A 522**, 252 (2004); W. J. Llope (STAR TOF Group), Nucl. Instr. Meth. **A 241**, 306 (2005).

[14] B. Bonner *et al*., Nucl. Instr. Meth. **A 508**, 181 (2003); E. C. Zeballos *et al*., Nucl. Inst. and Meth. **A 374**, 132 (1996).

[15] M. Beddo *et al*., Nucl. Instr. Meth. **A 499**, 725 (2003).

[16] C. E. Allgower *et al*., Nucl. Instr. Meth. **A 499**, 740 (2003).

[17] https://drupal.star.bnl.gov/STAR/starnotes/public/sn0600.

[18] https://cerncourier.com/the-time-projection-chamber-turns-25/.

[19] M. Anderson *et al*., Nucl. Instr. Meth. **A 499**, 679 (2003).

[20] D. Liko, STAR Note 00087, **1** (1992).

[21] H. Bichsel, Nucl. Instr. Meth. **A 562**, 154 (2006).

[22] W. M. Yao *et al*., J. Phys. G: Nucl. Part. Phys. **33, 1** (2006).

[23] W. J. Llope, Nucl. Instr. Meth. **661**, S110 – S113 (2012).

[24] M. Shao *et al*, Nucl. Instrum. Methods Phys. Res. **A 558**, 419 (2006).

[25] A. Ljubicic *et al*., IEEE Trans. Nucl. Sci., **99**, NS-47 (2000); J. M. Landgraf *et al*., Nucl. Instr. and Meth. **A, 499**, 758 (2003).

[26] F. S. Beiser *et al*., Nucl. Instr. and Meth. **A, 499**, 762 (2003).

[27] http://www.star.bnl.gov/public/trg/trouble/operating-trigger/.

[28] C. Adler *et al*., Nucl. Instr. Meth. **A 470**, 488 (2001).

[29] H. Appelshauser *et al*., Eur. Phys. J. **A 2**, 383 (1998).

[30] B. I. Abelev *et al*. (STAR Collaboration), Phys. Rev. Lett. **101**, 252301 (2008); STAR ZDC-SMD proposal, STAR Note SN-0448 (2003).

[31] M. Shao *et al*., Nucl. Instr. Meth. **A 492**, 344 (2002).

Chapter 3

Identified Particle Production in Au+Au Collisions at $\sqrt{s_{NN}} = 14.5$ GeV in STAR

For both theorists and experimentalists, to arrive at any conclusion or result various hurdles and steps have to be crossed. The combination of human idea, intelligence and patience gives birth to any relevant science. Though there is a standard analysis platform laid for us now a days, still it needs each individuals effort to add something new to it. This is what we are going to do in the current chapter of this thesis.

In the current chapter, the results of the analysis on identified particle production in Au+Au collisions at $\sqrt{s_{NN}} = 14.5$ GeV are systematically presented.

3.1   Introduction

The Relativistic Heavy Ion Collider experiment at BNL functions with its physics motivations and continuing its journey till date. The recreation of QGP medium, which is a hot-dense sea of free quarks and gluons require high temperature or energy density for its existence, [1] is one of the primary goals of RHIC. The exploration of the conjectured phase diagram of QCD, showing the relationship between temperature T and baryon chemical potential μ_B [2] falls within the RHIC physics outlook. The QCD phase diagram shows a separation between the QGP phase and the hadron gas. A crossover near zero μ_B [3], a first order phase transition line at sufficiently higher μ_B [4] are predicted from lattice QCD calculations. The turning

point of the first order phase transition line is suspected to be a second order phase transition point, popularly known as the QCD critical point [5]. All these features of the nice QCD phase diagram needs its exploration via experiments.

The above underlying physics directed the RHIC experiment to run its phase-I of Beam Energy Scan (BES-I) program. In this program, Au+Au collisions are recorded in a wide range of center of mass energies with each energy giving a single point in the (T, μ_B) phase diagram. The STAR detector at RHIC took data in the year 2010-2011 with Au+Au collisions at $\sqrt{s_{NN}} = 7.7$, 11.5, 19.6, 27 and 39 GeV. In the year 2014, another beam energy point at $\sqrt{s_{NN}} = 14.5$ GeV is added to this BES-I program.

This thesis chapter concentrates on analyzing the data in Au+Au collisions at $\sqrt{s_{NN}} = 14.5$ GeV. The analysis begins with the identification of π^+, K^+, p and their anti-particles and measurement of their transverse momentum (p_T) spectra. Next, we have extracted the basic observables from the p_T spectra as average transverse momentum ($\langle p_T \rangle$), particle yields (dN/dy) and different particle ratios. From these observables follow the calculation of freeze-out properties of the medium. All these observables are investigated as a function of collision centrality and energy. Analysis of similar type at the other BES energies is reported in ref. [6]. A one-to-one comparison with models like A Multi Phase Transport (AMPT) model [7] and Ultra relativistic Quantum Molecular Dynamics (UrQMD) [8] are also presented in this chapter.

3.2 Flow of Analysis

The analysis is carried out systematically following a multi-step procedure to finally obtain the results as mentioned below. There is a standard platform designed for these type of analysis with proper tools and techniques as reported in earlier publications from the STAR collaboration [6].

1. Suitable and standardized event and track selection cuts are applied for the selection of good tracks.

2. The tracks within rapidity acceptance $|y| < 0.1$ are specifically selected for this analysis.

3. The momentum and energy loss (dE/dx) information obtained from the TPC is utilized to perform the identification of pions, kaons and protons. A multi-Gaussian fit to the normalized dE/dx distribution estimates the raw yields for each particle type.

4. Time of flight information obtained from the TOF detector is used to count the raw yields of particles by predicted mass-square method.

5. The momentum of particles like kaon and proton are corrected from energy loss.

6. The correction for the track reconstruction efficiency and acceptance of the detector is applied p_T by p_T to the raw yields of each particle type.

7. Since the raw yields are obtained from two individual sub-detectors, a matching correction termed as TOF matching efficiency is applied to the raw p_T spectra obtained from TOF.

8. The yield of pions is corrected from contaminations from muon and weak decays.

9. The background protons are subtracted from the yields of proton p_T spectra.

10. Systematic uncertainties are estimated from various sources and added in quadrature to the statistical errors.

After following all the above sequential procedure, we obtain finally corrected transverse momentum spectra for each particle.

3.3 Data Set, Triggers and Analysis Cuts

The immediate recorded electronic pulses of the high-energy heavy-ion collision experiment is not used directly for physics analysis purpose. Rather, these basic electronic signals are processed through various standard STAR software reconstruction chains. The application of the proper track reconstruction algorithm reconstructs a track. All the information about each particle track with relevant quantities from each of the sub-detector system are finally recorded in disks for each run and each beam energies separately. These are called as μ-Data Summary

Tapes (μ-DSTs) in the language of STAR. These μ-DSTs are made available for any physics analysis.

The results presented in this thesis chapter analyzes the last data point of Au+Au collisions at $\sqrt{s_{NN}} = 14.5$ GeV recorded by the STAR detector at RHIC in the year 2014 under BES-I program. Minimum-biased triggered data are selected from the Beam-Beam Counters (BBCs) [9, 10]. The BBCs are two scintillator based detector situated on either side of the STAR detector. It has a pseudo-rapidity coverage of $2.2 < |\eta| < 5.1$ and full azimuthal coverage. These triggers do their basic job of selection of events for physics analysis as well as provide the position of the z-component of primary vertex position through the co-incidence signal of the two BBCs. These BBC triggered data of Au+Au collisions at $\sqrt{s_{NN}} = 14.5$ GeV is analyzed in the subsequent sections to arrive at the desired results.

3.3.1   Event Selection

A single collision in heavy-ion experiments produces a large number of particles. For a given data set, there is a wide range of interaction points associated with each collision along the beam axis. The track reconstruction algorithm by the method of back extrapolation determines for each event the common point of origin of primary tracks, called as the primary vertex position. So in reality, it is a three dimensional distribution of collision points in space with x, y and z-components. All the distances are measured with respect to the (0, 0, 0) of the local co-ordinate system of STAR, i.e the center of STAR TPC.

In a particular physics analysis, all the events stored in the $\mu-$DSTs are not usually analyzed. Rather the event statistics are optimized according to the requirement of a particular physics analysis which is done as per the other BES analysis in this type [6]. In order to avoid events from beam gas and beam material interaction, we apply a vertex position cut of $|V_z| < 30$ cm along the beam axis to select the events. The transverse plane perpendicular to the beam axis is the xy-plane containing vertex co-ordinates V_x and V_y. A radial vertex position cut defined as $V_r = \sqrt{V_x^2 + V_y^2} < 1$ cm is used in this analysis. In Au+Au collisions at $\sqrt{s_{NN}} = 14.5$ GeV, the mean vertex position in the xy-plane is not centered at (0, 0) cm, but slightly offset at (0, 0.89) cm. This offset has been considered in the definition of V_r in Au+Au
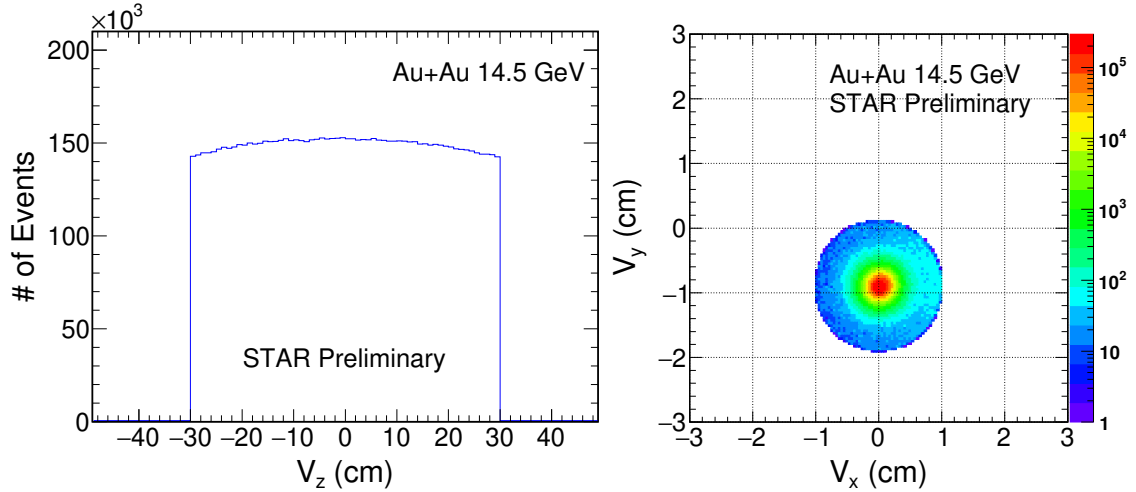
Figure 3.1: Distribution of z-component of vertex V_z (left panel) and V_x vs. V_y (right panel) distributions after all the event cuts in Au+Au collisions at $\sqrt{s_{NN}} = 14.5$ GeV in STAR.

collisions at $\sqrt{s_{NN}} = 14.5$ GeV. After all trigger selection and event selection cuts, the number of events analyzed is nearly 10 Million. The V_z and V_x vs. V_y distributions in Au+Au collisions at $\sqrt{s_{NN}} = 14.5$ GeV are shown in Figure 3.1.

3.3.2 Track Selection

We have used those track selection criteria as reported in previous analysis in STAR [6]. Only the primary tracks are chosen for this analysis and optimum filters are applied to avoid mixing of secondary tracks. The Distance of Closest Approach (DCA) from the track to the collision vertex is taken to be less than equal to 3 cm to suppress tracks from the secondary vertex. Another criterion is the number of fit points cut defined as nFitPts is the number of fit points associated with the track is taken to be greater than 25 is used to avoid split tracks. The tracks traversing through the TPC volume can have a maximum 45 possible number of hits. The frac-

Table 3.1: Track selection criteria for the tracks in Au+Au collisions at $\sqrt{s_{NN}} = 14.5$ GeV

Source	Value
$|y|$	< 0.1
$|$DCA$|$ (cm)	< 3
nFitPts	≥ 25
$\frac{\text{nFitPts}}{\text{nFitPoss}}$	≥ 0.52
ndEdx	≥ 15

tion of points used in the fit is required to be greater than 52% of the total fit points (nFitPoss). These two track cuts are to avoid over counting of split tracks (one track but counted as two). In order to ensure tracks must have good $\langle dE/dx \rangle$ resolution values, a condition is applied to the number of hits used to calculate $\langle dE/dx \rangle$ to be greater than 15. The rapidity window selected to perform the analysis is $|y| < 0.1$. The track selection criteria used in Au+Au collisions at $\sqrt{s_{NN}} = 14.5$ GeV is listed in Table 3.1.

3.3.3 Centrality Selection

As the name suggests, the collision centrality is related with the center-to-center distance at the time overlap between the two colliding nuclei in heavy-ion collisions. General terminology used for this is the "impact parameter" (b), which defines the perpendicular distance between the centers of the two colliding nuclei at the time of closest approach. Depending on the overlapping area or impact parameter value, the centrality of a collision is determined. The collisions are called more central if it has a smaller value of impact parameter (near to zero) or larger area of overlap. On the other side, if the impact parameter is large or the area of overlap between the two colliding nuclei is small, then the collision is called as a peripheral collision. The collisions having impact parameters in between these values are assigned with definite mid centrality values. Though the definition of collision centrality appears to be quite simple, but the evaluation of centrality of a collision is a complex procedure. This is usually done in STAR by the combination of information from data itself as well as comparing with Monte-Carlo Glauber simulations.

From an experiment, the direct measurement of the impact parameter is not possible. However, there are otherwise ways developed to calculate the centrality of a collision. In STAR, the observable called as the "reference multiplicity" (N_{ch}) serves this purpose. It is the number of charged particles produced having at least 10 fit points, within pseudo-rapidity $|\eta| < 0.5$ and DCA less than 3 cm. These track cuts are optimized with the required physics reasons. The chances of change in centrality values with collision vertex are eliminated by the η cut. The chances of intermixing of secondary interactions and decays is minimized by the application of the DCA cut. Bad run numbers are identified and corrected in the definition of reference multi-

plicity. Efficiency×acceptance and trigger inefficiency corrections are applied to the reference multiplicity for different ranges of z-vertex positions. The measured reference multiplicity from data is compared with simulation obtained from a two component model [11] as follows

$$\frac{dN_{ch}}{d\eta} = n_{pp}\left[(1-x) + \frac{N_{\text{part}}}{2} + xN_{\text{coll}}\right],$$ (3.1)

where n_{pp} is the average charged particle multiplicity in minimum-bias p+p collisions and x is the hard component. N_{part} is the total number of nucleons undergone at least one collision. N_{coll} represents the number of nucleon-nucleon binary collisions. A geometrical model reproducing the features of nucleus-nucleus collisions known as the Glauber model [12] is used to calculate the N_{part}, N_{coll} and b of a collision. In a Monte-Carlo Glauber model, the distribution of nucleons inside a nucleus is given by the Wood-Saxon density:

$$\rho(r) = \frac{\rho_0}{1 + e^{\frac{r-r_0}{a}}},$$ (3.2)

where ρ_0 is the normal nuclear density, r_0 is the nuclear radius and a is the skin depth. The nucleons inside the nucleus are separated by a distance greater than the minimum inter-nucleon distance. The nuclei, as well as the nucleon-nucleon pairs are selected with random impact parameter b. These are analyzed in terms of the geometrical total cross-section (σ). The distributions like $d\sigma/db$, $d\sigma/dN_{\text{part}}$ and $d\sigma/dN_{\text{coll}}$ are determined. Each distribution are sliced as a fraction of the measured total cross-section and the average value of N_{part} and N_{coll} are calculated for each centrality bins. The systematic uncertainties associated with N_{part} and N_{coll} are estimated by varying the value of σ_{pp} and x in the two-component model as well as the input parameters in Glauber Monte-Carlo simulations which are added in quadrature to the statistical errors. In order to introduce the event-by-event variation in multiplicity, a convolution of the Negative Binomial Distribution (NBD) for multiplicities in p+p collisions with N_{part} and N_{coll} are performed. The NBD distribution in multiplicity n is defined through two parameters n_{pp} and k given by

$$P_{NBD}(n_{pp}, k; n) = \frac{\Gamma(n+k)}{\Gamma(n+1)\Gamma(k)} \times \frac{(n_{pp}/k)^n}{(n_{pp}/k + 1)^{n+k}},$$ (3.3)
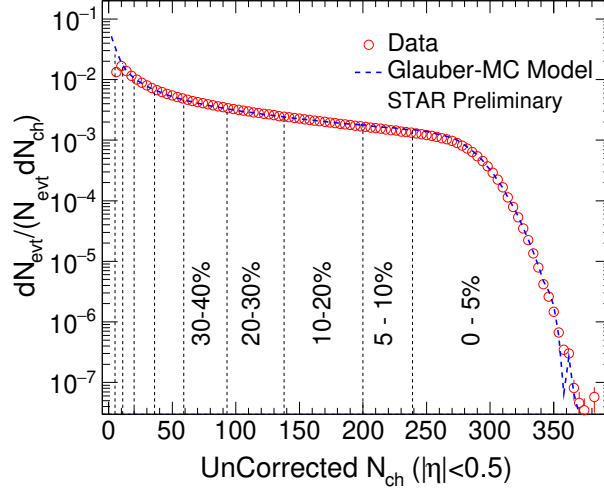
Figure 3.2: Uncorrected charged-particle multiplicity distribution (open circles) measured in the TPC within $|\eta| < 0.5$ in Au+Au collisions at $\sqrt{s_{NN}}$ = 14.5 GeV. The blue dashed line represents the charged particle multiplicity distribution from a MC Glauber model. The vertical dashed lines represent the centrality selection criteria used. The errors are statistical only.

where Γ is the Gamma function. The values of n_{pp} and k are estimated by fitting the measured multiplicities with those from simulations. The simulated multiplicity distribution is found to be quite stable to the change in k parameter [13]. The fraction of the total cross-section from the simulated events gives the centrality estimation. The refmult distribution obtained from data and compared with Glauber model calculations depicting the centrality bins in Au+Au collisions at $\sqrt{s_{NN}}$ = 14.5 GeV is presented in Figure 3.2. The minimum-bias trigger events are divided into nine centrality classes: 0-5%, 5-10%, 10-20%, 20-30%, 30-40%, 40-50%, 50-60%, 60-70% and 70-80%. The last centrality bin corresponding to 80-100% centrality is

Table 3.2: Summary of centrality bins, average number of participants N_{part}, number of binary collisions N_{coll} and the corresponding values of Refmult in Au+Au collisions at $\sqrt{s_{NN}}$ =14.5 GeV. The errors are systematic uncertainties.

Centrality (%)	$\langle N_{\text{part}} \rangle$	$\langle N_{\text{coll}} \rangle$	Refmult
$0-5$	338 ± 2	788 ± 30	> 239
$5-10$	289 ± 6	634 ± 20	> 200
$10-20$	226 ± 8	454 ± 24	> 138
$20-30$	159 ± 10	283 ± 24	> 93
$30-40$	108 ± 10	168 ± 22	> 59
$40-50$	70 ± 8	94 ± 18	> 36
$50-60$	44 ± 8	50 ± 12	> 20
$60-70$	26 ± 7	25 ± 9	> 11
$70-80$	14 ± 5	12 ± 5	> 5

excluded from calculation due to significant trigger and vertex inefficiency associated with this centrality region. The average number of participant nucleons $\langle N_{\text{part}} \rangle$ is also evaluated for each of these nine centrality bins. The value of N_{part}, N_{coll} and corresponding values of reference multiplicity are listed in Table 3.2 for Au+Au collisions at $\sqrt{s_{NN}} = 14.5$ GeV.

3.4 Procedure of Particle Identification

To proceed deeper into the analysis, the first step is to identify and count the particle of your choice among all the particles. Among various physical properties, a particle is mostly identifiable from its mass being unique for a particle and charge to discriminate between particle and anti-particle. In a heavy-ion collision experiment, the charge of the track can only be determined from its curvature when subjected to a magnetic field, whereas there are no direct measurements about its mass. However, there are other informations stored in the detector which opens up the path to reach the mass of the particle. Such informations are the energy loss (dE/dx) of a track measured in TPC and the time of flight obtained from TOF. The methodology of particle identification using these detectors are briefly discussed below. The performances of these detectors can be found in detail in refs. [14]

3.4.1 Particle Identification Using TPC

TPC has excellent particle tracking and identification capability, especially in the low momentum range. The TPC is a gas detector filled up with P10 gas at above 2 mbar atmospheric pressure. The charged particles passing through the TPC volume, encounter the gas molecules on their path, as a result of which they lose a significant amount of energy followed by ionization of the gas molecules inside TPC. This ionization energy loss is represented by dE/dx and is related to the particles momentum and its mass. The dE/dx distributions do not follow the Gaussian shape due to the random nature of interactions. Rather, it follows the Landau distribution [15] accompanied by a long tail towards higher ionization region. The average values of dE/dx are sensitive to any fluctuations in the tail part of the Landau distribution. To take care of these fluctuations, the truncated mean value of $\langle dE/dx \rangle$ is mostly used in calculation
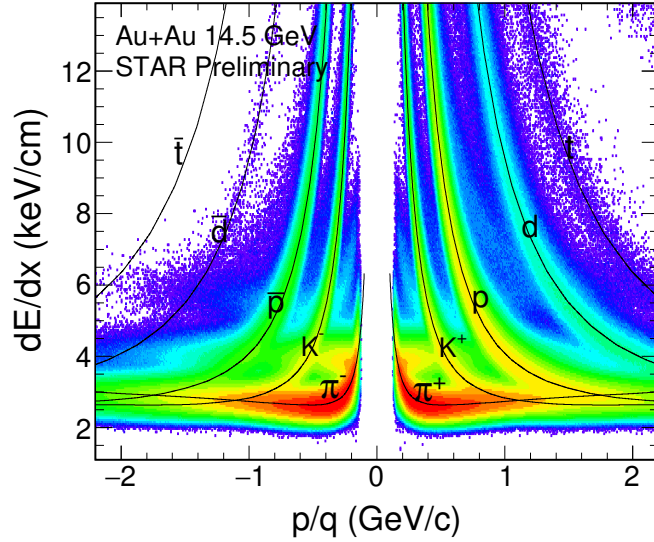
Figure 3.3: The $\langle dE/dx \rangle$ distribution of charged particles as a function of (momentum/charge) for Au+Au collisions at $\sqrt{s_{NN}} = 14.5$ GeV. The curves represents the expected mean value of $\langle dE/dx \rangle$ for the corresponding particle [17].

purposes to characterize the ionization energy loss of charged particles. The value of the mean truncated $\langle dE/dx \rangle$ is evaluated by discarding the highest 30% of the of the measured dE/dx values of the hits for each track and considering the remaining 70%, which represents the average ionization energy loss. The theoretical description for the average ionization energy loss of a particular particle in a given material is given by the Bethe-Bloch formula [16]. However, for the TPC detector material type of STAR, the Bethe-Bloch formula has been modified and is known as the Bichsel formula [17]. A comparison of the measured $\langle dE/dx \rangle$ as a function of momentum with the theoretical expectation value obtained from the Bichsel formula identifies the particle type. This characteristic plot in Au+Au collisions at $\sqrt{s_{NN}} = 14.5$ GeV depicting $\langle dE/dx \rangle$ as function of charge/momentum (p/q) is shown in Fig. 3.3. As can be seen from Fig. 3.3, different particles fall on a specified band of $\langle dE/dx \rangle$ around their expectation values obtained from the Bichsel function shown by solid curves. It follows from the figure that, the dependence of $\langle dE/dx \rangle$ on the particle mass becomes weak with increasing particle momentum. As we can see that, the $\langle dE/dx \rangle$ band of $\pi^{\pm}$, $K^{\pm}$ and $p(\bar{p})$ start merging around 1.0 GeV/c. Owing to this, pion, kaon identification is limited to 0.8 GeV/c, whereas proton upto 1.0 GeV/c by this procedure.

3.4.2 Particle Identification Using TOF

The particle identification has been pushed further to relatively higher momentum by considering the time of flight information (t_{tof}) provided by the TOF detector. The time of flight (t_{tof}) of a particle is the time taken by it from the primary vertex to reach TOF. The mass of the particle is calculable from this t_{tof} in terms of the velocity of the particle defined as $\beta = l/t_{\text{tof}}$, where l is the path length of the particle. The measured mass-square (m^2) value of a particle is related to $1/\beta$ by the mathematical expression

$$m^2 = p^2 \left(\frac{1}{\beta^2} - 1 \right) = p^2 \left(\frac{t_{\text{tof}}^2}{l^2} - 1 \right), \tag{3.4}$$

where p is the momentum of the particle. This $1/\beta$ as a function of momentum/charge is presented in Fig. 3.4 in Au+Au collisions at $\sqrt{s_{NN}} = 14.5$ GeV. We can visualize that, the bands of particles are well separable to a higher momentum, which is upto 2.0 GeV/c specifically for $\pi^{\pm}$, $K^{\pm}$ and $p(\bar{p})$.

The combination of the dE/dx information obtained from TPC and the time of flight information measured by TOF provides good particle identification for $\pi^{\pm}$, $K^{\pm}$ and $p(\bar{p})$ within mid-rapidity window of $|y| < 0.1$.
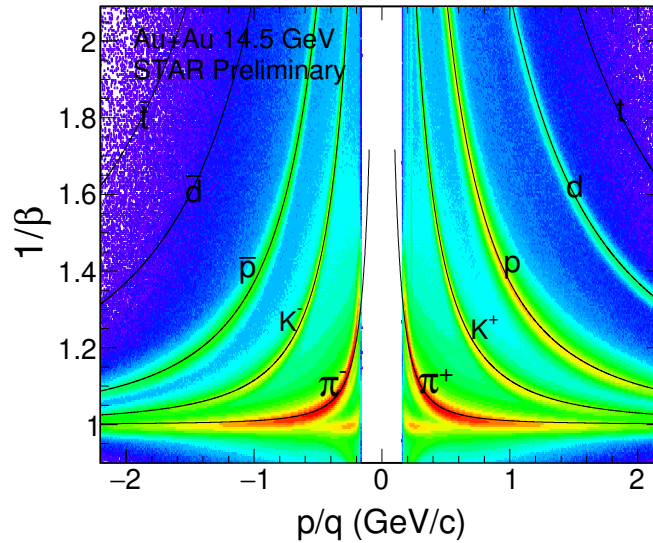
Figure 3.4: $1/\beta$ as function of (momentum/charge) for Au+Au collisions at $\sqrt{s_{NN}} = 14.5$ GeV. The curves represent the theoretical values of $1/\beta$ for the corresponding particle.

3.5 Raw Yield Extraction Techniques

We will discuss separately the techniques which are being popularly used for raw yield extraction of particles like $\pi^{\pm}$, $K^{\pm}$ and $p(\bar{p})$ in TPC and TOF below. These techniques can be found in detail in refs. [6, 18].

3.5.1 Raw yield extraction Using TPC

As we have seen that, for a specific particle type $\langle dE/dx \rangle$ is not purely Gaussian in nature [19]. So, in order to extract the raw yields using TPC, at first a suitable choice of a Gaussian variable constructed from the $\langle dE/dx \rangle$ is required. In the present analysis to extract the raw yields of π^{+}, K^{+}, p and their anti-particles, the z-variable [19] is being used, defined as

$$z_i = \ln\left(\frac{\langle dE/dx \rangle_{measured}}{\langle dE/dx \rangle_{theory}}\right),$$ (3.5)

where $\langle dE/dx \rangle_{theory}$ is the expected dE/dx value of the ith particle species (e, π, K, p) obtained from the modified Bethe-Block (Bichsel) formula [17]. The $\langle dE/dx \rangle_{theory}$ is mathematically parameterized as

$$\langle dE/dx \rangle_{theory} = A_i\left(1 + \frac{m_i^2}{p_{\mathrm{mag}}^2}\right),$$ (3.6)

where A_i is the normalization factor determined from data, m_i is the mass of the particle under consideration and p_{mag} is the magnitude of particle momentum. From the very construction, the expectation of z_i for the particle under consideration peaks around "0". The technique which is used in the present analysis can be found in detail in refs. [6, 18]. This procedure is also briefly discussed here.

The z_i distribution is constructed for a given particle type in a given p_T range within rapidity $|y| < 0.1$. The z_{π} distribution for π^{+} for $0 - 5\%$ in centrality in Au+Au collisions at $\sqrt{s_{NN}} = 14.5$ GeV is presented in Fig. 3.5. A multi-Gaussian fit to the z-distribution is performed to extract the raw yields for each particle for each p_T bin . The area under the Gaussian curve for the particle under consideration gives the yield of that particle for that p_T range. The width
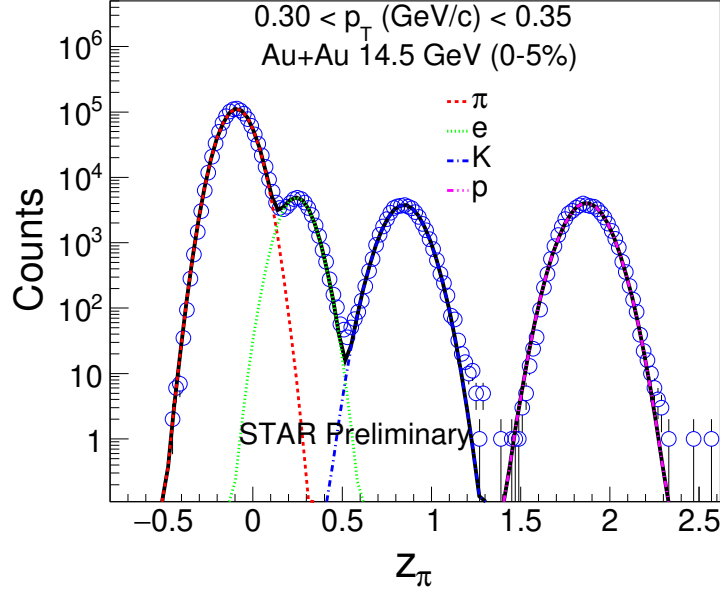
Figure 3.5: The z_π distribution of π^+ for $0.30 < p_T < 0.35$ GeV/c in $0 - 5\%$ centrality in Au+Au collisions at $\sqrt{s_{NN}} = 14.5$ GeV. The curves are Gaussian fits representing contributions from pions (dashed red), electrons (dotted green), kaons (dash-dotted blue), and protons (dash-dot-dotted magenta). The errors are statistical only.

of the peaks are sensitive to detector resolution. From theoretical considerations during the multi-Gaussian fit, the width of the electron peak is set to be equal to that of the width of pion peak. This method is applicable for low p_T values, up to the point where the distributions for pions, kaons and protons are well separated. For higher values of p_T, where the distributions start to overlap, the widths of the Gaussian distributions are constrained according to the values at lower p_T upto the range the peaks can be distinguished. The same procedure is followed for each particle type and the raw yields are extracted for different p_T ranges in nine different centrality classes. Using this method, pions and kaons are identified up to p_T of 0.8 GeV/c and protons up to 1.0 GeV/c.

3.5.2 Raw yield extraction Using TOF

The m^2 variable proves its beneficiality in extracting the raw yields of $\pi^\pm$, $K^\pm$ and $p(\bar{p})$ upto a relatively higher momentum range. But, the hurdle here is that the m^2 distribution for a given particle is not Gaussian. So, rather than Gaussian fitting, a different approach for raw yield extraction is being used [6, 14].

The raw yield of charged particles in TOF is extracted from the m^2 variable given by
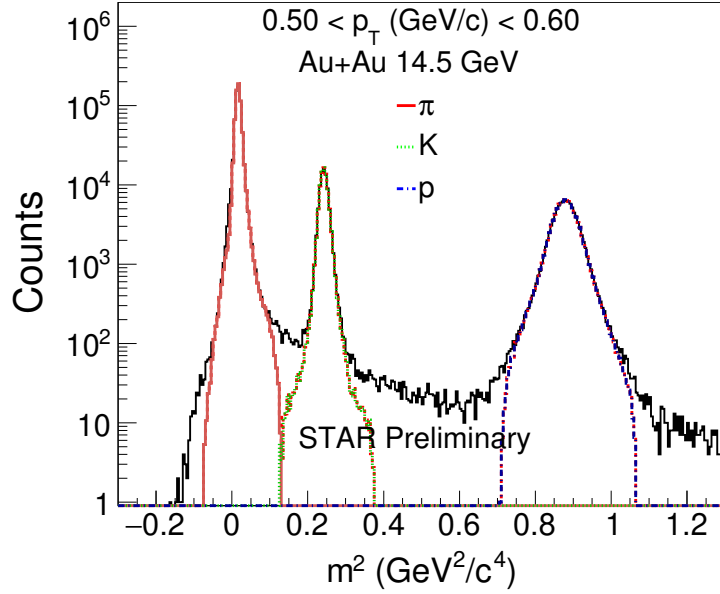
Figure 3.6: The m^2 distributions used to obtain the raw yields of π^+ within $|y| < 0.1$ for $0.50 < p_T < 0.60$ GeV/c in $0-5\%$ centrality for Au+Au collisions at $\sqrt{s_{NN}} = 14.5$ GeV. The curves are fits to m^2 distributions representing contributions for pion (solid-red), kaon (dotted-green) and proton (dash-dotted-blue). The errors are statistical only.

$$m^2 = p^2 \left(\frac{c^2 T^2}{l^2} - 1 \right), \tag{3.7}$$

where p, T, L and c are the momentum, time-of-flight, path length of a particle and velocity of light respectively. Within $|y| < 0.1$, the m^2 distributions are obtained for the particle of interest in a given p_T range, and is shown in Fig. 3.6 for the case of π^+ for p_T range 0.50-0.60 GeV/c. To extract the raw yields using m^2 distributions, we follow the same procedure as done in Refs. [6, 14] and are briefly described below.

We calculate the predicted m^2 distributions to fit these distributions. First, we calculate the expected time-of-flight T_{expected} for the particle of interest using the theoretical mass of the particle of choice. Then we calculate the difference distribution $\Delta t = T_{\text{measured}} - T_{\text{expected}}$ in a given p_T range within rapidity $|y| < 0.1$. These Δt distributions carry the behavior of TOF detector response. The Δt distributions are obtained in each p_T bin and are used to generate a random time shift t_{random}. i.e., we generate a random distribution of similar shape as that of Δt distributions. Then we calculate the predicted time-of-flight $T_{\text{predicted}}$ as $T_{\text{predicted}} = T_{\text{expected}} + t_{\text{random}}$. The $T_{\text{predicted}}$ values are then used to calculate the predicted m^2 by using the formula as

$$m^2_{\text{predicted}} = p^2 \left(\frac{c^2 T^2_{\text{predicted}}}{l^2} - 1 \right). \tag{3.8}$$

These predicted m^2 distributions for pions, kaons and protons taken together are used to si-multaneously fit the measured m^2 distributions as shown in Fig. 3.6. In this figure, the contri-butions from pions, kaons and protons are respectively shown by solid red, dotted green and dash-dotted blue lines. The black histogram represents the measured m^2 distribution and the dotted red lines represent the total fit. Using a χ^2 minimization procedure, the raw yields of each particle are obtained for each p_T bin in nine centrality classes. Using this technique, pions and kaons are identified in the p_T range of 0.4-2.0 GeV/c and protons within 0.5-2.0 GeV/c in Au+Au collisions at $\sqrt{s_{NN}} = 14.5$ GeV.

The raw yields are obtained by using the above procedure in both TPC and TOF and are properly combined to obtain the whole p_T spectra for each particle in nine different centrality classes.

3.6 Correction Factors

The STAR detector undoubtedly proves its beneficiality in tracking the charged particles, but also is associated with its own limitations, imperfections and demerits. One needs to identify these factors and properly apply the corrections.

The yields extracted from the above procedure for each p_T bin for each particle in nine different centrality classes are used to calculate the raw spectra given by the factor: $\frac{d^2N}{(2\pi p_T dp_T dy)}$. However, this raw spectra are associated with detector inefficiency as well as contamination from various sources as we will discuss later. Hence, various correction factors are calculated to correct the raw p_T spectra. The procedure especially involves the Monte-Carlo simulation known as embedding technique [6, 18, 20] as described in the subsequent subsection.

3.6.1 Monte-Carlo Embedding Technique

Simulated events are generated from a flat p_T and η distribution using Heavy Ion Jet Interaction Generator (HIGING) [21] to ensure equal statistics in each p_T bin. These generated tracks are

called embedded tracks with initial momentum p_T^{MC}. It is then mixed with the real events at 5% level and is allowed to pass through the GSTAR [22] (the software package to run STAR detector simulation using GEANT [23]) and TRS (the TPC response simulator) [22]. The data is reconstructed as that of the real data taking into consideration all the detector effects. Then an association mapping is performed between the reconstructed tracks and the input MC tracks. For each MC track in GEANT, a search for reconstructed track is performed within a window of ± 0.6 cm in x, y and z [18, 24]. If the track is found, then the reconstructed track is marked as a matched track. If more than 10 hits of the MC track match with a single reconstructed track in the embedded event, then the track is called a reconstructed track with a momentum assigned p_T^{REC}. After this, a quality assurance of the embedding sample is done to make sure that the MC simulation sample reproduces the characteristics of real data. For this, we compare distributions such as DCA, nFit points, nHits dEdx and ϕ between real data
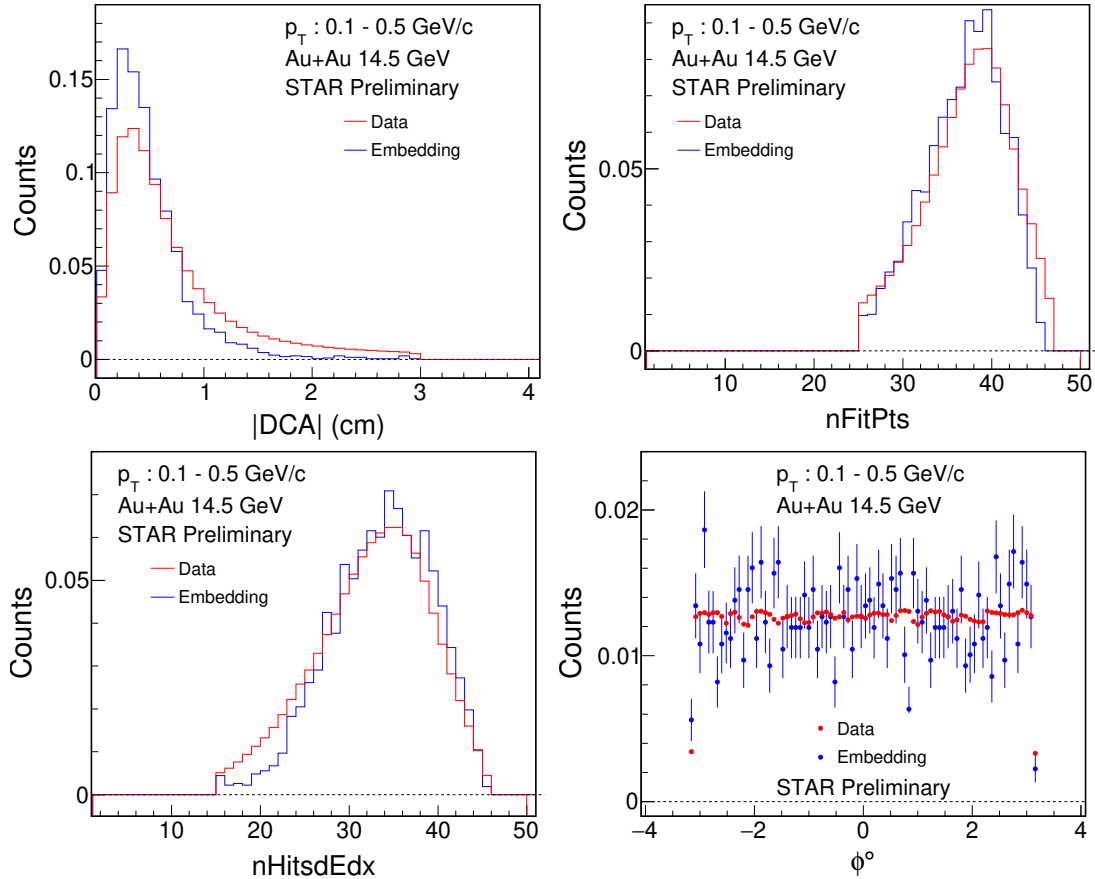
Figure 3.7: (Top left) DCA, (Top right) nFitPts, (Bottom left) nHitsdEdx, (Bottom right) phi comparison between reconstructed embedding tracks and real tracks with reference to π^+ embedding sample in Au+Au collisions at $\sqrt{s_{NN}} = 14.5$ GeV. The errors are statistical only.

112

and those obtained from embedding in mid-rapidity ($|y| < 0.1$) as shown in Fig. 3.7 in Au+Au collisions at $\sqrt{s_{NN}} = 14.5$ GeV.

In the next subsections, we will discuss about the various correction factors and their calculation procedure used to correct the raw spectra p_T bin by bin.

3.6.2 Energy Loss Correction

As a particle moves through the detector material it suffers from interactions and multiple Coulomb scattering on its path. As a result of which, the particle loses its energy and so its momentum changes. This loss of energy typically depends on the momentum of the charged particle. More particularly, a low momentum particle loses more energy in comparison to high momentum particles [16]. Due to this, the momentum measured by the TPC is lower than the actual momentum of the particle at the time of freeze-out. The track reconstruction algorithm assumes the pion mass for each particle to correct for this effect of Coulomb scattering and energy loss for each particle track. Hence, a correction for momentum for heavier particles ($K^{\pm}, p(\bar{p})$) need to be done. This correction factor is essentially calculated from MC simulation or embedding technique.
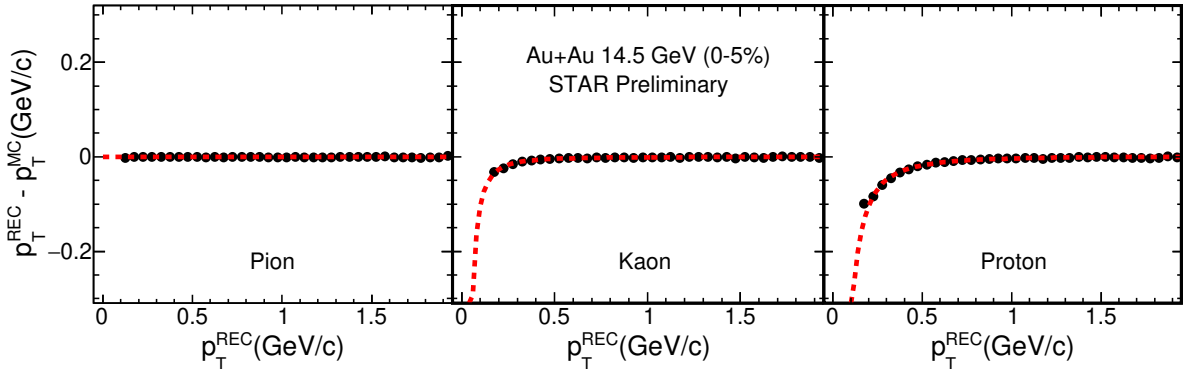
Figure 3.8: The difference of p_T between the reconstructed tracks and embedded tracks as a function of p_T of reconstructed tracks for pion (left), kaon (middle) and proton (right) in Au+Au collisions at $\sqrt{s_{NN}} = 14.5$ GeV. The curve represents the functional fit to the data. The errors are statistical only.

The energy loss correction factor is estimated from the distribution of the momentum difference between the reconstructed momentum (p_T^{REC}) and the initial momentum (p_T^{MC}) as a function of p_T^{REC}. Fig. 3.8 shows the energy loss as a function of p_T^{REC} for pion (left), kaon (middle) and proton (right) in Au+Au collisions at $\sqrt{s_{NN}} = 14.5$ GeV. The curve represents

the functional fit to the data points, whose functional form is given by

$$p_T^{\text{REC}} - p_T^{\text{MC}} = A + B \left(1 + \frac{C}{(p^{\text{REC}})_T^2}\right)^D,$$ (3.9)

where A, B, C, D are the fit parameters. The particular values of these parameters in Au+Au collisions at $\sqrt{s_{NN}} = 14.5$ GeV for kaon and proton is listed in Table 3.3.

Table 3.3: Values of energy loss parameters for kaons and protons in Au+Au collisions at $\sqrt{s_{NN}} = 14.5$ GeV

Parameters	Kaon	Proton
A (GeV/c)	2.55501e-05	2.12770e-03
B (GeV/c)	-1.16103e-05	-9.10954e-05
C (GeV/c)^2	9.47638e+01	9.29762e+01
D	9.96323e-01	9.11240e-01

The values of these parameters are applied to correct the momenta of kaons and protons at the very initial stage of selection tracks. As can be seen from the Fig.3.8, the pion p_T distribution is flat and hovers around '0' verifying the fact that it has been already corrected at the time of track reconstruction as mentioned earlier. For kaons and proton, the energy loss is typically associated in the low momentum range as debated earlier. The energy loss correction only depends on the particle momentum for a particular choice of particle. Hence, a single energy loss correction is applied for all centrality classes for kaons and protons.

3.6.3   TOF Matching Efficiency

The barrel of TOF detector surrounds TPC just above it and has a little less acceptance of 0.1 unit in pseudo-rapidity than TPC on both sides. Due to this, occasions may arise when a TPC track will fail to reach the TOF detector, especially low momentum tracks. In addition, the TOF detector inefficiency, as well as dead regions of TOF detector also results in missing tracks. As a result of this, the number of tracks in TOF is less than that in TPC. As our spectra are obtained from both TPC and TOF, it needs to be well matched. This correction factor is known as the TOF matching efficiency and is calculated from real data for each particle. We have adopted the technique as described in ref. [6]. The TOF matching efficiency as a function

of p_T is the ratio of the number of TOF matched tracks to the total number of tracks in TPC within the rapidity window under study.

$$\epsilon_{\text{match-eff}} = \frac{\text{Number of TOF Matched Tracks}}{\text{Number of TPC Tracks}}. \qquad (3.10)$$
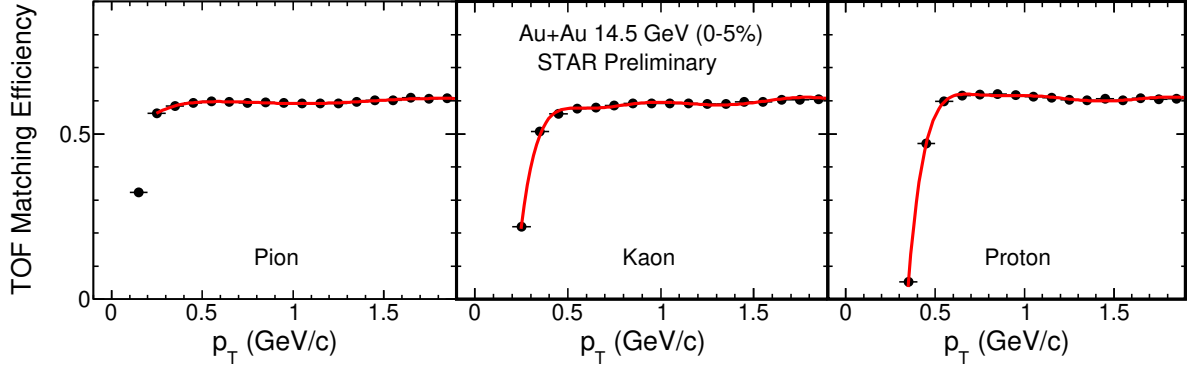
Figure 3.9: TOF matching efficiency of pions (left), kaons (middle) and protons (right) as a function of p_T for 0-5% centrality classes in Au+Au collisions at $\sqrt{s_{NN}} = 14.5$ GeV. The curve represents a higher order polynomial fit to the data. The errors are statistical only.

Figure 3.9 presents the TOF matching efficiency of pions (left), kaons (middle) and protons (right) as a function of p_T for 0-5% centrality classes in Au+Au collisions at $\sqrt{s_{NN}} = 14.5$ GeV. The curves represent a 9th order polynomial fit to the data. This TOF matching efficiency is applied to the raw yields of each particle extracted from TOF in each p_T bin in nine centrality classes.

3.6.4 Tracking Efficiency and Acceptance

The detector has its own limitations while reconstructing the tracks. All the particles may not be detected due to the geometry and dead regions of the detector or some of the tracks may not be well reconstructed due to missing hits. So a correction factor estimating the detector efficiency and acceptance needs to be applied to the p_T spectra of each particle. This correction factor is calculated from Monte-Carlo simulations or embedding technique as discussed in refs. [6, 18]. The tracking efficiency $\times$ acceptance is the ratio of the distribution of reconstructed to original Monte-Carlo tracks as a function of p_T in the given rapidity range. It is defined as

$$\epsilon_{\text{track-eff}} = \frac{\text{Number of matched MC tracks}}{\text{Number of input MC tracks}}. \qquad (3.11)$$
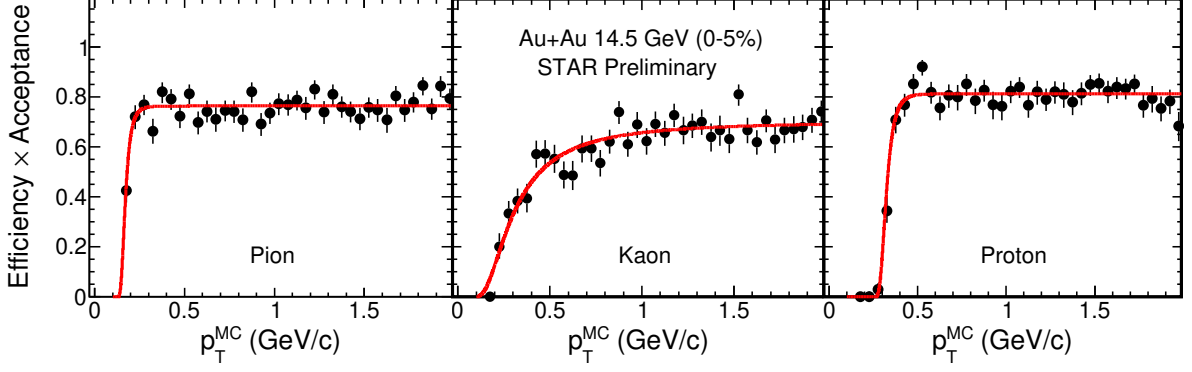
Figure 3.10: Tracking efficiency ($\times$ acceptance) as a function of p_T^{MC} calculated from embedding technique for the reconstructed tracks of pions (left), kaons (middle) and protons (right) for 0-5% centrality classes in Au+Au collisions at $\sqrt{s_{NN}} = 14.5$ GeV. The curve represents a functional fit to the data. The errors are statistical only.

Table 3.4: Values of the parameters of the functional fit to the efficiencies of π^+, K^+ and p in Au+Au collisions at $\sqrt{s_{NN}} = 14.5$ GeV

Parameters	π^+	K^+	p
P_0	0.763	0.702	0.812
P_1 (GeV/c)	0.163	0.262	0.312
P_2	8.67	2.02	11.3

This tracking efficiency $\times$ acceptance as a function of p_T^{MC} for pions (left), kaons (middle) and protons (right) for 0-5% centrality classes in Au+Au collisions at $\sqrt{s_{NN}} = 14.5$ GeV is shown in Fig. 3.10. The curves represent a functional fit to the data whose functional form is given by

$$f(p_T) = P_0 \exp\left[-(P_1/p_T)^{P_2}\right], \tag{3.12}$$

where P_0, P_1 and P_2 are the fit parameters. As can be observed from Fig. 3.10, the efficiency of pion is almost independent of p_T above 0.3 GeV/c, but sharply falls at low p_T. The low momentum pion tracks fail to travel the whole TPC volume due to their high curvature in the influence of the solenoidal magnetic field gives rise to such a sharp fall of efficiency at low momentum. A smooth increase of kaon efficiency as a function of p_T can be inferred from Fig. 3.10. The kaon efficiency is found to be significantly smaller than pion for low momentum due to loss of kaon tracks as a consequence of decays. The efficiency of proton shows almost a flat behavior above $p_T > 0.4$ GeV/c and falls steeply at low momentum. Due to the high mass

116

of (anti)protons, it suffers from multiple scattering resulting in a drop of efficiency affecting the low momentum range.

3.6.5 Pion Feed-down Correction

Since pion is the lightest meson, higher resonance particles like K_s^0 and Λ decay into pions. Also, muons having similar mass as that of pions can be misidentified as pions. Background pions coming from the detector material also has contributions to the yield of pions. As a result of this, the measured charged pion spectra obtained after all the above corrections contains contributions from weak decays, contaminations from muons as well as background pions.
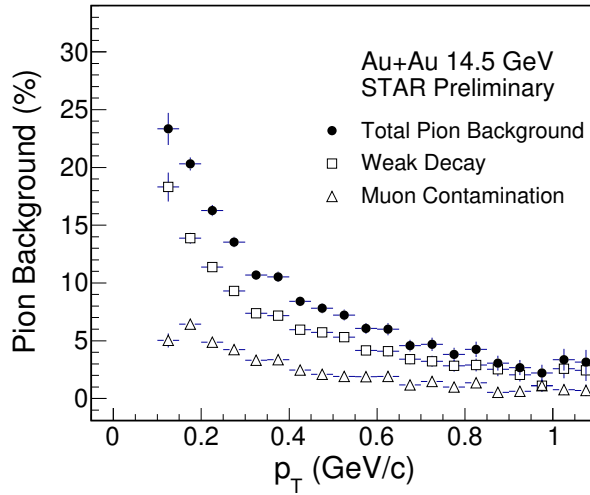
Figure 3.11: Total pion feed-down fraction to the yield of pion as function of p_T showing individual contributions from weak decay and muon contamination in Au+Au collisions at $\sqrt{s_{NN}} = 14.5$ GeV. The errors are statistical only.

The correction of the pion spectra from weak decay pions and muon contaminations is done through Monte-Carlo simulations as presented in refs. [6, 18]. In this technique, Monte-Carlo simulated events from HIJING [21] are generated, which are allowed to pass through the STAR detector simulation using the GEANT [23] package. These are finally reconstructed as that of real data [6, 18]. In this case, we know the parent particle information of each of the reconstructed track. This information is used to estimates the weak decay contribution to pion yields mainly coming from K_s^0 and Λ. The mis-identified muons as pions are filtered out from the parent particle information and their contribution to the pion yield is calculated. The total feed-down contribution to the pion yield is the sum of the weak decay contribution

and muon contamination. Figure 3.11 shows the total pion feed-down contribution to the yield of pion as a function of p_T displaying separate contributions coming from weak decay and muon contamination in Au+Au collisions at $\sqrt{s_{NN}} = 14.5$ GeV. Then, these contributions are subtracted from the raw yield of pions in each p_T bin. This pion feed-down fraction shows only p_T dependence and no centrality dependence. Hence, a single correction is applied for all the nine different centrality classes [25]. Its value decreases exponentially with value at low p_T(=0.225 GeV/c) around $\sim 16\%$ and becomes negligible above $p_T > 0.8$ GeV/c.

3.6.6 Proton Background Correction

Highly energetic particles produced in collision traveling through the detector material suffer from interactions producing secondary particles including protons. As a result of this, the yield of protons has contributions from these secondary protons produced near beam pipe. Since these protons are coming from detector material, they are produced far from the primary collision vertex. These so-called knock-out protons appear as a long trail in the DCA distribution of protons. On the other hand, anti-protons are not produced by such interactions, as a result, the long trail in the DCA distribution of anti-proton is absent. In order to correct the proton yield from these background protons, a mapping between the DCA distributions of proton and anti-proton is done in real data as discussed in refs. [6, 18].
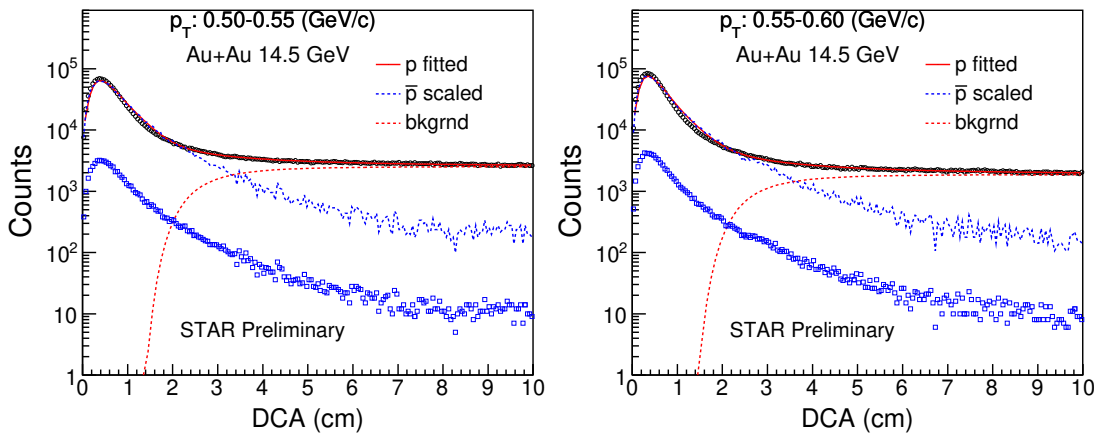
Figure 3.12: The DCA distributions of protons and anti-protons for $0.50 < p_T$ (GeV/c)$<$ 0.55 and $0.55 < p_T$ (GeV/c)< 0.60 in $0 - 5\%$ centrality in Au+Au collisions at $\sqrt{s_{NN}} = 14.5$ GeV. The dashed curve is the fit to the proton background; the dotted histogram is the DCA distribution of $\bar{p}$ scaled by $r_{\bar{p}/p}$; the solid histogram is the fit to the proton DCA distribution. The errors are statistical only.

The protons and anti-protons are selected with dE/dx cut of $|n\sigma_p| < 2$, where σ_p is the dE/dx resolution of TPC for proton track. In the analysis, the primary tracks are selected within $|DCA| < 3$ cm. To estimate the proton background correction, global tracks information upto DCA of 10 cm are extracted. This is achieved through the mapping of global tracks to primary tracks, which is used to compare the DCA distributions of protons and anti-protons upto $|DCA| \sim 10$ cm. To evaluate the proton background fraction, the DCA dependence at DCA < 3 cm is estimated for the knock-out protons. It can be seen that the DCA distribution of proton coming mostly from the knock-out proton from detector material can be described by the following function

$$p_{bkgd}(\text{DCA}) \propto [1 - \exp(-\text{DCA/DCA}_0)]^\alpha, \tag{3.13}$$

where DCA_0 and α are fit parameters. Assuming the shape of background subtracted proton DCA distribution to be similar as that of anti-proton distribution, the DCA distribution of proton can be fit by

$$p(\text{DCA}) = \bar{p}(\text{DCA})/r_{\bar{p}/p} + A p_{bkgd}(\text{DCA}). \tag{3.14}$$

Here, $r_{\bar{p}/p}$ and A are fit parameters. By using the functional fit to the proton DCA distribution, the proton background fraction in different p_T bins in nine different centrality classes are calculated.

Figure 3.12 shows the DCA distribution of protons and anti-protons for p_T ranges of 0.50-0.55 GeV/c and 0.55-0.60 GeV/c for $0 - 5\%$ centrality for Au+Au collision at $\sqrt{s_{NN}} = 14.5$ GeV. As shown in the figure, the black histogram is the DCA distribution of proton and the red-solid line is the fit to this DCA distribution. The blue-dotted histogram is the $\bar{p}$ DCA distribution and is scaled by the $p/\bar{p}$ ratio. This proton background fraction exhibits both p_T and centrality dependence. The proton background fraction within $|DCA| < 3$ cm is greatest at low p_T and is almost negligible above $p_T > 1.2$ GeV/c and are listed in Table 3.5 for 0-5% centrality in Au+Au collisions at $\sqrt{s_{NN}} = 14.5$ GeV. This fraction progressively increases as we go from central to peripheral collisions.

Table 3.5: The proton background fraction as a function of p_T in 0-5% centrality for Au+Au collisions at $\sqrt{s_{NN}} = 14.5$ GeV.

p_T (GeV/c)	Proton Background (%)		
	0-5%	40-50%	70-80
0.50-0.55	4.9	21.3	49.6
0.55-0.60	4.2	15.6	41.5
0.60-0.65	1.4	11.2	39.1
0.65-0.70	0.5	7.6	30.5
0.70-0.75		5.3	21.8
0.75-0.80		3.3	18.4
0.80-0.85		1.1	11.4
0.85-0.90		1.3	11.5
0.90-0.95		0.2	7.4
0.95-1.00		0.5	5.5

3.7   Systematic Uncertainties

Measured experimental observables are always associated with uncertainties from systematic sources. The event and track selection cuts, the PID procedure, the methods of estimation of correction factors, errors associated with extrapolation with functional fits contribute to systematic uncertainties of the measurables. The fractions of errors associated with all these sources are calculated.

Variation in event and track cuts and the quality of fits to dE/dx measurements are the major contributors to the systematic uncertainty associated with the p_T spectra of the particles under study. In order to estimate these systematic errors, event and track cuts are varied whose default values used in this analysis and the changed values for systematic uncertainties measurement are listed in Table 3.6. The variation in the fit range of the Gaussian function for dE/dx and the PID cut n_σ (from $|n_\sigma| < 2$ to $|n_\sigma| < 1$) used for the predicted m^2 distribution also adds to the source of systematic uncertainty.

The calculation of integrated particle yields (dN/dy) and $\langle p_T \rangle$ require a fitting function to extrapolate the p_T spectra to the unmeasured p_T region. The main source of systematic uncertainty in dN/dy and $\langle p_T \rangle$ is due to extrapolation. In order to estimate this systematic error, several fit functions are used. For pions, kaons and protons, the default fit functions used to extract yields are Bose-Einstein, m_T-exponential and double exponential, respectively. To es-

Table 3.6: The default and changed values of event and track cuts for systematic uncertainties measurement.

Cut Type	Default Value	Changed Value
V_z (cm)	< 30	< 50
$|y|$	< 0.1	< 0.5
DCA (cm)	< 3 cm	< 2
nFit Points	≥ 25	≥ 20
nHits dEdx	≥ 15	≥ 10
p_T GeV/c	> 0.10	> 0.15

timate the systematic uncertainty, these fit functions for pions, kaons and protons are changed to p_T-exponential, Boltzmann and m_T-exponential functions, respectively. The relevant functional forms are

- Bose-Einstein: $\propto 1/\exp(m_T/T_{\mathrm{BE}} - 1)$

- p_T-exponential: $\propto \exp(-p_T/T_{p_T})$

- m_T-exponential: $\propto \exp(-m_T/T_{m_T})$

- Boltzmann: $\propto m_T \exp(-m_T/T_B)$

- Double-exponential: $A\, e^{-p_T^2/T_1^2} + B\, e^{-p_T^2/T_2^2}$

Where m_T is the transverse mass of the particle under consideration, T_{BE} is the Bose-Einstein temperature, which is a fit parameter. T_{p_T} and T_{m_T} are also the temperatures obtained from fitting in the respective fit functions. A, B, T_1 and T_2 are all fit parameters.

Apart from these systematic errors for the case of p_T spectra, an additional error of 5% is added in quadrature due to detector tracking efficiency and acceptance [6]. The procedure of determination of pion feed-down correction and the proton background fraction also contribute to the systematic uncertainty; however, the former is negligible and the latter is significant only at low p_T. The proton background fraction contributes about 5-6% systematic error in the proton spectra at low p_T. All the sources of systematic errors are added in quadrature with the statistical error, and are tabulated in Table 3.7. The total systematic errors on pion, kaon and proton yields are 10%, 10% and 12%, respectively.

Table 3.7: Systematic uncertainties related to the yields of π, K and $p(\bar{p})$ in Au+Au collisions at $\sqrt{s_{NN}} = 14.5$ GeV.

	π	K	$p\,\bar{p}$
V_z	1%	1%	1%
Track Cuts	4%	4%	6%
PID	6%	8%	7%
Extrapolation	5%	4%	6%
Corrections	5%	5%	5%
Proton Background	-	-	$5 - 6\%$
Total	10%	10%	12%

The systematic error on mean p_T mainly comes from the errors associated with the extrapolation of p_T spectra. The fitting range of the fit function also affects the value of $\langle p_T \rangle$, which is included as a source of systematic uncertainty. The systematic errors on $\langle p_T \rangle$ for pions, kaons and protons are estimated to be 5%, 2% and 6%, respectively.

The systematic error on p_T integrated particle ratios are calculated from the systematic error on dN/dy. The systematic uncertainty due to tracking efficiency cancels in particle ratios. The error associated with extrapolation mostly cancels in the case of anti-particle to particle ratios, but does not cancel for the case of unlike particle ratios (e.g., K/π and p/π ratios).

The calculation of the chemical freeze-out parameters takes the particle yields and particle ratios as input. The systematic uncertainty associated with particle yields and particle ratios contribute to the systematic error on chemical freeze-out parameters.

The Blast-Wave fit [26] to particle p_T spectrum provides the kinetic freeze-out parameters. The point-to-point systematic uncertainty associated with the p_T spectra propagates to the systematic errors on the kinetic freeze-out parameters. The p_T ranges used for fitting also affect the results. These variations are included in the systematic error on kinetic freeze-out parameters.

3.8 Results and Discussions

In this section, we will present and discuss about the results of transverse momentum spectra of $\pi^{\pm}$, $K^{\pm}$ and $p(\bar{p})$ in Au+Au collisions at $\sqrt{s_{NN}} = 14.5$ GeV. The centrality and energy dependence of the extracted observables like average transverse momentum ($\langle p_T \rangle$), dN/dy, particle ratios, chemical and kinetic freeze-out parameters are discussed. A comparison of

all the results in Au+Au collisions at $\sqrt{s_{NN}} = 14.5$ GeV with models like AMPT [7] and UrQMD [8] are also presented here.

3.8.1 Transverse Momentum Spectra

The transverse momentum spectrum of a particle contains all the hidden information about the production and transverse dynamics experienced by the particle throughout its journey from creation in heavy-ion collision. So, as the first step of the analysis, it is essential to get the invariant yield of a particle as a function of p_T which constitutes the p_T spectra of that particle. The invariant yield of $\pi^{\pm}$, $K^{\pm}$ and $p(\bar{p})$ can be expressed by the following mathematical expression after applying all the above mentioned corrections as

$$\frac{1}{N_{\text{events}}} \frac{d^2N}{2\pi p_T dp_T dy} = \frac{1}{N_{\text{events}}} \times \frac{1}{2\pi p_T} \times \frac{1}{\Delta p_T \Delta y} \times \frac{1}{C(p_T)} \times Y(p_T), \qquad (3.15)$$

where $Y(p_T)$ symbolizes for the raw yield of the particle and $C(p_T)$ represents the product of all the correction factor as a function of p_T respectively.

The transverse momentum spectra for π^+, π^-, K^+, K^-, p, and $\bar{p}$ in Au+Au collisions at $\sqrt{s_{NN}} = 14.5$ GeV are presented in Fig. 3.13. The Y-axis represents the invariant yield and the X-axis represents p_T. The spectra are plotted for nine different centrality classes 0-5%, 5-10%, 10-20%, 20-30%, 30-40%, 40-50%, 50-60%, 60-70%, 70-80%. Some of the p_T spectra are scaled for clarity. The obtained spectra are fitted with different functions to extract dN/dy and mean p_T in each centrality. The fit functions being Bose-Einstein for pions, m_T- exponential for kaons and double exponential for (anti) protons. These fit functions are so chosen that, it best describes the spectral shape of the particle. It can be inferred from the figure that the p_T spectra exhibit both p_T dependence as well as centrality dependence. It can be seen that the shape of the pion spectra looks similar in each centrality class. Also, with increase in p_T, the pion spectra falls faster, which is a consequence of significant contribution from resonance decays. For Kaons and (anti)protons a gradual flattening with increasing centrality of the spectra is observed. The shape of proton spectra exhibits more concave nature from peripheral to central collisions which is an indication of progressively stronger radial flow effects. In central collisions, more number of particles are produced resulting in stronger collective flow effects.
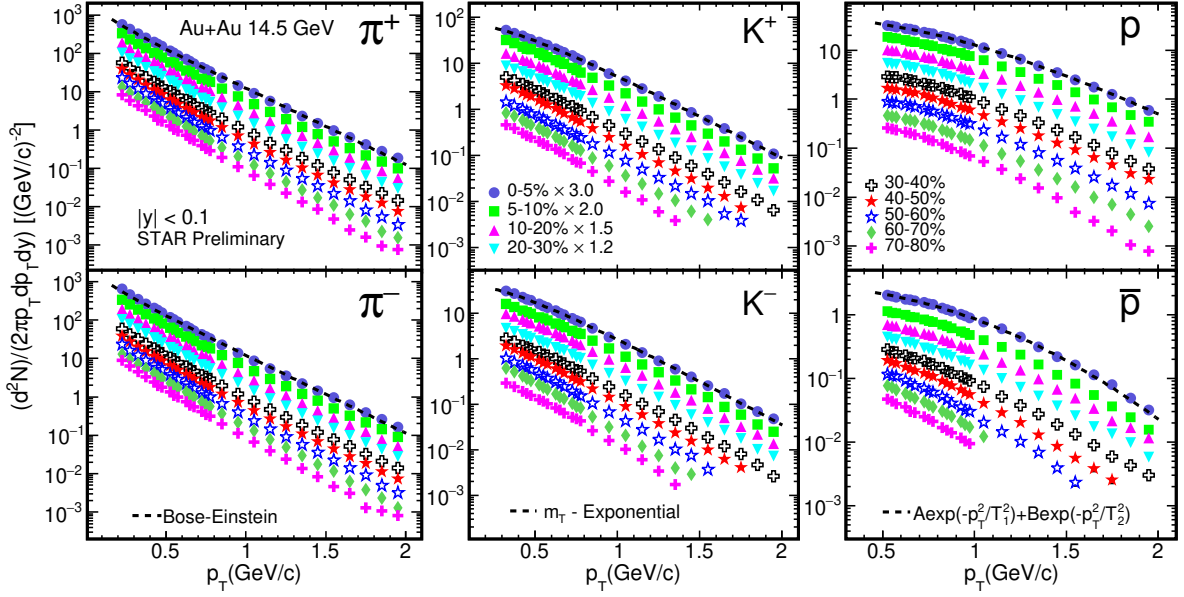
Figure 3.13: The p_T spectra of $\pi^\pm$, $K^\pm$, p ($\bar{p}$) measured at midrapidity ($|y| < 0.1$) in Au+Au collisions at $\sqrt{s_{NN}} = 14.5$ GeV. Spectra are plotted for nine centrality classes, with some spectra multiplied by a scale factor to improve clarity, as indicated in the legend. The data points shown for $p_T = 0.4$-2.0 GeV/c for pions and kaons, and for 0.5-2.0 GeV/c for protons, are obtained using both TPC and TOF. Data points measured using only the TPC are shown for p_T in the range 0.2-0.8, 0.3-0.8 and 0.5-1.0 GeV/c for pions, kaons and protons, respectively. The p_T range 0.4-1.0, 0.4-1.0 and 0.5-1.0 for pions, kaons and protons, respectively, are the overlap region containing data measurements in both categories, namely, TPC only, and TPC+TOF. The p_T-spectra are fitted with a Bose-Einstein function for pions, an m_T-exponential for kaons, and a double exponential for (anti)protons. Statistical and systematic errors are added in quadrature.

As a result of this, heavier particles should be boosted to higher transverse momentum. This effect can be seen in respect of protons to kaons and kaons to pions. Thus, the collective flow effect results in the inverse slope of the p_T spectra and rises with the mass of the particle ($\pi <$ $K < p$).

These observations are similar to the previously published results in Au+Au collisions at RHIC energies of $\sqrt{s_{NN}} = 7.7$, 11.5, 19.6, 27, 39, 62.4, 130 and 200 GeV [6, 18, 25, 28].

3.8.2 Average Transverse Momentum ($\langle p_T \rangle$)

Average transverse momentum quantitatively characterizes the slope of the measured p_T spectra of the particles and can be studied in terms of collision energy and centrality. i.e., the transverse dynamics of the particles is reflected in terms of $\langle p_T \rangle$. It is calculated as

$$\langle p_T \rangle = \frac{\int p_T 2\pi p_T f(p_T) dp_T}{\int 2\pi p_T f(p_T) dp_T}, \tag{3.16}$$

where $f(p_T)$ is the function used to fit the p_T spectra of the particles in the measured range and is extrapolated to the unmeasured region. The integration is performed in the p_T range of 0-10 GeV/c.
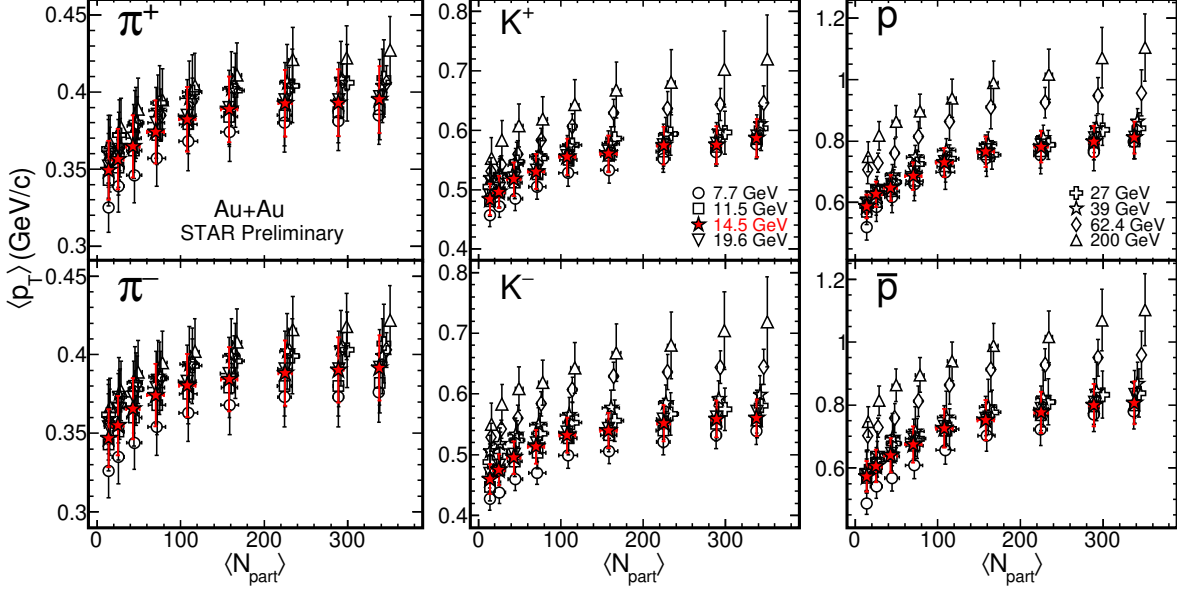
Figure 3.14: $\langle p_T \rangle$ of π^+, π^-, K^+, K^-, p and $\bar{p}$ as a function of $\langle N_{\mathrm{part}} \rangle$ for Au+Au collisions at $\sqrt{s_{NN}} = 14.5$ GeV. These averages are compared with the corresponding results from Au+Au collisions at $\sqrt{s_{NN}} = 7.7$, 11.5, 19.6, 27, 39, 62.4 and 200 GeV measured by STAR in earlier runs [6, 18, 25, 28]. Statistical and systematic uncertainties have been added in quadrature.

Table 3.8: $\langle p_T \rangle$ (GeV/c) values for π^+ and π^- from Au+Au collisions at $\sqrt{s_{NN}} = 14.5$ GeV. The quoted errors are statistical and systematic uncertainties respectively.

Centrality(%)	$\langle p_T \rangle$ (GeV/c)	
	π^+	π^-
$0-5$	$0.395 \pm 0.0001 \pm 0.022$	$0.392 \pm 0.0001 \pm 0.021$
$5-10$	$0.393 \pm 0.0001 \pm 0.022$	$0.390 \pm 0.0001 \pm 0.021$
$10-20$	$0.393 \pm 0.0002 \pm 0.022$	$0.388 \pm 0.0002 \pm 0.021$
$20-30$	$0.389 \pm 0.0002 \pm 0.021$	$0.384 \pm 0.0002 \pm 0.020$
$30-40$	$0.382 \pm 0.0002 \pm 0.021$	$0.380 \pm 0.0002 \pm 0.020$
$40-50$	$0.374 \pm 0.0003 \pm 0.021$	$0.374 \pm 0.0003 \pm 0.020$
$50-60$	$0.365 \pm 0.0003 \pm 0.020$	$0.366 \pm 0.0003 \pm 0.019$
$60-70$	$0.356 \pm 0.0004 \pm 0.020$	$0.355 \pm 0.0004 \pm 0.019$
$70-80$	$0.349 \pm 0.0005 \pm 0.019$	$0.347 \pm 0.0005 \pm 0.018$

The functional dependence of $\langle p_T \rangle$ on the number of nucleon participants $\langle N_{\mathrm{part}} \rangle$ is presented in Fig. 3.14 for Au+Au collisions at $\sqrt{s_{NN}} = 14.5$ GeV. These results are compared

Table 3.9: $\langle p_T \rangle$ (GeV/c) values for K^+ and K^- from Au+Au collisions at $\sqrt{s_{NN}} = 14.5$ GeV. The quoted errors are statistical and systematic uncertainties respectively.

Centrality(%)	$\langle p_T \rangle$ (GeV/c)	
	K^+	K^-
$0 - 5$	$0.586 \pm 0.0001 \pm 0.032$	$0.560 \pm 0.0001 \pm 0.030$
$5 - 10$	$0.575 \pm 0.0001 \pm 0.032$	$0.559 \pm 0.0001 \pm 0.030$
$10 - 20$	$0.574 \pm 0.0001 \pm 0.032$	$0.552 \pm 0.0001 \pm 0.030$
$20 - 30$	$0.560 \pm 0.0002 \pm 0.031$	$0.540 \pm 0.0001 \pm 0.029$
$30 - 40$	$0.555 \pm 0.0002 \pm 0.031$	$0.532 \pm 0.0001 \pm 0.029$
$40 - 50$	$0.530 \pm 0.0002 \pm 0.029$	$0.513 \pm 0.0001 \pm 0.028$
$50 - 60$	$0.518 \pm 0.0003 \pm 0.029$	$0.495 \pm 0.0002 \pm 0.027$
$60 - 70$	$0.496 \pm 0.0004 \pm 0.027$	$0.475 \pm 0.0002 \pm 0.026$
$70 - 80$	$0.484 \pm 0.0005 \pm 0.027$	$0.460 \pm 0.0003 \pm 0.025$

Table 3.10: $\langle p_T \rangle$ (GeV/c) values for p, and $\bar{p}$ from Au+Au collisions at $\sqrt{s_{NN}} = 14.5$ GeV. The quoted errors are statistical and systematic uncertainties respectively.

Centrality(%)	$\langle p_T \rangle$ (GeV/c)	
	p	$\bar{p}$
$0 - 5$	$0.811 \pm 0.0005 \pm 0.053$	$0.807 \pm 0.0002 \pm 0.069$
$5 - 10$	$0.798 \pm 0.0005 \pm 0.052$	$0.800 \pm 0.0002 \pm 0.068$
$10 - 20$	$0.781 \pm 0.0006 \pm 0.051$	$0.776 \pm 0.0002 \pm 0.066$
$20 - 30$	$0.765 \pm 0.0007 \pm 0.050$	$0.751 \pm 0.0003 \pm 0.064$
$30 - 40$	$0.730 \pm 0.0009 \pm 0.048$	$0.726 \pm 0.0003 \pm 0.062$
$40 - 50$	$0.686 \pm 0.0011 \pm 0.045$	$0.675 \pm 0.0004 \pm 0.057$
$50 - 60$	$0.646 \pm 0.0012 \pm 0.042$	$0.640 \pm 0.0004 \pm 0.054$
$60 - 70$	$0.627 \pm 0.0014 \pm 0.040$	$0.606 \pm 0.0005 \pm 0.052$
$70 - 80$	$0.587 \pm 0.0016 \pm 0.038$	$0.573 \pm 0.0006 \pm 0.049$

with the corresponding results from Au+Au collisions at $\sqrt{s_{NN}} = 7.7, 11.5, 19.6, 27, 39, 62.4$ and 200 GeV measured by STAR detector in earlier runs [6, 18, 25, 28]. It can be inferred from the figure that, $\langle p_T \rangle$ of $\pi^\pm$, $K^\pm$ and $p(\bar{p})$ increases with increasing $\langle N_{\text{part}} \rangle$ or centrality. This is an indication of increasing radial flow effect as we go from peripheral to central collisions. Mean p_T and thereby radial flow also increase from pions to kaons, and from kaons to protons. This is consistent with the observations from the p_T spectra, where we have argued that this is a consequence of collective flow affecting more strongly the heavier particles. The behavior of $\langle p_T \rangle$ in Au+Au collisions at $\sqrt{s_{NN}} = 14.5$ GeV is similar within error bars to what is observed at other measured BES energies [6, 18, 25, 28]. Although there is a gradual increase of $\langle p_T \rangle$ with collision energy. The values of $\langle p_T \rangle$ for π^+, π^-, K^+, K^-, p, and $\bar{p}$ are listed in Tables 3.8,

3.9 and 3.10 for Au+Au collisions at $\sqrt{s_{NN}} = 14.5$ GeV respectively.

3.8.3 Particle Yields (dN/dy)

The total particle abundance is a reflective of the total entropy produced in the collision. In a particular collision centrality at midrapidity ($|y| < 0.1$), it is defined by dN/dy or particle yield. This is obtained by integrating the p_T spectra of the particles over p_T.

$$\frac{dN}{dy} = \int f(p_T) 2\pi p_T dp_T, \tag{3.17}$$

where $f(p_T) = \frac{1}{2\pi p_T} \frac{d^2N}{dp_T dy}$. The dN/dy of π^+, π^-, K^+, K^-, p and $\bar{p}$ are summed in midrapidity ($|y| < 1$) for the measured p_T region and are extrapolated to unmeasured p_T region ($p_T = 10$ GeV/c) using a suitable fit function. The fit functions being used are Bose-Einstein for pions, m_T- exponential for kaons and double exponential for (anti) protons.

Table 3.11: dN/dy values for π^+ and π^- from Au+Au collisions at $\sqrt{s_{NN}} = 14.5$ GeV. The quoted errors are statistical and systematic uncertainties respectively.

Centrality(%)	dN/dy	
	π^+	π^-
$0-5$	$141.0 \pm 0.17 \pm 14.6$	$145.2 \pm 0.16 \pm 15.0$
$5-10$	$112 \pm 0.15 \pm 11.5$	$116.3 \pm 0.14 \pm 12.0$
$10-20$	$87.3 \pm 0.11 \pm 9.1$	$90.0 \pm 0.11 \pm 9.2$
$20-30$	$59.1 \pm 0.08 \pm 6.1$	$61.3 \pm 0.08 \pm 6.4$
$30-40$	$38.6 \pm 0.06 \pm 4.0$	$40.0 \pm 0.06 \pm 4.1$
$40-50$	$24.6 \pm 0.05 \pm 2.6$	$25.5 \pm 0.05 \pm 2.6$
$50-60$	$14.7 \pm 0.04 \pm 1.5$	$15.4 \pm 0.04 \pm 1.5$
$60-70$	$8.5 \pm 0.03 \pm 0.9$	$8.8 \pm 0.03 \pm 0.9$
$70-80$	$4.5 \pm 0.03 \pm 0.5$	$4.8 \pm 0.03 \pm 0.6$

3.8.3.1 Centrality Dependence of dN/dy

The measured dN/dy for π^+, π^-, K^+, K^-, p and $\bar{p}$, normalized with $\langle N_{\text{part}} \rangle$, as a function of $\langle N_{\text{part}} \rangle$ is shown in Fig. 3.15 in Au+Au collisions at $\sqrt{s_{NN}} = 14.5$ GeV. These yields are compared with the corresponding published results from Au+Au collisions at $\sqrt{s_{NN}} = 7.7$, 11.5, 19.6, 27, 39, 62.4 and 200 GeV measured by the STAR detector at RHIC [6, 18, 25, 28].

The values of dN/dy for π^+, π^-, K^+, K^-, p, and $\bar{p}$ are also tabulated in Table 3.11, 3.12 and 3.13 respectively for Au+Au collisions at $\sqrt{s_{NN}} = 14.5$ GeV.
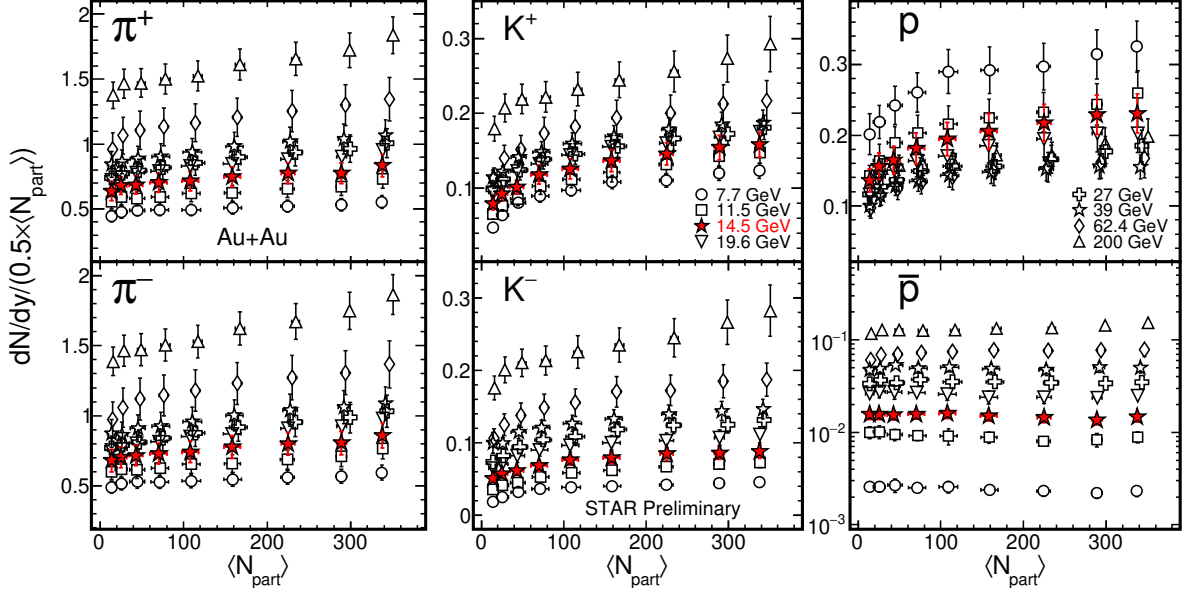
Figure 3.15: dN/dy of π^+, π^-, K^+, K^-, p and $\bar{p}$ scaled by $(0.5 \times \langle N_{\text{part}} \rangle)$ as a function of $\langle N_{\text{part}} \rangle$ for Au+Au collisions at $\sqrt{s_{NN}} = 14.5$ GeV. These yields are compared with the corresponding results from Au+Au collisions at $\sqrt{s_{NN}} = 7.7, 11.5, 19.6, 27, 39, 62.4$ and 200 GeV measured by STAR in earlier runs [6,18,25,28]. Statistical and systematic uncertainties have been added in quadrature.

Table 3.12: dN/dy values for K^+ and K^- from Au+Au collisions at $\sqrt{s_{NN}} = 14.5$ GeV. The quoted errors are statistical and systematic uncertainties respectively.

Centrality(%)	dN/dy	
	K^+	K^-
$0 - 5$	$26.7 \pm 0.04 \pm 2.8$	$14.9 \pm 0.03 \pm 1.6$
$5 - 10$	$22.3 \pm 0.04 \pm 2.4$	$12.4 \pm 0.03 \pm 1.2$
$10 - 20$	$16.4 \pm 0.03 \pm 1.7$	$9.5 \pm 0.02 \pm 1.0$
$20 - 30$	$10.8 \pm 0.02 \pm 1.1$	$6.3 \pm 0.015 \pm 0.6$
$30 - 40$	$6.8 \pm 0.016 \pm 0.7$	$4.1 \pm 0.010 \pm 0.4$
$40 - 50$	$4.1 \pm 0.013 \pm 0.4$	$2.4 \pm 0.007 \pm 0.3$
$50 - 60$	$2.2 \pm 0.011 \pm 0.2$	$1.3 \pm 0.006 \pm 0.1$
$60 - 70$	$1.2 \pm 0.007 \pm 0.1$	$0.72 \pm 0.005 \pm 0.07$
$70 - 80$	$0.55 \pm 0.005 \pm 0.06$	$0.36 \pm 0.0004 \pm 0.04$

It can be observed from the figure that, dN/dy of pions per participant nucleon has a little centrality dependence. This is an indication of the scaling behavior of dN/dy with the number of participant pairs. On the other side, for kaons and protons, particle yield gradually increases from peripheral to central collisions. This indicates that particle production from soft and

hard processes involving nucleon-nucleon binary collisions. The decrease of proton yield with increase in collision centrality is also a consequence of baryon stopping at this low collision energy. The anti-proton yield exhibits almost a flat behavior with collision centrality.

3.8.3.2   Energy Dependence of $\mathrm{dN/dy}$

Figure 3.16 shows dN/dy normalized by $0.5 \times \langle N_{\text{part}} \rangle$ as a function of collision energy from AGS [29], SPS [30], STAR [6, 18, 25, 28] and ALICE [31] energies. The yields of pions, kaons and anti-protons all increase with increasing collision energy. However ,the yield of protons behave oppositely and decreases with collision energy. This is a reflection of the increase in baryon density due to baryon stopping at lower energy. The results in Au+Au collisions at $\sqrt{s_{NN}} = 14.5$ GeV show a similar behavior as observed at AGS [29], SPS [30], STAR [6, 18,
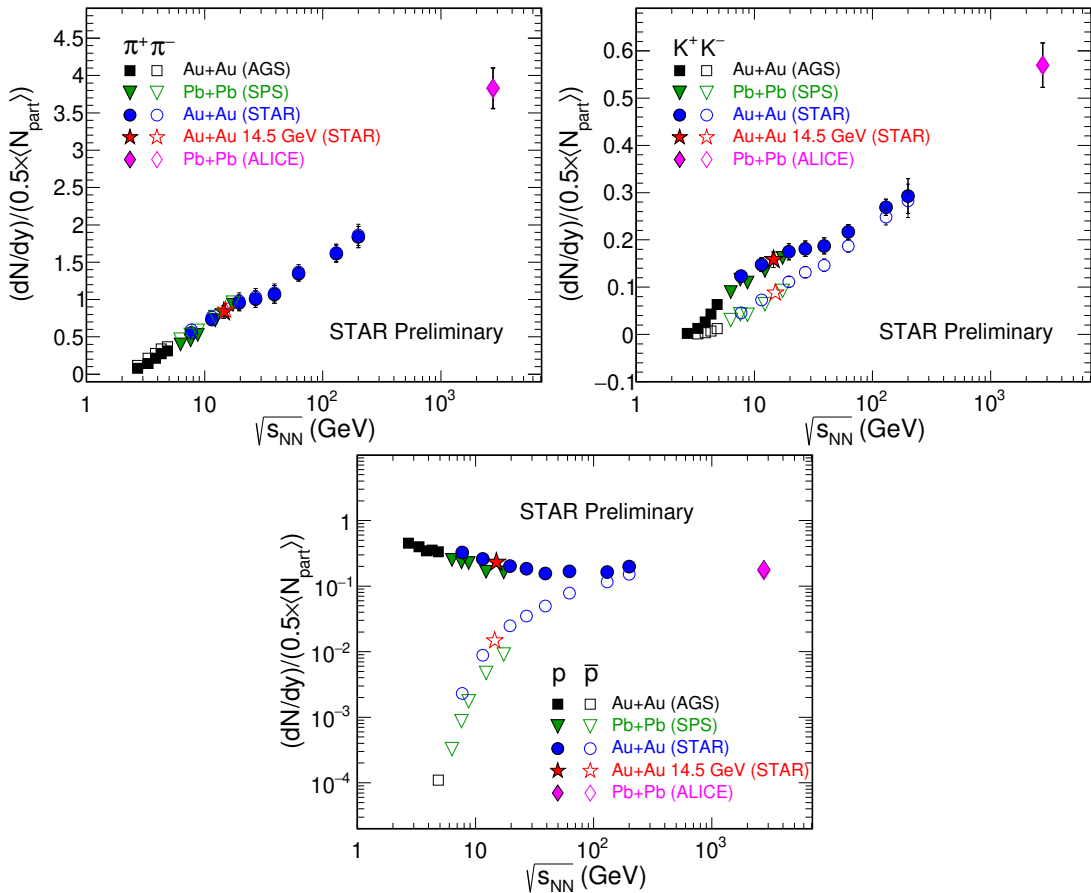
Figure 3.16: dN/dy of π^+, π^-, K^+, K^-, p and $\bar{p}$ scaled by $0.5 \times \langle N_{\text{part}} \rangle$ as a function of $\sqrt{s_{NN}}$ in Au+Au collisions at $\sqrt{s_{NN}} = 14.5$ GeV in comparison with AGS [29], SPS [30], STAR [6, 18, 25, 28] and ALICE [31] energies. The statistical and systematic uncertainties have been added in quadrature.

Table 3.13: dN/dy values for p, and $\bar{p}$ from Au+Au collisions at $\sqrt{s_{NN}} = 14.5$ GeV. The quoted errors are statistical and systematic uncertainties respectively.

Centrality(%)	dN/dy	
	p	$\bar{p}$
$0 - 5$	$39.0 \pm 0.034 \pm 4.7$	$2.5 \pm 0.017 \pm 0.3$
$5 - 10$	$33.1 \pm 0.031 \pm 4.0$	$2.0 \pm 0.014 \pm 0.2$
$10 - 20$	$24.5 \pm 0.028 \pm 2.9$	$1.6 \pm 0.011 \pm 0.2$
$20 - 30$	$16.2 \pm 0.024 \pm 2.0$	$1.2 \pm 0.008 \pm 0.1$
$30 - 40$	$10.5 \pm 0.019 \pm 1.3$	$0.9 \pm 0.005 \pm 0.1$
$40 - 50$	$6.3 \pm 0.014 \pm 0.8$	$0.6 \pm 0.004 \pm 0.07$
$50 - 60$	$3.5 \pm 0.011 \pm 0.4$	$0.33 \pm 0.003 \pm 0.04$
$60 - 70$	$1.9 \pm 0.008 \pm 0.2$	$0.16 \pm 0.003 \pm 0.02$
$70 - 80$	$0.6 \pm 0.005 \pm 0.1$	$0.11 \pm 0.002 \pm 0.01$

25, 28] and LHC [31] energies for the most central collisions.

3.8.4   Particle Ratios

Particle ratios prove to be a very useful tool in extracting information about particle production and the system evolution in high-energy heavy-ion collisions. Information like relative particle abundance, baryon content, strangeness production and Coulomb potential of the charged particles can be inferred from the study different particle ratios in terms of p_T, centrality and collision energy. In this context, we have analyzed π^-/π^+, K^-/K^+, $\bar{p}/p$, K^+/π^+, K^-/π^-, p/π^+ and $\bar{p}/\pi^-$ ratios as a function of p_T, $\langle N_{\text{part}} \rangle$ and $\sqrt{s_{NN}}$ in Au+Au collisions at $\sqrt{s_{NN}} = 14.5$ GeV. The results are compared with published results of AGS [29], SPS [30], RHIC [6, 18, 25, 28] and LHC [31] energies.

3.8.4.1 p_T Dependence of Particle Ratios

Figure 3.17 presents the π^-/π^+, K^-/K^+ and $\bar{p}/p$ ratios as a function of p_T in Au+Au collisions at $\sqrt{s_{NN}} = 14.5$ GeV for nine different centrality classes. The anti-particle to particle ratios has a very little p_T dependence. This is an indication that particles and anti-particles freeze-out at the same time and moves with similar radial flow.
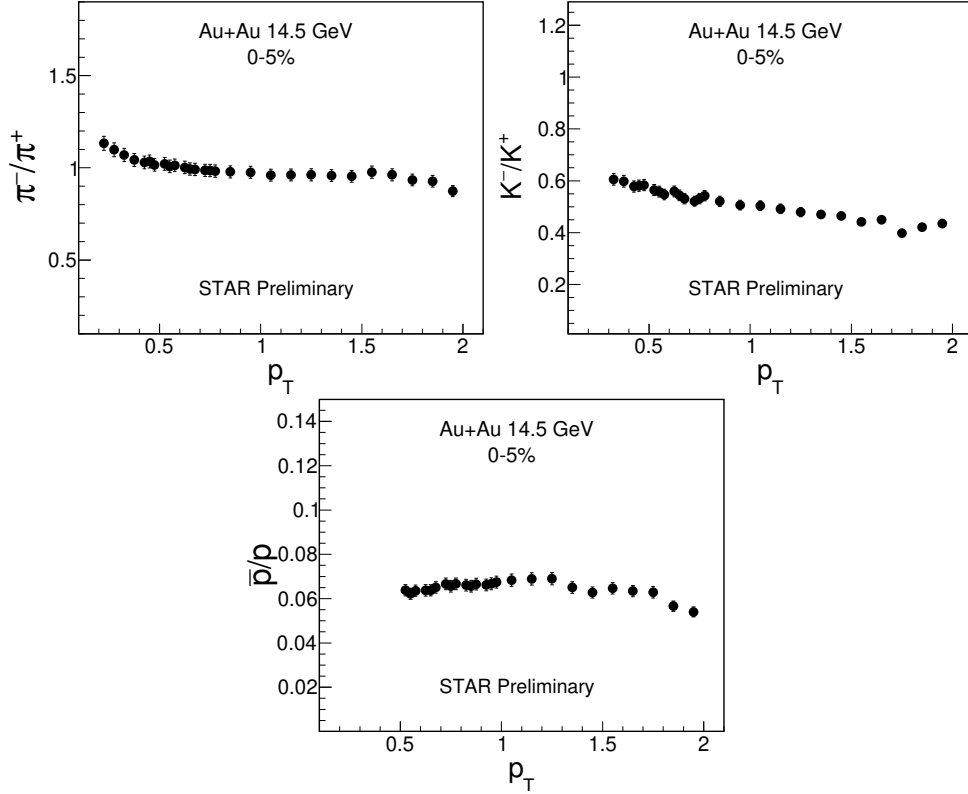
Figure 3.17: π^-/π^+, K^-/K^+ and $\bar{p}/p$ ratios as function of p_T in 0-5% centrality class in Au+Au collisions at $\sqrt{s_{NN}} = 14.5$ GeV measured by the STAR detector at RHIC.

3.8.4.2 Centrality Dependence of Particle Ratios

Figure 3.18 shows the dependence on collision centrality of three anti-particle to particle ratios (π^-/π^+, K^-/K^+ and $\bar{p}/p$) in Au+Au collisions at $\sqrt{s_{NN}} = 14.5$ GeV. These ratios are compared with the corresponding results from Au+Au collisions at $\sqrt{s_{NN}} = 7.7$, 11.5, 19.6, 27, 39, 62.4 and 200 GeV measured by STAR detector at RHIC [6,18,25,28].

The π^-/π^+ ratio has no significant centrality dependence and hovers around unity for all energies. At lower energies, including in Au+Au collisions at $\sqrt{s_{NN}} = 14.5$ GeV, this ratio is slightly greater than one, which is due to isospin and remarkable contribution from the decay of resonances like Δ baryons.

The K^-/K^+ ratio shows almost a flat behavior within errors across all centralities, suggesting that K^- and K^+ undergo similar collective flow. The results in Au+Au collisions at $\sqrt{s_{NN}} = 14.5$ GeV shows similar behavior as that of other published results at RHIC energies [6,18,25,28].

The $\bar{p}/p$ ratio shows a moderate increase from central to peripheral collisions. This charac-

terizes the net anti-baryon to baryon density at RHIC energies. This observation is consistent with the fact that there is more annihilation of protons and anti-protons in central collisions relative to peripheral collisions. This can also be interpreted as a consequence of baryon stopping in central collisions.
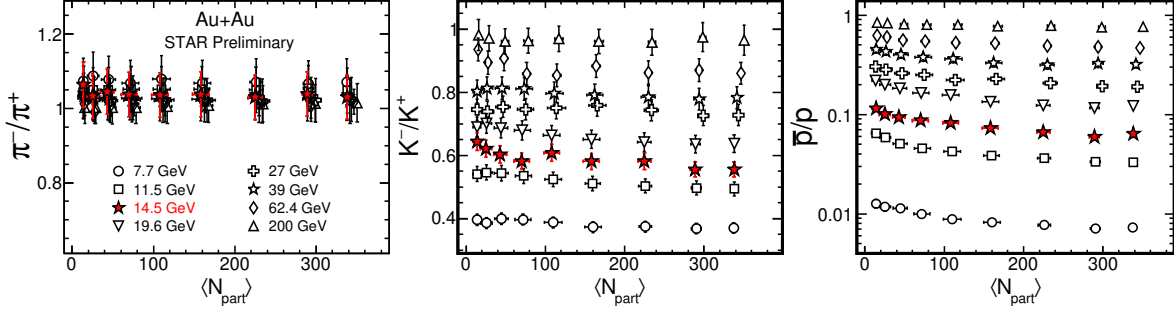
Figure 3.18: π^-/π^+, K^-/K^+ and $\bar{p}/p$ ratios as a function of $\langle N_{\text{part}} \rangle$ in Au+Au collisions at $\sqrt{s_{NN}} = 14.5$ GeV. These ratios are compared with the corresponding results from Au+Au collisions at $\sqrt{s_{NN}} = 7.7, 11.5, 19.6, 27, 39, 62.4$ and 200 GeV measured by STAR in earlier runs [6, 18, 25, 28]. Statistical and systematic uncertainties have been added in quadrature.

Various unlike particle ratios such as K^+/π^+, K^-/π^-, p/π^+ and $\bar{p}/\pi^-$ are shown in Fig. 3.19 for Au+Au collisions at $\sqrt{s_{NN}} = 14.5$ GeV. Previously published results from the STAR experiment at other beam energies [6, 18, 25, 28] are also shown for comparison.

Both K^+/π^+ and K^-/π^- ratios increase from peripheral to mid-central collisions and then remain almost flat with $\langle N_{\text{part}} \rangle$. This pattern is related to the strangeness equilibrium described in various thermodynamical models [32, 33]. These models describe this behavior with system size from peripheral to central collision following a transition from canonical to grand-canonical explanation of the system [34, 35]. This ratio is also influenced by baryon stopping at mid-rapidity. The general behavior with energy is respected by the results in Au+Au collisions at $\sqrt{s_{NN}} = 14.5$ GeV.

The p/π^+ ratio gives relative information about net-baryon production in a collision in high-energy heavy-ion experiments. The production mechanism of proton in a collision involves both the processes of pair production and baryon transport. The occurrence of these two processes at these lower energies is quite competitive. The p/π^+ ratio is observed to increase slowly from peripheral to central collisions in Au+Au collisions at $\sqrt{s_{NN}} = 14.5$ GeV. This is an effect of the baryon stopping and is consistent with other RHIC energies [6, 18, 25, 28]. On the side, the $\bar{p}/\pi^-$ ratio stays flat across all values of $\langle N_{\text{part}} \rangle$. It characterizes the net-antibaryon
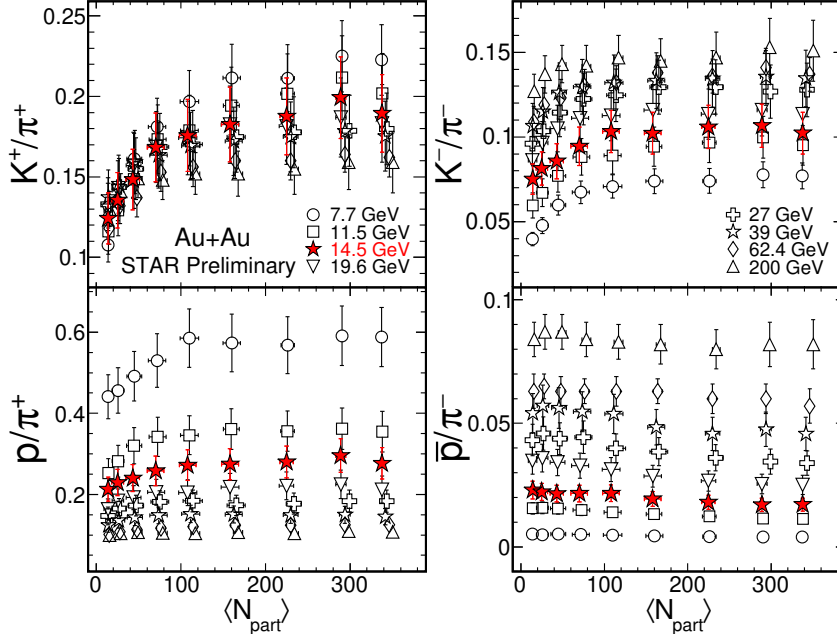
Figure 3.19: K^+/π^+, K^-/π^-, p/π^+ and $\bar{p}/\pi^-$ ratios as a function of $\langle N_{\mathrm{part}} \rangle$ in Au+Au collisions at $\sqrt{s_{NN}} = 14.5$ GeV. These ratios are compared with the corresponding results from Au+Au collisions at $\sqrt{s_{NN}} = 7.7, 11.5, 19.6, 27, 39, 62.4$ and 200 GeV measured by STAR in earlier runs [6, 18, 25, 28]. Statistical and systematic uncertainties have been added in quadrature.

production relative to the total particle multiplicity. Here, the $\bar{p}$ yield being inclusive contains weak decay contributions. This ratio is also affected by net baryon density as well as baryon stopping at these lower energies.

3.8.4.3 Energy Dependence of Particle Ratios

Different integrated particle ratios in Au+Au collisions at $\sqrt{s_{NN}} = 14.5$ GeV are shown in the Figure 3.20. This figure shows π^-/π^+, K^-/K^+, K^+/π^+, k^-/π^-, $\bar{p}/p$, p/π^+ and $\bar{p}/\pi^-$ ratios as a function of $\sqrt{s_{NN}}$ for Au+Au collisions at $\sqrt{s_{NN}} = 14.5$ GeV in comparison with AGS [29], SPS [30], STAR [6, 18, 25, 28] and ALICE [31] energies. The observations and conclusions from the Fig. 3.20 are as follows.

The higher value of π^-/π^+ ratio from unity at low beam energies could be due to more contribution of resonance decays to π^+ production. As with increasing in collision energy, the pair production dominates over this effect, π^-/π^+ closes to unity at higher beam energies.

The K^-/K^+ ratio gradually increases with collision energy and approaches unity. This can be explained in terms of the production mechanism of K^+ and K^- from the combines contribution of pair production and associated production. In pair production both K^+ and
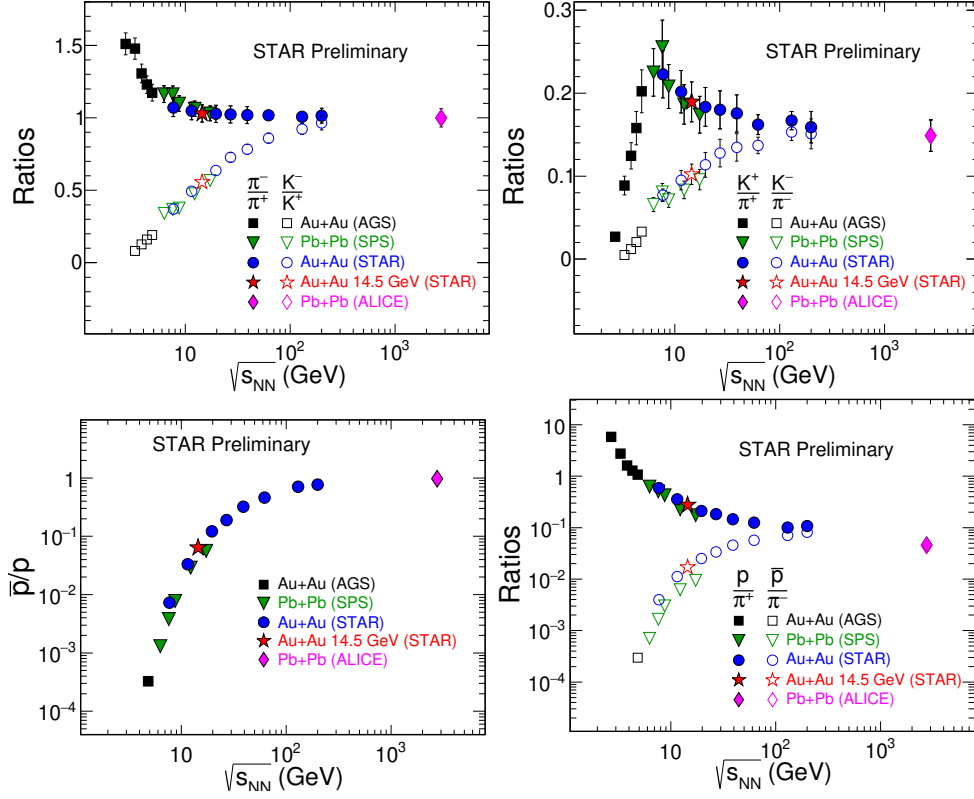
Figure 3.20: π^-/π^+, K^-/K^+, $\bar{p}/p$, K^+/π^+, K^-/π^-, p/π^+ and $\bar{p}/\pi^-$ ratios as a function of $\sqrt{s_{NN}}$ for 0-5% centrality in Au+Au collisions at $\sqrt{s_{NN}} = 14.5$ GeV in comparison with AGS [29], SPS [30], STAR [6,18,25,28] and ALICE [31] energies. The statistical and systematic uncertainties have been added in quadrature.

K^- are produced in equal numbers. Whereas, in associated production only K^+ is produced via; $N + N \rightarrow N + X + K^+$ or $\pi + N \rightarrow X + K^+$, where N is a nucleon and X is a hypernon (Λ or Ξ). So, the K^+ is produced in an heavy-ion collision by both pair production and associated production, whereas K^- are mainly produced via pair production. At lower energy, associated production dominates over pair production producing only K^+. Whereas at higher beam energies pair production is the dominant mechanism which produces equal number of K^+ and K^-. With an increase in collision energy, the net baryon density decreases leading to the decrease of production of K^+ via associated production. Also, the gluon-gluon fusion to strange quark-antiquark pair increases the pair production rate with an increase in collision energy [36, 37]. All these effects combined together describe the behavior of K^-/K^+ ratio as a function of collision energy.

The K/π ratio being describing the strangeness production with respect to non-strange particles is very much interesting to analyze. K^+/π^+ ratio increases with $\sqrt{s_{NN}}$ at lower beam

energy attains a maximum and then decreases with $\sqrt{s_{NN}}$ and saturates. The peak or the horn in the K^+/π^+ ratio is suggested to be a signature of phase transition from hadron gas to Quark-Gluon-Plasma [38]. There are models predicting this horn in the K^+/π^+ ratio near 7.62 GeV. But, the experimentally observed peak is much sharper than the theoretical predictions [39–41]. The K^-/π^- ratio gradually increases with beam energy and finally saturates. The behavior of K^+/π^+ and K^-/π^- ratio can also be understood from its quark content. The quark content of K^+ and K^- are $u\bar{s}$ and $\bar{u}s$ respectively. The initial colliding system is enriched of u and d quarks, where there are no $\bar{u}$ quarks. So, all the $\bar{u}$, $\bar{d}$ and $\bar{s}$ quarks are created during collision. But, the up quark comes both from the colliding nuclei and also are created in the fireball. All these particle production mechanisms along with net-baryon density is reflected in the behavior of K^+/π^+ and K^-/π^- ratio as a function of energy.

The integrated $\bar{p}/p$ ratio increases as a function of $\sqrt{s_{NN}}$ and approaches to unity at higher collision energies. This ratio conveys the change in baryon density as a function of beam energy. As the net baryon density approaches zero with increase in collision energy at the top RHIC [18, 25] and LHC energies [31], the $\bar{p}/p$ approaches unity.

The p/π^+ ratio describes the baryon to meson ratio, which decreases with collision energy. The net anti-baryon to meson content of the fireball formed in high-energy heavy-ion collisions is described by the $\bar{p}/\pi^-$ ratio, which increases with $\sqrt{s_{NN}}$ and saturates at unity at higher $\sqrt{s_{NN}}$. The behavior of these ratios can be attributed to the trend of net baryon content ($p - \bar{p}$ values) with collision energy.

3.8.5 Freeze-out Dynamics

The invariant yields and p_T spectra of particles provide an excellent tool to look at the freeze-out properties of the system. Two distinct freeze-out scenarios are observed in high-energy heavy-ion collision experiments: chemical freeze-out and kinetic freeze-out in particular order of their occurrence during the evolution of the system. First, inelastic collisions among the particles cease, defining the chemical freeze-out stage. After that point, there is no further production of new particles, and the yields of various particle types get fixed. Various thermodynamic models are widely applied to extract the information of this stage mainly in terms of chemical freeze-

out temperature and baryon chemical potential [6,47–49]. After this stage, the particles collide only elastically. After further expansion of the system, as the inter-particle separation becomes large ceasing even the elastic collision among the particles, leads to the kinetic freeze-out stage. The momentum of the particles gets fixed after this point, and the particles freely propagate to the detector. The particle p_T spectra thus contain information about the kinetic freeze-out stage. Hydrodynamic-based models such as the Blast-Wave model [6,18,26,47] are used to extract the kinetic freeze-out properties. This stage is characterized by the kinetic freeze-out temperature T_k and radial flow velocity β, which carry information about the transverse expansion of the system. Here, we follow the previously adopted procedures to study the chemical and kinetic freeze-out properties in Au+Au collisions at $\sqrt{s_{NN}} = 14.5$ GeV [6].

3.8.5.1   Chemical Freeze-out

Chemical freeze-out parameters are extracted from the measured particle yields or particle ratios by using the publicly available THERMUS [48] package. In this statistical framework, we can obtain the freeze-out parameters by two different statistical approaches. One is the Grand Canonical Ensemble (GCE), in which the energy and quantum numbers of the particles are assumed to be conserved on average. The other is the Strangeness Canonical Ensemble (SCE) in which strangeness (S) is assumed to be conserved exactly, and the baryon number and charge content of the system is considered to be conserved on an average. As the number of particles in the system in high-energy heavy-ion collisions is large, GCE is widely considered to be acceptable [6]. Also, at low energies, the number of strange particles produced is relatively small, and hence the SCE treatment of the system is appropriate in this case [50].

In the Grand Canonical Ensemble approach, the logarithm of the total partition function is given by

$$\ln Z^{GC}(T, V, \mu_i) = \sum_{\text{species i}} \frac{g_i V}{(2\pi)^3} \int d^3 p \ln(1 + e^{\beta(E_i - m_i)})^{\pm 1}. \tag{3.18}$$

Where V is the fireball volume, g_i is the degeneracy, $E_i = \sqrt{p^2 + m^2}$ with m_i as the particle mass and $\beta = \frac{1}{T}$, where T is the chemical freeze-out temperature. The plus sign corresponds

to fermions and minus sign to bosons. The hadron chemical potential μ_i can be written as

$$\mu_i = B_i \mu_B + S_i \mu_S + Q \mu_Q. \tag{3.19}$$

The corresponding particle multiplicity can be written as

$$N_i^{GC} = \frac{g_i V}{2\pi^2} \sum_{k=1}^{\infty} (\pm 1)^{k+1} \frac{m_i T^2}{k} K_2\left(\frac{km_i}{T}\right) \times \exp(\beta k \mu_i) \gamma_S^{k|S_i|}. \tag{3.20}$$

K_2 is the second order Bessel function and the extra parameter γ_S introduced here is the strangeness saturation factor which corresponds to any non-equilibrium production of strange particles. Again in the Strangeness or mixed Canonical Ensemble, the particle multiplicity is given by

$$\ln Z^S(T, V, \mu_i) = \int_{-\pi}^{+\pi} d\phi_S e^{-iS\phi_S} \exp\left[\sum_{\text{species i}} \frac{g_i V}{(2\pi)^3} \int d^3 p\, e^{\beta(E_i - m_i)} e^{iS_i \phi_S} \right]. \tag{3.21}$$

Here, ϕ_S has been introduced to conserve S exactly. In this case, the hadron chemical potential μ_i of hadron species i is

$$\mu_i = B_i \mu_B + Q \mu_Q. \tag{3.22}$$

and corresponding particle multiplicity is given by

$$N_i^S = \left(\frac{Z^{S-S_i}}{Z^S} \right) N_i^{GC}|_{\mu_S=0}. \tag{3.23}$$

We have studied both GCE and SCE approach by fitting particle yields as well as particle ratios. The fit parameters extracted are chemical freeze-out temperature T_{ch}, baryon chemical potential μ_B, strangeness chemical potential μ_S, strangeness saturation factor γ_S, radius parameters R or R_c. For fitting strangeness canonical ensemble we consider in general, $R_c = R$. The results presented in the following section are obtained by putting $\mu_Q = 0$. The measured particles have decay contributions from higher mass resonance particles, so it is necessary to put a particular decay channel closed or open in the THERMUS code in accordance with the experimentally measured particles. In our, case the particle yields we have used are π^+, π^-,

Table 3.14: The conditions used in THERMUS for the decay contribution to the particle yields used in fit. "1" represents that the higher mass particle is taken as stable, whereas "0" represents it is taken as unstable and contributes to the measured yields.

	K_S^0	Λ	Σ^+	Σ^-	Ξ^0	Ξ^-	Ω
$\pi^\pm$	1	1	1	1	1	1	1
$K^\pm$	1	1	1	1	1	1	1
$p(\bar{p})$	1	0	0	1	0	0	1
$\Lambda(\bar{\Lambda})$	1	1	1	1	1	1	1
$\Xi(\bar{\Xi})$	1	1	1	1	1	1	1

K^+, K^-, p, $\bar{p}$, Λ^-, $\bar{\Lambda}^+$, Ξ^-, $\bar{\Xi}^+$. Out of these particles, p and $\bar{p}$ are not feed-down corrected, whereas π, Λ and Ξ particles are feed-down corrected. The particle ratio combinations used are π^-/π^+, K^-/K^+, $\bar{p}/p$, $\bar{\Lambda}/\Lambda$, $\bar{\Xi}^+/\Xi^-$, K^-/π^-, $\bar{p}/\pi^-$, Λ/π^- and $\bar{\Xi}^+/\pi^-$. Table 3.14 lists the conditions used in THERMUS for the decay contribution to the particle yields used in the fit. In which, "1" represents that the higher mass particle is taken as stable, whereas "0" represents it is taken as unstable and contributes to the measured yields.

Figure 3.21 presents a comparison between experimental data and thermal model fits to particle yields (left panel) and particle ratios (right panel) in GCE and SCE for the most central 0-5% Au+Au collisions at $\sqrt{s_{NN}} = 14.5$ GeV. The lower part of each plot presents deviations defined as (model−data)/(error on data). It can be observed that for the thermal model fits, particle yields and ratios remain well within 2 on this scale, indicating fits of acceptable quality.

The extracted chemical freeze-out parameters T_{ch}, μ_B, μ_S, γ_S and R as a function of $\langle N_{\text{part}} \rangle$
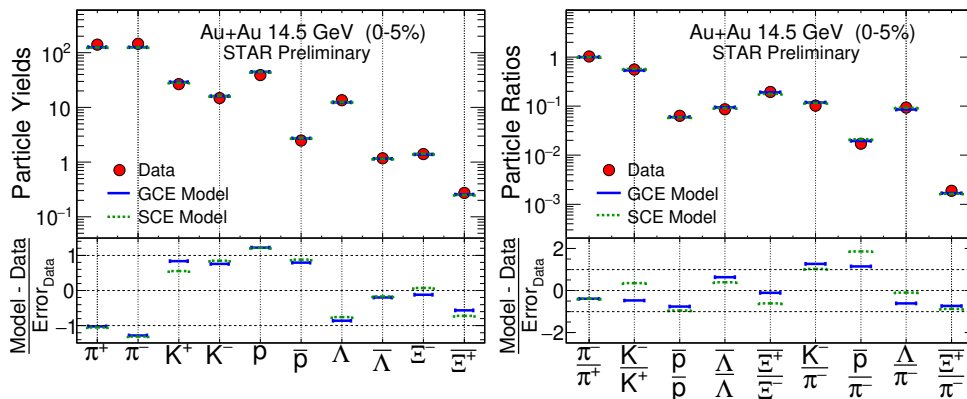
Figure 3.21: The upper panel of each figure shows the thermal model fits with GCE and SCE to particle yields (left panel) and particle ratios (right panel) for 0-5% centrality in Au+Au collisions at $\sqrt{s_{NN}} = 14.5$ GeV in mid-rapidity ($|y| < 0.1$). The lower panels show the deviation of particle yields and ratios from experimental data.
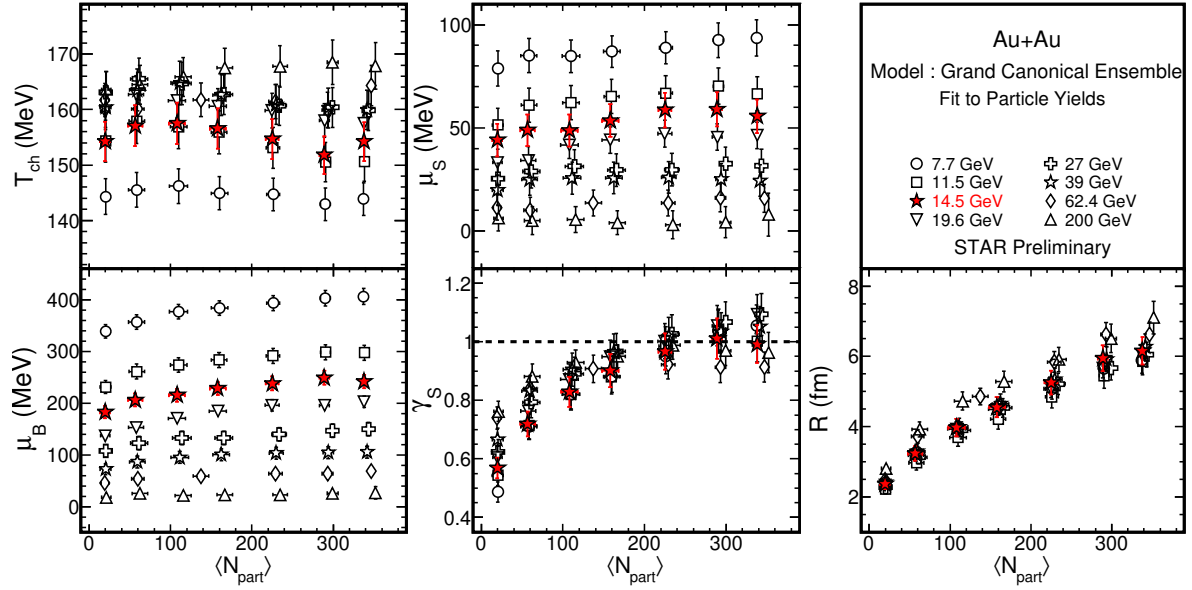
Figure 3.22: T_{ch}, μ_B, μ_S, γ_S, and R as a function of $\langle N_{\text{part}} \rangle$ from thermal model fit to particle yields in GCE for Au+Au collisions at $\sqrt{s_{NN}} = 14.5$ GeV. The results are compared with the corresponding results from Au+Au collisions at $\sqrt{s_{NN}} = 7.7$, 11.5, 19.6, 27, 39, 62.4 and 200 GeV measured by STAR in earlier runs [6].

from the thermal model fits to particle yields in GCE for Au+Au collisions at $\sqrt{s_{NN}} = 14.5$ GeV are presented in Fig. 3.22. The results are compared with corresponding results in Au+Au collisions at $\sqrt{s_{NN}} = 7.7$, 11.5, 19.6, 27, 39, 62.4 and 200 GeV measured by STAR detector at RHIC [6]. It can be observed that T_{ch} have similar values within errors for all centrality classes in Au+Au collisions at $\sqrt{s_{NN}} = 14.5$ GeV. T_{ch} shows a slight increase with collision energy from 7.7-19.6 GeV, after which it remains almost constant. Baryon chemical potential μ_B increases from peripheral collisions to central collisions. An energy dependence is also observed for μ_B, as it decreases with increasing collision energy. The strangeness chemical potential increases slowly from peripheral to central collisions. μ_s has a similar dependence on collision energy as μ_B. The strangeness saturation factor γ_S increases with increasing centrality for Au+Au collisions at $\sqrt{s_{NN}} = 14.5$ GeV. Values of γ_s do not significantly change with collision energy. The fireball radius R increases from peripheral to central collisions and has a very minor increase with collision energy. All the patterns for Au+Au collisions at $\sqrt{s_{NN}} = 14.5$ GeV are consistent with previous observations [6].

The extracted chemical freeze-out parameters T_{ch}, μ_B, μ_S and γ_S as a function of $\langle N_{\text{part}} \rangle$ from the thermal model fits to particle ratios in GCE for Au+Au collisions at $\sqrt{s_{NN}} = 14.5$
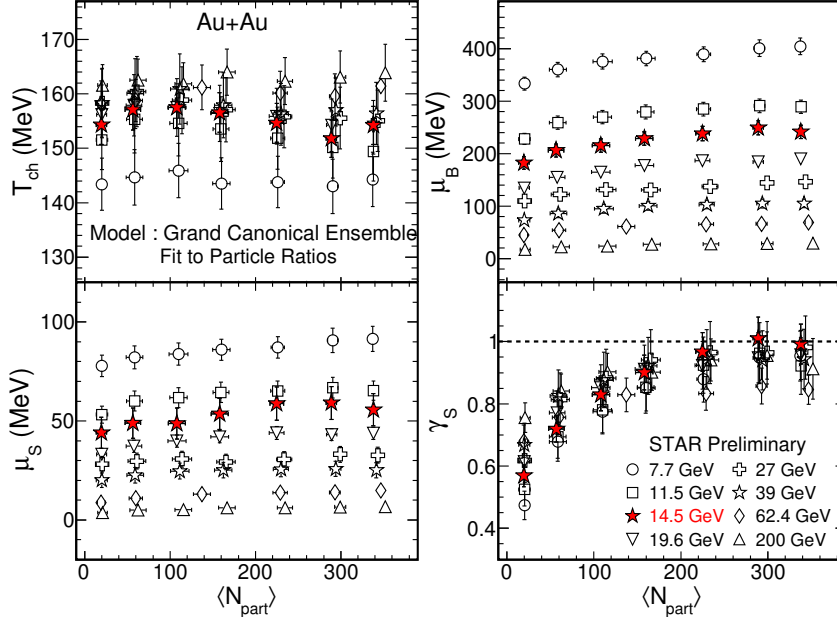
Figure 3.23: T_{ch}, μ_B, μ_S and γ_S as a function of $\langle N_{\mathrm{part}} \rangle$ from thermal model fit to particle ratios in GCE for Au+Au collisions at $\sqrt{s_{NN}} = 14.5$ GeV. The results are compared with the corresponding results from Au+Au collisions at $\sqrt{s_{NN}} = 7.7$, 11.5, 19.6, 27, 39, 62.4 and 200 GeV measured by STAR in earlier runs [6].

GeV are presented in Fig. 3.23 in comparison with corresponding results in Au+Au collisions at $\sqrt{s_{NN}} = 7.7$, 11.5, 19.6, 27, 39, 62.4 and 200 GeV measured by STAR in earlier runs [6]. The observations from these fits are similar to that we found above in the fits to particle yields in the framework of GCE.

The centrality dependence of chemical freeze-out parameters T_{ch}, μ_B, γ_S and $R(=R_c)$ from thermal model fit to particle yields in SCE for Au+Au collisions at $\sqrt{s_{NN}} = 14.5$ GeV is shown in Fig. 3.24. The corresponding results for Au+Au collisions at $\sqrt{s_{NN}} = 7.7$, 11.5, 19.6, 27, 39, 62.4 and 200 GeV measured by STAR in earlier runs [6] are shown in comparison. The conclusions for the chemical freeze-out parameters in thermal model fits to particle yields in SCE are qualitatively similar to the corresponding observations in GCE. However, in this case, a slightly higher value of T_{ch} in peripheral collisions can be noticed for Au+Au collisions at $\sqrt{s_{NN}} = 14.5$ GeV, consistent with previous observations [6].

The corresponding results from the thermal model fit to particle ratios in SCE showing T_{ch}, μ_B, μ_S and γ_S with collision centrality for Au+Au collisions at $\sqrt{s_{NN}} = 14.5$ GeV are shown in Fig. 3.25 in comparison with published results in other Au+Au energies by the STAR experiment [6]. The observations from these fits identical to that we found above in the fits to
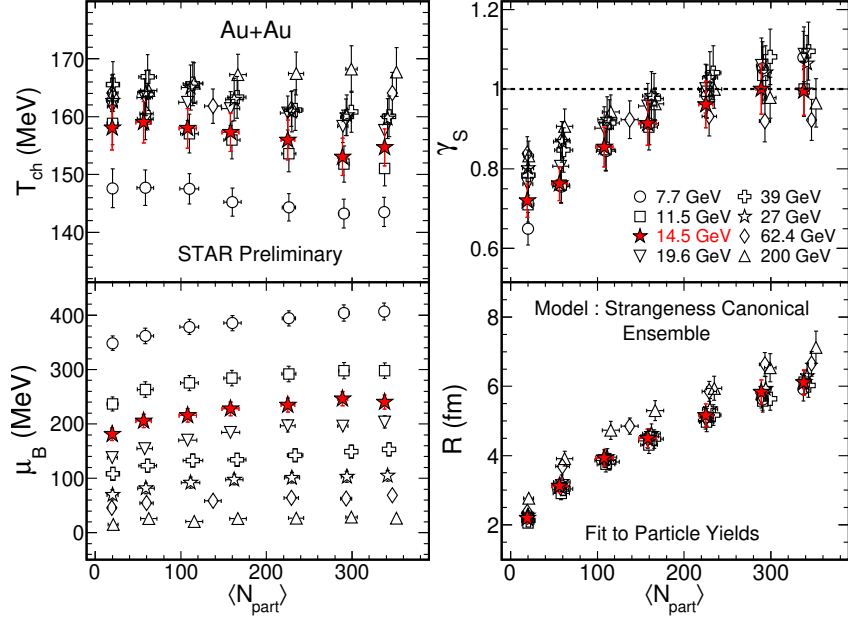
Figure 3.24: T_{ch}, μ_B, γ_S, and R as a function of $\langle N_{\text{part}} \rangle$ from thermal model fits to particle yields in SCE for Au+Au collisions at $\sqrt{s_{NN}} = 14.5$ GeV. The results are compared with the corresponding results from Au+Au collisions at $\sqrt{s_{NN}} = 7.7, 11.5, 19.6, 27, 39, 62.4$ and 200 GeV measured by STAR in earlier runs [6].
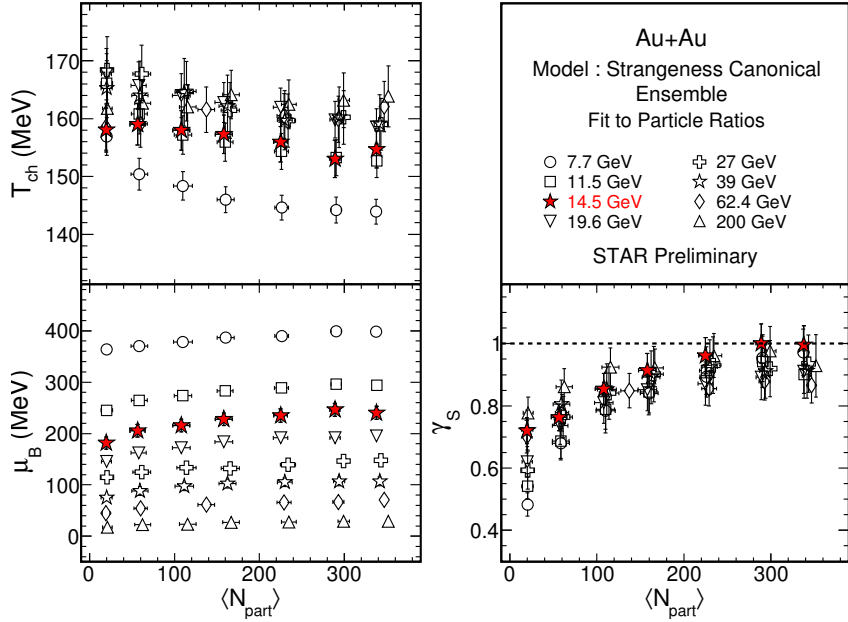
Figure 3.25: T_{ch}, μ_B and γ_S as a function of $\langle N_{\text{part}} \rangle$ from thermal model fits to particle ratios in SCE for Au+Au collisions at $\sqrt{s_{NN}} = 14.5$ GeV. The results are compared with the corresponding results from Au+Au collisions at $\sqrt{s_{NN}} = 7.7, 11.5, 19.6, 27, 39, 62.4$ and 200 GeV measured by STAR in earlier runs [6].

particle yields in the framework of SCE.

The ratios of chemical freeze-out parameters obtained from the thermal model fit to particle yields and particle ratios in both GCE and SCE as a function of N_{part} are presented in Fig. 3.26
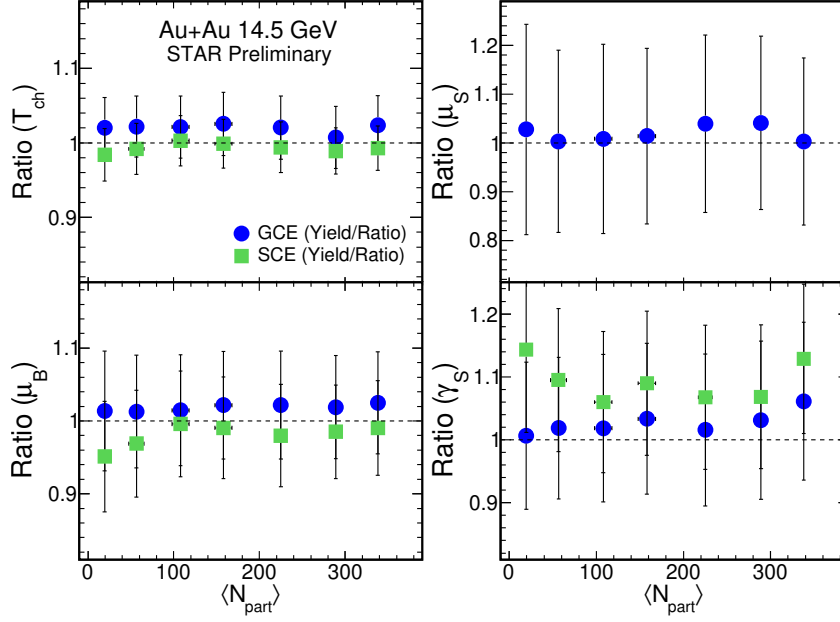
Figure 3.26: Ratio of chemical freeze-out parameters (T_{ch}, μ_B, μ_S and γ_S) obtained from thermal model fits using particle yields and particle ratios in GCE and SCE as a function of $\langle N_{part} \rangle$ in Au+Au collisions at $\sqrt{s_{NN}} = 14.5$ GeV.

Table 3.15: Chemical freeze-out parameters based on a Grand-Canonical Ensemble assumption, using both particle yields (GCEY) and ratios (GCER) in mid-rapidity ($|y| < 0.1$) for Au+Au collisions at $\sqrt{s_{NN}} = 14.5$ GeV. The quoted errors are errors on the parameters obtained from statistical model fit and are quadrature sum statistical and systematic uncertainties.

Centrality(%)	T_{ch} (MeV)		μ_B (MeV)		μ_S (MeV)		γ_S		R (fm)	χ^2/ndf	
	GCEY	GCER	GCEY	GCER	GCEY	GCER	GCEY	GCER	GCEY	GCEY	GCER
$0-5$	154.2±3.5	150.6±4.7	241.5±13.0	235.6±10.0	55.7±8.1	55.5±5.0	0.99±0.06	0.93±0.09	6.16±0.39	1.4	1.3
$5-10$	151.8±3.4	150.7±5.2	249.2±12.2	244.6±11.0	59.1±8.3	56.8±5.5	1.01±0.07	0.98±0.10	5.94±0.37	1.4	2.4
$10-20$	154.6±3.6	151.5±5.3	238.2±13.5	233.1±10.6	58.7±8.4	56.5±5.7	0.97±0.06	0.95±0.10	5.26±0.34	1.5	1.8
$20-30$	156.6±3.6	152.6±5.2	228.5±12.7	223.7±10.3	53.5±7.9	52.8±5.2	0.90±0.06	0.87±0.09	4.55±0.29	1.2	0.9
$30-40$	157.5±3.7	154.1±5.1	215.5±12.7	212.4±10.0	48.7±7.9	48.3±5.1	0.83±0.05	0.81±0.08	3.97±0.25	0.9	0.6
$40-60$	157.1±3.7	153.7±5.0	206.0±12.4	203.4±9.5	48.9±7.7	48.7±4.9	0.72±0.04	0.71±0.07	3.23±0.20	1.7	0.8
$60-80$	154.3±3.5	151.2±4.9	182.3±2.0	179.8±8.5	44.1±7.9	42.9±4.7	0.57±0.04	0.56±0.06	2.37±0.15	0.9	0.6

for Au+Au collisions at $\sqrt{s_{NN}} = 14.5$ GeV. For all centralities, the ratio hovers around unity, and the final result is almost independent of whether we use particle yields or particle ratios for fitting. The conclusion is the same for both the GCE and SCE approaches.

The extracted chemical freeze-out parameters in the framework of GCE and SCE using particle yields and particle ratios for Au+Au collisions at $\sqrt{s_{NN}} = 14.5$ GeV are listed in Tables 3.15 and 3.16.

Table 3.16: Chemical freeze-out parameters based on a Strangeness-Canonical Ensemble assumption, using both particle yields (GCEY) and ratios (GCER)in mid-rapidity ($|y| < 0.1$) for Au+Au collisions at $\sqrt{s_{NN}} = 14.5$ GeV. The quoted errors are errors on the parameters obtained from statistical model fit and are quadrature sum statistical and systematic uncertainties.

Centrality(%)	T_{ch} (MeV)		μ_B (MeV)		γ_S		R (fm)	χ^2/ndf	
	GCEY	GCER	GCEY	GCER	GCEY	GCER	GCEY	GCEY	GCER
$0-5$	154.6±3.2	155.8±3.3	240.2±12.6	242.5±9.5	1.00±0.06	0.88±0.07	6.11±0.36	1.2	1.4
$5-10$	153.0±3.2	154.7±3.6	246.1±12.8	249.8±9.7	1.00±0.06	0.94±0.08	5.84±0.35	1.3	2.1
$10-20$	156.0±3.5	156.9±4.1	234.8±13.2	239.6±10.7	0.96±0.06	0.90±0.08	5.16±0.32	1.4	1.8
$20-30$	157.2±3.3	157.4±4.0	227.6±12.5	229.8±10.2	0.91±0.05	0.84±0.07	4.50±0.27	1.0	1.0
$30-40$	158.0±3.4	157.4±4.1	215.5±12.3	216.4±9.7	0.85±0.05	0.81±0.07	3.93±0.23	0.7	0.6
$40-60$	159.0±3.6	160.3±4.2	205.2±12.2	211.7±9.9	0.76±0.04	0.70±0.06	3.11±0.19	1.4	1.2
$60-80$	158.0±3.8	160.6±4.3	181.3±11.6	190.6±9.1	0.72±0.04	0.63±0.06	2.19±0.15	0.9	2.0

3.8.5.2 Kinetic Freeze-out

The kinetic freeze-out parameters are calculated through a Blast-Wave model [26] fit to the measured particle p_T spectra in Au+Au collisions at $\sqrt{s_{NN}} = 14.5$ GeV. This model is a hydrodynamics based approach in which the particles are assumed to be locally thermalized at the kinetic freeze-out temperature T_k and move with a common radial flow velocity β. For such a radially boosted uniform hard sphere, the transverse momentum distribution of the produced particles can be written as

$$\frac{dN}{p_T dp_T} \propto \int_0^R r dr\, m_T I_0 \left(\frac{p_T \sinh \rho(r)}{T_k} \right) \times K_1 \left(\frac{m_T \cosh \rho(r)}{T_k} \right), \tag{3.24}$$

where $m_T = \sqrt{p_T^2 + m^2}$ is the transverse mass of the particle, $\rho(r) = \tanh^{-1} \beta$, and I_0 and K_1 are modified Bessel functions. A flow velocity profile of the following form is used.

$$\beta = \beta_s (r/R)^n, \tag{3.25}$$

where β_S is the surface velocity, r/R is the radial position in the thermal source, and the exponent n in the flow velocity profile is a parameter. The average radial flow velocity $\langle \beta \rangle$ is given by $\langle \beta \rangle = \frac{2}{2+n} \beta_S$.

The kinetic freeze-out parameters are extracted through the simultaneous blast-wave model fits to the $\pi^{\pm}$, $K^{\pm}$ and $p(\bar{p})$ spectra are performed [6, 18, 26] as depicted in Fig. 3.27 in three
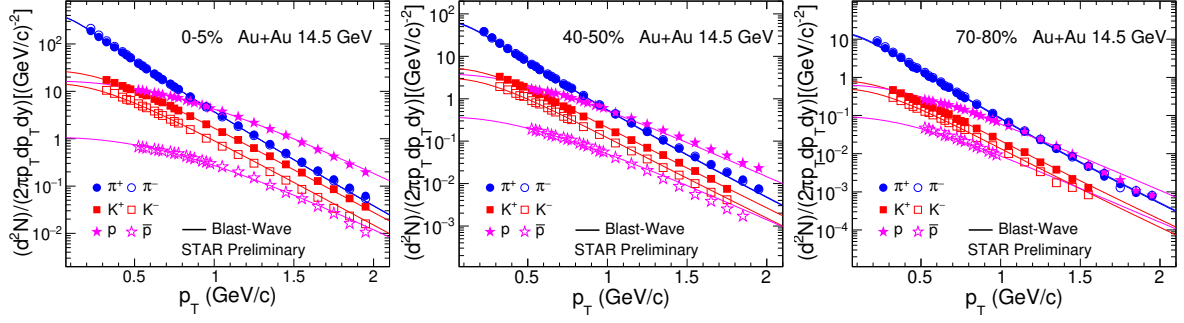
Figure 3.27: Simultaneous blast-wave model fits to the p_T-spectra of $\pi^{\pm}$, $K^{\pm}$, $p(\bar{p})$ for 0-5%, 40-50% and 70-80% centrality class within mid-rapidity ($|y| < 0.1$) for Au+Au collisions at $\sqrt{s_{NN}} = 14.5$ GeV.

different centralities for Au+Au collisions at $\sqrt{s_{NN}} = 14.5$ GeV. The low p_T region of the pion spectra is affected by resonance decays, and therefore the pion spectra are fitted above $p_T > 0.5$ GeV/c. However, the blast-wave model is not very suitable for fitting the high p_T region of the p_T spectra [51]. Hence, the blast-wave model fits are very sensitive to the p_T range used [52]. The previously optimized p_T ranges [6, 18, 52] are used for Au+Au collisions at $\sqrt{s_{NN}} = 14.5$ GeV to extract the kinetic freeze-out parameters.
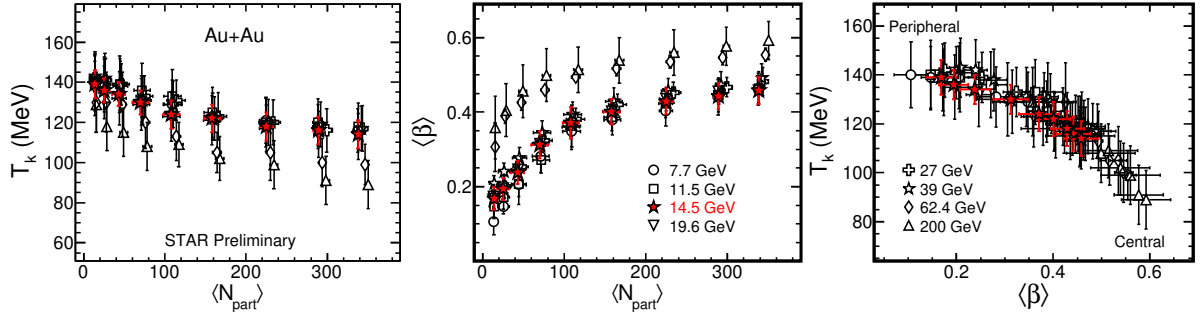
Figure 3.28: Left panel: T_k as a function of $\langle N_{\mathrm{part}} \rangle$. Middle panel: β as a function of $\langle N_{\mathrm{part}} \rangle$. Right panel: variation of T_k with β. All three panels, present results in mid-rapidity ($|y| < 0.1$) for Au+Au collisions at $\sqrt{s_{NN}} = 14.5$ GeV are shown in comparison with the same quantities for Au+Au collisions at $\sqrt{s_{NN}} = 7.7$, 11.5, 19.6, 27, 39, 62.4 and 200 GeV measured by STAR in earlier runs [6]. Statistical and systematic errors are added in quadrature.

Figure 3.28 presents the kinetic freeze-out parameters T_k (left) and $\langle \beta \rangle$ (middle) as a function of N_{part} along with the correlation between T_k and β (right) for Au+Au collisions at $\sqrt{s_{NN}} = 14.5$ GeV. These results are compared with the corresponding published results for Au+Au collisions at $\sqrt{s_{NN}} = 7.7$, 11.5, 19.6, 27, 39, 62.4 and 200 GeV measured by STAR detector at RHIC [6, 18]. T_k shows a dependence on N_{part} and it decreases from peripheral to central collisions. This observation supports the prediction of a short-lived fireball in the

case of peripheral collisions [53]. The average flow velocity $\langle \beta \rangle$, on the other hand, increases from peripheral to central collisions. This indicates a higher rate of expansion of the system in central collisions. Lastly, the correlation plot between T_k and β confirms an anti-correlation between these two quantities. i.e., as T_k decreases, β increases, and vice-versa. The behavior of the kinetic freeze-out parameters in Au+Au collisions at $\sqrt{s_{NN}} = 14.5$ GeV is consistent with previous observations [6, 18]. The extracted kinetic freeze-out parameters T_k, $\langle \beta \rangle$, n, and the values of the corresponding χ^2/ndf obtained from blast-wave model fits in Au+Au collisions at $\sqrt{s_{NN}} = 14.5$ GeV are reported in Table 3.17.

Table 3.17: Kinetic freeze-out parameters T_k, $\langle \beta \rangle$, n and χ^2/ndf values from blast-wave fits in mid-rapidity ($|y| < 0.1$) for Au+Au collisions at $\sqrt{s_{NN}} = 14.5$ GeV. The quoted errors are errors on the parameters obtained from Blast-wave fit and are quadrature sum of statistical and systematic uncertainties.

Centrality(%)	T_k (MeV)	$\langle \beta \rangle c$	n	χ^2/ndf
$0 - 5$	114 ± 7	0.485 ± 0.036	0.972 ± 0.285	0.119
$5 - 10$	116 ± 7	0.442 ± 0.035	0.982 ± 0.297	0.097
$10 - 20$	118 ± 7	0.429 ± 0.034	0.987 ± 0.338	0.119
$20 - 30$	122 ± 7	0.401 ± 0.034	0.997 ± 0.399	0.056
$30 - 40$	124 ± 8	0.371 ± 0.042	1.343 ± 0.427	0.123
$40 - 50$	130 ± 6	0.312 ± 0.036	1.732 ± 0.618	0.232
$50 - 60$	134 ± 6	0.238 ± 0.031	2.264 ± 0.787	0.398
$60 - 70$	136 ± 6	0.194 ± 0.030	2.755 ± 0.873	0.484
$70 - 80$	139 ± 7	0.168 ± 0.030	2.830 ± 1.208	0.354

3.8.6 Model Comparisons

Measurements from STAR suggest that at energies such as 7.7 GeV, particle production may be dominated by hadronic processes, whereas at energies around 20 GeV and above, partonic degrees of freedom might be more important [42–46]. The $\sqrt{s_{NN}} = 14.5$ GeV Au+Au collisions analyzed here thus lie in a transition region of great potential interest. Various bulk properties of the system like mean-p_T, dN/dy and particle ratios measured in Au+Au collisions at $\sqrt{s_{NN}} = 14.5$ GeV are compared with calculations from AMPT (version 2.25t7d) [7] and UrQMD (version 3.3p1) [8]. The initial parameter settings for the models follow the recommendations in the cited papers [7, 8]. The UrQMD model treats only hadronic interactions whereas AMPT has two versions — a string melting version (denoted AMPT-SM) which allows for both partonic and hadronic interactions among the particles, while the default version

of AMPT treats only hadronic interactions. We have generated AMPT-SM events with two possible partonic cross sections (1.5 mb and 10 mb), and those are denoted AMPT 1.5mb and AMPT 10mb. The larger the partonic cross section, the later the hadronic cascade begins. The number of minimum biased events analyzed for each of these models are nearly 2 M.

3.8.6.1 Transverse Momentum Spectra

Figure 3.29 shows the transverse momentum spectra of π^+, K^+ and p in Au+Au collisions at $\sqrt{s_{NN}} = 14.5$ GeV obtained from STAR data and compared with the two sets of AMPT data
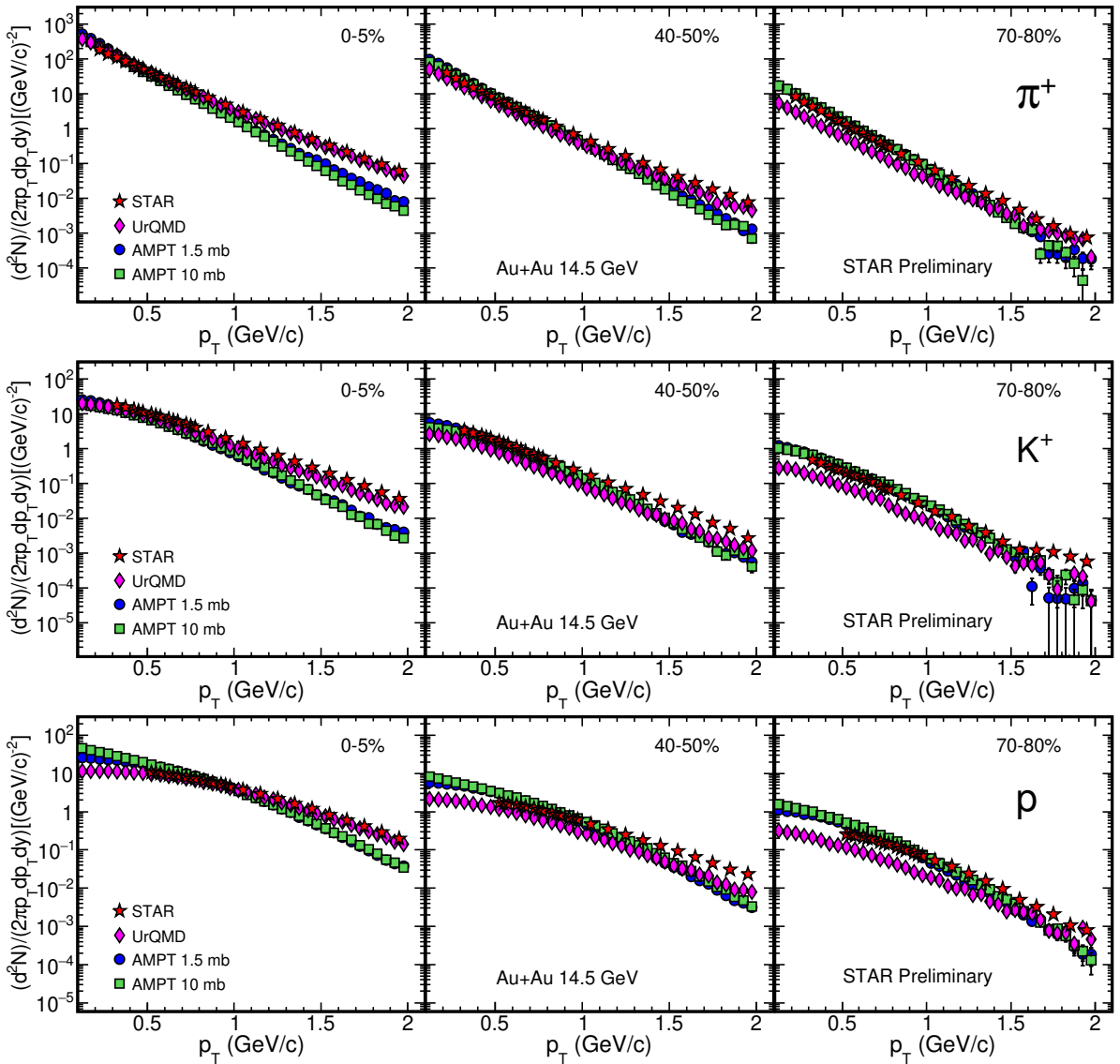
Figure 3.29: Transverse momentum (p_T) spectra comparison of π^+, K^+ and p for the two sets of AMPT data (AMPT 1.5 mb and AMPT 10 mb) and UrQMD data in comparison with STAR results in Au+Au collisions at $\sqrt{s_{NN}} = 14.5$ GeV in three different collision centrality classes.

and UrQMD data in three different collision centralities. The p_T spectra comparison of the corresponding anti-particles π^-, K^- and $\bar{p}$ are identical in shape to this. From the figure, we can observe that the spectral shape obtained from AMPT model deviates from the STAR results at high p_T and remains below. The results from AMPT 1.5 mb and 10 mb sets are almost similar to each other and do not change much. On the other hand, the results from UrQMD model up to a good extent qualitatively describes the shape of the p_T spectra, but not quantitatively in Au+Au collisions at $\sqrt{s_{NN}} = 14.5$ GeV.

3.8.6.2 Mean Transverse Momentum

The average p_T of π^+, K^+ and p as a function of $\langle N_{\text{part}} \rangle$ obtained from UrQMD, AMPT 1.5mb and AMPT 10mb model calculations are compared with STAR's measurements for Au+Au collisions at $\sqrt{s_{NN}} = 14.5$ GeV in Fig. 3.30. The value of $\langle p_T \rangle$ for all the studied particles is found to be lower in all AMPT-SM calculations. UrQMD though generally under predicts $\langle p_T \rangle$, but shows the trend similar to data and shows good agreement for protons.
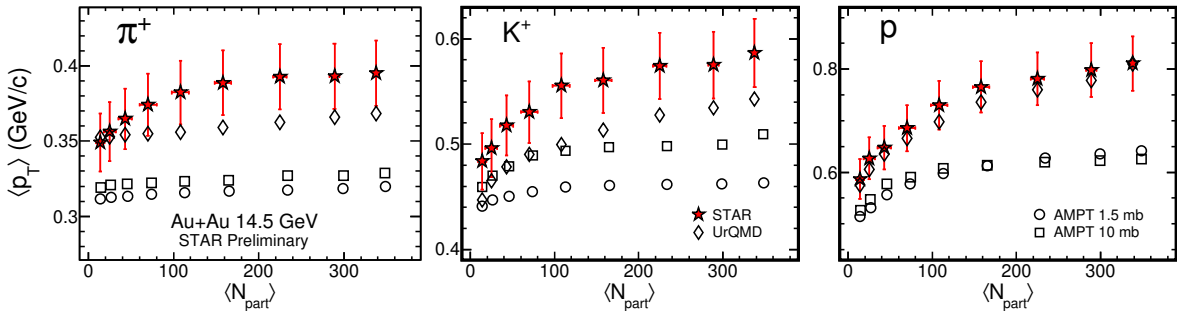
Figure 3.30: $\langle p_T \rangle$ of π^+, K^+ and p as a function of $\langle N_{\text{part}} \rangle$ for Au+Au collisions at $\sqrt{s_{NN}} = 14.5$ GeV in STAR. These experimental measurements are compared with UrQMD, AMPT 1.5 mb and AMPT 10 mb.

3.8.6.3 Particle Yields

Figure 3.31 shows dN/dy divided by $0.5 \times \langle N_{\text{part}} \rangle$ versus $\langle N_{\text{part}} \rangle$ for π^+, K^+ and p from Au+Au collisions at $\sqrt{s_{NN}} = 14.5$ GeV. Results from STAR are compared with UrQMD and with AMPT 1.5mb and AMPT 10mb. UrQMD and AMPT are close to the π^+ data for central collisions, but deviate for peripheral collisions. We can observe that the AMPT string melting data and UrQMD data describes the dN/dy values of $\pi^\pm$ in central collisions, but fails to de-
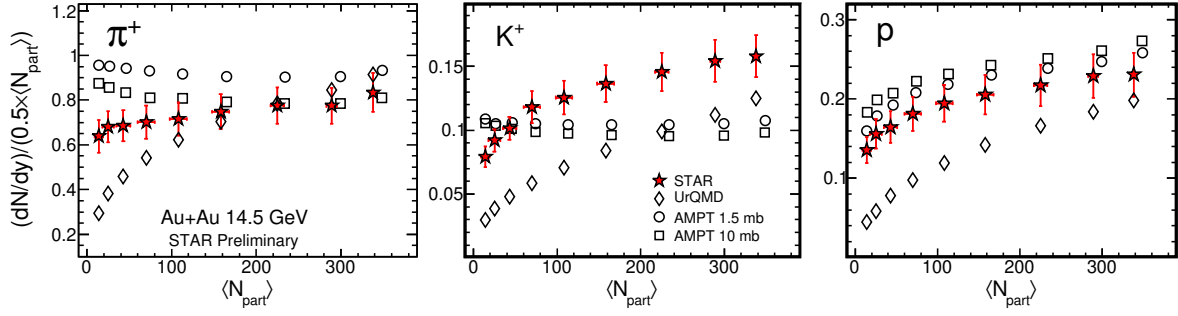
Figure 3.31: $(dN/dy)/(0.5 \times \langle N_{\text{part}} \rangle)$ for π^+, K^+ and p as a function of $\langle N_{\text{part}} \rangle$ within mid-rapidity ($|y| < 0.1$) in Au+Au collisions at $\sqrt{s_{NN}} = 14.5$ GeV in STAR. These experimental measurements are compared with UrQMD, AMPT 1.5 mb and AMPT 10 mb.

scribe in peripheral collisions. Predictions from all the models disagree to K^+ measurements. The values of dN/dy for proton and anti-proton is described by both the sets of AMPT-SM data to a good extent for central to mid-central collisions, but data from UrQMD model fails to describe it for all centrality classes.

3.8.6.4 Particle Ratios

Anti-particle to particle ratios (π^-/π^+, K^-/K^+ and $\bar{p}/p$) as a function of $\langle N_{\text{part}} \rangle$ in Au+Au collisions at $\sqrt{s_{NN}} = 14.5$ GeV are shown in Fig. 3.32. These measured ratios are compared with UrQMD and AMPT-SM calculations. The pion ratios from all models are in close agreement with experiment, while the kaon ratios from all models are too high, apart from AMPT-SM in peripheral collisions. The proton ratios from AMPT-SM are in good agreement with experiment, while UrQMD shows poor agreement.
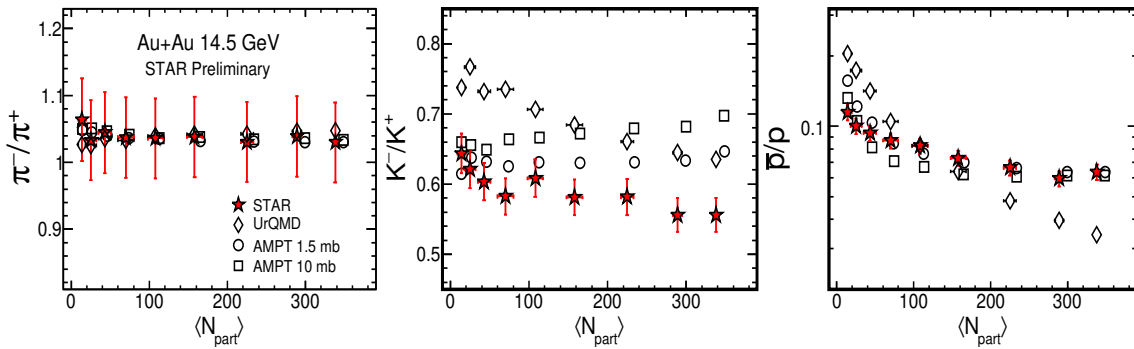
Figure 3.32: π^-/π^+, K^-/K^+ and $\bar{p}/p$ ratios as a function of $\langle N_{\text{part}} \rangle$ in Au+Au collisions at $\sqrt{s_{NN}} = 14.5$ GeV in STAR. These experimental ratios are compared with UrQMD, AMPT 1.5 mb and AMPT 10 mb.

Figure 3.33 shows STAR's K^+/π^+, K^-/π^-, p/π^+ and $\bar{p}/\pi^-$ ratios as a function of $\langle N_{\text{part}} \rangle$

148

in Au+Au collisions at $\sqrt{s_{NN}} = 14.5$ GeV, along with UrQMD and AMPT-SM model calculations. K^+/π^+ and K^-/π^- ratios are under-predicted by all model calculations. In the case of p/π^+, AMPT-SM mounts the data, and in the case of $\bar{p}/\pi^-$, AMPT-SM shows good agreement. On the other hand, the latter two ratios are not tracked by UrQMD at any centrality.
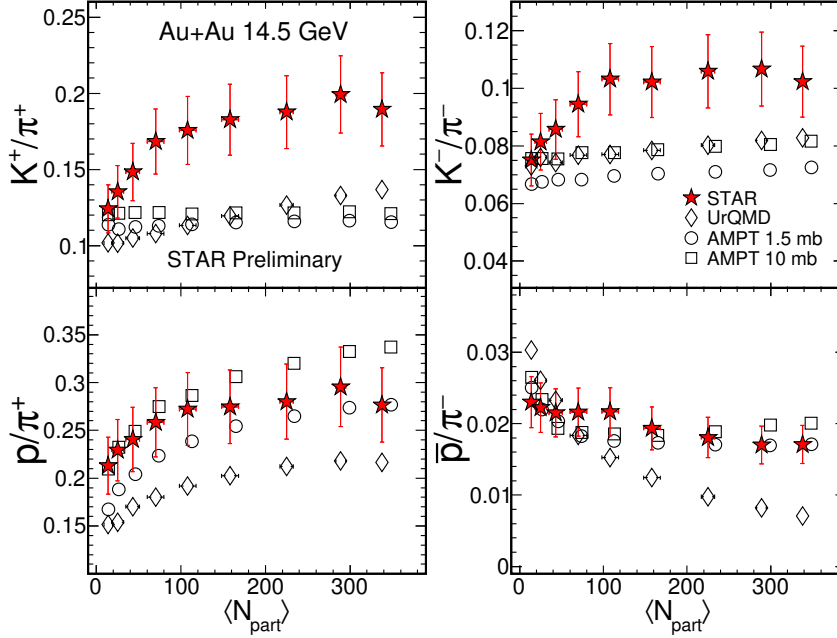
Figure 3.33: K^+/π^+, K^-/π^-, p/π^+ and $\bar{p}/\pi^-$ ratios as a function of $\langle N_{\text{part}} \rangle$ in Au+Au collisions at $\sqrt{s_{NN}} = 14.5$ GeV in STAR. These experimental ratios are compared with UrQMD, AMPT 1.5 mb and AMPT 10 mb.

3.9   Summary

We have reported basic observables for produced identified particles in Au+Au collisions at $\sqrt{s_{NN}} = 14.5$ GeV. The transverse momentum spectra of π, K, p, and $\bar{p}$ at midrapidity ($|y| < 0.1$) are measured for nine centralities: 0-5%, 5-10%, 10-20%, 20-30%, 30-40%, 40-50%, 50-60%, 60-70% and 70-80%. Observables like average transverse momentum ($\langle p_T \rangle$), particle yields (dN/dy), particle ratios, chemical and kinetic freeze-out properties are extracted for Au+Au collisions at $\sqrt{s_{NN}} = 14.5$ GeV. All the obtained results are compared with published measurements at other STAR beam energies and LHC energies.

The mean $\langle p_T \rangle$ values for π, K and p increase from peripheral to central collisions in Au+Au collisions at $\sqrt{s_{NN}} = 14.5$ GeV indicating increasing radial flow effects in central

collisions. Also, the mean p_T and inferred radial flow increase from pions to kaons and from kaons to protons.

The dN/dy of particles in mid-rapidity for π, K and p show a slight centrality dependence, while a flat behavior with centrality is observed for $\bar{p}$ in Au+Au collisions at $\sqrt{s_{NN}} = 14.5$ GeV. The dN/dy for π, K and $\bar{p}$ increase with collision energy, while for p, it decreases with collision energy. This is a direct effect of baryon stopping at lower RHIC energies.

No significant centrality dependence is observed in the case of π^-/π^+ and K^-/K^+ ratios. π^-/π^+ is slightly greater than unity in Au+Au collisions at $\sqrt{s_{NN}} = 14.5$ GeV, which is due to isospin and the contribution from the decay of resonances like the Δ. The $\bar{p}/p$ ratio slightly decreases from peripheral to central collisions as a consequence of increasing baryon stopping in central collisions. The K^+/π^+ and K^-/π^- ratios increase with increasing centrality as well as with collision energy. This energy dependence is due to the dominance of pair production over associated production as we consider higher energies. The p/π^+ ratio increases from peripheral to central collisions, but no significant dependence on collision centrality is observed in the case of $\bar{p}/\pi^-$ ratio in Au+Au collisions at $\sqrt{s_{NN}} = 14.5$ GeV.

Chemical freeze-out parameters are extracted by fitting particle yields as well as ratios in the framework of a statistical thermal model with the Grand Canonical Ensemble or Strangeness Canonical Ensemble approaches. Freeze-out parameters are almost insensitive, within errors, to the choice of ensemble, and to the choice to fit particle yields or ratios in Au+Au collisions at $\sqrt{s_{NN}} = 14.5$ GeV. The chemical freeze-out temperature T_{ch} has no significant centrality dependence, while the baryon chemical potential has a weak centrality dependence. The extracted values of T_{ch} and μ_B in Au+Au collisions at $\sqrt{s_{NN}} = 14.5$ GeV using particle yields in GCE is calculated to be 154.2(3.5) MeV and 241.5(13.0) respectively.

Kinetic freeze-out parameters are obtained in Au+Au collisions at $\sqrt{s_{NN}} = 14.5$ GeV from simultaneous blast-wave model fits to the p_T spectra for $\pi^\pm$, $K^\pm$ and $p\,(\bar{p})$. The kinetic freeze-out temperature T_k decreases from peripheral to central collisions suggesting a short-lived fireball in Au+Au collisions at $\sqrt{s_{NN}} = 14.5$ GeV. On the other hand, average flow velocity $\langle \beta \rangle$ increases from peripheral to central collisions, indicating large radial flow for central collisions. This leads to an interesting anti-correlation between T_k and β. The values

of T_k varies in the range 114 to 139 MeV and $\langle \beta \rangle c$ in the range 0.485 to 0.168 from central to peripheral collisions.

All the measured bulk observables in Au+Au collisions at $\sqrt{s_{NN}} = 14.5$ GeV are compared with UrQMD and AMPT model calculations. Values of $\langle p_T \rangle$ in Au+Au collisions at $\sqrt{s_{NN}} = 14.5$ GeV are underestimated by both the UrQMD and AMPT models. AMPT agrees with the measured dN/dy for pions and protons but does not reproduce kaon dN/dy. The UrQMD model shows poor agreement with dN/dy for all the measured particles. π^-/π^+ ratios are reproduced within errors by both AMPT and UrQMD models. All models show poor agreement with STAR's K^-/K^+ and K/π ratios. The $\bar{p}/p$ ratio is well described by AMPT but not by UrQMD. The measured p/π^+ and $\bar{p}/\pi^-$ ratios are poorly reproduced by UrQMD, while AMPT does better.

All the measured observables ($\langle p_T \rangle$, dN/dy, particle ratios, chemical and kinetic freeze-out parameters) in Au+Au collisions at $\sqrt{s_{NN}} = 14.5$ GeV respect the smooth trend of beam energy dependence reported in earlier publications. These results therefore lay a concrete way for the clear understanding of the beam energy dependence of bulk observables of the system at BES energies. A new experimental data point in the ($T - \mu_B$) plane of the QCD phase diagram is given by this analysis.

Bibliography

[1] J. C. Collins and M. J. Perry; Phys. Rev. Lett. **34**, 1353 (1975); E. V. Shuryak, Phys. Rept. **61**, 71 (1980), ibid. **115**, 151 (1984; J. Adams *et al*. (STAR Collaboration), Nucl. Phys. **A 757**, 102 (2005).

[2] P. Braun-Munzinger et al., arXiv:**1101.3167** (2011); B. Mohanty, Nucl. Phys. **A 830**, 899C (2009).

[3] Y. Aoki *et al*., Nature 443, 675 (2006); Phys. Lett. **B 643**, 46 (2006); A. Bazavov *et al*., Phys. Rev. **D 85**, 054503 (2012).

[4] S. Ejiri, Phys. Rev. **D 78**, 074507 (2008); E. S. Bowman and J. I. Kapusta, Phys. Rev. **C 79**, 015202 (2009).

[5] S. Gupta *et al*., Science **332**, 1525 (2011).

[6] L. Adamczyk *et al*. (STAR Collaboration), Phys. Rev. **C 96**, 044904 (2017).

[7] Z.W. Lin, C.M. Ko, B.A. Li, B. Zhang and S. Pal, Phys.Rev. **C 72**, 064901, (2005).

[8] S. A. Bass *et al*. Prog. Part. Nucl. Phys. **41**, 255 (1998); M. Bleicher *et al*. J. Phys. **G 25**, 1859 (1999).

[9] F. Bieser, H. Crawford, J. Engelage *et al*., Nucl. Instrum. Methods Phys. Res. **A 499**, 766 (2003).

[10] C. A. Whitten (STAR Collaboration), AIP Conf. Proc. **980**, 390 (2008).

[11] D. Kharzeev and M. Nardi, Phys. Lett. **B 507**, 121 (2001).

[12] R. J. Glauber, in Lectures in Theoretical Phys, edited by W. E. Brittin and L. G. Dunham (Interscience, N.Y., 1959), Vol. 1, p. 315.

[13] B. B. Back *et al.* (PHOBOS collaboration), Phys. Rev. **C 70**, 021902 (2004).

[14] M. Shao, O. Barannikova, X. Dong, Y. Fisyak, L. Ruan, P. Sorensen, and Z. Xu, Nucl. Instr. Meth. **A 558**, 419 (2006).

[15] S. Eidelman *et al.*, Phys. Lett. **B 592**, 1 (2004); H. Fanchiotti, C. A. G. Canal and M. D. Marucho, hep-ph/**0305310**.

[16] W. M. Yao *et al.* (Particle Data Group), J. Phys. **G 33**, 1 (2006).

[17] H. Bichsel, Nucl. Instr. Meth. **A 562**, 154 (2006).

[18] B. I. Abelev *et al.* (STAR Collaboration), Phys. Rev. **C 79**, 034909 (2009).

[19] M. Aguilar-Benitez, W. Allison, A. Batalov *et al.*, Z. Phys. **C 50**, 405 (1991).

[20] B. Abelev *et al.* (STAR Collaboration), Phys. Rev. **C 81**, 024911 (2010).

[21] X.-N. Wang and M. Gyulassy, Phys. Rev. **D 44**, 3501 (1991).

[22] H. Long, Ph.D. thesis, UCLA, 2002.

[23] V. Fine and P. Nevski, Proc. CHEP **2000**, 143 (2000).

[24] M. Calderón de la Barca Sánchez, Ph.D. thesis (Yale University, 2001), arXiv:nucl-ex/**0111004**.

[25] J. Adams *et al.* (STAR Collaboration), Phys. Rev. Lett. **92**, 112301 (2004).

[26] E. Schnedermann, J. Sollfrank, and Y.W. Hienz, Phys. Rev. **C 48** 2462, (1993).

[27] H. Petersen *et al.*, arxiv:**0805.0567**.

[28] J. Adams *et al.* (STAR Collaboration), Phys. Rev. Lett. **91**, 072304 (2003); Phys. Rev. Lett. **91**, 172302 (2003); B. I. Abelev *et al.* (STAR Collaboration), Phys. Rev. Lett. **97**, 152301 (2006); Phys. Lett. **B 655**, 104 (2007).

[29] L. Ahle *et al.*, (E866 Collaboration and E917 Collaboration), Phys. Lett. **B 490**, 53 (2000); L. Ahle *et al.*, (E866 Collaboration and E917 Collaboration), Phys. Lett. B **476, 1** (2000); J. L. Klay *et al.*, (E895 Collaboration), Phys. Rev. Lett. **88**, 102301 (2002); J. Barrette *et al.*, (E877 Collaboration), Phys. Rev. **C 62**, 024901 (2000); Y. Akiba *et al.*, (E802 Collaboration), Nucl. Phys. **A 610**, 139c (1996); L. Ahle *et al.*, (E802 Collaboration), Phys. Rev. **C 60**, 064901, (1999); L. Ahle *et al.*, (E802 Collaboration and E866 Collaboration), Phys. Rev. **C 60**, 044904, (1999); L. Ahle *et al.*, (E802 Collaboration), Phys. Rev. **C 57**, 466, (1998).

[30] S. V. Afanasiev *et al.* (NA49 Collaboration), Phys. Rev. **C 66**, 054902, (2002); C. Alt *et al.* (NA49 Collaboration), Phys. Rev. **C 77**, 024903, (2008); Phys. Rev. **C 73**, 044910, (2006); T. Anticic *et al.* (NA49 Collaboration), Phys. Rev. **C 69**, 024902 (2004)

[31] B. Abelev *et al.*, (ALICE Collaboration), Phys. Rev. **C 88** 044910, (2013).

[32] M. Kaneta and Nu Xu, nucl-th/**0405068**, (2004).

[33] J. Cleymans, Burkhard Kampfer, M. Kaneta, S. Wheaton and N. Xu, Phys. Rev. **C 71**, 054901, (2005).

[34] J. Rafelski and M. Danos, Phys. Lett. **B 97**, 279 (1980).

[35] R. Hagedorn and K. Redlich, Z. Phys. **C 27**, 541 (1985).

[36] J. Rafelski and B. Muller, Phys. Rev. Lett. **48**, 1066 (1982).

[37] R. Koch *et al.*, Phys. Rep. **142**, 167 (1986).

[38] S. V. Afanasiev *et al.* (NA49 Collaboration), Phys. Rev. **C 66**, 054902 (2002).

[39] F. Wang et al., Phys. Lett. **B 489**, 273 (2000).

[40] F. Wang and N. Xu, Phys. Rev. **C 61**, 021904 (2000).

[41] P. Braun-Munzinger et al, Nucl. Phys. **A 697**, 902 (2002).

[42] L. Adamczyk *et al.* (STAR Collaboration), Phys. Rev. Lett. **110**, 142301 (2013).

[43] L. Adamczyk *et al*. (STAR Collaboration), Phys. Rev. **C 88**, 014902 (2013).

[44] L. Adamczyk *et al*. (STAR Collaboration), Phys. Rev. **C 93**, 021903(R) (2016).

[45] Md. Nasim, Phys. Rev. **C 89**, 034909 (2014).

[46] L. Adamczyk *et al*. (STAR Collaboration), Phys. Rev. Lett. **116**, 062301 (2016).

[47] J. Adams *et al*. (STAR Collaboration), Nucl. Phys. **A 757**, 102 (2005).

[48] S. Wheaton and J. Cleymans, Comput. Phys. Commun. **180**, 84 (2009).

[49] A. Andronic, F. Beutler, P. Braun-Munzinger, *et al*., Phys. Lett. **B 675**, 312 (2009).

[50] J. Cleymans, D. Elliott, A. Keranen, *et al*., Phys. Rev. **C 57**, 3319 (1998).

[51] G. Wilk and Z. Wlodarczyk, Phys. Rev. Lett. **84**, 2770 (2000).

[52] B. Abelev *et al*. (ALICE Collaboration), Phys. Rev. **C 88**, 044910 (2013).

[53] U. W. Heinz, arXiv:hep-ph/**0407360**.

Chapter 4

Pion, Kaon and (Anti-)Proton Production in U+U Collisions at $\sqrt{s_{NN}} = 193$ GeV in STAR

A single achievement, of course brings the time for celebration, additionally opens up new frontiers of research. The enthusiasm and confidence build a solid platform for a new dimension of scientific outlook to grow up. This universality never allows to put an end to any scientific program from both theoretical and experimental view point. Motivated by such an opinion, in the current chapter of the thesis we will explore another direction of RHIC physics.

4.1 Introduction

The experiments at RHIC mainly focuses on the exploration of the QCD phase diagram, finding the signatures of the QGP formation, search for the QCD critical point and understanding the properties of the QGP medium. Further at RHIC the physics processes are understood through the variation of colliding system type, shape and geometry. The initial stage dynamics of the two colliding systems cast its effect on the final state observables. Hence, the study of initial stage effect by changing the shape and geometry of the two colliding nuclei opens an exciting frontier of a field of physics research in heavy-ion collisions [1–7]. Till date the various colliding systems explored at RHIC are p+p, p+Al, p+Au, d+Au, He+Au, Cu+Cu, Cu+Au,

Zr+Zr, Ru+Ru, Au+Au and U+U. However, in this chapter of the thesis, we will discuss the results from U+U collisions.

In the year 2012, the STAR detector has taken data for the U+U collision at $\sqrt{s_{NN}} = 193$ GeV [8]. Uranium ($_{92}U^{238}$) is a prolate shaped nucleus [9–11] in contrast to the nearly spherical shaped Gold nucleus ($_{79}Au^{197}$). As a result of this prolate shape, the Uranium nucleus is associated on the geometrical sense with one long or major axis and another short or minor axis. Due to this, even for the most central collisions very interesting orientations of the two colliding nuclei is possible in U+U collisions [1,2]. Among all other possible random orientations, three physically interesting orientations have been figured out. Those are termed as : tip-tip, body-body and body-tip. When the major axes of the two colliding nuclei lie parallel to the beam axis resulting in the tip of both nuclei to collide head-on is classified as the tip-tip collisions. Another orientation is when the major axes of the two colliding nuclei are perpendicular and the minor axes are parallel to the beam axis, the resulting collision is known as body-body. The body-tip orientation of the two colliding nuclei is straightforward from the above two explanations. One interesting feature to point out is that in the tip-tip collision, the number of binary nucleon-nucleon collisions are substantially higher than the body-body orientation. This leads to the production of higher particle multiplicity in case of the tip-tip collisions [1,2,12,13]. There are also studies suggesting that the maximum transverse particle density in U+U collisions could become $6\% - 35\%$ higher than the corresponding Au+Au collisions subjected to the colliding configurations [14–16]. As a consequence of this, we can expect all the possible orientations combined together will also give rise to higher energy density and particle multiplicity in U+U collisions.

In this thesis chapter, the bulk properties of the medium produced in U+U collisions are measured without selecting any specific orientation of the colliding nuclei. The results of transverse momentum spectra, particle yields (dN/dy), mean transverse momentum ($\langle p_T \rangle$), particle ratios and kinetic freeze-out parameters for $\pi^{\pm}$, $K^{\pm}$ and $p(\bar{p})$ produced in U+U collisions at $\sqrt{s_{NN}} = 193$ GeV are presented. Observables are studied as a function of p_T and collision centrality. All the results are compared with the corresponding published results from Au+Au collisions at $\sqrt{s_{NN}} = 200$ GeV [17]. A comparative study with models like AMPT [18] modi-

fied to incorporate the deformation of the Uranium nucleus [2] is also carried out.

The similar techniques and systematic procedure has been adopted as discussed in the previous chapter to analyze the data to arrive at the desired results. In the subsequent sections, we will dedicatedly discuss about the data selection procedure, particle identification techniques, correction factors calculation, systematic uncertainty estimation and finally the results on U+U collisions at $\sqrt{s_{NN}} = 193$ GeV.

4.2 Data Set, Triggers and Analysis cuts

The results presented in this chapter of the thesis, are performed on the data of U+U collisions at $\sqrt{s_{NN}} = 193$ GeV taken by the STAR detector at RHIC in the year 2012. Minimum biased triggered data from Zero Degree Calorimeter (ZDC) [19] are selected for analysis. The ZDC's are a pair of hadronic calorimeters placed on both sides at a distance of 18 m from the center of the STAR detector close to the zero degree angle ($\theta < 2$ mrad) from the beam axis. These triggers in addition to selecting events for physics analysis also provides the position of the z-component of primary vertex position through the co-incidence signal of the two ZDCs.

4.2.1 Event Selection

The common point of origin of all the primary tracks in a given collision is determined by the STAR reconstruction algorithm and is termed as the primary vertex position. This point of interaction is randomly distributed in x, y and z-direction for a given data set.

A vertex position cut of $|V_z| < 30$ cm is applied to the event selection in U+U collisions at $\sqrt{s_{NN}} = 193$ GeV. In addition to this, to reduce pile-up events a cut of $|V_z - vpdV_Z| < 3$ is applied to event selection in U+U collisions at $\sqrt{s_{NN}} = 193$ GeV. Here $vpdV_z$ is the vertex position along beam direction measured by the Vertex Position Detector (VPD) [20]. The plane perpendicular to beam direction contains the x- and y-axis defining the transverse direction of an event. A radial vertex cut defined by $V_r = \sqrt{V_x^2 + V_y^2}$ is taken to be less than 2 cm. The number of minimum bias events analyzed in U+U collisions at $\sqrt{s_{NN}} = 193$ GeV after all these event selection cuts is ~ 270 Million. The V_z and V_x versus V_y distributions in U+U
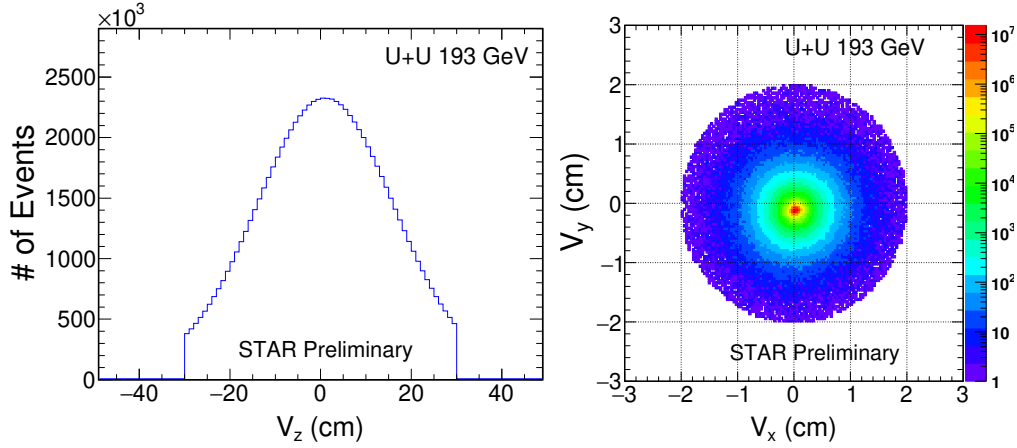
Figure 4.1: Distribution of z-component of vertex V_z (left panel) and V_x vs. V_y (right panel) distributions after all the event cuts in U+U collisions at $\sqrt{s_{NN}} = 193$ GeV in STAR.

collisions at $\sqrt{s_{NN}} = 193$ GeV are presented in Fig. 4.1.

4.2.2 Centrality Selection

As discussed in the previous chapter, the collision centrality is the technical term used in heavy-ion collision experiment in substitution of impact parameter of the collision and is directly related to it. Where the impact parameter (b) is the perpendicular distance between the centers of the two nuclei at the time of closest approach. Small impact parameter means central collision
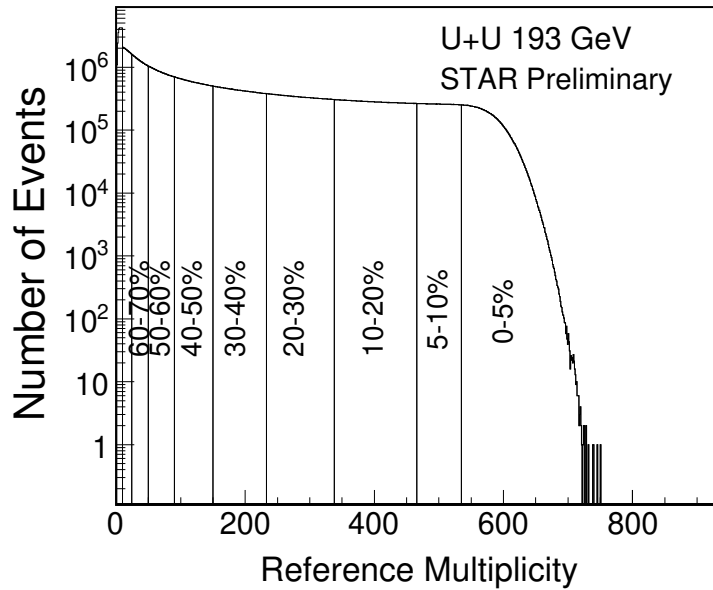
Figure 4.2: Charged particle multiplicity distribution (uncorrected for efficiency and acceptance) measured by TPC within $|\eta| < 0.5$ in U+U collisions at $\sqrt{s_{NN}} = 193$ GeV in STAR. The vertical lines represents the centrality selection criteria used. The errors are statistical only.

and large impact parameter means peripheral collisions. Since impact parameter is not a directly measurable quantity in an experiment. An indirect procedure combining the information from experimental data and simulation is usually used in STAR to determine the centrality of a collision.

Table 4.1: The average number of participant nucleons $\langle N_{\mathrm{part}} \rangle$, average number of nucleon-nucleon binary collisions $\langle N_{\mathrm{coll}} \rangle$ and number of events in different collision centrality classes in U+U collisions at $\sqrt{s_{NN}} = 193$ GeV.

Centrality	$\langle N_{\mathrm{part}} \rangle$	$\langle N_{\mathrm{coll}} \rangle$	No. of Events
$0 - 5\%$	414.87	1281.26	15.7 M
$5 - 10\%$	355.42	1010.97	17.8 M
$10 - 20\%$	277.52	714.081	36.0 M
$20 - 30\%$	195.36	435.854	35.5 M
$30 - 40\%$	133.08	253.489	35.8 M
$40 - 50\%$	86.17	137.384	35.1 M
$50 - 60\%$	52.63	69.3415	33.7 M
$60 - 70\%$	29.38	31.8468	33.4 M
$70 - 80\%$	14.66	13.1883	25.9 M

The centrality classes are selected from the measured charged particle multiplicity given by the TPC over the full azimuthal coverage and within pseudo-rapidity $|\eta| < 0.5$. This is termed as "Reference Multiplicity" or simply "Refmult" in STAR. The "Refmult" distribution so obtained is fitted with Glauber Model Monte-Carlo simulations [7, 21] as discussed in the previous chapter. The centrality class for each event is determined as the fraction of the total cross-section obtained from the simulated events. The Reference Multiplicity distribution in U+U collisions at $\sqrt{s_{NN}} = 193$ GeV depicting the centrality selection is shown in Fig. 4.2. In the current analysis of U+U collisions at $\sqrt{s_{NN}} = 193$ GeV, the minimum biased triggered events are divided into 9 different centrality classes as $0-5\%, 5-10\%, 10-20\%, 20-30\%, 30-40\%, 40-50\%, 50-60\%, 60-70\%, 70-80\%$.

Using the Glauber Model Monte-Carlo simulations, the average number of participant nucleons $\langle N_{\mathrm{part}} \rangle$ and number of nucleon-nucleon binary collisions $\langle N_{\mathrm{coll}} \rangle$ is also evaluated. These values for U+U collisions at $\sqrt{s_{NN}} = 193$ GeV in each centrality bin is listed in Table 4.1. One can find from Table 4.1 that, 0-5% centrality class in U+U collision allows us to extend our measurements to a higher value of $\langle N_{\mathrm{part}} \rangle > 400$ in contrast to the corresponding value of

$\langle N_{\text{part}} \rangle$ in Au+Au collisions at $\sqrt{s_{NN}} = 200$ GeV being 350.6.

4.2.3 Track Selection

The selection of good tracks is ensured by the application of some standard track quality cuts. The track selection procedure adopted for U+U collisions at $\sqrt{s_{NN}} = 193$ GeV is similar to that discussed in the previous chapter and reported in the previous STAR papers [17, 22].

Table 4.2: Track selection criteria for the tracks used in the analysis.

Cut Type	Value
$|y|$	< 0.1
$|DCA|$	< 3 cm
nFitPts	≥ 25
nFitPts/nFitPoss	≥ 0.52
ndEdx	≥ 15

The track cuts applied in U+U collisions at $\sqrt{s_{NN}} = 193$ GeV are given in Table 4.2. Only primary tracks are used for analysis with proper application of track selection criteria. To avoid intermixing of tracks from the secondary vertex, the Distance of Closest Approach (DCA) of the tracks to the primary tracks is taken to be less than 3 cm. The number of fit points associated with each track denoted as "nFitPts" obtained from TPC is needed to be greater than 25 out of possible maximum 45 hits (nFitPoss). The ratio of nFitPts to nFitPoss is taken to greater than 0.52 to exclude over counting of split tracks. A good dE/dx resolution of the tracks is ensured by applying a cut of greater than 15 on the number of samplings used to calculate $\langle dE/dx \rangle$. The rapidity window chosen for this analysis is $|y| < 0.1$.

4.3 Particle Identification and Raw Yield Extraction

The first step of the analysis involves the identification and counting of the number of particles of $\pi^{\pm}$, $K^{\pm}$ and $p(\bar{p})$ produced in U+U collisions at $\sqrt{s_{NN}} = 193$ GeV. The Time Projection Chamber (TPC) [23] serves as the primary tracking device in STAR. The ionization energy loss (dE/dx) provided by TPC is mostly used to identify particles with relatively lower momentum. The identification of particle is pushed further to higher momentum range by the inclusion

of information from the Time Of Flight (TOF) [24] detector along with TPC. The particle identification and raw yield extraction technique followed in this chapter can be found in earlier STAR papers [17,22]. This procedure has already been discussed in the previous chapter of this thesis and for completeness is briefly described below for U+U collisions at $\sqrt{s_{NN}} = 193$ GeV.

4.3.1 Using TPC

The ionization energy loss (dE/dx) information obtained for each particle track stored in TPC is used for particle identification. These experimentally measured values of dE/dx in U+U collisions at $\sqrt{s_{NN}} = 193$ GeV as a function of momentum by charge (p/q) are depicted in Fig. 4.3. The behavior of this dE/dx distribution is theoretical predicted from the Bichsel [25] formula in STAR and are shown as solid black lines in Fig. 4.3. A visible dependence of dE/dx on particle mass can be observed, which gradually weakens with the increasing momentum. The bands of pions, kaons and protons start merging after at relatively higher momentum near 1.0 GeV/c. Hence, TPC is extensively used to identify pions, kaons, and protons upto a p_T value of 0.8, 0.8 and 1.0 GeV/c respectively.
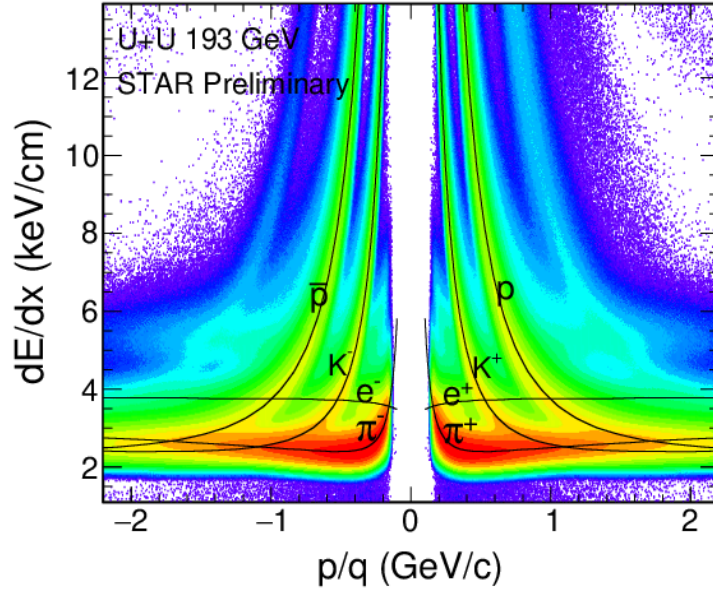
Figure 4.3: The dE/dx distribution of charged particles as a function of momentum/charge (p/q) obtained from TPC in U+U collisions at $\sqrt{s_{NN}} = 193$ GeV. The curves represents the expected mean value of dE/dx for the corresponding particle.

As described in the previous chapter, the raw yields of particles are obtained using the z-variable [26] as described in refs. [17,22]. For a particular particle type (X) it is given by the

mathematical expression

$$z_X = \ln\left(\frac{\langle dE/dx\rangle}{\langle dE/dx\rangle_X^B}\right),\qquad(4.1)$$

where X is the particle type chosen ($e^\pm$, $\pi^\pm$, $K^\pm$ and $p\bar{p}$ in the present analysis) and $\langle dE/dx\rangle_X^B$ is the theoretical value of dE/dx obtained from Bichsel formula [25] for the corresponding particle.
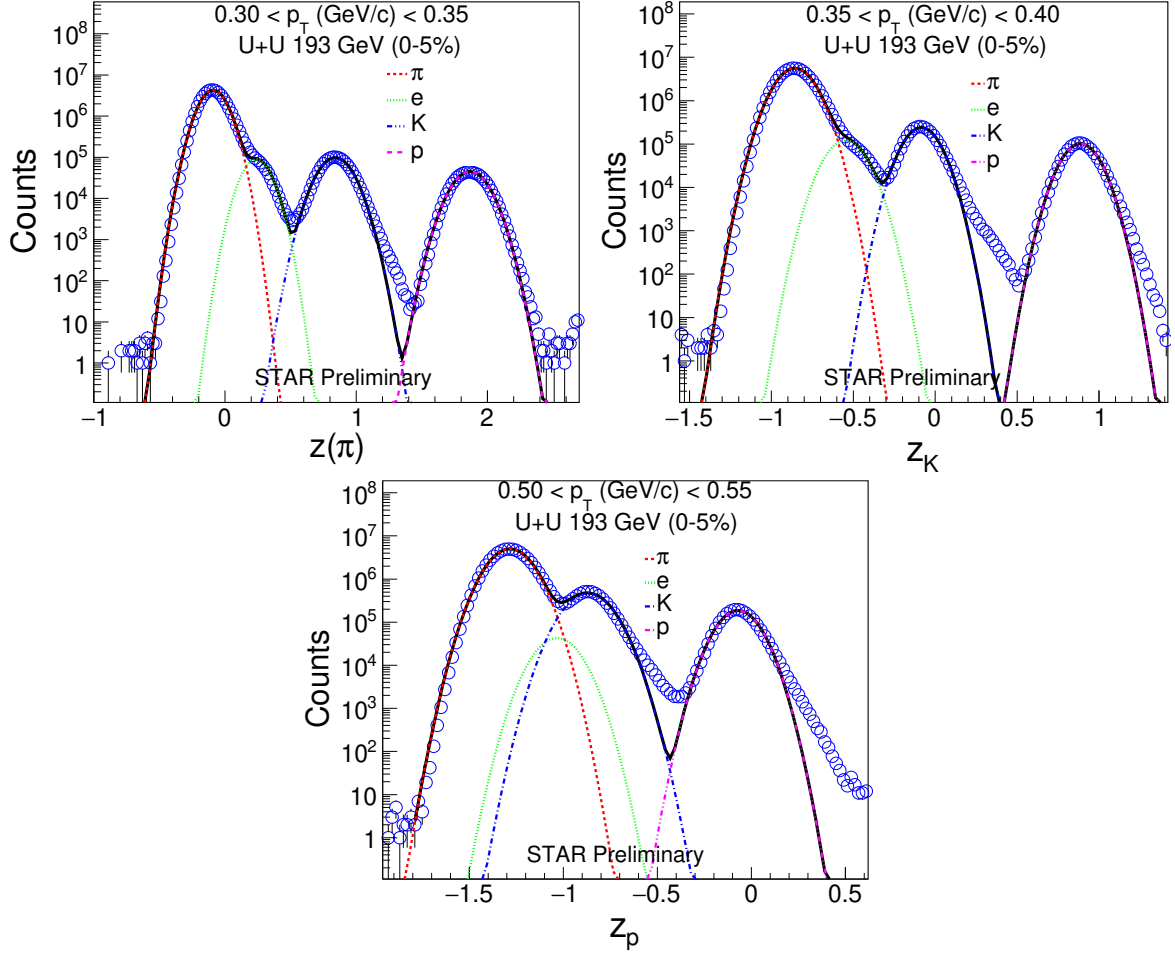
Figure 4.4: The z_π, z_K and z_p distributions of π^+, K^+ and p at mid-rapidity ($|y| < 0.1$) for different p_T ranges in $0-5\%$ centrality from TPC in U+U collisions at $\sqrt{s_{NN}} = 193$ GeV. The curves are Gaussian fits representing contributions from pions (dashed-red), electrons (dotted-green), kaons (dash-dotted-blue), and protons (dash-dot-dotted-magenta). The errors are statistical only.

Figure 4.4 shows z_π, z_K and z_p distributions of π^+, K^+ and p at mid-rapidity ($|y| < 0.1$) for different p_T ranges in $0-5\%$ centrality from TPC in U+U collisions at $\sqrt{s_{NN}} = 193$ GeV. The peaks correspond to various particles such as pions, kaons, and protons. By construction, the pion peak for $z(\pi)$ is expected to be around zero. For this data set, the peak is slightly

off-set from zero. This is a consequence of the calibration procedure in which the pion mass is assumed for each particle track and is fixed for pion as a reference particle. However, since the yields are obtained as the area under the Gaussian peaks, the shift does not affect the raw yield estimation. The curves represent the multi-Gaussian fit to the data to extract the raw yield as long as the peaks are well distinguishable. The same procedure as discussed in the previous chapter is applied for all p_T bins, centralities in the case of each particle to obtain the raw yields.

4.3.2   Using TOF

The particle identification has been extended to momentum range higher than specified above by using the TOF detector information in addition to TPC. The time-of-flight (t_{tof}) information provided by TOF proves its excellence in the particle identification technique. This procedure of particle identification using TOF has already been described in the previous chapter and is briefly written here for completeness. The inverse of particle velocity in the units of speed of light $1/\beta$ as a function of p/q is illustrated in Fig. 4.5. The solid black curves are the mean values of $1/\beta$ for a particular particle species. As can be observed the $1/\beta$ lines remains clearly separated upto $p_T = 2$ GeV/c.

The raw yield extraction technique using TOF is same as mentioned in the previous chapter
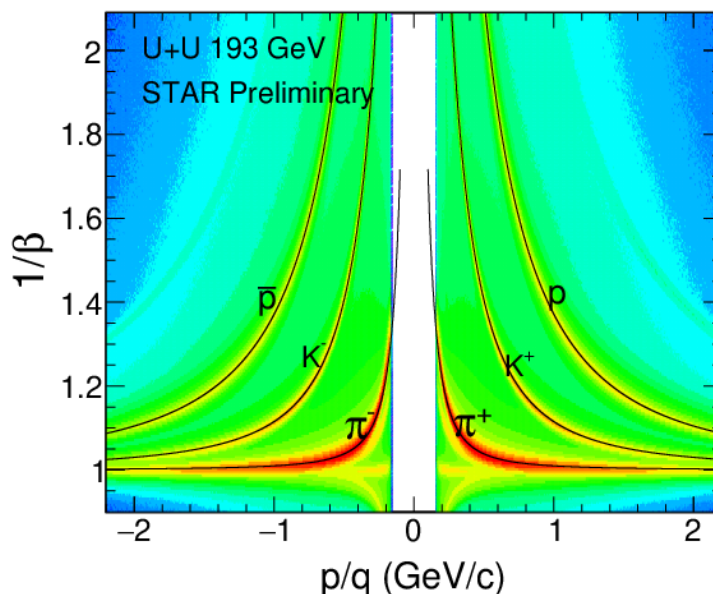
Figure 4.5: $1/\beta$ as function of momentum/charge (p/q) in U+U collisions at $\sqrt{s_{NN}} = 193$ GeV. The curves represent the theoretical values of $1/\beta$ for the corresponding particle.

and reported in earlier STAR publications [17, 22]. To extract the raw yields using TOF we make use of the m^2 variable defined as

$$m^2 = p^2 \left(\frac{c^2 T^2}{L^2} - 1 \right),\tag{4.2}$$

where p, T, L, and c are momentum, time-of-flight, the path length of the particle, and the speed of light, respectively. Fig. 4.6 shows the m^2 distribution used to extract raw yield for π^+ within $|y| < 0.1$ and for p_T bin $0.5 - 0.6$ GeV/c in U+U collisions at $\sqrt{s_{NN}} = 193$ GeV. To extract the raw yields using m^2 distributions, we follow the same procedure as done in Refs. [22, 27]. In this method, the m^2 distributions from data are fitted with the predicted m^2 distributions. The predicted m^2 distributions are generated by using the predicted time-of-flight information that include the TOF detector response behavior as

$$m^2_{\text{predicted}} = p^2 \left(\frac{c^2 T^2_{\text{predicted}}}{L^2} - 1 \right).\tag{4.3}$$

These m^2 distributions for pions, kaons and protons in a given p_T range taken together are used simultaneously to fit the measured m^2 distributions as shown in Fig. 4.6. In this figure, the contributions from pions, kaons and protons are shown by solid red, dotted green and dash-dotted blue lines, respectively. The black histogram is the measured m^2 distribution and the
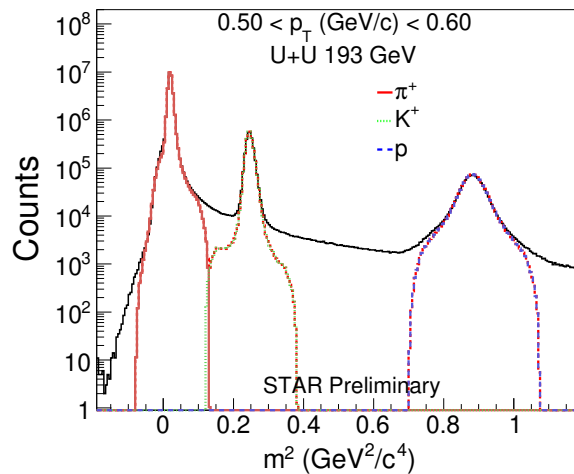
Figure 4.6: The m^2 distribution used to obtain the raw yields from TOF for π^+ within $|y| < 0.1$ in p_T range $0.50 - 0.60$ (GeV/c) in $0 - 5\%$ centrality in U+U collisions at $\sqrt{s_{NN}} = 193$ GeV. The curves are fits to m^2 distributions representing contributions for pions (solid-red), kaons (dotted-green) and protons (dash-dotted-blue). The errors are statistical only.

dotted red lines represent the total fit. Using a χ^2 minimization procedure, the raw yields of each particle are obtained for each p_T bin in nine centrality classes. In the present analysis, TOF information is particularly used above 0.4 GeV/c for pions and kaons and above 0.5 GeV/c for protons.

4.4   Correction Factors

We will present the procedure to calculate correction factors such as energy loss correction, detector efficiency, TOF matching efficiency, pion feed-down correction and proton background correction. The Monte-Carlo embedding technique proves to be beneficial in estimating some of these errors. This method as discussed previously is briefly mentioned here and can be found in detail in refs [17, 22, 28].

4.4.1   Monte-Carlo Embedding Technique

The event generator Heavy Ion Jet Interaction Generator (HIJING) model [29] is primarily used to simulate events by generating tracks with a flat p_T and y distribution, to ensure equal statistics in each p_T bin. These generated tracks have transverse momentum termed as p_T^{MC}. These tracks are mixed with the real data tracks at 5% level and allowed to pass through the response of the STAR detector using GEANT package [30]. These embedded events are reconstructed like real events taking into consideration all the detector effects. After a proper association mapping with input MC tracks, the reconstructed tracks are marked to have momentum p_T^{REC}. After this a quality assurance of the embedding sample is done to make sure that the MC simulation sample reproduces the characteristics of real data. For this, we compare distributions such as DCA, nFit points, nHits dEdx and ϕ between real data and embedding. These comparison plots are shown in Fig. 4.7 with reference to π^+ embedding sample. From these plots, we can observe that there is a good matching of the embedding data with the real data in U+U collision at $\sqrt{s_{NN}} = 193$ GeV.

The subsequent subsections discusses about the estimation of the various correction factors in U+U collisions at $\sqrt{s_{NN}} = 193$ GeV.
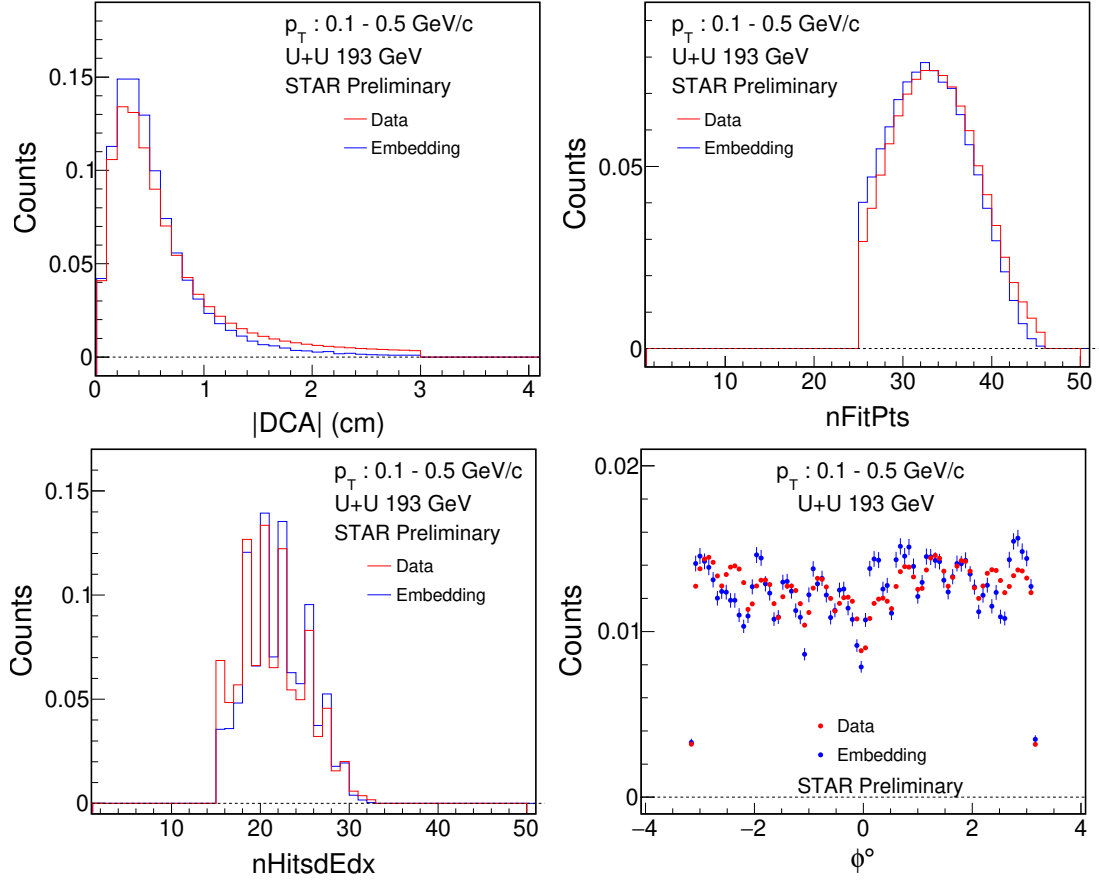
Figure 4.7: (Top left) DCA, (Top right) nFitPts, (Bottom left) nHitsdEdx, (Bottom right) phi comparison between reconstructed embedding tracks and real tracks with reference to π^+ embedding sample in U+U collisions at $\sqrt{s_{NN}} = 193$ GeV. The errors are statistical only.

4.4.2 Energy Loss Correction

In the track reconstruction procedure, the Coulomb scattering and energy loss of a charged particle are corrected by assuming the pion mass for each particle track [17, 22]. Thus, a momentum correction is needed for higher mass particles such as kaons and protons. This energy loss typically affects the particles with low momentum. That is why a correction has to be made in the low momentum range for kaons and protons.

This factor is calculated from the Monte-Carlo embedding data. The difference between the reconstructed momentum p_T^{REC} and initial momentum p_T^{MC} as a function of p_T^{REC} estimates the energy loss correction track by track. The corresponding plot to this in U+U collisions at $\sqrt{s_{NN}} = 193$ GeV is shown in Fig. 4.8 for pions, kaons and protons. The curve in red line
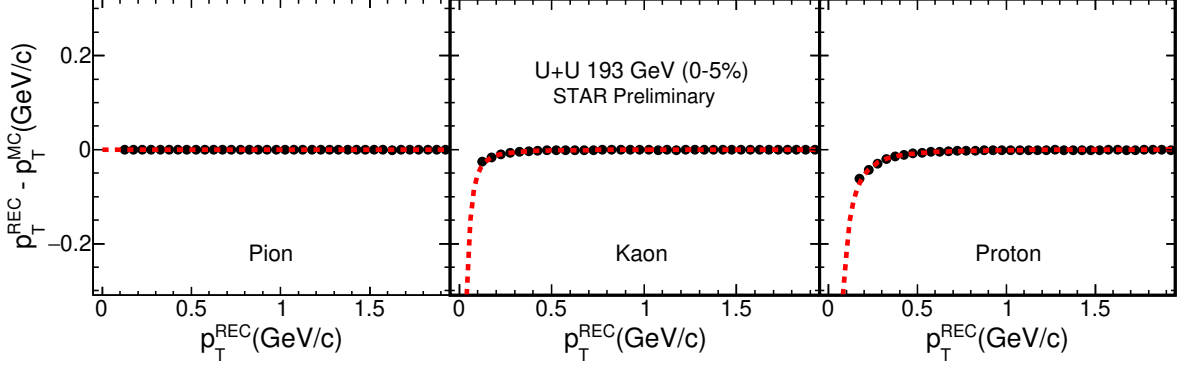
Figure 4.8: The difference between p_T^{REC} and p_T^{MC} as function of p_T^{REC} for pions (left), kaons (middle) and protons (right) in U+U collisions at $\sqrt{s_{NN}} = 193$ GeV. The errors are statistical only.

represents a functional fitting to the data points given by

$$f(p_T) = A + B + \left(1 + \frac{C}{p_T^2}\right)^D,$$ (4.4)

where A, B, C and D are the fit parameters. The particular values of these parameters in U+U collisions at $\sqrt{s_{NN}} = 193$ GeV for kaon and proton is tabulated in Table 4.3. This energy loss fraction has only p_T dependence, particle type dependence, but has no centrality dependence. All the results presented in this chapter are corrected for this energy loss effect.

Table 4.3: Values of energy loss parameters for kaons and protons in U+U collisions at $\sqrt{s_{NN}} = 193$ GeV

Parameters	Kaon	Proton
A (GeV/c)	2.94097e-04	1.03326e-03
B (GeV/c)	-4.75968e-06	-2.34481e-05
C (GeV/c)^2	9.19009e+01	9.25430e+01
D	1.02223e+00	1.00186e+00

4.4.3 TOF Matching Efficiency

The TOF detector circumscribes the TPC detector within $|y| < 0.9$ with full azimuth coverage. Not all TPC tracks reach the TOF detector, hence a track matching correction between TPC and TOF is needed. This correction factor is estimated from data for each particle species. This is obtained from the ratio of the number of tracks detected in TOF to the total number of tracks in
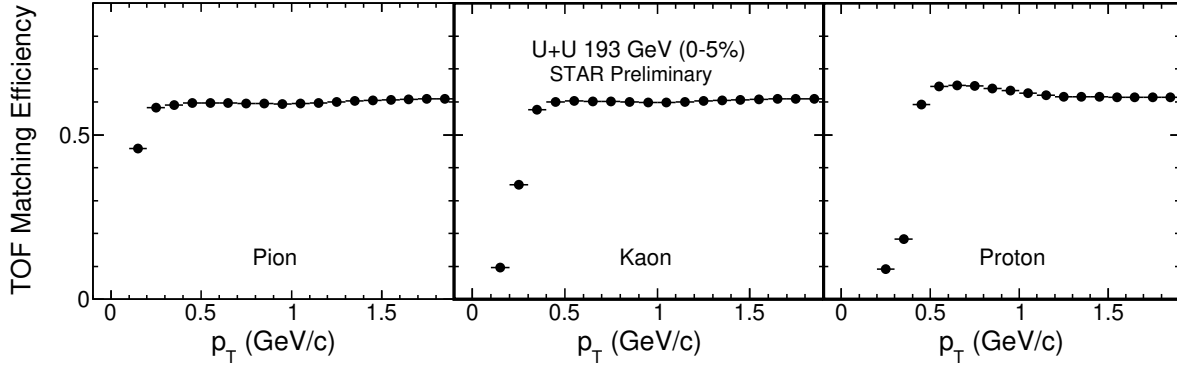
Figure 4.9: TOF matching efficiency factor as a function of p_T for pions (left), kaons (middle) and protons (right) obtained from real data in U+U collisions at $\sqrt{s_{NN}} = 193$ GeV. The errors are statistical only.

TPC within the acceptance under analysis. This quantity as a function of p_T is shown in Fig. 4.9 for pions (left), kaons (middle) and protons (right) in U+U collisions at $\sqrt{s_{NN}} = 193$ GeV. This matching efficiency typically varies within $\sim 60 - 70\%$ between central to peripheral collisions in U+U collisions at $\sqrt{s_{NN}} = 193$ GeV. The p_T spectra in each centrality is divided by this TOF matching efficiency factor for each p_T bin.

4.4.4 Track Reconstruction Efficiency and Detector Acceptance

A correction factor considering the efficiency of the detector in reconstructing tracks and its acceptance is applied to the p_T spectra. The MC generated embedding sample provides this correction fraction for each particle species for each centrality. It is given by the ratio of the p_T distribution of reconstructed Monte-Carlo to initial Monte-Carlo tracks as a function of p_T^{MC} in the selected rapidity window. Figure 4.10 represents the fraction of efficiency $\times$ acceptance as a function of p_T^{MC} for reconstructed pions (left), kaons (middle), protons (right) in central 0-5% U+U collisions at $\sqrt{s_{NN}} = 193$ GeV. The form of the function used for fitting is given by

$$f(p_T) = P_0 \exp(-P_1/p_T)^{P_2} \tag{4.5}$$

where P_0, P_1 and P_2 are the fit parameters and typical values is listed in Table 4.4 for 0-5% centrality for U+U collisions at $\sqrt{s_{NN}} = 193$ GeV.

This factor shows a centrality dependence as it increases from central to peripheral collisions. The raw p_T spectra of each particle species and centrality are corrected for the efficiency
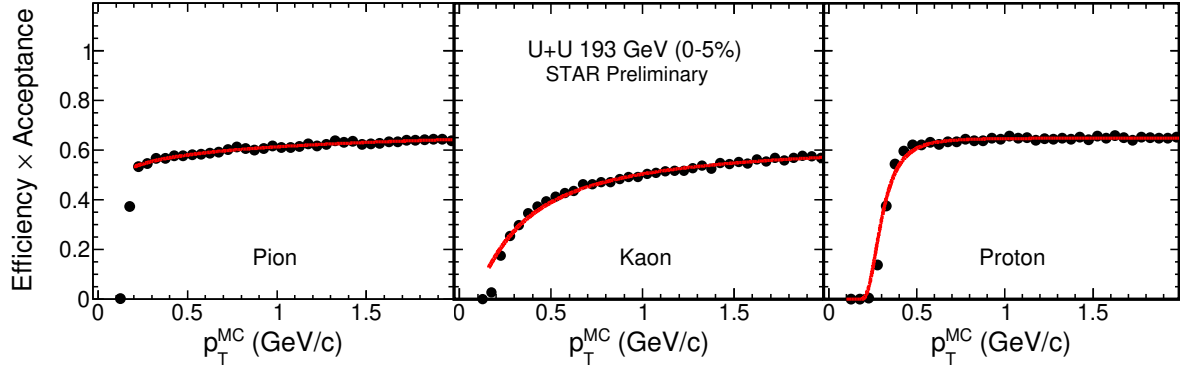
Figure 4.10: Track reconstruction efficiency $\times$ acceptance as function of p_T^{MC} for reconstructed pions (left), kaons (middle) and protons (right) obtained from embedding in U+U collisions at $\sqrt{s_{NN}} = 193$ GeV. The red lines are the functional fit to the data. The errors are statistical only.

Table 4.4: Values of the parameters of the functional fit to the track reconstruction efficiency $\times$ acceptance as a function of p_T of π^+, K^+ and p for 0-5% centrality class in U+U collisions at $\sqrt{s_{NN}} = 193$ GeV.

Parameters	π^+	K^+	p
P_0	0.874	0.645	0.648
P_1 (GeV/c)	0.007	0.256	0.277
P_2	0.207	1.025	4.651

$\times$ acceptance.

4.4.5 Pion Feed-down Correction

The yields of pions extensively contain contributions from resonance weak decay of particles like K_s^0 and Λ. Also, muons which has a similar order of mass as that of pions can be misidentified as pions. Hence, a correction factor estimating these weak decay contributions, muon contamination and background pions to the pion yield is needed [17, 22]. This is obtained from Monte-Carlo simulation, where the events generated from HIJING [29] passes through the STAR detector response using GEANT package [30]. The events are reconstructed in the same manner as that of the real data. In this case, we have the parent particle information prior in our hand. From the final reconstruction, the secondary pions, muons misidentified as pions can be easily calculated. The pion yields are subtracted from these background contribution in each p_T bin. Figure 4.11 shows the background contribution to the yield of pion as a function of p_T along with separate contribution coming from weak decay and muon contamination. The total
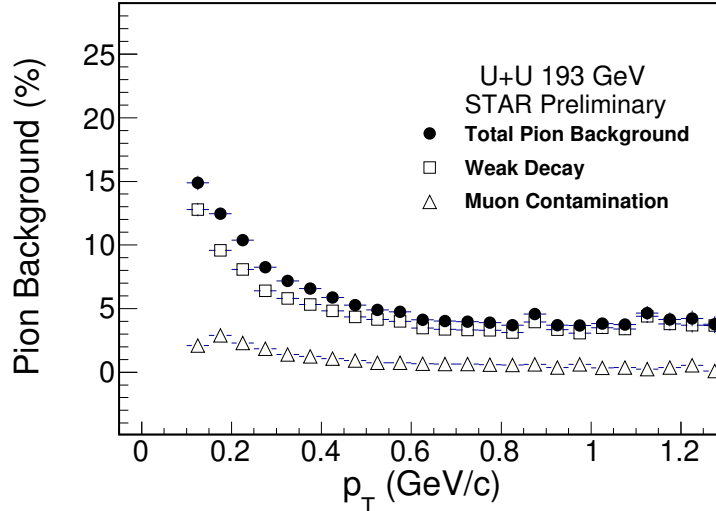
Figure 4.11: Total background fraction to the yield of pion as function of p_T showing individual contributions from weak decay and muon contamination in U+U collisions at $\sqrt{s_{NN}} = 193$ GeV. The errors are statistical only.

pion feed-down fraction shows only p_T dependence with no centrality dependence. Its value is maximum around 15% at $p_T = 0.2$ GeV/c and almost negligible above $p_T > 1.2$ GeV/c.

4.4.6 Proton Background Fraction

The estimation of background contribution to the yields of the proton has been already discussed in the previous chapter which are also reported in earlier STAR publications [17, 22]. This method is briefly presented here for U+U collisions at $\sqrt{s_{NN}} = 193$ GeV for completeness.

Highly energetic particles typically interact with the detector material producing secondary protons, which significantly gets added to the yields of the protons. However, as these secondary protons are produced far from the primary vertex, it appears as a long trail in the DCA distributions of the proton. On the other hand, the anti-particle of protons i.e., anti-protons, does not have this background associated with it. This idea is utilized in the estimation of proton background fraction through a mapping of DCA distribution of proton and anti-proton on real data [17, 22, 28, 31]. In this method, protons and anti-protons are selected within $|n\sigma_p| < 2$, where σ_p is the inverse of dE/dx resolution of protons in TPC. The typical plot illustrating this technique in U+U collisions at $\sqrt{s_{NN}} = 193$ GeV is shown in Fig. 4.12. The difference between the DCA distributions of protons and anti-protons estimates the proton background
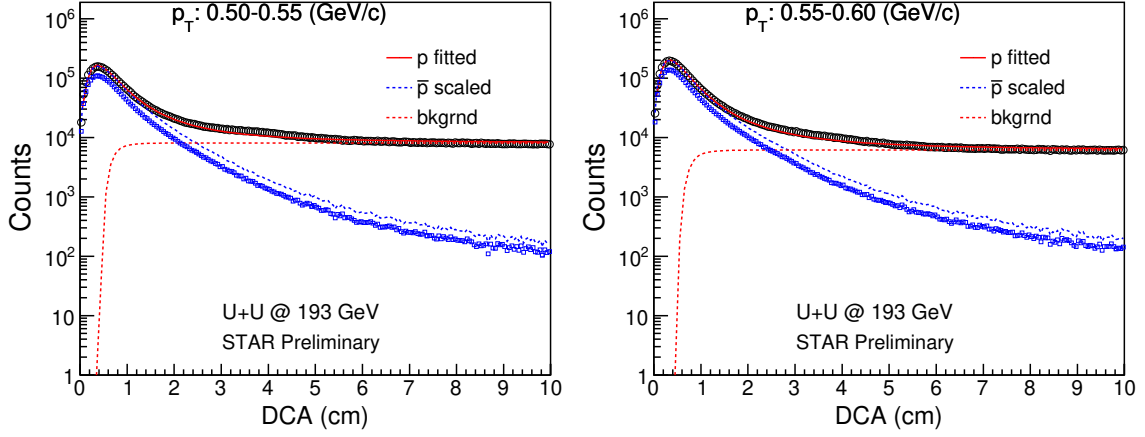
Figure 4.12: The DCA distributions of protons and anti-protons for $0.50 < p_T$ (GeV/c)< 0.55 and $0.55 < p_T$ (GeV/c)< 0.60 in $0-5\%$ centrality in U+U collisions at $\sqrt{s_{NN}} = 193$ GeV. The dashed curve is the fit to the proton background; the dotted histogram is the $\bar{p}$ DCA distribution scaled by $r_{\bar{p}/p}$; the solid histogram is the fit to the proton DCA distribution. The errors are statistical only.

fraction. This quantity is estimated in each centrality for each p_T bin. The proton background fraction is found to decrease with an increase in p_T as well as from peripheral to central collisions. This fraction within $|DCA| < 3$ is maximum at low p_T and becomes almost negligible for $p_T > 1.2$ GeV/c. The values of this proton background fraction in 0-5% centrality in U+U collisions at $\sqrt{s_{NN}} = 193$ GeV is listed in Table. 4.5.

Table 4.5: The proton background fraction as a function of p_T in 0-5% centrality for U+U collisions at $\sqrt{s_{NN}} = 193$ GeV.

p_T (GeV/c)	Proton Background (%)
0.50-0.55	7.2
0.55-0.60	4.4
0.60-0.65	3.6
0.65-0.70	3.1
0.70-0.75	2.6
0.75-0.80	2.1
0.80-0.85	1.6
0.85-0.90	1.3
0.90-0.95	0.9
0.95-1.00	0.7
1.00-1.05	0.6
1.05-1.10	0.3

4.5 Systematic Uncertainties

In this section, we will discuss about the various systematic sources of uncertainty associated with the extraction of the observables such as particle spectra, particle yields, average transverse momentum and kinetic freeze-out parameters.

The event and track selection cuts, the PID procedure, the methods of estimation of correction factors, errors associated with extrapolation with functional fits contribute to systematic uncertainties of the measurables. The errors associated with all these sources are calculated and are added in quadrature.

The systematic errors accompanied with the event and track cuts are estimated by varying one of the selected cut, while other cuts are kept at their default values. The set of event and track cuts which are varied are the following : V_z cut (from $V_z < 30$ cm to $V_z < 40$ cm), DCA cut (from 3 cm to 2 cm), the cut on number of fit points (from 25 to 20) and number of dE/dx points (from 15 to 10). In the identification of particle type, the fit range of the Gaussian function for dE/dx, bin counting and the n_σ cut used in calculation of predicted m^2 distribution is also varied (from $|n\sigma| < 2$ to $|n\sigma| < 1$).

The procedure of calculation of dN/dy and $\langle p_T \rangle$ involves the fitting of the spectra by the most suitable function to extrapolate the spectra to the unmeasured p_T region. As a result of which the main source of uncertainty on dN/dy and $\langle p_T \rangle$ comes from this extrapolation. In order to estimate the uncertainty associated with extrapolation different fit functions are used. The default fit functions used for pions, kaons and protons are respectively Bose-Einstein, m_T exponential and double exponential respectively [22]. For the systematic uncertainty estimation, the functions used are p_T exponential, Boltzmann and m_T exponential for pions, kaons and protons respectively. The functional form of all these functions are given as

- Bose-Einstein: $\propto 1/\exp(m_T/T_{\mathrm{BE}} - 1)$

- p_T-exponential: $\propto \exp(-p_T/T_{p_T})$

- m_T-exponential: $\propto \exp(-m_T/T_{m_T})$

- Boltzmann: $\propto m_T \exp(-m_T/T_B)$

- Double-exponential: $A\,e^{-p_T^2/T_1^2} + B\,e^{-p_T^2/T_2^2}$

Where m_T is the transverse mass of the particle under consideration, T_{BE} is the Bose-Einstein temperature, which is a fit parameter. T_{p_T} and T_{m_T} are also the temperatures obtained from fitting in the respective fit functions. A, B, T_1 and T_2 are all fit parameters.

Augment to this, a systematic error of 5% is added in quadrature to the systematic uncertainty of p_T spectra of particle in order to facilitate the systematic uncertainty coming from the estimation of detector efficiency and acceptance. The uncertainties associated with the calculation procedure of pion feed-down and proton background corrections are also estimated. However, the contribution from the former is negligible, but the later significantly affects the low p_T part of the proton spectra. The proton background fraction adds up about $6-7\%$ systematic uncertainty at low p_T of proton spectra. Different sources of systematic errors are tabulated in Table 4.6.

The uncertainty on mean transverse momentum $\langle p_T \rangle$ is effectively due to extrapolation. The fitting range and the fit functions are varied to obtain the systematic uncertainty accompanied with $\langle p_T \rangle$ for each particle type. The percentage of systematic uncertainties estimated on $\langle p_T \rangle$ for pions, kaons and protons are 9%, 10% and 10% respectively.

Table 4.6: Systematic uncertainties related to the yields of π, K and $p(\bar{p})$ in U+U collisions at $\sqrt{s_{NN}} = 193$ GeV.

	π	K	$p(\bar{p})$
V_z	1%	1%	1%
Track Cuts	4%	5%	7%
PID	5%	9%	8%
Extrapolation	9%	10%	10%
Corrections	5%	5%	5%
Proton Background	-	-	$6-7\%$
Total	12%	15%	16%

The systematic errors on the particle ratios are obtained from the systematic errors from particle yields, however the correlated errors due to tracking efficiency cancel out mostly in anti-particle to particle ratios and upto an extent in mixed particle ratios. The errors due to extrapolation also get canceled to a great extent while calculating the systematic errors on anti-particle to particle ratios.

As the kinetic freeze-out parameters are obtained from fitting simultaneously the pion, kaon and proton spectra, point-to-point systematic uncertainty on the particle spectra propagates to the calculation of kinetic freeze-out parameters. In addition to this, the systematic uncertainties are also evaluated by varying the fit range of the p_T spectra which are added in quadrature to the errors associated with the calculated kinetic freeze-out parameters.

4.6 Results and Discussions

This section presents the results obtained in the analysis of U+U collisions at $\sqrt{s_{NN}} = 193$ GeV. The measured transverse momentum spectra of $\pi^\pm$, $K^\pm$ and $p(\bar{p})$ are presented in the subsequent section. The centrality and energy dependence of the extracted observables such as average transverse momentum ($\langle p_T \rangle$), particle yields(dN/dy), particle ratios and kinetic freeze-out parameters are discussed. The comparison of the results obtained in U+U collisions at $\sqrt{s_{NN}} = 193$ GeV with the AMPT model modified to incorporate the deformation in Uranium nuclei [2] are also discussed subsequently.

4.6.1 Transverse Momentum Spectra

The final transverse momentum spectra of the particles represent the invariant yield as a function of transverse momentum (p_T) after properly applying all the correction factors as discussed above. This transverse momentum spectra contain all the historical foot prints and dynamics of the system produced in U+U collisions. So, primarily we will discuss about the transverse momentum spectra of $\pi^\pm$, $K^\pm$ and $p(\bar{p})$ in U+U collisions at $\sqrt{s_{NN}} = 193$ GeV.

The transverse momentum spectra in U+U collisions at $\sqrt{s_{NN}} = 193$ GeV for π^+, π^-, K^+, K^-, p and $\bar{p}$ within $|y| < 0.1$ is shown in Fig. 4.13. The spectra are presented in nine different centrality classes as $0-5\%, 5-10\%, 10-20\%, 20-30\%, 30-40\%, 40-50\%, 50-60\%, 60-70\%$ and $70-80\%$. The data points shown for $p_T = 0.4$-2.0 (GeV/c) for pions and kaons and 0.5-2.0 (GeV/c) for protons are obtained using both TPC and TOF. Data points measured using only TPC are shown for p_T range 0.2-0.8, 0.3-0.8 and 0.5-1.0 (GeV/c) for pions, kaons and protons respectively. The p_T range 0.4-0.8, 0.4-0.8 and 0.5-1.0 (GeV/c) for pions, kaons and
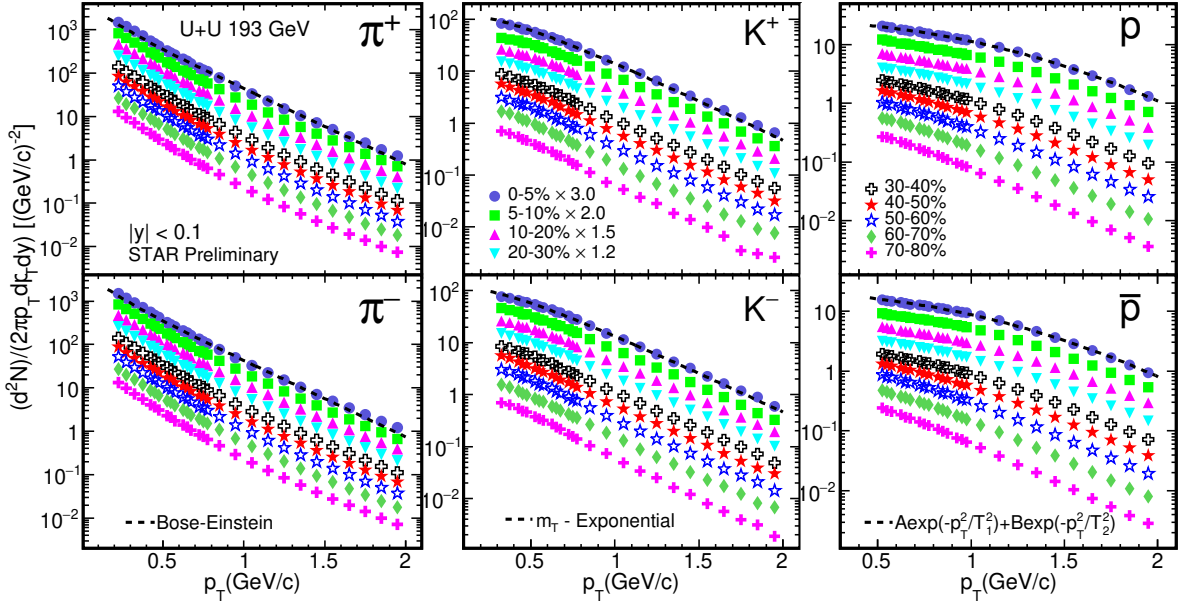
Figure 4.13: p_T spectra of $\pi^{\pm}$, $K^{\pm}$ and $p(\bar{p})$ measured at mid-rapidity ($|y| < 0.1$) in U+U collisions at $\sqrt{s_{NN}} = 193$ GeV in STAR. Spectra are plotted for nine different centrality classes and some of them are scaled for clarity. The p_T- spectra are fitted, with Bose-Einstein function for pions, m_T-exponential for kaons, and double exponential for (anti)protons are shown for 0-5% centrality classes in the figure. The uncertainties represent total systematic and statistical uncertainties added in quadrature and are mostly dominated by systematic errors with the statistical errors being very small.

protons respectively are the overlap region containing data points measured using only TPC and TPC along with TOF. A good agreement can be observed from the measurements of the two detectors in the overlapping p_T range. The curves represent fit to the spectra, which is shown only for 0-5% central collisions. The respective functions for pion, kaons and protons are Bose-Einstein, m_T exponential and double exponential. The particle yields (dN/dy) and average transverse momenta ($\langle p_T \rangle$) are extracted by using these p_T spectra. For the unmeasured p_T regions, these values are extracted by extrapolating the fit functions. The yields of particles decreases with increase in p_T as well as from central to peripheral collisions. As can be observed from Fig. 4.13, the shape of pion spectra appears to be almost identical in all centrality classes exhibiting a fast fall with an increase in p_T. This is a consequence of contribution from resonance decays specifically in the low p_T region. On the other hand, the slope of kaon and proton spectra shows a gradual flattening as one goes from peripheral to central collisions. This is an indication of stronger radial flow effects for heavier particles with increasing centrality. The inverse slope of the p_T spectra increases with increase in the mass of the particle in the

order $\pi < K < p$.

4.6.2 Average Transverse Momentum ($\langle p_T \rangle$)

The transverse dynamics of the spectra is reflected from the slope of the p_T spectra and is given by the observable $\langle p_T \rangle$. It is extracted by integrating the p_T spectra within the p_T range 0-10 GeV/c. The $\langle p_T \rangle$ of π^+, π^-, K^+, K^-, p and $\bar{p}$ plotted as a function of $\langle N_{\mathrm{part}} \rangle$ is presented
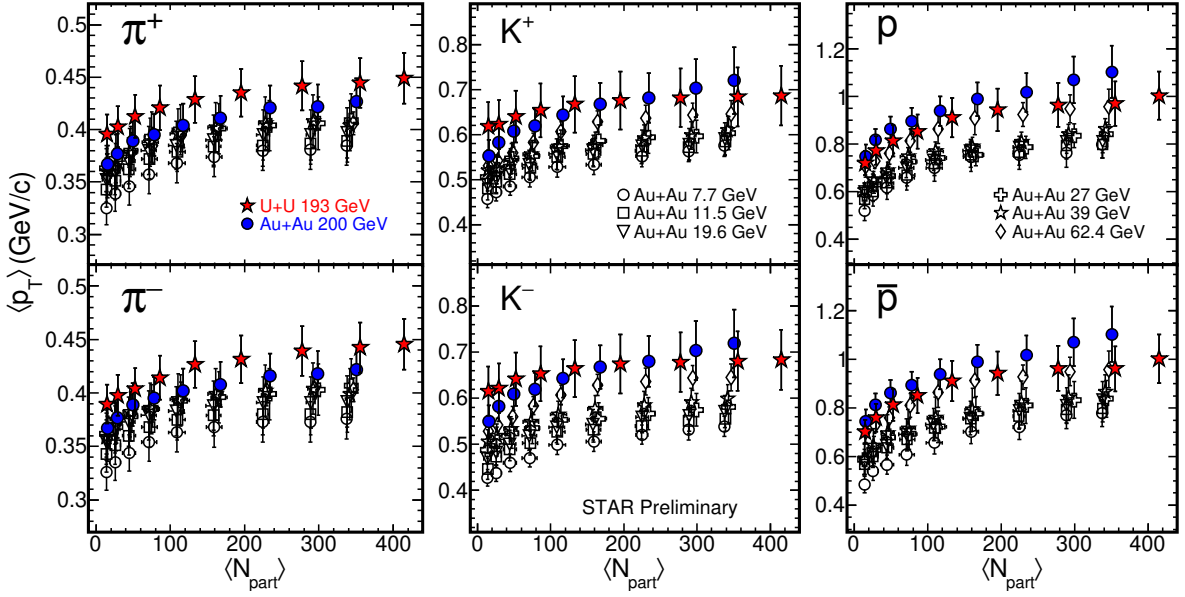
Figure 4.14: $\langle p_T \rangle$ of π^+, π^-, K^+, K^-, p and $\bar{p}$ as a function of $\langle N_{\mathrm{part}} \rangle$ for U+U collisions at $\sqrt{s_{NN}} = 193$ GeV. The results are compared with Au+Au collisions at $\sqrt{s_{NN}} = 200$ GeV [17] along with various beam energies from STAR [22, 28, 32–36]. The uncertainties represent total systematic and statistical uncertainties added in quadrature.

Table 4.7: $\langle p_T \rangle$ (GeV/c) values for π^+ and π^- from U+U collisions at $\sqrt{s_{NN}} = 193$ GeV within rapidity $|y| < 0.1$. The quoted errors are statistical and systematic uncertainties respectively.

Centrality(%)	$\langle p_T \rangle$ (GeV/c)	
	π^+	π^-
$0 - 5$	$0.4490 \pm 0.0001 \pm 0.0242$	$0.4456 \pm 0.0001 \pm 0.0238$
$5 - 10$	$0.4447 \pm 0.0001 \pm 0.0237$	$0.4425 \pm 0.0001 \pm 0.0235$
$10 - 20$	$0.4417 \pm 0.0002 \pm 0.0234$	$0.4391 \pm 0.0002 \pm 0.0231$
$20 - 30$	$0.4350 \pm 0.0002 \pm 0.0227$	$0.4316 \pm 0.0002 \pm 0.0224$
$30 - 40$	$0.4288 \pm 0.0002 \pm 0.0221$	$0.4267 \pm 0.0002 \pm 0.0219$
$40 - 50$	$0.4207 \pm 0.0003 \pm 0.0212$	$0.4143 \pm 0.0003 \pm 0.0206$
$50 - 60$	$0.4127 \pm 0.0003 \pm 0.0204$	$0.4037 \pm 0.0003 \pm 0.0196$
$60 - 70$	$0.4027 \pm 0.0004 \pm 0.0194$	$0.3978 \pm 0.0004 \pm 0.0189$
$70 - 80$	$0.3957 \pm 0.0005 \pm 0.0188$	$0.3895 \pm 0.0005 \pm 0.0182$

Table 4.8: $\langle p_T \rangle$ (GeV/c) values for K^+ and K^- from U+U collisions at $\sqrt{s_{NN}} = 193$ GeV within rapidity $|y| < 0.1$. The quoted errors are statistical and systematic uncertainties respectively.

Centrality(%)	$\langle p_T \rangle$ (GeV/c)	
	K^+	K^-
$0 - 5$	$0.6990 \pm 0.0001 \pm 0.0684$	$0.6971 \pm 0.0001 \pm 0.0680$
$5 - 10$	$0.6925 \pm 0.0002 \pm 0.0671$	$0.6872 \pm 0.0002 \pm 0.0661$
$10 - 20$	$0.6852 \pm 0.0002 \pm 0.0657$	$0.6854 \pm 0.0002 \pm 0.0658$
$20 - 30$	$0.6774 \pm 0.0003 \pm 0.0642$	$0.6753 \pm 0.0003 \pm 0.0638$
$30 - 40$	$0.6624 \pm 0.0003 \pm 0.0614$	$0.6555 \pm 0.0003 \pm 0.0602$
$40 - 50$	$0.6454 \pm 0.0004 \pm 0.0583$	$0.6381 \pm 0.0004 \pm 0.0570$
$50 - 60$	$0.6294 \pm 0.0005 \pm 0.0555$	$0.6226 \pm 0.0005 \pm 0.0543$
$60 - 70$	$0.6083 \pm 0.0006 \pm 0.0517$	$0.6108 \pm 0.0006 \pm 0.0522$
$70 - 80$	$0.5953 \pm 0.0007 \pm 0.0496$	$0.5801 \pm 0.0007 \pm 0.0471$

Table 4.9: $\langle p_T \rangle$ (GeV/c) values for p and $\bar{p}$ from U+U collisions at $\sqrt{s_{NN}} = 193$ GeV within rapidity $|y| < 0.1$. The quoted errors are statistical and systematic uncertainties respectively.

Centrality(%)	$\langle p_T \rangle$ (GeV/c)	
	p	$\bar{p}$
$0 - 5$	$1.0037 \pm 0.0002 \pm 0.1007$	$1.0025 \pm 0.0003 \pm 0.101$
$5 - 10$	$0.9694 \pm 0.0003 \pm 0.0940$	$0.9613 \pm 0.0003 \pm 0.0924$
$10 - 20$	$0.9641 \pm 0.0003 \pm 0.0930$	$0.9630 \pm 0.0004 \pm 0.0927$
$20 - 30$	$0.9440 \pm 0.0004 \pm 0.0891$	$0.9432 \pm 0.0004 \pm 0.0890$
$30 - 40$	$0.9118 \pm 0.0003 \pm 0.0831$	$0.9109 \pm 0.0005 \pm 0.0830$
$40 - 50$	$0.8522 \pm 0.0004 \pm 0.0726$	$0.8520 \pm 0.0006 \pm 0.0726$
$50 - 60$	$0.8136 \pm 0.0006 \pm 0.0662$	$0.8127 \pm 0.0007 \pm 0.0661$
$60 - 70$	$0.7725 \pm 0.0007 \pm 0.0597$	$0.7597 \pm 0.0009 \pm 0.0577$
$70 - 80$	$0.7207 \pm 0.0008 \pm 0.0519$	$0.7018 \pm 0.0010 \pm 0.0493$

in Fig. 4.14 for U+U collisions at $\sqrt{s_{NN}} = 193$ GeV. A comparison with the published results in Au+Au collisions at $\sqrt{s_{NN}} = 200$ GeV [17] along with $\langle p_T \rangle$ values for various other beam energies from STAR [22, 28, 32–36] is also presented. The Fig. 4.14 infers that $\langle p_T \rangle$ increases gradually from peripheral to central collisions as well as from pions to kaons and kaons to protons in U+U collisions at $\sqrt{s_{NN}} = 193$ GeV. Results from U+U collisions at $\sqrt{s_{NN}} = 193$ GeV respects the usual energy trend as $\langle p_T \rangle$ increases from peripheral to central collisions. It can be inferred from Fig. 4.14 that, irrespective of the different geometrical shapes of the colliding Uranium and Gold nucleus, $\langle p_T \rangle$ values are comparable for similar values of $\langle N_{\text{part}} \rangle$

within systematic uncertainty for both the cases. Through U+U collisions we have made the $\langle p_T \rangle$ measurements to the highest $\langle N_{\text{part}} \rangle$ values at RHIC. The $\langle p_T \rangle$ values or $\pi^\pm$, $K^\pm$ and $p\bar{p}$ are tabulated in Tables 4.7, 4.8 and 4.9 respectively for U+U collisions at $\sqrt{s_{NN}} = 193$ GeV.

4.6.3   Particle Yields (dN/dy)

The total yield of a particle in a given centrality is obtained by integrating the spectra over the full p_T range.   It is represented by the observable dN/dy within rapidity $|y| < 0.1$ as
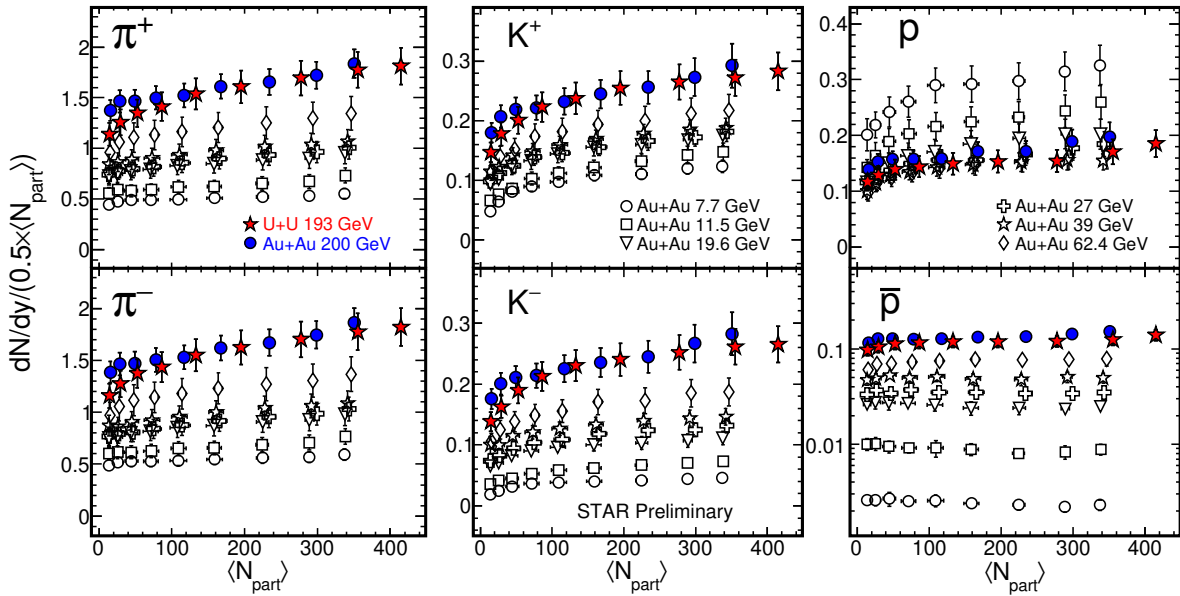
Figure 4.15: dN/dy of π^+, π^-, K^+, K^-, p and $\bar{p}$ scaled by $0.5 \times \langle N_{\text{part}} \rangle$ as a function of $\langle N_{\text{part}} \rangle$ for U+U collisions at $\sqrt{s_{NN}} = 193$ GeV. The results are compared with Au+Au collisions at $\sqrt{s_{NN}} = 200$ GeV [17] along with the dN/dy values various other beam energies from STAR [22, 28, 32–36]. The uncertainties represent total systematic and statistical uncertainties added in quadrature.

mentioned in the previous chapter. The normalized dN/dy with $0.5 \times \langle N_{\text{part}} \rangle$ of π^+, K^+, p and $\bar{p}$ measured in U+U collisions at $\sqrt{s_{NN}} = 193$ GeV as a function of $\langle N_{\text{part}} \rangle$ is depicted in Fig. 4.15. The presented results are compared with the published results of Au+Au collisions at $\sqrt{s_{NN}} = 200$ GeV [17] along with various beam energies from STAR [22, 28, 32–36]. The values of dN/dy for $\pi^\pm$, $K^\pm$ and $p\bar{p}$ are listed in Tables 4.10, 4.11 and 4.12 respectively for U+U collisions at $\sqrt{s_{NN}} = 193$ GeV.

At first observation, it can be noticed that the current measurements extends the observables to a higher value of $N_{\text{part}} > 400$. From Fig. 4.15 it can be noticed that, the values of dN/dy

Table 4.10: dN/dy values for π^+ and π^- from U+U collisions at $\sqrt{s_{NN}} = 193$ GeV within rapidity $|y| < 0.1$. The quoted errors are statistical and systematic uncertainties respectively.

Centrality(%)	dN/dy	
	π^+	π^-
$0-5$	$375.9 \pm 0.06 \pm 37.59$	$377.9 \pm 0.06 \pm 37.79$
$5-10$	$315.4 \pm 0.05 \pm 31.55$	$316.0 \pm 0.05 \pm 31.61$
$10-20$	$235.1 \pm 0.04 \pm 23.51$	$236.4 \pm 0.04 \pm 23.65$
$20-30$	$157.1 \pm 0.04 \pm 15.72$	$158.9 \pm 0.04 \pm 15.89$
$30-40$	$102.4 \pm 0.03 \pm 10.24$	$103.3 \pm 0.03 \pm 10.332$
$40-50$	$60.86 \pm 0.03 \pm 6.09$	$61.91 \pm 0.03 \pm 6.19$
$50-60$	$35.47 \pm 0.03 \pm 3.55$	$36.62 \pm 0.03 \pm 3.62$
$60-70$	$18.47 \pm 0.02 \pm 1.85$	$18.72 \pm 0.02 \pm 1.87$
$70-80$	$8.35 \pm 0.01 \pm 0.84$	$8.51 \pm 0.01 \pm 0.86$

Table 4.11: dN/dy values for K^+ and K^- from U+U collisions at $\sqrt{s_{NN}} = 193$ GeV within rapidity $|y| < 0.1$. The quoted errors are statistical and systematic uncertainties respectively.

Centrality(%)	dN/dy	
	K^+	K^-
$0-5$	$58.30 \pm 0.05 \pm 6.52$	$54.68 \pm 0.05 \pm 6.11$
$5-10$	$47.96 \pm 0.04 \pm 5.36$	$46.51 \pm 0.04 \pm 5.20$
$10-20$	$36.24 \pm 0.04 \pm 4.05$	$34.85 \pm 0.04 \pm 3.89$
$20-30$	$24.90 \pm 0.03 \pm 2.78$	$23.42 \pm 0.03 \pm 2.62$
$30-40$	$15.75 \pm 0.03 \pm 1.76$	$15.23 \pm 0.03 \pm 1.70$
$40-50$	$9.59 \pm 0.02 \pm 1.07$	$9.15 \pm 0.02 \pm 1.02$
$50-60$	$5.28 \pm 0.02 \pm 0.59$	$4.99 \pm 0.02 \pm 0.56$
$60-70$	$2.59 \pm 0.01 \pm 0.29$	$2.38 \pm 0.01 \pm 0.27$
$70-80$	$1.07 \pm 0.01 \pm 0.12$	$1.03 \pm 0.01 \pm 0.11$

of π^+, π^-, K^+, K^- and p increase with the number of participant pairs in U+U collisions at $\sqrt{s_{NN}} = 193$ GeV. This signifies particle production mechanism involves both soft and hard processes attributed to nucleon-nucleon binary collisions. However, this behavior is a little less in case of anti-protons. The values of dN/dy are consistent in both U+U collisions at $\sqrt{s_{NN}} = 193$ GeV and Au+Au collisions at $\sqrt{s_{NN}} = 200$ GeV within the similar range of $\langle N_{\text{part}} \rangle$ within the systematic uncertainties.

Table 4.12: dN/dy values for p and $\bar{p}$ from U+U collisions at $\sqrt{s_{NN}} = 193$ GeV within rapidity $|y| < 0.1$. The quoted errors are statistical and systematic uncertainties respectively.

Centrality(%)	dN/dy	
	p	$\bar{p}$
$0-5$	$38.49 \pm 0.07 \pm 5.00$	$29.18 \pm 0.09 \pm 3.79$
$5-10$	$30.37 \pm 0.06 \pm 3.95$	$22.25 \pm 0.07 \pm 2.89$
$10-20$	$21.40 \pm 0.04 \pm 2.78$	$16.69 \pm 0.05 \pm 2.17$
$20-30$	$14.98 \pm 0.03 \pm 1.95$	$11.65 \pm 0.04 \pm 1.51$
$30-40$	$9.94 \pm 0.03 \pm 1.29$	$7.92 \pm 0.03 \pm 1.03$
$40-50$	$6.21 \pm 0.02 \pm 0.81$	$5.00 \pm 0.02 \pm 0.65$
$50-60$	$3.65 \pm 0.02 \pm 0.47$	$2.97 \pm 0.02 \pm 0.39$
$60-70$	$1.89 \pm 0.01 \pm 0.25$	$1.54 \pm 0.01 \pm 0.20$
$70-80$	$0.856 \pm 0.008 \pm 0.111$	$0.717 \pm 0.009 \pm 0.093$

4.6.4 Particle Ratios

Particle ratios are found to be an excellent observable in investigating the particle production

mechanism as well as the evolution of the system in high-energy heavy-ion collisions. In
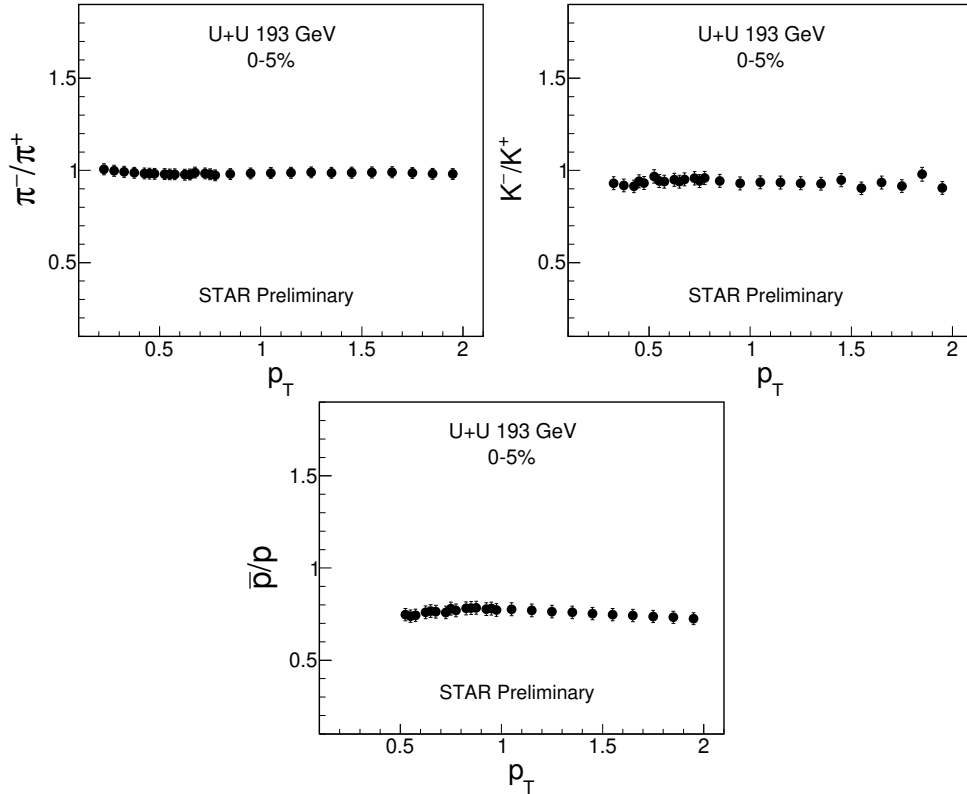
Figure 4.16: π^-/π^+, K^-/K^+ and $\bar{p}/p$ ratios as function of p_T in 0-5% centrality class in U+U collisions at $\sqrt{s_{NN}} = 193$ GeV measured by the STAR detector at RHIC.

the context of this chapter, we will discuss about the p_T, centrality and energy dependence of various particle ratios such as π^-/π^+, K^-/K^+, $\bar{p}/p$, K^+/π^+, K^-/π^-, p/π^+ and $\bar{p}/\pi^-$ in U+U collisions at $\sqrt{s_{NN}} = 193$ GeV. The results are compared with the earlier publications from STAR [17, 22, 28, 32–36].

4.6.4.1 p_T Dependence of Particle Ratios

Figure 4.16 shows the π^-/π^+, K^-/K^+ and $\bar{p}/p$ ratios as a function of p_T in U+U collisions at $\sqrt{s_{NN}} = 193$ GeV for 0-5% centrality classes. The anti-particle to particle ratios remains almost flat as a function of p_T. This indicates that particles and anti-particles freeze-out at the same time and moves with similar radial flow.

4.6.4.2 Integrated Particle Ratios

Different integrated particle ratios are constructed from the ratio of particle yields (dN/dy) in nine centrality classes in U+U collisions at $\sqrt{s_{NN}} = 193$ GeV. The different integrated particle ratios measured in U+U collisions at $\sqrt{s_{NN}} = 193$ GeV along with a comparative study with the published results from Au+Au collisions at various energies [17,22,28,32–36] are discussed below.

Ratios constructed from similar flavors of particles like π^-/π^+, K^-/K^+ and $\bar{p}/p$ as a function of $\langle N_{\text{part}} \rangle$ in U+U collisions at $\sqrt{s_{NN}} = 193$ GeV is shown in Fig. 4.17. These ratios
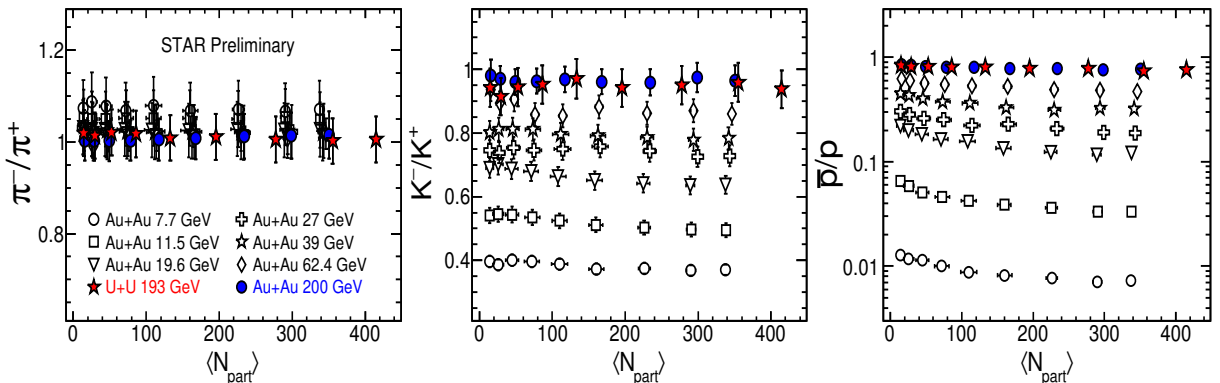
Figure 4.17: π^-/π^+, K^-/K^+ and $\bar{p}/p$ ratios as a function of $\langle N_{\text{part}} \rangle$ in U+U collisions at $\sqrt{s_{NN}} = 193$ GeV. The results are compared with Au+Au collisions at $\sqrt{s_{NN}} = 200$ GeV [17] along with corresponding values for various other beam energies from STAR [22, 28, 32–36]. The uncertainties represent total systematic and statistical uncertainties added in quadrature.
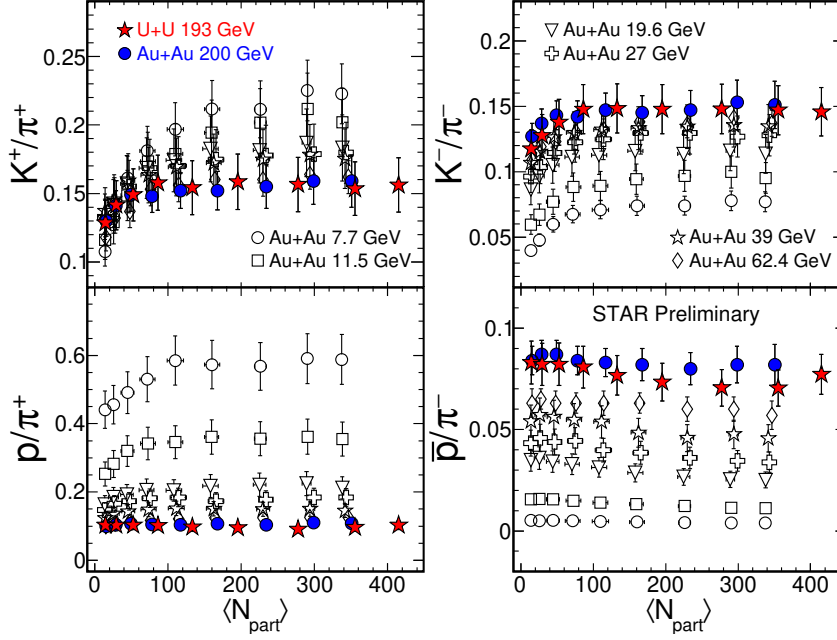
Figure 4.18: K^+/π^+, K^-/π^-, p/π^+ and $\bar{p}/\pi^-$ ratios as a function of $\langle N_{\text{part}} \rangle$ in U+U collisions at $\sqrt{s_{NN}} = 193$ GeV. The results are compared with Au+Au collisions at $\sqrt{s_{NN}} = 200$ GeV [17] along with the corresponding values for various other beam energies from STAR [22, 28, 32–36]. The uncertainties represent total systematic and statistical uncertainties added in quadrature.

are compared with the published results of Au+Au collisions at $\sqrt{s_{NN}} = 200$ GeV [17] along with various beam energies from STAR [22, 28, 32–36]. The π^-/π^+ ratio stays almost flat at unity with $\langle N_{\text{part}} \rangle$ for U+U collisions at $\sqrt{s_{NN}} = 193$ GeV. This is an indication that the particle production mechanism for π^+ and π^- does not change significantly from central to peripheral collisions. However, at lower energies, this ratio is slightly above one, which is due to isospin and significant decay contribution from heavier resonances like Δ to the pion yields. The behavior of K^-/K^+ ratio with centrality is also almost flat suggesting that K^+ and K^- are produced through the pair production process. In terms of energy dependence, this ratio increases with increasing energy. This is because, at lower energy particle production is mainly due to associated production giving more K^+, but with increase in collision energy particle production due to pair production becomes more dominant producing the similar number of K^+ and K^-. There is a slight increase of $\bar{p}/p$ ratio from central to peripheral collision. As a reflective of baryon stopping, this ratio also increases with an increase in collision centrality. These ratios within systematic uncertainty agrees with the published results in Au+Au collisions at $\sqrt{s_{NN}} = 200$ GeV [17].

183

Various mixed particle ratios like K^+/π^+, K^-/π^-, p/π^+ and $\bar{p}/\pi^-$ as a function of $\langle N_{\text{part}} \rangle$ in U+U collisions at $\sqrt{s_{NN}} = 193$ GeV is presented in Fig. 4.18. Earlier published results from STAR in Au+Au collisions at $\sqrt{s_{NN}} = 200$ GeV [17] along with various beam energies [17, 22, 28, 32–36] are also shown in comparison. The K^+/π^+ and K^-/π^- ratios gradually increase from peripheral to mid-central collisions and saturate then after from mid-central to central collisions behaving independent of $\langle N_{\text{part}} \rangle$. It could be due to strangeness equilibrium described in various thermodynamical models [37, 38] as well as an impulse of baryon stopping at mid-rapidity [39–41]. K^+/π^+ decreases whereas K^-/π^- increases with an increase in collision energy. This is a direct consequence of the different particle production mechanisms associated with lower and higher energies as described earlier in explaining the K^-/K^+ ratio. The p/π^+ ratio as well as $\bar{p}/\pi^-$ remains almost independent of collision centrality in U+U collisions at $\sqrt{s_{NN}} = 193$ GeV. The decrease of p/π^+ ratio and increase of $\bar{p}/\pi^-$ ratio with an increase in collision energy as seen from Fig. 4.18, is due to baryon stopping in low energies. The behavior of all these unlike particle ratios in U+U collisions at $\sqrt{s_{NN}} = 193$ GeV is similar within uncertainty to Au+Au collisions at $\sqrt{s_{NN}} = 200$ GeV [17].

4.6.5 Kinetic Freeze-out

The evolution of the system with time in high-energy heavy-ion collisions takes the system through different stages. These stages are the QGP phase, phase transition/cross-over, hadron gas, chemical freeze-out and kinetic freeze-out. The stage at which the particles decouple from the system, i.e. the particles neither interact with the medium nor among themselves either inelastically or elastically is termed as the "kinetic freeze-out" stage. After this stage, the particle's momenta get fixed and they free flow towards the detector. This stage is characterized by the kinetic freeze-out temperature T_k and radial flow velocity β.

The kinetic freeze-out parameters are usually calculated from the hydrodynamics based Blast-Wave model [42]. This model assumes that at each point of time a locally thermalized system with temperature T_k and moving with a common radial velocity β. The transverse
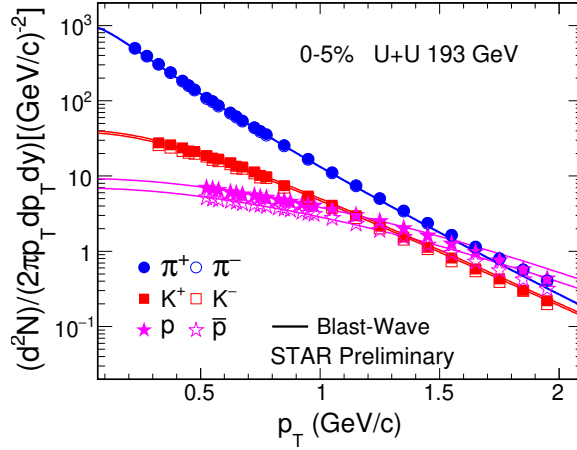
Figure 4.19: Simultaneous Blast-wave fit to the $\pi^{\pm}$, $K^{\pm}$, $p(\bar{p})$ p_T spectra in U+U collisions at $\sqrt{s_{NN}} = 193$ GeV in $0 - 5\%$ centrality class within $|y| < 0.1$. The uncertainties represent total systematic and statistical uncertainties added in quadrature.

distribution of particles for such a radially boosted hard sphere can be written as

$$\frac{dN}{p_T dp_T} \propto \int_0^R r dr \, m_T I_0 \left(\frac{p_T \sinh \rho(r)}{T_k} \right)$$
$$\times K_1 \left(\frac{m_T \cosh \rho(r)}{T_k} \right), \tag{4.6}$$

where $m_T = \sqrt{p_T^2 + m^2}$, m being the mass of the hadron; $\rho(r) = \tanh^{-1} \beta$; I_0 and K_1 are the modified Bessel functions. We use the radial flow velocity profile of the form

$$\beta = \beta_s (r/R)^n, \tag{4.7}$$

where β_s is the surface velocity and r/R is the relative radial position in the thermal source with n being the exponent of the flow velocity profile. Average radial flow velocity $\langle \beta \rangle$ can be calculated as : $\langle \beta \rangle = \frac{2}{2+n} \beta_s$.

Kinetic freeze-out parameters are extracted through a simultaneous Blast-wave fit to the $\pi^{\pm}$, $K^{\pm}$ and $p(\bar{p})$ spectra [22, 28, 42] as depicted in Fig. 4.19 for U+U collisions at $\sqrt{s_{NN}} = 193$ GeV. The low p_T part of the pion spectra is mostly affected by resonance decays, due to this, the pion spectra is fitted above $p_T > 0.5$ GeV/c. Also, the Blast-wave model do not suitably fit the high p_T part of the spectra [43]. Owing to this, Blast-wave model is very sensitive to the p_T range of the spectra [44]. The Blast-wave parameters are extracted in U+U collisions at $\sqrt{s_{NN}} = 193$ GeV with similar p_T range as that of Au+Au collisions at $\sqrt{s_{NN}} = 200$ GeV [17].

185
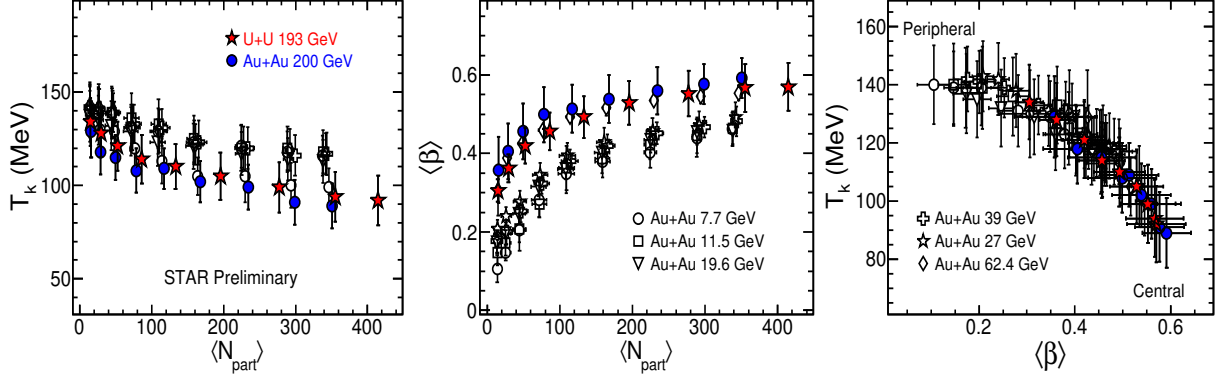
Figure 4.20: Left panel: T_k as a function of $\langle N_{\text{part}} \rangle$, Middle panel: $\langle \beta \rangle$ as a function of $\langle N_{\text{part}} \rangle$, Right panel: variation of T_k with $\langle \beta \rangle$ in U+U collisions at $\sqrt{s_{NN}} = 193$ GeV. All the results are compared with Au+Au collisions at $\sqrt{s_{NN}} = 200$ GeV [17] along with lower beam energies from STAR [22, 28, 32–36]. The uncertainties represent total systematic and statistical uncertainties added in quadrature.

The kinetic freeze-out parameters T_k (left), $\langle \beta \rangle$ (middle) as a function of $\langle N_{\text{part}} \rangle$ and T_k versus $\langle \beta \rangle$ (right) in U+U collisions at $\sqrt{s_{NN}} = 193$ GeV is shown in Fig. 4.20. The results are compared with Au+Au collisions at $\sqrt{s_{NN}} = 200$ GeV [17] along with various beam energies from STAR [22, 28, 32–36]. T_k decreases slowly with $\langle N_{\text{part}} \rangle$ supporting the prediction of a short-lived fireball in the case of peripheral collisions [45]. Whereas $\langle \beta \rangle$ increases with $\langle N_{\text{part}} \rangle$ in U+U collisions at $\sqrt{s_{NN}} = 193$ GeV. This suggests a higher rate of expansion in central collisions. The right most plot of Fig. 4.20 shows the correlation between T_k and $\langle \beta \rangle$. From this, we can observe that in U+U collisions at $\sqrt{s_{NN}} = 193$ GeV, an increase in T_k refers to a

Table 4.13: Kinetic freeze-out parameters in U+U collisions at $\sqrt{s_{NN}} = 193$ GeV. Quoted errors are the errors on the parameters obtained from Blast-wave fitting which are quadrature sum of statistical and systematic errors.

Centrality	T_k (MeV)	$\langle \beta \rangle c$	n	χ^2/ndf
$0 - 5\%$	92 ± 12	0.570 ± 0.041	0.970 ± 0.074	0.097
$5 - 10\%$	$94 \pm {}'12$	0.567 ± 0.040	0.947 ± 0.152	0.043
$10 - 20\%$	99 ± 12	0.553 ± 0.037	0.987 ± 0.153	0.042
$20 - 30\%$	105 ± 11	0.529 ± 0.037	1.035 ± 0.183	0.049
$30 - 40\%$	110 ± 10	0.493 ± 0.036	1.180 ± 0.210	0.054
$40 - 50\%$	114 ± 11	0.457 ± 0.031	1.449 ± 0.229	0.052
$50 - 60\%$	121 ± 11	0.420 ± 0.030	1.564 ± 0.272	0.061
$60 - 70\%$	128 ± 10	0.362 ± 0.021	2.292 ± 0.269	0.062
$70 - 80\%$	134 ± 10	0.305 ± 0.015	3.158 ± 0.554	0.102

decrease in $\langle \beta \rangle$ and vice-versa. The values of kinetic freeze-out parameters in U+U collisions at $\sqrt{s_{NN}} = 193$ GeV are consistent within errors with the published results in Au+Au collisions at $\sqrt{s_{NN}} = 200$ GeV [17]. The results in U+U collisions at $\sqrt{s_{NN}} = 193$ GeV favor the general energy trend as that of other energies in STAR [17, 22, 28, 32–36]. The extracted kinetic freeze-out parameters in U+U collisions at $\sqrt{s_{NN}} = 193$ GeV are listed in Table 4.13.

4.6.6 Comparison with AMPT Model

A detailed comparison of the results obtained in U+U collisions at $\sqrt{s_{NN}} = 193$ GeV from the STAR data is presented here with the corresponding AMPT model [18] results.

In AMPT model, the initial particle distribution is generated by the Heavy Jet Ion Interaction (HIGING) model [29]. In the string melting version of the AMPT model used here, all hadrons are produced by string fragmentation in the HIGING model. It incorporates both partonic and hadronic interactions. To incorporate the deformation of Uranium nuclei the AMPT model is modified, which can be found in [2] and briefly discussed as follows. The nucleon density distribution is parameterized as a deformed Woods-Saxon profile [46]

$$
\begin{aligned}
\rho &= \frac{\rho_0}{1 + \exp([r - R']/d)} & (4.8) \\
R' &= R\left[1 + \beta_2 Y_2^0(\theta) + \beta_4 Y_4^0(\theta)\right] & (4.9)
\end{aligned}
$$

where ρ_0 is the normal nuclear density, R is the radius of the nucleus, $Y_l^m(\theta)$ denotes the spherical harmonics, θ is the polar angle and d is the surface diffuseness parameter. For Uranium nucleus $R = 6.81$ fm, $d = 0.55$ fm and the surface deformation parameters $\beta_2 = 0.28$ and $\beta_4 = 0.093$ are taken. The presence of β_4 modifies the shape of the Uranium nucleus compared to only with β_2. We have used two sets of AMPT data with two different partonic cross-section for which the two initial parameter settings are taken from the cited reference paper [18] and is given in Table 4.14.

In the Table 4.14, a and b are the parameters in the Lund string fragmentation function [47] : $f(z) \propto z^{-1}(1 - z)^1 \exp(-bm_\perp^2/z)$, where z is the light-cone momentum of the produced hadron of transverse mass $m_\perp$ with respect to that of fragmenting string. The parton scattering

Table 4.14: Values of parameters in Lund string fragmentation and parton scattering cross-section for the two sets of AMPT data used here.

Cross-section (σ)	a	b (GeV^{-2})	α_s	μ (fm^{-1})
1.5 mb	0.5	0.9	0.33	3.2
10 mb	2.2	0.5	0.47	1.8

cross-section $\sigma \approx 9\pi\alpha_s^2/(2\mu^2)$, where α_s is the QCD coupling constant and μ is the screening mass of a gluon in QGP.

So, depending on the parton scattering cross-section and initial parameter values, we have
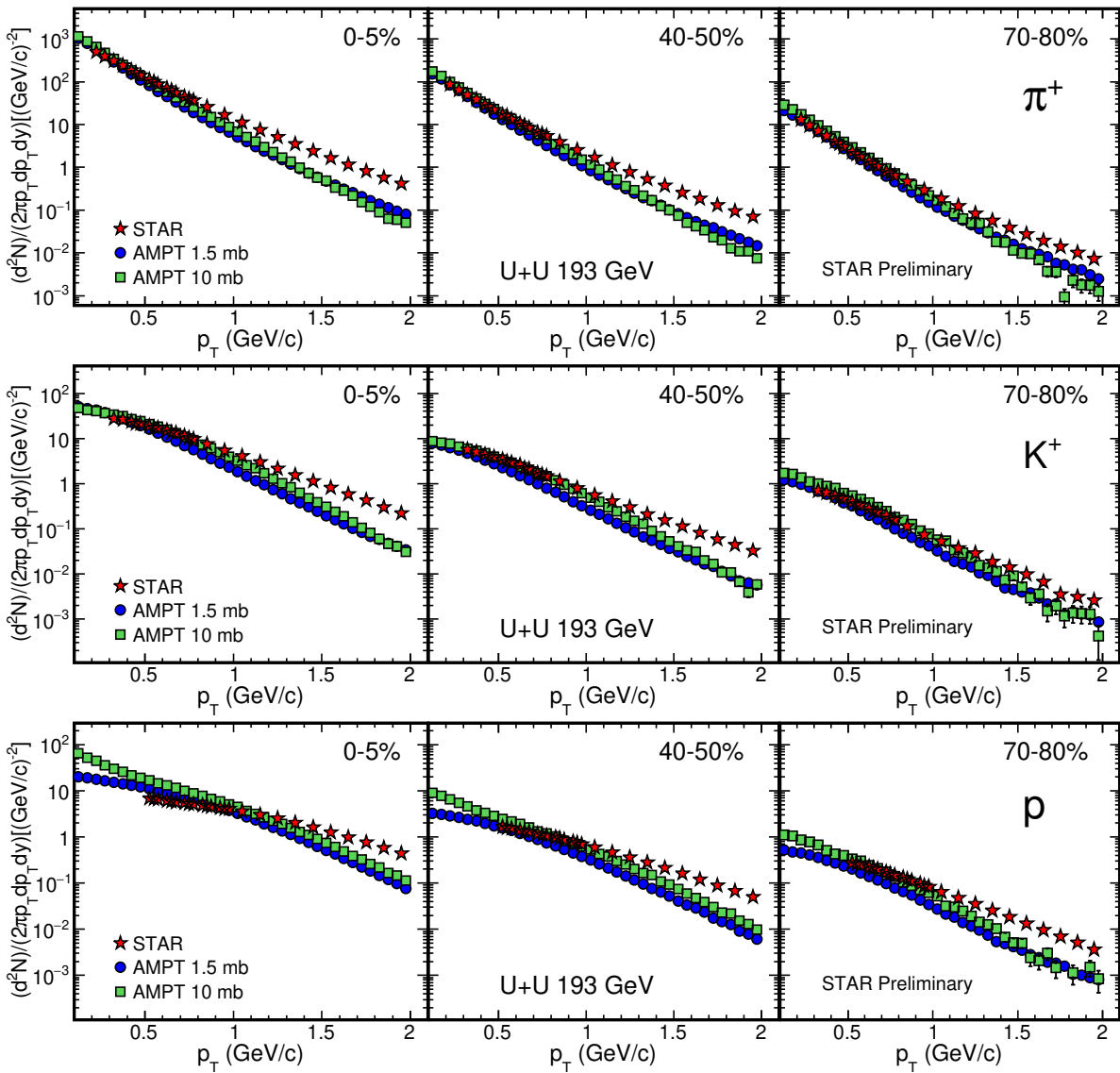
Figure 4.21: p_T spectra comparison of π^+, K^+ and p for the two sets of AMPT data and compared with STAR results in U+U collisions at $\sqrt{s_{NN}} = 193$ GeV in three different collision centralities.

two sets: AMPT 1.5 mb and AMPT 10 mb . The statistics analyzed here in AMPT 1.5 mb set is ~ 6 M and AMPT 10 mb set is ~ 0.4 M.

4.6.6.1 Transverse Momentum Spectra

Figure 4.21 shows the transverse momentum spectra of π^+, K^+ and p in U+U collisions at $\sqrt{s_{NN}} = 193$ GeV obtained from STAR data and compared with the AMPT data for two different cases in three different collision centralities. The transverse momentum spectra in Au+Au collision at $\sqrt{s_{NN}} = 200$ GeV [17] is also shown in comparison. The p_T spectra comparison of the corresponding anti-particles π^-, K^- and $\bar{p}$ are identical in shape to this. From the Figure, we can observe that the spectral shape obtained from AMPT model in both the two sets deviates from STAR results at high p_T and remains below. The results from AMPT 1.5 mb and 10 mb sets are almost similar to each other and do not change much except for protons at low p_T.

4.6.6.2 Average Transverse Momentum

Mean p_T of π^+, K^+ and p as a function of $\langle N_{\text{part}} \rangle$ for two sets of AMPT data are compared with STAR results in U+U collisions at $\sqrt{s_{NN}} = 193$ GeV is shown in Fig. 4.22. The figure shows that the value of $< p_T >$ is lower than the STAR results in both the sets of AMPT data in U+U collisions at $\sqrt{s_{NN}} = 193$ GeV. The results for 10 mb case are relatively closure to data than for 1.5 mb.
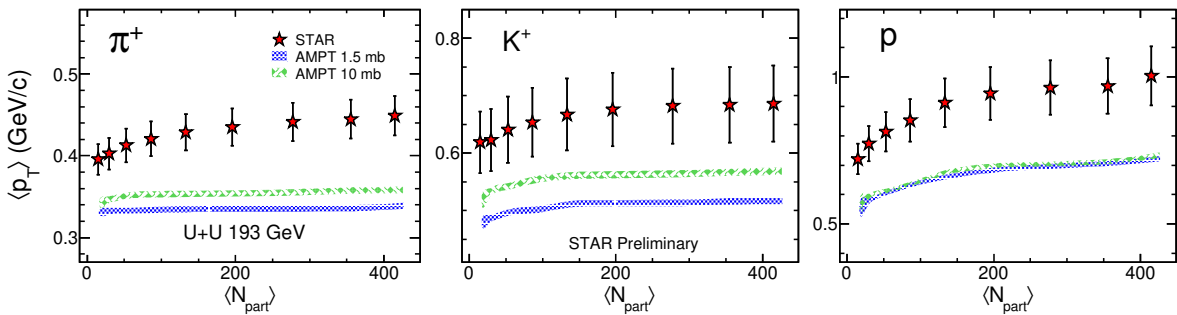
Figure 4.22: $\langle p_T \rangle$ of π^+, K^+ and p as a function of $\langle N_{\text{part}} \rangle$ obtained for two sets of AMPT data (AMPT 1.5 mb and AMPT 10 mb) in comparison with the STAR results obtained in U+U collisions at $\sqrt{s_{NN}} = 193$ GeV. The width of the bands corresponds to the statistical uncertainty associated with the calculation in AMPT model.

4.6.6.3 Particle Yields

The comparison of dN/dy scaled by $(0.5 \times \langle N_{\text{part}} \rangle)$ as a function of $\langle N_{\text{part}} \rangle$ for the two sets of AMPT data and STAR results in U+U collisions at $\sqrt{s_{NN}} = 193$ GeV are shown in Fig. 4.23. For pion and Kaon AMPT 10 mb shows better agreement that AMPT 1.5 mb. But for protons in peripheral collisions, AMPT 10 mb agrees in peripheral collisions whereas in central collisions the agreement of AMPT 1.5 mb is better. On the other hand, in the case of Au+Au collisions at $\sqrt{s_{NN}} = 200$ GeV, the calculations from AMPT 1.5 mb data shows good agreement than AMPT 10 mb data in explaining the charged particle multiplicity density in mid-pseudorapidity as in refs. [48].
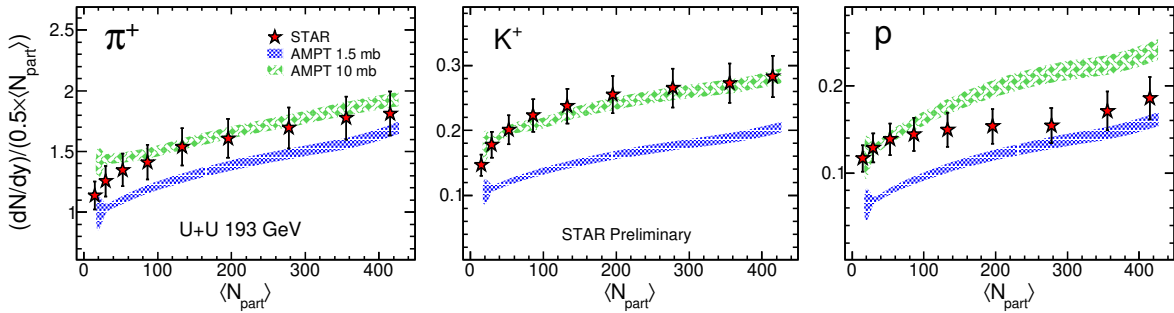
Figure 4.23: dN/dy of π^+, K^+ and p scaled by $(0.5 \times \langle N_{\text{part}} \rangle)$ as a function of $\langle N_{\text{part}} \rangle$ obtained for two sets of AMPT data (AMPT 1.5 mb and AMPT 10 mb) in comparison with the STAR results obtained in U+U collisions at $\sqrt{s_{NN}} = 193$ GeV. The width of the bands corresponds to the statistical uncertainty associated with the calculation in AMPT model.

4.6.6.4 Particle Ratios

A comparison of various anti-particle to particle ratios such as π^-/π^+, K^-/K^+ and $\bar{p}/p$ as a function of $\langle N_{\text{part}} \rangle$ obtained for two sets of AMPT data (AMPT 1.5 mb and AMPT 10 mb) in U+U collisions at $\sqrt{s_{NN}} = 193$ GeV is shown in Fig. 4.24. The results are compared with the results obtained in this analysis from STAR data. It is observed that these ratios have similar values in both the sets of AMPT data and agree with STAR data in U+U collisions at $\sqrt{s_{NN}} = 193$ GeV across all centrality classes.

Different unlike flavor particle ratios such as K^+/π^+, K^-/π^-, p/π^+ and $\bar{p}/\pi^-$ as a function of $\langle N_{\text{part}} \rangle$ obtained for two sets of AMPT data (AMPT 1.5 mb and AMPT 10 mb) in comparison with the STAR results obtained in U+U collisions at $\sqrt{s_{NN}} = 193$ GeV are presented in
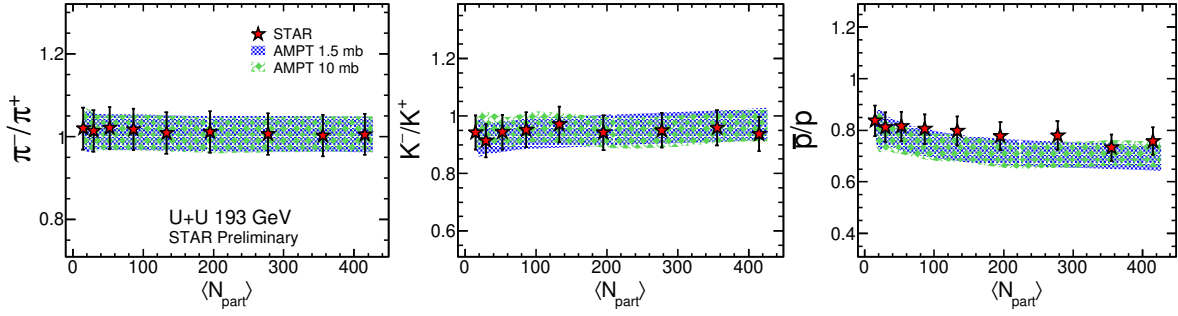
Figure 4.24: π^-/π^+, K^-/K^+ and $\bar{p}/p$ ratios as a function of $\langle N_{\text{part}} \rangle$ obtained for two sets of AMPT data (AMPT 1.5 mb and AMPT 10 mb) in comparison with the STAR results obtained in U+U collisions at $\sqrt{s_{NN}} = 193$ GeV. The width of the bands corresponds to the statistical uncertainty associated with the calculation in AMPT model.

Figure 4.25: K^+/π^+, K^-/π^-, p/π^+ and $\bar{p}/\pi^-$ ratios as a function of $\langle N_{\text{part}} \rangle$ obtained for two sets of AMPT data (AMPT 1.5 mb and AMPT 10 mb) in comparison with the STAR results obtained in U+U collisions at $\sqrt{s_{NN}} = 193$ GeV. The width of the bands corresponds to the statistical uncertainty associated with the calculation in AMPT model.

Fig. 4.25. K^+/π^+ and K^-/π^- ratios for AMPT 10 mb case are closer to STAR data, however, the AMPT 1.5 mb case gives lower values for these ratios. In the case of p/π^+, $\bar{p}/\pi^-$, AMPT 1.5 mb case is more closer to STAR results in central collisions while AMPT 10 mb case seems to be closer to STAR results for peripheral collisions.

191

4.7 Summary

Various basic observables concerned with identified particle production in U+U collisions at $\sqrt{s_{NN}} = 193$ GeV are presented. The transverse momentum spectra of $\pi^{\pm}$, $K^{\pm}$ and $p(\bar{p})$ in mid-rapidity ($|y| < 0.1$) are measured for nine centrality classes : 0-5%, 5-10%, 10-20%, 20-30%, 30-40%, 40-50%, 50-60%, 60-70% and 70-80%. Other extracted observables from p_T spectra such as average transverse momentum ($\langle p_T \rangle$), particle yields (dN/dy), particle ratios and kinetic freeze-out properties in U+U collisions at $\sqrt{s_{NN}} = 193$ GeV are also presented as a function of collision centrality or $\langle N_{\mathrm{part}} \rangle$. These observables are compared with the corresponding results from Au+Au collisions at $\sqrt{s_{NN}} = 200$ GeV and AMPT model modification to incorporate the deformation in the Uranium nucleus at this center of mass energy.

The current measurements in U+U collisions extend the centrality dependence of the measured observables upto a value of $\langle N_{\mathrm{part}} \rangle > 400$.

The mean $\langle p_T \rangle$ values for π, K and p increase from peripheral to central collisions in U+U collisions at $\sqrt{s_{NN}} = 193$ GeV. This is an indication of increasing radial flow effects in more central collisions. The increase in $\langle p_T \rangle$ from π to K and to p indicates that the radial flow increases with the mass of the particle.

The integrated particle yields dN/dy in mid-rapidity $|y| < 0.1$ of $\pi^{\pm}$, $K^{\pm}$ and p do not scale with $\langle N_{\mathrm{part}} \rangle$, rather it slowly increases from peripheral to central collisions in U+U collisions at $\sqrt{s_{NN}} = 193$ GeV. This indicates that at this energy particle production mechanism has contribution from soft and hard processes involving nucleon-nucleon binary collisions. On the other hand, $\bar{p}$ shows no such dependence with the centrality of the collision.

Anti-particle to particle ratios are close to unity in U+U collisions at $\sqrt{s_{NN}} = 193$ GeV, indicating pair production is the dominant mechanism of particle production at this energy. Their values are also close to those obtained from Au+Au collisions at $\sqrt{s_{NN}} = 200$ GeV. The K^+/π^+ and K^-/π^- ratio increases from peripheral to mid-central collision after which they saturate upto central collision. The p/π^+ and $\bar{p}/\pi^-$ ratios do not show any significant centrality dependence in U+U collisions at $\sqrt{s_{NN}} = 193$ GeV.

The kinetic freeze-out parameters are obtained from the simultaneous Blast-wave fit to $\pi^{\pm}$, $K^{\pm}$ and $p(\bar{p}\ p_T$ spectra in U+U collisions at $\sqrt{s_{NN}} = 193$ GeV. The kinetic freeze-out

temperature T_k decreases from peripheral to central collisions suggesting the fact of a short-lived fireball in central collisions. On the contrary, average flow velocity $\langle \beta \rangle$ increases from peripheral to central collisions, indicating large radial flow effects for central collisions. This follows up an interesting anti-correlation between T_k and β. The extracted T_k and $\langle \beta \rangle$ values for similar $\langle N_{\text{part}} \rangle$ values are consistent between Au+Au collisions at $\sqrt{s_{NN}} = 200$ GeV and U+U collisions at $\sqrt{s_{NN}} = 193$ GeV.

A detailed comparison of integrated particle yields, mean transverse momentum, particle ratios from STAR results in U+U collisions at $\sqrt{s_{NN}} = 193$ GeV is carried out with two cases of AMPT string melting version (AMPT parton-parton interaction cross-section of 1.5 mb and 10 mb), which is modified to incorporate the deformation in the Uranium nucleus. $\langle p_T \rangle$ obtained from AMPT model have lower values than STAR results in U+U collisions at $\sqrt{s_{NN}} = 193$ GeV for all centrality classes. The dN/dy from AMPT 10 mb data are closer to the STAR results for pions and kaons relatively compared to AMPT 1.5 mb data. Whereas for protons, dN/dy in central collisions are better explained by AMPT 1.5 mb data and for peripheral collisions the agreement of AMPT 10 mb data is good. Anti-particle to particle ratios are successfully explained by both the data sets of AMPT model. The K/π ratios from AMPT 10 mb data have closer values to STAR results across all centrality classes, but the data from AMPT 1.5 mb under predicts the STAR results. In the case of p/π ratios, AMPT 1.5 mb case more closely explains the STAR results in central collisions while AMPT 10 mb case seems to be closer to STAR results for peripheral collisions.

We compared the results from U+U collisions to those in Au+Au collisions at similar center of mass energies, having different geometrical shapes and hence initial collision conditions. However, the presented physical observables (dN/dy, $\langle p_T \rangle$, particle ratios, T_k and $\langle \beta \rangle$) are consistent between U+U and Au+Au for the similar range of $\langle N_{\text{part}} \rangle$ values. In future measuring various observables by separating the initial state configurations for U+U collisions will be interesting to study [1].

Bibliography

[1] Vipul Bairathi, Md. Rihan Haque, and Bedangadas Mohanty, Phys. Rev. **C 91**, 054903 (2015).

[2] Md. Rihan Haque, Zi-Wei Lin and Bedangadas Mohanty, Phys. Rev. **C 85, 034905**, (2012).

[3] Md. Rihan Haque, Md. Nasim, and Bedangadas Mohanty, Phys. Rev. **C 84**, 067901 (2011).

[4] Hiroshi Masui, Bedangadas Mohanty and Nu Xu, Phys. Lett. **B 679**, 440 (2009).

[5] A. Adare *et al*. (PHENIX Collaboration), Phys. Rev. **C 94**, 054910 (2016).

[6] L. Adamczyk *et al*. (STAR Collaboration), Phys. Rev. Lett. **118**, 012301 (2017).

[7] L. Adamczyk *et al*. (STAR Collaboration), Phys. Rev. Lett. **115**, 222301 (2015).

[8] J.G. Alessi *et al*., The Proceedings of Particle Accelerator Conference (PAC 05), Knoxville, Tennessee, 16–20 May 2005, p. 363.

[9] T. Hirano, U. W. Heinz, D. Kharzeev, R. Lacey and Y. Nara, Phys. Lett. **B 636**, 299 (2006).

[10] C. Nepali, G. Fai, D. Keane, Phys. Rev. **C 73**, 034911 (2006).

[11] U.W. Heinz, A. Kuhlman, Phys. Rev. Lett., **94**, 132301 (2005).

[12] D. Kharzeev and M. Nardi, Phys. Lett. **B 507**, 121 (2001).

[13] M. L. Miller, K. Reygers, S. J. Sanders and P. Steinberg, Ann. Rev. Nucl. Part. Sci. **57**, 205 (2007).

[14] U. Heniz and A. Kuhlman, Phys. Rev. Lett. **94**, 132301 (2005); A. Kuhlman and U. Heniz, Phys. Rev. **C 72**, 037901 (2005).

[15] T. Hirano, P. Huovinen and Y. Nara, Phys. Rev. **C 83**, 021902(R) (2011).

[16] C. Nepali, G. Fai and D. Keane, Phys. Rev. **C 76**, 051902(R) (2007); Phys. Rev. **C 73**, 034911 (2006).

[17] B. Abelev *et al.* (STAR Collaboration), Phys. Rev. **C 79**, 034909 (2009).

[18] Z.W. Lin, C.M. Ko, B.A. Li, B. Zhang and S. Pal, Phys.Rev. **C 72**, 064901, (2005).

[19] C. Adler *et al.*, Nucl. Instr. Meth. **A 470**, 488 (2001).

[20] W. J. Llope *et al.*, Nucl. Instr. Meth. **A 522**, 252 (2004).

[21] L. Adamczyk *et al.* (STAR Collaboration), Phys. Rev. **C 94**, 064904 (2016).

[22] L. Adamczyk *et al.* (STAR Collaboration), Phys. Rev. **C 96**, 044904 (2017).

[23] M. Anderson, J. Berkovitz, W. Betts *et al.*, Nucl. Instrum. Methods Phys. Res. **A 499**, 659 (2003).

[24] W. Llope, Nucl. Instrum. Meth. **B 241**, 306 (2005).

[25] H. Bichsel, Nucl. Instrum. Methods Phys. Res. **A 562**, 154 (2006).

[26] M. Aguilar-Benitez, W. Allison, A. Batalov *et al.*, Z. Phys. **C 50**, 405 (1991).

[27] M. Shao *et al*, Nucl. Instrum. Methods Phys. Res. A **558**, 419 (2006).

[28] B. Abelev *et al.* (STAR Collaboration), Phys. Rev. **C 81**, 024911 (2010).

[29] X.-N. Wang and M. Gyulassy, Phys. Rev. **D 44**, 1372 (1991).

[30] V. Fine and P. Nevski, Proc. CHEP **2000**, 143 (2000).

[31] J. Adams *et al.* (STAR Collaboration), Phys. Rev. **C 70**, 041901 (2004).

[32] K. Rajagopal and F. Wilczek, arXiv:hep-ph/**0011333** (2000).

[33] E. Laermann and O. Philipsen, Ann.Rev.Nucl. Part. Sci. **53**, 163 (2003).

[34] M. Stephanov, PoS **LAT2006**, 024 (2006).

[35] J. Adams *et al*. (STAR Collaboration), Phys. Rev. Lett. **91**, 072304 (2003).

[36] J. Adams *et al*. (STAR Collaboration), Phys. Rev. Lett. **92**, 112301 (2004).

[37] M. Kaneta and Nu Xu, nucl-th**/0405068**, (2004).

[38] J. Cleymans, Burkhard Kampfer, M. Kaneta, S. Wheaton and N. Xu, Phys. Rev. **C 71**, 054901, (2005).

[39] F. Wang, Phys. Lett. **B 489**, 273 (2000).

[40] F. Wang *et al*., Phys. Rev. **C 61**, 064904 (2000).

[41] P. Braun-Munzinger *et al*., Nucl. Phys. A697, 902 (2002).

[42] E. Schnedermann, J. Sollfrank, and Y.W. Hienz, Phys. Rev. **C 48** 2462, (1993).

[43] G. Wilk and Z. Wlodarczyk, Phys. Rev. Lett. **84**, 2770 (2000).

[44] B. Abelev et al. (ALICE Collaboration), Phys. Rev.**C 88**, 044910 (2013).

[45] U. W. Heinz, arXiv:hep-ph/0407360.

[46] K. Hagino, N. W. Lwin and M. Yamagami, Phys. Rev. C **74**, 017310 (2006).

[47] Z. W. Lin, S. Pal, C.M. Ko, B.A. Li and B. Zhang, Phys. Rev. C **64**, 011902(R), (2001).

[48] Jun Xu and Che Ming Ko, Phys. Rev. **C 84**, 014903 (2011).

Chapter 5

Freeze-out Conditions in proton-proton Collisions From SPS to LHC Energies

The theoretical tools and phenomenological models are continuing their decades of successful journey in explaining the physical phenomena and experimental observations. Research in this direction adds many interesting points to physics. In the current chapter of the thesis, we will explore such a direction of explaining the hadron yields obtained from proton-proton collision data by implementing the statistical thermal model.

5.1   Introduction

The surface of the last scattering is known as the freeze-out surface. The number of particles in an event, as well as the momenta of the particles freezes after this stage [1]. The freeze-out surface can be classified into two categories depending on the type of interactions (elastic or inelastic) ongoing among the particles. In the first step, the inelastic collision among the particles ceases leading to a stage of a fixed number of particles with a fixed chemical composition. This stage is known as the chemical freeze-out (CFO) stage. The particles after this stage collide only elastically leading to changes in their momenta. Further expansion of the system, even ceases these elastic collisions to occur, there by leading to the kinetic freeze-out (KFO) stage.

In the context of this chapter, we will mainly focus on analyzing the chemical freeze-out surface in proton-proton collisions at the energies available at SPS, RHIC and LHC using a

statistical model of hadrons. This study will put to test the validity of such models, given that we do not expect p+p collisions to create a thermalized medium.

5.2 Chemical Freeze-out

The chemical freeze-out stage corresponds to the start of the phase of the hadron gas with fixed chemical composition and number of particles. This chemical freeze-out stage can be analyzed from the experimentally observed particle yields and particle ratios. This surface is characterized by the chemical freeze-out temperature and thermodynamic potential by assuming the system to be in thermal and chemical equilibrium [2,3]. The statistical model of non-interacting gas of hadrons and resonances at some volume V, temperature T and conserved charge chemical potentials μ_B, μ_S and μ_Q corresponding to three conserved charges namely baryon number B, strangeness S and electric charge Q have been remarkably successful in providing a good qualitative description of the mean hadron yields in heavy-ion collisions [4–6] as well as in p+p collisions [7–10].

In spite of the success of thermodynamical models in explaining the small systems of p+p or e+e collisions, the microscopic understanding of such fast thermal equilibration is still an open question. It is believed that, in the small systems of p+p collisions, the formation of the thermally equilibrated fireball is less likely to be formed as in A+A collisions. However, thermal model studies have demonstrated that the description of the system in p+p and A+A collisions are very much similar [11]. So, there is an interesting platform laid to apply the predictions of thermal models in explaining the experimental data in small systems.

There are recent results in Pb+Pb collisions at $\sqrt{s_{NN}} = 2.76$ TeV, which shows a discrepancy in explaining the experimental data of proton to pion ratio through the unified (CFO and KFO occurs at the same time) freeze-out scheme [12, 13], where all the hadrons considered to freeze-out at the same thermodynamic conditions. Therefore alternative freeze-out schemes have been proposed to address the above issue [14–17]. Here we will discuss in detail one of them, the double freeze-out scheme (2CFO) where those hadrons with non-zero strangeness content are allowed to freeze-out at a different surface as compared to those with zero strangeness [16, 17]. The 2CFO scheme has shown its success in describing the proton

anomaly [16] and transverse momentum spectra [18] at LHC, the $\frac{{}^{3}_{\Lambda}H}{{}^{3}He}$ ratio at $\sqrt{s_{NN}} = 200$ GeV and $\frac{\bar{\Lambda}}{p}$ ratio at lower beam energies which can not be described by the 1CFO scheme [19, 20].

Here we will present the application of the thermal model to p+p collisions at $\sqrt{s_{NN}} =$17.3 (SPS), 200 (RHIC), and to new data from LHC at 900 and 7000 GeV. We will study the systematics of the extracted thermal parameters by employing different ensembles and freeze-out schemes in detail in this chapter.

5.3   The Statistical Thermal Model

The statistical thermal models are developed to explain the measured mean hadron yields by assuming a system to be in thermal and chemical equilibrium. These models treat the system as an ideal gas of locally thermalized hadrons and resonances, sharing a common pool with the freeze-out parameters same for all the particles [?]. In the current structure of the thermal model used here, the hadrons composed of only light quarks (u, d, s and their anti-quarks) are considered. The hadrons composed of heavy quarks are excluded in the model as they are not created by thermal production and their yields are suppressed due to the Boltzmann factor.

In the statistical analysis applied to high-energy collision experiments, three distinct ensembles can be visualized depending on the conservation laws: Baryon number and Strangeness number. Those are Grand Canonical Ensemble (GCE) , Strangeness Canonical Ensemble (SCE) and Canonical Ensemble. The details about these ensembles will be discussed in the subsequent sections of this chapter.

5.4   The THERMUS Package

The theory of statistical thermal physics applied to the field of high energy nucleus collision experiments is well developed in terms of computer software packages. Some of these packages which are widely used are THERMUS [21], SHARE (Statistical Hadronization with Resonances) [22] and THERMINATOR (Thermal Heavy-ion Generator) [23]. The chosen package for the analysis in the current chapter is the THERMUS package. THERMUS is a code written

in C++ language based on the object oriented programming ROOT [24]. This package is structured with many classes and functions. Three distinct statistical thermal ensembles, i.e. grand-canonical, strangeness-canonical and canonical ensembles are incorporated in the THERMUS package. A particle list containing all the particles with light quarks flavors (u, d and s) listed in Particle Physics Booklet of 2002 [25] below mass 2.6 GeV/c^2 is included in THERMUS. THERMUS also includes the decay text file for all the unstable particles in the particle list. Like every model, THERMUS also have a certain set of parameters for each ensemble. A set of thermalized particles with the set of parameters for a given choice of ensemble serves as the input to the THERMUS model. This information is then used to calculate the thermodynamical quantities such as the number density, energy, entropy density and compared with the experiment. The TMinuit class of ROOT is used to fit the experimental data to provide the best fit result. The standard χ^2 minimization method is exploited to provide the best fit thermal parameters giving the yields of particles as close as to the experimental value. Additionally, mass and width of resonances can also be included in the calculation using THERMUS package. The specific decay channels provided by THERMUS can be switched "off" and "on" in the model to allow the feed-down corrections to match the experimental data.

In the subsequent subsections, we will discuss the various ensembles employed within THERMUS package along with their structure in this package. The implementation of feed-down correction within the package will also be discussed subsequently.

5.4.1 Grand Canonical Ensemble

Within the grand canonical ensemble, the quantum numbers such as baryon number (B), strangeness (S) and charge (Q) are conserved on an average through the requirement of their corresponding chemical potentials μ_B, μ_S, μ_Q. In high energy collisions, as the system involves large particle densities, this ensemble finds its useful application.

Consider an ideal gas of hadrons and resonances in thermal and chemical equilibrium. In the grand canonical ensemble approach, the logarithm of total partition function is given by [21]

$$\ln Z^{GCE}(T, V, \mu_i) = \sum_{\text{species i}} \frac{g_i V}{(2\pi)^3} \int d^3p \ln(1 + e^{\beta(E_i - m_i)})^{\pm 1}, \qquad (5.1)$$

200

where V is the fireball volume, g_i is the degeneracy, $E_i = \sqrt{p^2 + m_i^2}$ with m_i as the particle mass and $\beta = \frac{1}{T}$, where T is the chemical freeze-out temperature. The plus sign corresponds to fermions and minus sign to bosons. The hadron chemical potential μ_i can be written as

$$\mu_i = B_i\mu_B + S_i\mu_S + Q_i\mu_Q. \tag{5.2}$$

From the partition function, the thermodynamical quantities like particle multiplicity (N_i^{GCE}). entropy (S_i^{GCE}), pressure (P_i^{GCE}) and energy (E_i^{GCE}) can be calculated. The particle multiplicity is obtained from Eq. 5.1 by the relation

$$N_i^{GCE} = T\frac{\partial}{\partial \mu_i}ln|Z|. \tag{5.3}$$

Thereby, the particle multiplicity obtained from the above calculation is

$$N_i^{GCE} = \frac{g_iV}{2\pi^2}\sum_{k=1}^{\infty}(\pm 1)^{k+1}\frac{m_iT^2}{k}K_2\left(\frac{km_i}{T}\right) \times \exp(\beta k\mu_i), \tag{5.4}$$

where K_2 is the second order Bessel function. The plus sign is for bosons and the minus sign is for fermions. Within the Maxwell Boltzmann approximation, it is sufficient to keep only the first term by taking $k = 1$ in Eq. 5.4 for most of the particles. The use of Quantum statistical mechanics (Bose-Einstein or Fermi-Dirac) complicates the problem as they require the computation of infinite sums or integrals. Again to avoid Bose-Einstein condensation, it is required that the chemical potentials of all the bosons in hadron gas are smaller than their masses ($\mu_i < m_i$).

An additional phenomenological parameter γ_S is introduced here to account for any non-equilibrium production of strange particles. The value of $\gamma_S = 1$ corresponds to the complete strangeness equilibrium. It is multiplied with the partition function such that;
$N_i^{GCE} \rightarrow N_i^{GCE}\gamma_S^{|S_i|}$, where $|S_i|$ is the number of strange and anti-strange quarks in species i. This factor is introduced in all the ensembles incorporated in THERMUS.

Within the THERMUS package, the grand canonical ensemble is characterized primarily by the parameters : T, μ_B, μ_S, μ_Q, γ_S and R, where R is the radius of the fireball at the time

of chemical freeze-out with the assumption of a spherical fireball (i.e. $V = 4\pi R^3/3$). Each of the parameters is allowed to be set as free or fixed. Additionally, μ_Q and μ_S can be constrained to $B/2Q$ and 0 respectively.

5.4.2 Strangeness Canonical Ensemble

In strangeness canonical ensemble, similar to grand canonical ensemble the conservation of baryon number (B) and charge (Q) are allowed on an average. However, the exact conservation of strangeness is required by this ensemble. This treatment of strangeness considers the fact that strangeness is comparatively less abundant compared with baryon number and charge. Within the framework of strangeness canonical ensemble, the volume V with exact strangeness content S is allowed. The strangeness canonical ensemble has an exact conservation of strangeness with average conservation of baryon number and charge.

In the Maxwell Boltzmann approximation, the strangeness canonical ensemble partition function is given by [21]

$$Z_S^{SCE} = \frac{1}{2\pi} \int_{-\pi}^{\pi} d\phi e^{iS\phi_S} \exp\left(\sum_i \frac{g_i V}{2\pi^3} \int d^3p e^{-\beta(E_i - \mu_i)} e^{iS_i\phi_S} \right), \tag{5.5}$$

where ϕ_S is introduced to conserve strangeness and in this case the hadron chemical potential is given as

$$\mu_i = B_i\mu_B + Q_i\mu_Q. \tag{5.6}$$

The particle multiplicity can be calculated as

$$
\begin{aligned}
N_i^{SCE} &= \frac{\partial}{\partial\left(\frac{\mu_i}{T}\right)} \log[Z_S^{SCE}] \\
&= \left(\frac{Z_{S-S_i}}{Z_S}\right) N_i^{GCE}|_{\mu_S=0}.
\end{aligned}
\tag{5.7}
$$

Hence, the particle multiplicity in strangeness canonical ensemble is a multiplicative of that in grand canonical ensemble with $\mu_S = 0$. By the requirement of $\mu_S = 0$, the strangeness conservation is enforced in strangeness canonical ensemble.

Within the THERMUS package, the strangeness canonical ensemble is characterized pri-

marily by the parameters : T, μ_B, μ_Q, γ_S, R_c and R, where R_c is the canonical or correlation radius within which the strangeness is assumed to be exactly conserved. Each of the parameters is allowed to be set as free or fixed. Also, μ_Q and R_c can be constrained to $B/2Q$ and $R_c = R$ respectively.

5.4.3   Canonical Ensemble

The canonical ensemble requires the exact conservation of baryon number (B), strangeness (S) and charge (Q). Hence, it is advocated to be applicable to small systems of $p + p$, $p + \bar{p}$ and $p + A$ collisions [26, 27].

In the framework of both Boltzmann and quantum statistics, the canonical partition function is expressible in terms of grand canonical partition function as [21]

$$
\begin{aligned}
Z_{B,S,Q}^{CE} &= \frac{1}{2\pi} \int_{-\pi}^{\pi} d\phi_B e^{-iB\phi_B} \frac{1}{2\pi} \int_{-\pi}^{\pi} d\phi_S e^{-iB\phi_S} \frac{1}{2\pi} \int_{-\pi}^{\pi} d\phi_Q e^{-iB\phi_Q} \\
&\times \exp\left(\sum_i \frac{g_i V}{(2\pi)^3} \int d^3p\, e^{-\beta E_i} e^{i(B_i\phi_B + S_i\phi_S + Q_i\phi_Q)} \right),
\end{aligned}
\tag{5.8}
$$

where the introduction of ϕ_B, ϕ_S and ϕ_Q ensures exact conservation of B, S and Q. In the Maxwell Boltzmann approximation, the particle multiplicity in canonical ensemble is calculated as

$$
\begin{aligned}
N_i^{CE} &= \frac{Z_{B-B_i, S-S_i, Q-Q_i}}{Z_{B,S,Q}} \frac{g_i V}{2\pi^3} \int d^3p\, e^{-\beta E} \\
&= \frac{Z_{B-B_i, S-S_i, Q-Q_i}}{Z_{B,S,Q}} N_i^{GCE}|_{\mu_i = 0},
\end{aligned}
\tag{5.9}
$$

where $Z_{B-B_i, S-S_i, Q-Q_i}$ is the partition function with quantum numbers of the excluded particles i and $Z_{B,S,Q}$ is the total partition function. As can be inferred from the above equation, in large volume limit the calculations from canonical ensemble approach to that of grand canonical ensemble.

The THERMUS package characterizes the canonical ensemble by the following set of parameters : T, B, S, Q, γ_S and R. As the quantum numbers B, S and Q are exactly conserved in this ensemble, there are no appearance of corresponding chemical potentials in the formalism

of canonical ensemble.

5.4.4 Feed-down

At the chemical freeze-out stage, the hadron gas consists of a mixture of both stable hadrons and hadron resonances. The observed particle yield contains a combination of both primary yield as well as decay contribution from heavier particles. Hence, in general, the total particle multiplicity (N_i) can be factorized as

$$N_i = N_i^{prim} + \sum_{\text{states}} N_j^{prim} BR(j \to i), \qquad (5.10)$$

where N_i^{prim} and N_j^{prim} are the primordial particle multiplicities of species i and j respectively and $BR(j \to i)$ is the branching ratio of j to i through all possible channels. In the THERMUS package, it is allowed to switch "off" and "on" the decay channels in accordance with the specification of the experimental particle yields given as input. Through the feed-down study in thermal models, it has been observed that at high energy the majority contribution to feed-down comes from mesons, whereas at low energy feed-down contribution from baryons is more prominent [21, 28]. So, the particle yields which are weak decay corrected in experiments needs to be treated properly in the thermal model and is very sensitive in the calculation of final freeze-out parameters.

In addition to what we have discussed here, there are several features included in the THERMUS package. Some of those are mass cut-off, resonance width and excluded volume corrections and these are described in detail in refs. [21]. These additional features are not studied in this chapter.

5.5 Data Set and Analysis Details

We have analyzed the p+p collision datasets at SPS with $\sqrt{s_{NN}} = 17.3$ GeV [29–33], RHIC with $\sqrt{s_{NN}} = 200$ GeV [34–36] and at LHC with $\sqrt{s_{NN}} = 900$ GeV [37, 38] and 7 TeV [39–41]. The RHIC and LHC data are measured at mid-rapidity while the SPS data is with 4π coverage. The data of $\pi^{\pm}$ and Λ are feed-down corrected from weak decays whereas (anti-

$\sqrt{s_{NN}}$ (GeV)	Expt.	System	Particle yields (dN/dy)	Anti-particle yields (dN/dy)	Ref.
17.3*	SPS	p+p	π^+ : 3.018 ± 0.06	π^- : 2.36 ± 0.047	[29]
			K^+ : 0.227 ± 0.005	K^- : 0.130 ± 0.003	[30]
			p: 1.162 ±0.035	$\bar{p}$0.039 ± 0.001	[31]
			Λ : 0.116 ± 0.011	$\bar{\Lambda}$: 0.0137 ± 0.0007	[32]
			Ξ : 0.0031 ± 0.0003	$\bar{\Xi}$: 0.00092 ± 0.00009	[32]
			K_S^0 : 0.18 ± 0.04		[32]
			Ω : 0.00026 ± 0.00013	$\bar{\Omega}$: 0.00016 ± 0.00009	[32]
			ϕ : 0.012 ± 0.0015		[33]
200	STAR	p+p	π^+ : 1.44 ± 0.11	π^- : 1.42 ± 0.11	[34]
			K^+ : 0.150 ± 0.013	K^- : 0.145 ± 0.013	[34]
			p: 0.138±0.012	$\bar{p}$: 0.113 ± 0.010	[34]
			Λ : 0.0385 ± 0.0036	$\bar{\Lambda}$: 0.0351 ± 0.0033	[35]
			Ξ : 0.0026 ± 0.0009	$\bar{\Xi}$: 0.0029 ± 0.001	[35]
			K_S^0 : 0.134 ± 0.011		[35]
			$\Omega + \bar{\Omega}$: 0.00034 ± 0.00019		[35]
			ϕ : 0.018 ± 0.003		[36]
900	ALICE	p+p	π^+ : 1.493 ± 0.0741	π^- : 1.485 ± 0.0741	[37]
			K^+ : 0.183 ± 0.0155	K^- : 0.182 ± 0.0155	[37]
			p: 0.083±0.0063	$\bar{p}$: 0.079 ± 0.0063	[37]
			Λ : 0.048 ± 0.0041	$\bar{\Lambda}$: 0.047 ± 0.0054	[38]
			$\Xi^- + \overline{\Xi}^+$: 0.0101 ± 0.0022		[38]
			K_S^0 : 0.184 ± 0.0063		[38]
			ϕ : 0.021 ± 0.005		[38]
7000	ALICE	p+p	π^+ : 2.26 ± 0.1	π^- : 2.23 ± 0.1	[39]
			K^+ : 0.286 ± 0.016	K^- : 0.286 ± 0.016	[39]
			p: 0.124±0.009	$\bar{p}$: 0.123 ± 0.01	[39]
			Ξ : 0.008 ± 0.000608	$\bar{\Xi}$: 0.0078 ± 0.000608	[40]
			Ω : 0.00067 ± 0.000085	$\bar{\Omega}$: 0.00068 ± 0.000085	[40]
			ϕ : 0.032 ± 0.004		[41]

Table 5.1: Details of the data sets used for fitting with references. * represents the data from 4π rapidity where as the other data sets are from mid-rapidity.

) protons at RHIC are inclusive. The data sets from SPS and LHC of $\pi^\pm$, p, $\bar{p}$ and Λ are feed-down corrected from weak decays. The details about the data sets used in this study are summarized in Table 5.1. The statistical model analysis of particle multiplicities in p+p collisions has been studied earlier at SPS and RHIC which are reported in Ref. [7, 42]. Our study agrees with the results if we use the same data sets. Here we have extended these earlier studies for the new LHC data as well as repeated the analysis at SPS and RHIC with extended data sets for different thermal ensembles and freeze-out schemes.

These data sets are analyzed with the application of three ensembles; grand canonical, strangeness canonical and canonical ensemble. These ensembles are studied with implication to two freeze-out schemes; single freeze-out (1CFO) and double freeze-out (2CFO). In gen-

eral, the extracted chemical freeze-out parameters are chemical freeze-out temperature (T_{ch}), baryon chemical potential (μ_B), strangeness chemical potential (μ_S), strangeness saturation factor (γ_S) and fireball radius (R) in 1CFO scheme. However, there are three freeze-out parameters (T_s, V_s, μ_{B_s}) characterizing the strange freeze-out surface and another three freeze-out parameters characterizing the non strange freeze-out surface - ($T_{ns}, V_{ns}, \mu_{B_{ns}}$) under the 2CFO scheme. In 2CFO scheme, we have fixed the value of γ_S to 1.

However in accordance with the standard practice, we have constrained μ_S and μ_Q by the following relation

$$\text{Net } S \quad = \quad 0 \text{ and} \tag{5.11}$$

$$\text{Net } B / \text{Net } Q \quad = \quad 1. \tag{5.12}$$

The remaining parameters (T, μ_B, γ_S, R) are extracted from fits to hadron yields in 1CFO scheme.

In summary, we will analyze the systematics of the dependence of the freeze-out parameters in the data set of p+p collisions at $\sqrt{s_{NN}} = 17.3$ (SPS), 200 (RHIC), 900 (LHC) and 7000 GeV (LHC) with respect to the following choices:

1. Choice of ensemble: grand canonical, strangeness canonical and canonical.

2. Choice of freeze-out scheme: 1CFO and 2CFO.

All the results obtained here are compared with the corresponding published results from heavy ion collisions [6].

5.6   Results and Discussions

This section compiles all the results in p+p collisions studied at the center of mass energy of 17.3, 200, 900 and 7000 GeV. We will systematically present the results starting from the comparison between data and predictions from model to finally see the systematics of the freeze-out parameters on the choice of different ensembles and freeze-out schemes.
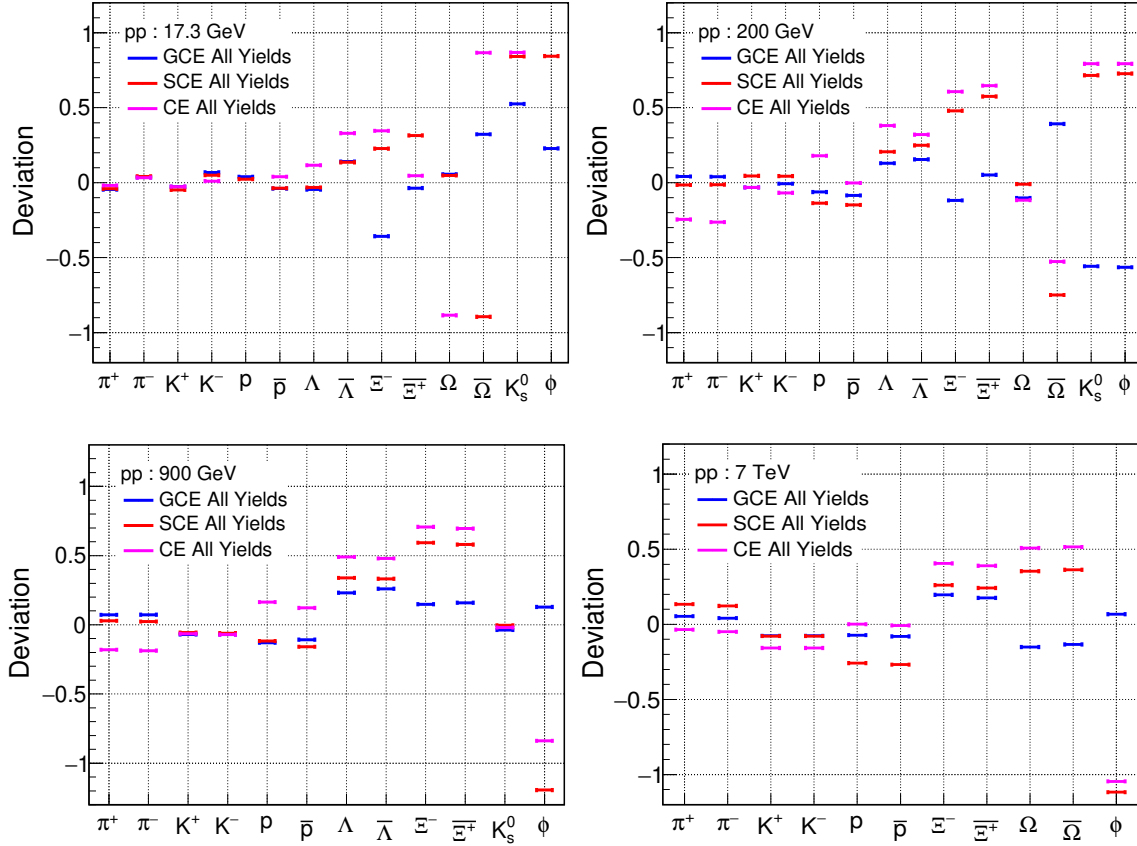
Figure 5.1: The deviation between data and model for each particle species in 1CFO in p+p collisions at $\sqrt{s_{NN}} = 17.3$, 200, 900 and 7000 GeV. For each of the data sets the comparison among the fits from grand canonical, strangeness canonical and grand canonical ensemble are shown.

At the first step of the analysis, it is required to compare the yields measured from experiments and that predicted from the model to have an idea on the description capability of the model. This quality check of the goodness of the fit is compared here through the deviation factor defined as

$$\text{Deviation} = \frac{\text{Exp. value - Model value}}{\text{Exp. value}}, \tag{5.13}$$

The experimental errors are not included in the definition of the deviation as they could be different from p+p to heavy-ions and later in this study we will look for the comparison between these two.

In Fig. 5.1, we have plotted this deviation between model and data for the particle yields used as input to the thermal model in p+p collisions at $\sqrt{s_{NN}} = 17.3$, 200, 900 and 7000 GeV. For each of the data sets the comparison among the fits from grand canonical, strangeness

canonical and grand canonical ensemble are shown. It can be well observed from the figure that, the deviation of the particle yields from model predictions to that obtained in the experiment are least with the choice of grand canonical ensemble. This suggests that better description of the particle yields is provided by grand canonical ensemble even for the small system of p+p collisions similar to heavy-ions [6,43]. The multi-strange particles like Ξ, Ω and especially the hidden strange particle like ϕ show maximum value of deviation especially in strange canonical and canonical ensemble. This might suggest that the freeze-out mechanism for these multi-strange and hidden strange particles is more involved and can not be explained alone in the simple 1CFO scheme.

In Fig. 5.2, the results on all the chemical freeze-out parameters T_{ch}, μ_B, γ_S, R and χ^2/ndf obtained from the thermal model fit in GCE, SCE and CE are presented. The χ^2/ndf represents the fit quality with ndf = number of data points − number of free parameters. The χ^2/ndf values plotted in the Fig. 5.2 agrees with our above remark that the grand canonical ensemble (GCE) describes the data best at all energies as it stays between $2-3$ for RHIC and higher energies while at $\sqrt{s_{NN}} = 17.3$ GeV the fit worsens to $\chi^2/ndf \sim 5$. The increase in the value of χ^2/ndf from RHIC to LHC energies can also be interpreted in terms of more precise measurements done at LHC than RHIC. This reduces, the error values on the particle yields resulting in the value of χ^2/ndf to go up. We can see that the freeze-out temperature T monotonically decreases from 170 MeV at $\sqrt{s_{NN}} = 17.3$ GeV to ~ 150 MeV at 7 TeV. μ_B shows a sharp fall from $\sqrt{s_{NN}} = 17.3$ GeV to $\sqrt{s_{NN}} = 200$ GeV beyond which it hovers around zero as in heavy ion collisions (HICs). The value of γ_S monotonically rises from 0.3 to 0.8 between SPS and LHC energies. The fireball radius rises from ~ 1.3 fm at $\sqrt{s_{NN}} = 200$ GeV to ~ 1.7 fm at $\sqrt{s_{NN}} = 7$ TeV. The canonical ensemble provides the worst fit with $\chi^2/ndf \geq 10$. The fitted temperature, in this case comes out to be greater than 170 MeV for all the energies. The fits from strangeness canonical ensemble also do not seem to be better as it has $\chi^2/ndf \geq 5$ for all the energies.

Previously, we have observed that the THERMUS model [21] does not estimate the yield of ϕ and hence we need to look systematic effect of the yield of ϕ on the values of extracted freeze-out parameters. To have a better understanding of the effect of the particle ϕ, we have
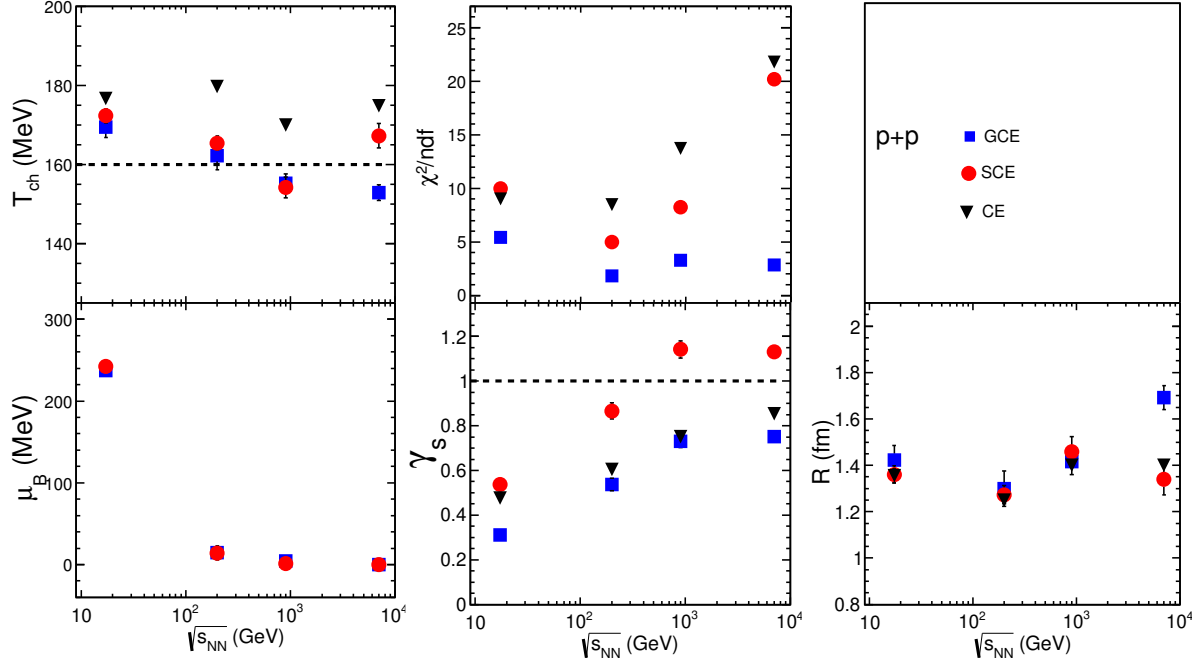
Figure 5.2: Freeze-out parameters T_{ch}, μ_B, γ_S, R and χ^2/ndf obtained from a statistical model fit [21] using particle yields in different ensembles. The errors are uncertainties on the parameters obtained from statistical model fit.

extracted the chemical freeze-out parameters in three different ensembles excluding the yield of ϕ in the thermal model fit. The T_{ch}, μ_B, γ_S, R and χ^2/ndf so obtained are shown in Fig. 5.3. We can observe that excluding ϕ from the thermal model fit slightly improves the value of χ^2/ndf especially at energies above $\sqrt{s_{NN}} = 200$ GeV. However, excluding ϕ from the thermal model fit has no significant effect on the extracted chemical freeze-out parameters. So, we do not gain much here, except the only plus point comes is the slightly better value of χ^2/ndf.

We have analyzed the data from the small system of p+p collisions in the 2CFO scheme as well. The strangeness canonical ensemble in 2CFO provide a better fit with reference to χ^2/ndf than 1CFO, however, the strange freeze-out temperatures turn out to be large (> 180 MeV). The 2CFO fits in the grand canonical ensemble yield reasonable temperatures. In Fig. 5.4, we have presented the comparison between 1CFO and 2CFO schemes in the GCE. The 1CFO parameters almost agree with the non-strange parameters of 2CFO. Unlike to HICs, where the 2CFO scheme provides a much better description of the hadron yields than 1CFO [16], here in p+p collisions we find the χ^2/ndf is similar and one does not gain much by introducing two additional parameters in 2CFO compared to γ_S included in 1CFO. The other noticeable dif-
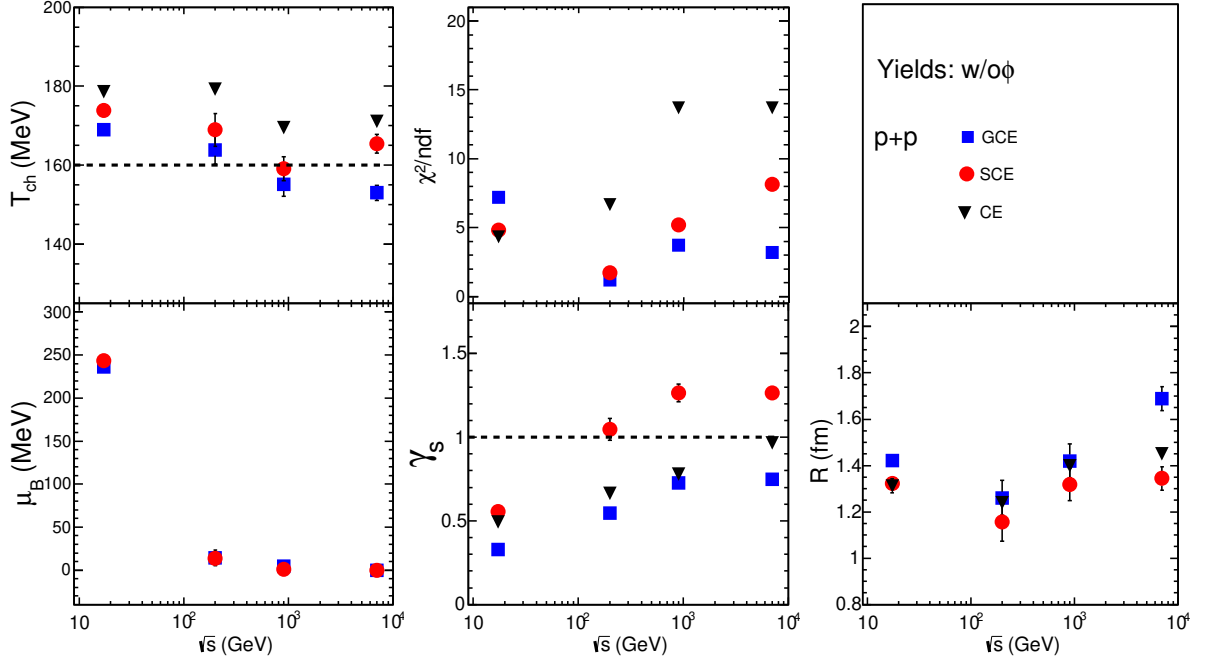
Figure 5.3: Freeze-out parameters T_{ch}, μ_B, γ_S, R and $\chi^2/$ndf obtained from a statistical model fit [21] using particle yields in different ensembles excluding the yield of ϕ. The errors are uncertainties on the parameters obtained from statistical model fit.
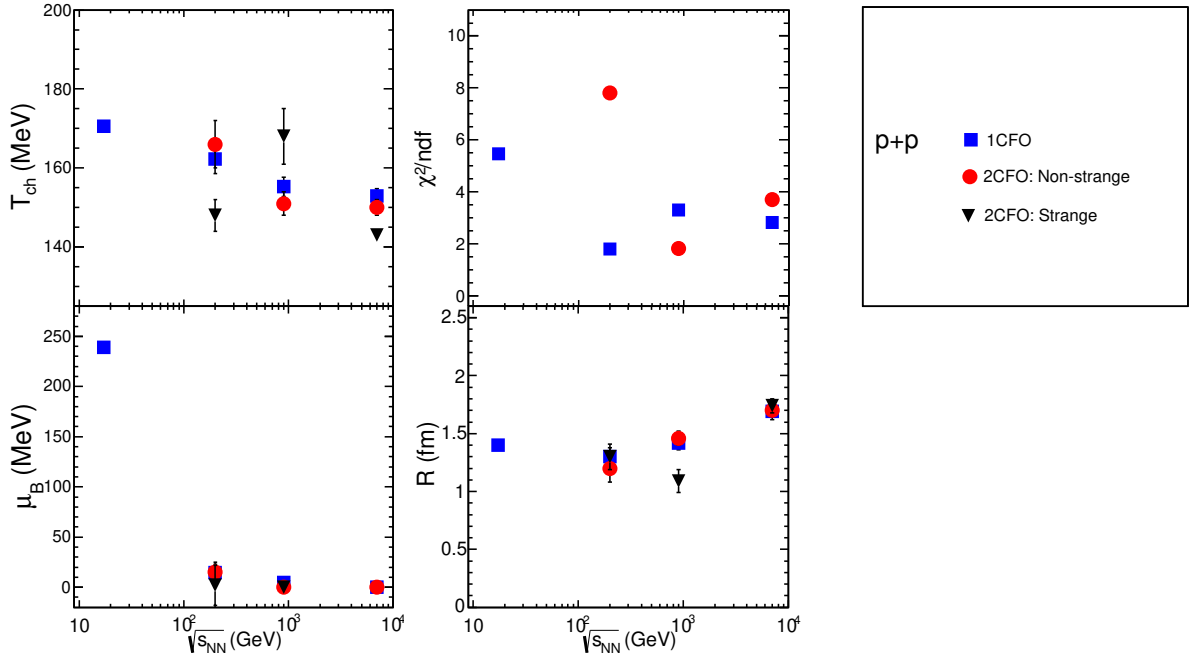
Figure 5.4: Freeze-out parameters T_{ch}, μ_B, R and $\chi^2/$ndf compared between 1CFO and 2CFO in the GCE. The errors are uncertainties on the parameters obtained from statistical model fit.

ference is that the phenomenon of early freeze-out for strangeness that was found in HICs for all $\sqrt{s_{NN}}$ with the strange freeze-out surface hotter and volume smaller compared to the non

$\sqrt{s_{NN}}$ (GeV)	Scheme	T_{ch} (MeV)	μ_B (MeV)	γ_s	R (fm)	χ^2	χ^2/ndf
17.3	1CFO	169.5 ± 3.0	237.1 ± 6.0	0.31 ± 0.01	1.4 ± 0.06	48.9	5.4
200	1CFO	162.2 ± 4.0	14.4 ± 8.5	0.54 ± 0.03	1.3 ± 0.08	16.3	1.8
	2CFO(S)	148.0 ± 4.0	2.0 ± 20.0	1 (Fixed)	1.3 ± 0.11	46.5	7.8
	2CFO(NS)	166.0 ± 6.0	15.0 ± 10.0		1.2 ± 0.12		
900	1CFO	155.4 ± 2.4	0.0 (Fixed)	0.73 ± 0.03	1.42 ± 0.06	27.0	2.7
	2CFO(S)	168.0 ± 7.0	0.0 (Fixed)	1 (Fixed)	1.09 ± 0.10	7.3	1.2
	2CFO(NS)	151.0 ± 3.0	0.0 (Fixed)		1.46 ± 0.06		
7000	1CFO	152.9 ± 2.0	0.0 (Fixed)	0.75 ± 0.02	1.69 ± 0.05	22.6	2.8
	2CFO(S)	143.1 ± 1.0	0.0 (Fixed)	1 (Fixed)	1.74 ± 0.06	26.4	3.7
	2CFO(NS)	150.0 ± 2.0	0.0 (Fixed)		1.70 ± 0.08		

Table 5.2: The chemical freeze-out parameters extracted in 1CFO and 2CFO schemes in Grand Canonical Ensemble. (S) and (NS) refer to the strange and non strange freeze-out surfaces respectively in 2CFO. The $\sqrt{s_{NN}} = 17.3$ GeV fits are for 4π data while the rest are for mid-rapidity data. The errors are uncertainties on the parameters obtained from statistical model fit.

strange freeze-out surface [16] is no more true in p+p collisions. While at $\sqrt{s_{NN}} = 200$ GeV and 7 TeV, the strange freeze-out temperature is lower than the non-strange freeze-out temperature, the reverse is obtained at $\sqrt{s_{NN}} = 900$ GeV. Thus in p+p collisions, the 1CFO scheme with the additional strangeness suppression factor γ_S seems to be a better scheme than the complete chemical equilibrated sequential freeze-out scheme of 2CFO. The expected shorter lifetime of the p+p fireball as compared to A+A could be the reason for such difference in this freeze-out behavior. The chemical freeze-out parameters obtained in 1CFO and 2CFO scheme in grand canonical ensemble for all the energies are tabulated in Table 5.2.

A quantitative look of the descriptive capability of the thermal model in explaining the particle yields in small systems in comparison to larger systems of heavy-ion collisions is presented here. So, the results obtained in the small system of p+p collisions are compared with the published results in heavy-ion collisions [6].

In Fig. 5.5, we have compared the goodness of the fits for each species of particles between p+p and to that in heavy-ion collisions for $\sqrt{s_{NN}} = 200$ GeV. The description capability of the thermal model when we consider only the non-strange and single strange particle are quite similar between p+p and heavy-ions. However, we find that the hadrons with multiple valence strange quarks like ϕ, Ξ and Ω show higher deviation in p+p case compared to heavy-ion collisions. This is reflected in the value of χ^2/ndf, which comes out to be much higher for the p+p data in comparison to published results in heavy-ions [6].
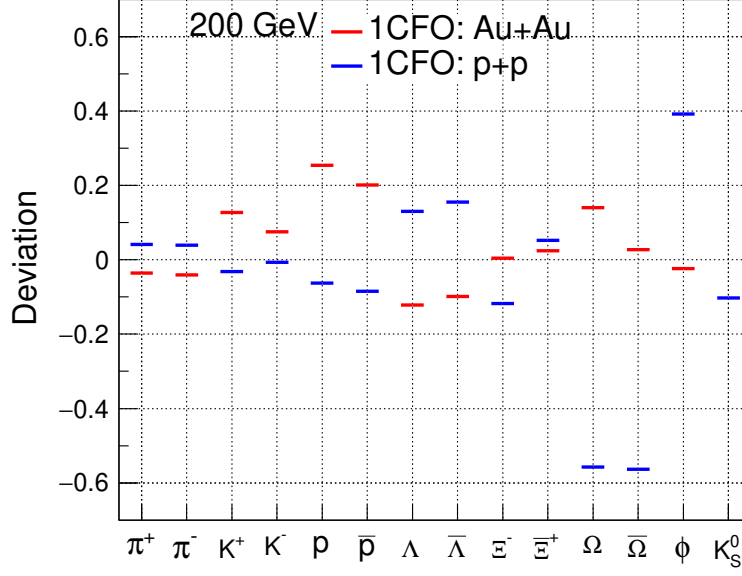
Figure 5.5: The deviation between thermal model and experimental data for each particle species in 1CFO at $\sqrt{s_{NN}} = 200$ GeV compared between p+p and heavy ions [6].

Finally, we have compared the freeze-out parameters T, μ_B, γ_S and R extracted in p+p collisions to that of the published results in heavy-ion collisions in 1CFO scheme. The compilation of all these results is shown in Fig. 5.6. At a lower center of mass energy, the freeze-out temperature obtained from p+p collisions are higher than in A+A as was recently reported [44]. However at higher beam energies ($\sqrt{s_{NN}} > 200$ GeV), the freeze-out T extracted in p+p and for heavy-ion collisions are similar. As we go from RHIC to LHC energies, the freeze-out temperature in both p+p, as well as A+A collisions show a decrease by about 10 MeV. The μ_B extracted from p+p collisions is similar to that obtained from A+A collisions. The value of γ_S and R are distinguishably different in p+p and heavy-ions, both being constantly lower in p+p than heavy-ions. In central A+A collisions, the value of γ_S consistently stays at unity while in p+p it is around 0.2 at SPS and then steadily rises and saturates near 0.8 at the LHC energies. So, even at the higher energies available at LHC the value of γ_S cease to approach unity to attain the strangeness equilibrium condition with $\gamma_S = 1$. This is an indication of significant strangeness suppression in p+p collisions as compared to heavy ion even at the LHC energies. In this context, we must note from Fig. 5.5 that in p+p there is large a deviation between
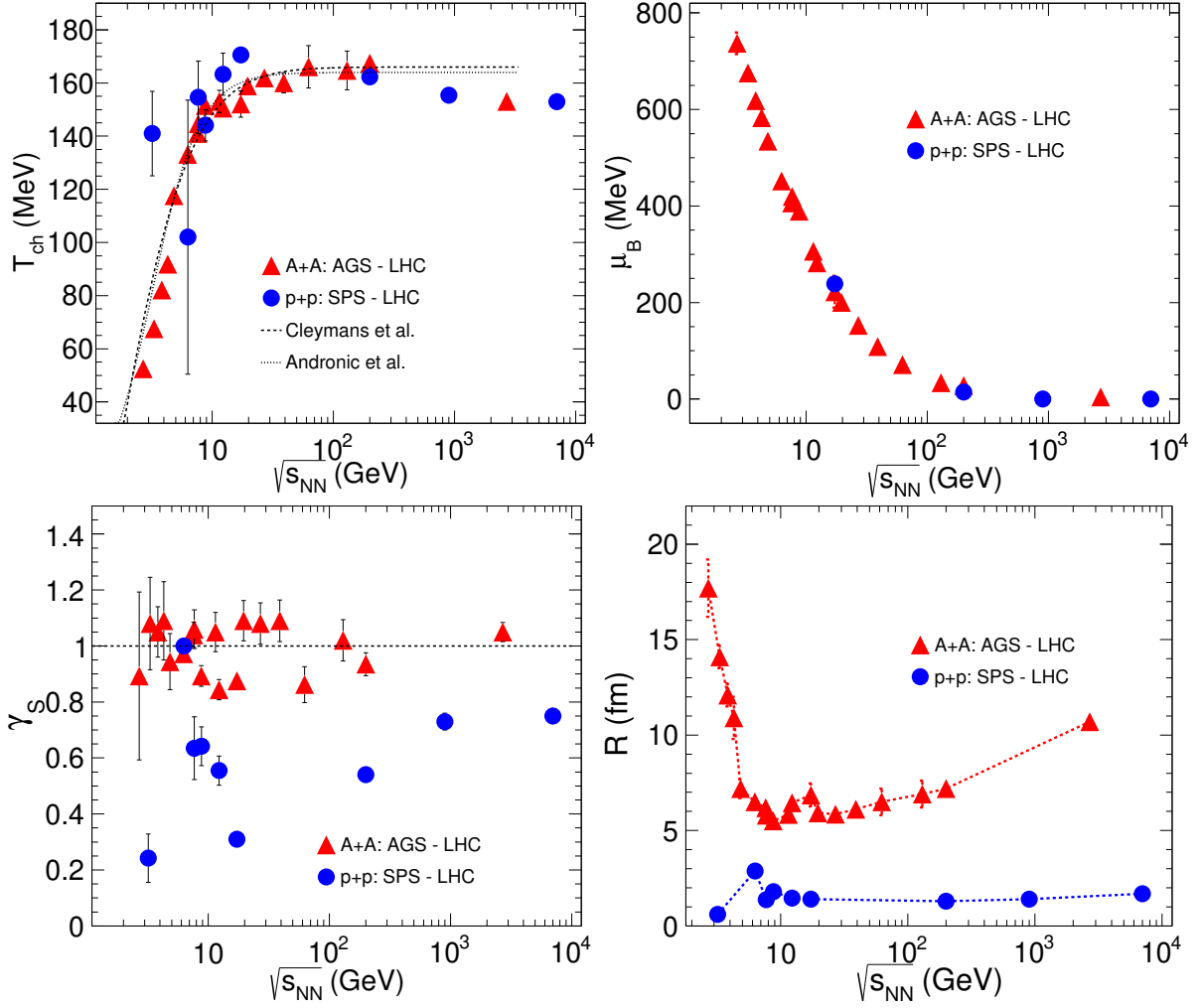
Figure 5.6: A compilation of T (top left), μ_B (top right), γ_S (bottom left) and R (bottom right) as a function of $\sqrt{s_{NN}}$ in p+p collisions shown in blue [44]. The results for A+A are shown in red for comparison [19]. The T vs $\sqrt{s_{NN}}$ parameterizations shown by dashed lines are from Refs. [45, 46]. The errors are uncertainties on the parameters obtained from statistical model fit.

data and model as compared to heavy ion for hadrons with multiple strange valence quarks in drawing the above conclusions. From the top SPS to LHC energies, the value of R doubles in A+A collisions, whereas the corresponding rise in p+p is only about 20%. In this entire range of beam energy, the radius extracted in p+p is almost $5 - 10$ times smaller in comparison to heavy-ions.

5.7   Summary

We have extracted the chemical freeze-out parameters in p+p collisions at $\sqrt{s_{NN}} = 17.3$ (SPS), 200 (RHIC), 900 (LHC) and 7000 GeV (LHC). The SPS data is for 4π rapidity, while the data

from RHIC and LHC are from mid-rapidity. The analysis has been performed with three different choices of ensembles: grand canonical, strangeness canonical and canonical ensemble. Two different freeze-out schemes are exploited - 1CFO, with a single freeze-out surface and 2CFO, with two distinct freeze-out surfaces for strange and non-strange particles. We have also carried out the comparison of chemical freeze-out parameters obtained in p+p collisions with that of A+A collisions.

We have observed that the thermal model fit in the grand canonical ensemble better describes the hadron yields in p+p collisions better in comparison to strangeness and canonical ensemble. This later gets reflected in the comparatively lower value of χ^2/ndf in GCE than SCE and CE. The freeze-out temperature as well μ_B decreases with an increase in beam energy with the later being 0 at LHC energies. The value of γ_S consistently comes out to be lower than unity in p+p system studied here. The value of the fireball radius increases slightly from RHIC to LHC energies in p+p collisions.

The comparison of results between p+p and heavy-ions shows that the deviation between data and model in p+p collision is higher than in A+A collisions for the multi-strange (Ξ, Ω) and hidden strange (ϕ) particles. The freeze-out temperature and μ_B agree between p+p and A+A collisions at the top beam energies. But, on the other hand, the value of γ_S and R comes out to be significantly lower in p+p collisions than in heavy-ion collisions. Even at the LHC energies, γ_S is found to be near 0.8. This indicates that the main difference lies in the freeze-out condition in the strange sector of p+p and A+A collision system. In A+A collision, a complete thermal and chemical equilibrium picture with early freeze-out for strange hadrons provides a good description of the data. While in p+p collisions, the strangeness saturation parameter serving for the non-equilibrium condition of strangeness in 1CFO picture happen to better describe the data. A strong suppression of strangeness across all the beam energies in p+p collisions has been observed which is about 20% even at the highest LHC energies. The expected shorter lifetime of the fireball in case of p+p collisions could be guessed as a reason of the difference for the freeze-out behavior of the strange hadrons relative to A+A collisions.

Bibliography

[1] U. W. Heinz, arXiv:**0407360**.

[2] P. Braun-Munzinger *et al*., Phys. Lett. **B 365**, 1 (1996); G. D. Yen and M. I. Gorenstein, Phys. Rev. **C 59**, 2788 (1999).

[3] F. Becattini *et al*., Phys. Rev. **C 64**, 024901 (2001); A. Andronic *et al*., Nucl. Phys. **A 772**, 167 (2006).

[4] F. Becattini, J. Cleymans, A. Keranen, E. Suhonen, and K. Redlich, Phys. Rev. **C 64**, 024901 (2001).

[5] A. Andronic, P. Braun-Munzinger, and J. Stachel, Nucl. Phys. **A 772**, 167 (2006).

[6] S. Chatterjee *etal*., Adv. in High Eng. Phys., **2015**, 349013 (2015).

[7] I. Kraus *etal*. Phys. Rev. **C 79**, 014901 (2009).

[8] I. Kraus, J. Cleymans, H. Oeschler, K. Redlich, and S.Wheaton, Phys. Rev. **C 76**, 064903 (2007).

[9] J. Cleymans *et al*., arXiv:**1603.09553**.

[10] F. Becattini and U. Heinz, Z. Phys. **C 76**, 269 (1997).

[11] F. Becattini, P. Castorina, A. Milov and H. Satz, Eur. Phys. J. **C 66** 377-386 (2010).

[12] M. Rybczynski, W. Florkowski and W. Broniowski, Phys. Rev. **C 85** 054907 (2012).

[13] J. Stachel *et al.*, J. Phys. Conf. Ser. **509**, 012019 (2014).

[14] J. Steinheimer, J. Aichelin and M. Bleicher, Phys. Rev. Lett. **110** 042501 (2013).

[15] M. Petrán, J. Letessier, V. Petráček and J. Rafelski, Phys. Rev. **C 88** 034907 (2013).

[16] S. Chatterjee, R. Godbole, and S. Gupta, Phys. Lett. **B 727**, 554 (2013).

[17] K. A. Bugaev *et. al.*, Europhys. Lett. **104** 22002 (2013).

[18] S. Chatterjee, B. Mohanty and R. Singh, Phys. Rev. **C 92**, 024917 (2015).

[19] S. Chatterjee *et al.*, Adv. in High Eng. Phys., **2015**, 349013 (2015).

[20] S. Chatterjee and B. Mohanty, Phys. Rev. **C 90**, 034908 (2014).

[21] S. Wheaton *et al.*, hep-ph/**0407174**; S. Wheaton and J. Cleymans, Comput. Phys. Commun. **180**, 84 (2009).

[22] P. Braun-Munzinger, K. Redlich, and J. Stachel, arXiv:**0304013** (2003).

[23] J. Rafelski. *et al.*, Comput. Phys. Commun. **167**, 229 (2005).

[24] R. Brun and F. Rademakers, Nucl. Inst. Meth. Phys. **389**, 81 (1997).

[25] K. Hagiwara *et al.*, Phys. Rev. **D 66**, 010001 (2002).

[26] F. Becattini, Z. Phys. **C 69**, 485 (1996).

[27] F. Becattini and U. Heinz, Z. Phys. **C 76**, 269 (1997).

[28] J. Cleymans and K. Redlich, Phys. Rev. Lett. **81**, 5284 (1998) ; J. Cleymans and K. Redlich, Phys. Rev. **C 60**, 054908 (1999).

[29] C. Alt *et al.* (NA49 Collaboration), Eur. Phys. J. **C 45**, 343 (2006).

[30] T. Anticic *et al.* [NA49 Collaboration], Eur. Phys. J. **C68**, 1 (2010).

[31] T. Anticic *et al.* [NA49 Collaboration], Eur. Phys. J. **C 65**, 9 (2010).

[32] https://edms.cern.ch/document/1075059/4

[33] S. V. Afanasev et al. [NA49 Collaboration], Phys. Lett. **B 491**, 59 (2000).

[34] B. I. Abelev *et al.*, Phys Rev. **C 79**, 034909 (2009).

[35] B. I. Abelev *et al.*, Phys Rev. **C 75**, 064901 (2007).

[36] B. I. Abelev *et al.*, Phys Rev. **C 79**, 064903 (2009).

[37] K. Aamodt *et al.*, Eur. Phys. J. **C 71**, 1655 (2011).

[38] K. Aamodt *et al.*, Eur. Phys. J. **C 71**, 1594 (2011).

[39] J. Adam *et al.*, Eur. Phys. J. **C 75**, 226 (2015).

[40] B. I. Abelev *et al.*, Phys. Lett. **B 712**, 309 (2012); E. Abbas *et al.*, Eur. Phys. J. **C73**, 2496 (2013).

[41] B. I. Abelev *et al.*, Eur. Phys. J. **C 72**, 2183 (2012).

[42] I. Kraus *et al.* Phys. Rev. **C 81**, 024903 (2010).

[43] L. Adamczyk *et al.* (STAR Collaboration), Phys. Rev. **C 96**, 044904 (2017).

[44] V. Vovchenko, V.V. Begun and M.I. Gorenstein, arXiv:1512.08025.

[45] J. Cleymans, H Oeschler, K Redlich and S Wheaton, J. Phys. **G 32**, 12 (2006).

[46] A. Andronic, P. Braun-Munzinger and J. Stachel, Nucl. Phys. **A834**, 237c-240c (2010).

Chapter 6

Freeze-out Systematics due to the Hadron Spectrum

Exploration of the experimental observations with theoretical models is always full of interest as at any point, there always remains a hope for something new to add. The field of experimental heavy-ion physics is in real sense a very good platform for the phenomenological models for their application. A new idea added to an existing phenomenological model may explain the experimental observations in heavy-ion physics in a better sense. Such a spirit is explored in the current chapter of this thesis.

6.1   Introduction

In most of the hadron resonance gas models, the fireball at the time of freeze-out is assumed to be an ideal gas consisting of all the confirmed hadrons and resonances as listed in Particle Data Group [1]. The Hadron Resonance Gas (HRG) Model has been successful in describing the mean hadron yields in high-energy heavy-ion collisions [2–8]. Another recent approach in this area is the explanation of the freeze-out surface through the moments of conserved charges of QCD such as Baryon number (B), Strangeness (S) and Charge (Q). With a few thermal parameters, this approach has also been proved to be very beneficial [9–12]. In this chapter, we will make use of these two types of observables in understanding how the change of input hadron spectrum affects the chemical freeze-out surface.

6.2 Thermodynamics of HRG

The hadron resonance gas model for the heavy-ion collisions is one of the biggest platforms to apply the standard tools and techniques of statistical physics. Thereby, it is possible to represent the system having volume V at a temperature T and thermodynamic potential μ in the language of the Grand Canonical Ensemble (GCE). The thermodynamic potential for the HRG gas is of three types μ_B, μ_S and μ_Q corresponding to the three conserved charges of QCD Baryon number B, strangeness S and Charge Q respectively.

The partition function of the hadron resonance gas in a thermodynamic state $(T, V, \mu_{B,Q,S})$ can be written as a summation of single-particle partition function

$$\ln Z = \sum_i VT^3 \frac{ag_i}{2\pi^2} \int dpp^2/T^3, \tag{6.1}$$

where $Z_i(T, V, \mu_{B,Q,S})$) is the single-particle partition function corresponding to i^{th} hadron species given by

$$\ln Z_i\left(T, \mu_{B,Q,S}\right) = VT^3 \frac{ag_i}{2\pi^2} \int dpp^2/T^3 \times \ln\left(1 + ae^{-\left(\sqrt{(p^2+m_i^2)}+\mu_i\right)/T}\right), \tag{6.2}$$

where $a = -1(+1)$ for mesons(baryons), g_i is the degeneracy, m_i is the mass of the ith hadron and μ_i is the hadron chemical potential which can be factorized as

$$\mu_i = B_i\mu_B + Q_i\mu_Q + S_i\mu_S, \tag{6.3}$$

where B_i, Q_i and S_i are respectively the baryon number, charge and strangeness of the ith species of hadron. Other thermodynamic quantities such as particle multiplicity (N_i) of a particular particle species, pressure (P) and entropy (S) of the HRG are derivable from the partition function of Eq. 6.1 by the following relations.

$$N_i = T\frac{\partial}{\partial\mu_i}\ln Z, \tag{6.4}$$

$$P = T\frac{\partial}{\partial V}\ln Z, \text{ and} \tag{6.5}$$

$$S = \frac{\partial}{\partial T}\left(T\ln Z\right). \tag{6.6}$$

Furthermore, the energy is given by

$$E = T^2 \frac{\partial}{\partial T} \ln Z + \sum_{\text{species i}} \mu_i N_i.$$ (6.7)

The summation is over all established hadrons and resonances contained in PDG. In addition to this, there are many more resonances that have been predicted by Quark model [13, 14] and lattice QCD studies [15] with supportive experimental evidences of occurrence. There are studies comparing the QCD thermodynamics on lattice and HRG that suggests that these extra resonances could significantly contribute to the thermodynamic quantities [16, 17]. Thereby, they can influence the extraction of the freeze-out surface within the framework of HRG [16]. The impact of the systematics of the hadron spectrum on several quantities has been developing as an interesting problem to study. [18–25].

In the context of the thesis, we have studied the systematics of the uncertainties of the hadron spectrum in determining the chemical freeze-out surface within the framework of HRG.

6.3 Extraction of Chemical Freeze-out Surface

From the statistical thermodynamics as discussed in the previous chapters, the yield of primary particles is derivable from the partition function of Eq. 6.1 as

$$N_i^p = \frac{\partial}{\partial \mu_i} \ln Z.$$ (6.8)

In experiments, the measured yield of particles is the sum of primordial yields and contribution from resonance decays. These experimentally measured total particle yields are the input data to be fitted to obtain any thermodynamic quantities. These total yield to those of a particle species is thus can be written by adding the contribution to the primary yield from resonance decays as

$$N_i^t = N_i^p + \sum_j BR_{j \to i} N_j^p,$$ (6.9)

where $BR_{j \to i}$ represents to the branching ratio (BR) of the decay of the jth to i^{th} hadron species.

In general practice, the thermodynamic quantities derived to express the system is the temperature T, the volume V and the thermodynamic potentials μ_B, μ_S and μ_Q. Another additional parameter introduced in the literature is the strangeness saturation factor γ_S, which we have discussed in the previous chapters.

In this work, the freeze-out surface is characterized by the three suitably chosen parameters. The temperature T is the only parameter having a dimension in this analysis and the other two properly scaled dimensionless parameters are μ_B/T and VT^3. μ_B/T governs the baryon fugacity factor and VT^3 can be interpreted in terms of the effective phase space volume occupied by the HRG at the instant of freeze-out. Definitely, the masses of the hadrons are the scale of this analysis which determines the freeze-out T. That is why any variations in the systematics of the hadron spectrum will obviously reflect itself by a change in T. On the other hand, the impact of these variation in the hadron spectrum is expected to be less on the dimensionless parameters μ_B/T and VT^3. This facilitates our choice to work on with $(T, \mu_B/T, VT^3)$ instead of the standard choice with (T, μ_B, V). The strangeness saturation factor is taken to be unity here considering strangeness equilibrium condition. Also, μ_Q and μ_S are consistently solved from the strangeness neutrality condition. This requires that the ratio of net B to net Q equal to that of the colliding nuclei (which is 2.5 for Au and Pb nuclei studied here):

$$\text{Net } S = 0 \text{ and} \tag{6.10}$$

$$\text{Net } B/\text{Net } Q = 2.5. \tag{6.11}$$

From Eq. 6.9, it is obvious that the branching ratio is necessary to calculate the contribution of resonances to the secondary yield to a particle species. These are the feed-down contributions from the heavier unstable hadrons to the observed stable hadrons. The decay properties of the additional resonances are not known. This happens to be a clear challenge to extract the freeze-out surface based on the hadron yields and so is always associated with uncertainty.

Being faced with the above limitation of using mean hadron yields in the HRG model, we have explored another way of determining the freeze-out surface. The comparison of higher moments of conserved charges obtained from experiment and theory can also estimate the chemical freeze-out surface [9–12, 26–29]. In this case, we gain the advantage that the decay

properties of the heavier unstable resonances are not needed. For the calculations using the fluctuations of conserved charges, it is sufficient to know only the quantum number of the unconfirmed states. Strong interaction decays conserve the charges B, S and Q. As a result of this, the uncertainty due to the BRs of the unconfirmed resonances can be eliminated from the estimation of the freeze-out surfaces by the use of conserved charge susceptibilities.

From the thermodynamical calculations, the conserved charge susceptibility of order $(i + j + k)$ is derivable from the partition function as

$$\chi_{BQS}^{ijk} = \frac{\partial^{i+j+k}(P/T^4)}{\partial_i(\mu_B/T)\partial^j(\mu_Q/T)\partial^k(\mu_S/T)},$$

(6.12)

where the pressure is obtained from the partition function as in Eq. 6.5. The estimation of the freeze-out surface using these conserved charge susceptibilities proceeds as follows. The conserved charge susceptibilities are first computed from the theoretical models. Then, they are converted into the moments to have a comparison with the experimentally measured data. There is a one-to-one correspondence between moments and conserved charge susceptibilities. The mean M and variance σ^2 of the conserved charge distributions are directly related to the first and second order susceptibilities of the respective charge c as

$$M_c = \langle N_c \rangle = VT^3 \chi_c^1,$$ (6.13)

$$\sigma_c^2 = \langle (N_c - \langle N_c \rangle)^2 \rangle = VT^3 \chi_c^2,$$ (6.14)

where N_c is the conserved net charge of type c in an event and $\langle N_c \rangle$ is the ensemble average.

For our purpose, we have calculated the conserved charge susceptibilities within HRG and observed the influence of the variation of the hadron spectrum on the description of the chemical freeze-out surface. It has been observed earlier that, the scaled variance σ^2/M of net B and net Q are well explained in the framework of HRG. However, the higher moments such as skewness and kurtosis show discrepancies especially for lower energies [12, 30, 31]. These higher moments also exhibit sensitiveness to non-ideal corrections of incorporating repulsive and attractive interaction within the HRG framework [32–35]. Therefore in the current frame of analysis, we have limited the calculations upto the evaluation of σ^2/M of net Q and net B.

Thereby, we have estimated the effect on the freeze-out surface due to the systematics of the hadron spectrum computed from the conserved charges.

The calculations based on conserved charge susceptibilities are carried out with the experimental constraints. The acceptance cut on transverse momentum and rapidity on the measurement of conserved charges are taken into account [10]. Another limitation is that the neutral hadrons like neutrons are generally are not detected. This means the net-proton fluctuations comes out to be only an approximation of net B [36]. The individual experimental measurements of PHENIX [37] and STAR [38, 39] also show differences in values due to differences in acceptances. We have analyzed the STAR data only. The results are expected to similarly hold for PHENIX data as well, after considering the experimental acceptance.

The first attempt to explain the hadron yield to extract the freeze-out surface through the single freeze-out scheme (1CFO), where all the hadrons are assumed to freeze-out at the same surface. Alternative is the sequential freeze-out scheme (2CFO), where strange and non-strange hadrons are assumed to freeze-out at two distinct freeze-out surfaces. The 1CFO picture explains most of the hadron yields in a wide range of energies, the 2CFO picture also has its remarkability in explaining the QCD thermodynamic quantities on the lattice [40], hadron-hadron cross-section [41, 42] and in-medium hadron masses [43]. The data of hadron yields are analyzed with both the 1CFO and 2CFO scheme. On the other side, for the calculations from the conserved charge fluctuations the data only for net protons [38] and net charge [39] are studied. The net B and net Q fluctuations are mainly dominated by the non-strange sector with most of the contributions coming from the light non-strange hadrons. Owing to this, the data of conserved charge fluctuations are analyzed only in 1CFO scheme.

6.4   Hadron Spectrum

The analysis is carried out by using two different spectrum of hadrons. In one spectrum we have considered all the confirmed hadrons and resonances listed in the PDG 2016 preview [1]. This set contains all the experimentally confirmed mesons from the Meson Summary Table [1] and baryons from the Baryon Summary Table [1] with 4-star and 5-star measurement status. This set is designated as PDG-2016. In the second set, in addition to all the confirmed hadrons and

Mesons		Baryons	
$h_1(1380)$	$f_2(1430)$	$N(1860)$	$N(1880)$
$f_1(1510)$	$f_2(1565)$	$N(1895)$	$N(1895)$
$\rho(1570)$	$h_1(1595)$	$N(2000)$	$N(2040)$
$a_1(1640)$	$f_2(1640)$	$N(2060)$	$N(2100)$
$a_2(1700)$	$\eta(1760)$	$N(2120)$	$N(2300)$
$f_2(1810)$	$a_1(1420)$	$N(2570)$	$N(2700)$
$\eta_2(1870)$	$\rho(1900)$	$\Delta(1750)$	$\Delta(1900)$
$f_2(1910)$	$a_0(1950)$	$\Delta(1940)$	$\Delta(2000)$
$\rho_3(1990)$	$f_0(2020)$	$\Delta(2150)$	$\Delta(2200)$
$\pi_2(2100)$	$f_0(2100)$	$\Delta(2300)$	$\Delta(2350)$
$f_2(2150)$	$\rho(2150)$	$\Delta(2390)$	$\Delta(2400)$
$f_0(2200)$	$f_4(2220)$	$\Delta(2750)$	$\Delta(2950)$
$\eta(2225)$	$\rho_3(2250)$		
$f_4(2300)$	$f_0(2330)$		
$\rho_5(2350)$	$a_6(2450)$		
$f_6(2510)$			
$K(1460)$	$K_2(1580)$	$\lambda(1710)$	$\lambda(2000)$
$K(1630)$	$K_1(1650)$	$\lambda(2020)$	$\lambda(2050)$
$K(1830)$	$K_0^*(1950)$	$\lambda(2325)$	$\lambda(2585)$
$K_2^*(1980)$	$K_2(2250)$	$\Sigma(1480)$	$\Sigma(1560)$
$K_3(2320)$	$K_5^*(2380)$	$\Sigma(1580)$	$\Sigma(1620)$
$K_4(2500)$	$K(3100)$	$\Sigma(1690)$	$\Sigma(1730)$
		$\Sigma(1770)$	$\Sigma(1840)$
		$\Sigma(1880)$	$\Sigma(1900)$
		$\Sigma(1940)$	$\Sigma(2000)$
		$\Sigma(2070)$	$\Sigma(2080)$
		$\Sigma(2100)$	$\Sigma(2455)$
		$\Sigma(2620)$	$\Sigma(3000)$
		$\Sigma(3170)$	$\Xi(1620)$
		$\Xi(2120)$	$\Xi(2250)$
		$\Xi(2370)$	$\Xi(2500)$
		$\Omega(2380)$	$\Omega(2470)$

Table 6.1: List of additional resonances in PDG-2016+ that are not included in PDG-2016. This consists of one- and two- stars measurement status baryons and unmarked mesons from PDG 2016 [1] that are yet to be confirmed experimentally.

resonances contained in PDG-2016, we have added the other unconfirmed mesons and baryons that are marked with one - or two - star experimental measurement status from the Mesons and Baryons Summary Tables. These additional mesons and baryons are still awaiting for experimental confirmation and are listed in Table 6.4. This new list of hadrons and resonances is referred to as the PDG-2016+ set. Only the hadrons with light flavor quark (up, down and strange) constituents are considered here. It has been observed that the set PDG-2016+ has

provided a satisfactory explanation to most of the thermodynamic quantities in the hadronic phase of continuum lattice QCD calculations [17].

Previously, we have pointed out that the BRs and decay properties of the heavier resonances are a key thing in computing the freeze-out surface using the hadron yields. For the states constituting the set PDG-2016, the Particle Data Group [1] provides BRs for most of the resonances. However, for the additional resonances listed in Table 6.4, the BRs for its decay channels are all unknown. Here comes the challenge and to proceed further we have made a simple assumption. The fact that the resonances falling on the same family has similar decay properties is implemented here. For an unconfirmed resonance R, we have assigned the decay properties of the known confirmed resonances having the same quantum number as that of R and has mass immediate to it. To estimate the systematic uncertainty associated with these unknown BRs, the analysis has been carried out by taking the BRs from known resonances that are both heavier and lighter than the unknown resonance R. This systematic variation in the BRs results in a large variation of χ^2 as well as larger error bars in the fits to the PDG-2016+ spectra in comparison to PDG-2016. This concern limits us to include further theoretically predicted resonance into the set of PDG-2016+. Because, in that case, the systematic uncertainty will become too large to draw any relevant physics conclusion from the study.

6.5   The μ_S/μ_B Ratio

The value of μ_S obtained from the strangeness neutrality condition of Eq. 6.10 is sensitive to the strange hadron spectrum [16]. There are also lattice based studies on the μ_S/μ_B ratio with constrained hadron spectrum as far as the hadrons in the strange sectors are considered [16,17]. For a given temperature T, it has been observed that the hadron spectrum of PDG-2012 under estimates the μ_S/μ_B ratio. This discrepancy might be solved by including more resonances into the hadron spectrum that are predicted from the quark-model based studies on lattice QCD calculations but are still waiting for the experimental verification. The particle list of PDG-2016 has confirmation for many such new resonances with some remaining unconfirmed. This μ_S/μ_B ratio has been extensively analyzed here by considering three distinct hadron spectrums: PDG-2012, PDG-2016 and PDG-2016+. This is especially done to note down the significance

of the added new resonances before presenting the final results of the interest of this study.
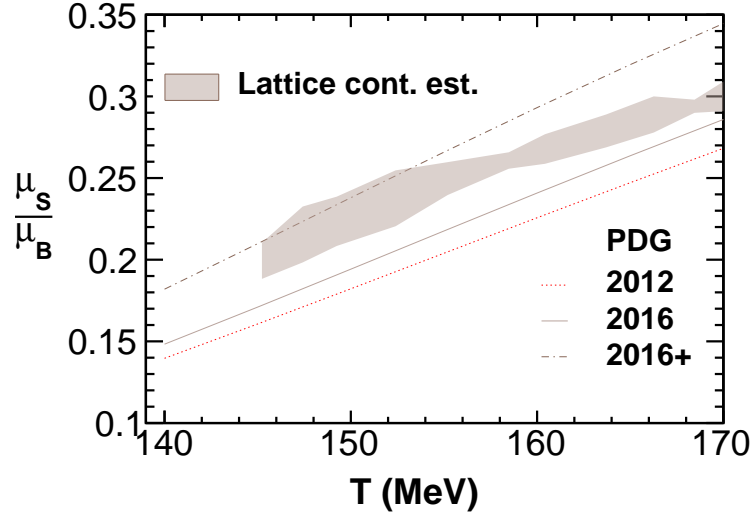
Figure 6.1: Leading order μ_S/μ_B from continuum estimate of lattice [16] compared to that of HRG with hadron spectrum from PDG 2012, 2016 and 2016+.

The μ_S/μ_B ratio is shown in Fig. 6.1 as a function of freeze-out temperature T. The results computed from the continuum estimate of lattice QCD calculations [16] are compared to that of HRG results with the hadron spectrum from PDG 2012, 2016 and 2016+. The significance of systematics of the hadron spectrum due to the addition of extra resonances can be clearly observed. The concerned issue of flavor hierarchy can be particularly observed by this study. We observed that at a lower temperature, the same value for μ_S/μ_B has been observed from both lattice studies as well from calculation in HRG by adding the new resonances into the hadron spectrum beyond what is listed in the particle list of PDG-2012 [44] as advocated in Ref [16]. There is a lowering in the strange freeze-out T, that could possibly customize the flavor hierarchy presented earlier with the 2CFO fit in HRG by considering the particle list of PDG-2012 [41]. It can be noticed from Fig. 6.1 that, the calculations from HRG using the particle list of PDG-2016 and PDG-2016+ lie on either side of the result of continuum estimate of the lattice. This suggests that, the under prediction of μ_S/μ_B ratio by the hadron spectrum of PDG-2012 is well solved by the particle set of PDG-2016+.

6.6 Results and Discussions

We have analyzed the data across a wide range of beam energy to investigate the systematics of the hadron spectrum on the extraction of chemical freeze-out surface. We have calculated the thermodynamic quantities $(T, \mu_B/T, VT^3)$ in both 1CFO and 2CFO schemes for the data of hadron yields. Whereas, for the data of conserved charges the analysis is only carried out in 1CFO picture as we have discussed earlier. The data on mean mid-rapidity hadron yields are taken from the experiments of SPS, STAR and ALICE for Pb+Pb and Au+Au collisions across a wide range of beam energies starting from 6.27 GeV to 2.76 TeV [45–65]. The analysis on the conserved charge of net B and net Q are carried out on the published STAR data in the energy range of 11.5-200 GeV [38, 39].

All the results on extracted thermodynamic parameters $(T, \mu_B/T, VT^3)$ compiled together in both 1CFO and 2CFO pictures as a function of beam energy are presented in Fig. 6.2. The calculations obtained from the hadron yields in HRG as well as results from the scaled variance of net B and net Q are shown in comparison. The left panel has the results from the calculations in 1CFO scheme, whereas the right panel contains the results from 2CFO scheme. The results are shown as a function of beam energy with the top panel showing freeze-out T, the middle panel showing μ_B/T and the bottom panel presenting $10^{-2}VT^3$.

From the top panel of Fig. 6.2, we can observe that the freeze-out temperature T in 1CFO as well as the strange and non-strange freeze-out T in 2CFO shows a lowering in values when we include more resonances into the hadron spectrum. However, the systematic errors being large are not making this conclusion concrete. Therefore, we have looked at the results from the calculations of conserved charge fluctuation shown in dashed and solid pink lines for the two sets of PDG-2016 and PDG-2016+ respectively. This result verifies our conclusion of the cooling behavior upon the addition of extra resonances to the HRG. As previously observed, that the resulting T obtained from conserved charge fluctuation is even lower from that obtained from the calculations on hadron yields [12]. The difference between the temperature obtained from these two types of calculations are more pronounced for $\sqrt{s_{NN}} < 20$ GeV. We can further notice from the right side plot of the top panel of Fig. 6.2 that, the extracted freeze-out T obtained from scaled variance data of net B and net Q are closer to the non-strange T in both
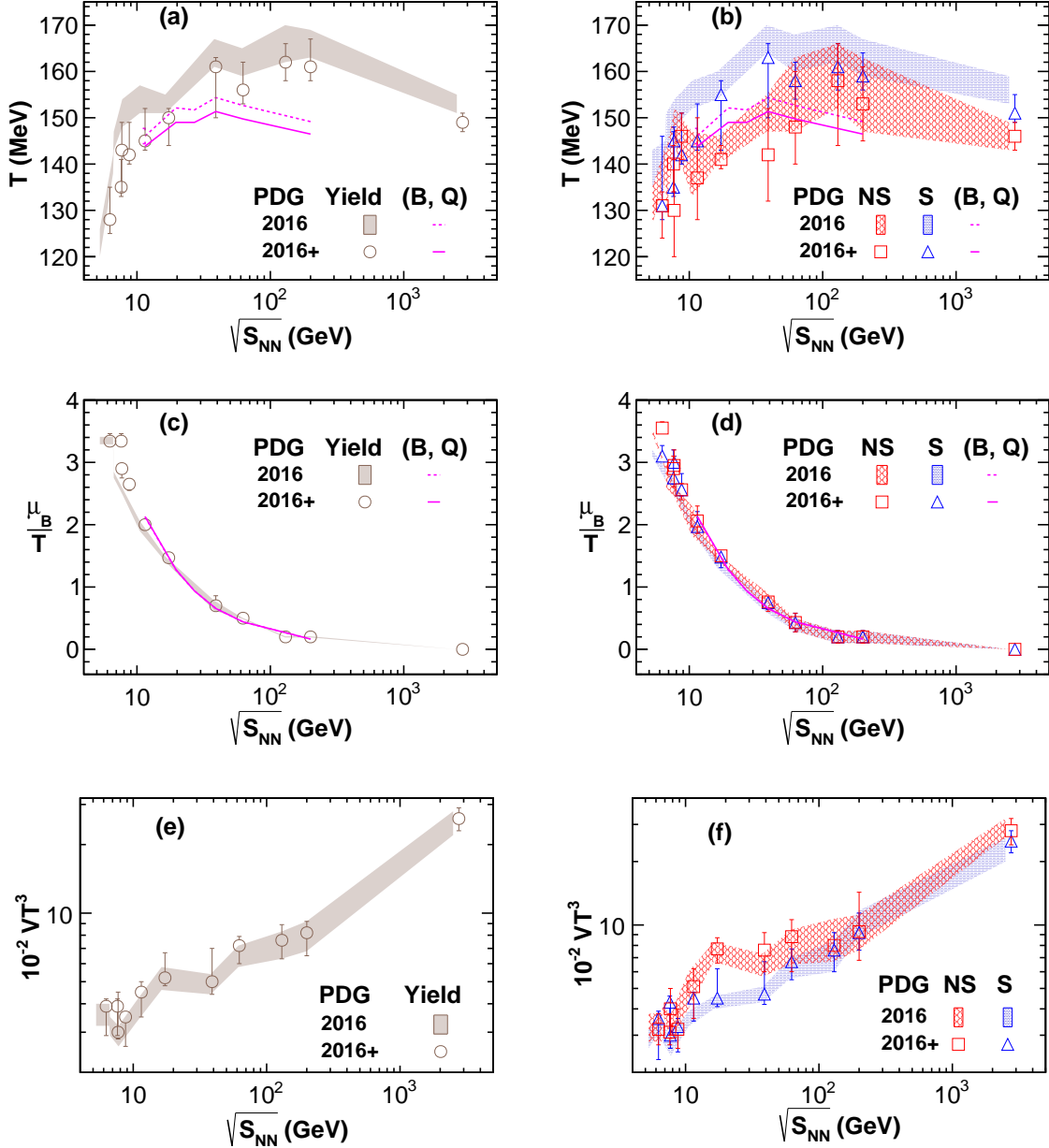
Figure 6.2: The extracted thermal parameters T, μ_B/T and $10^{-2}VT^3$ in 1CFO (left) and 2CFO (right) schemes with PDG-2016 and PDG-2016+ hadron spectra as a function of beam energy. (B,Q) refer to the use of data of conserved charges on net B and net Q to extract freeze-out parameters.

PDG-2016 and PDG-2016+ from calculations on hadron yields. This could be because the particles entering into the calculation of conserved charge fluctuations are dominated by the non-strange lightest meson π and baryon p.

The middle panel of Fig. 6.2 shows μ_B/T for various beam energies extracted in 1CFO (left) and 2CFO (right) schemes. This baryon fugacity parameter shows its stability across dif-

ferent freeze-out schemes as well as the results from data of hadron yields as well as conserved charge fluctuations are in agreement. The results obtained using the two different hadron spectrums are also consistent with each other. A closed look for $\sqrt{s_{NN}} < 10$ GeV reflects a slight dependence of μ_B/T on both flavors as well as hadron spectrum. This region corresponds to beam energy where the fireball is mostly dominated by baryonic matter.

The phase space volume factor VT^3 is plotted in the bottom panel for various $\sqrt{s_{NN}}$ in 1CFO (left) and 2CFO (right) schemes. Here V is the phase space volume of the fireball in co-ordinate space at the time of freeze-out. Similar to μ_B/T, this factor also exhibits its stability towards the addition of extra resonances. i.e., the results from PDG-2016 are in a good agreement with the results obtained from the set PDG-2016+. However, in contrast to μ_B/T, VT^3 shows its dependence on strange and non-strange particle flavors similar to T. The value of phase space volume for non-strange particles are found to larger than that of the strange particles in 2CFO picture of analysis.

In making the comments on flavor hierarchy structure of T and VT^3 in Fig. 6.2, we have not considered the correlation between the strange and non-strange freeze-out parameters. This correlation effect might influence the structure of flavor hierarchy. To address this scruple, we have also extracted the ratio of strange to non-strange freeze-out parameters directly from the fits. The ratio of strange to non-strange T and phase space volume factor VT^3 as a function of $\sqrt{s_{NN}}$ is plotted in Fig. 6.3. The results using the particle set PDG-2016 are shown in open circles, whereas that from the set PDG-2016+ are shown in bands.

We observed that the flavor hierarchy structure of freeze-out T obtained in PDG-2016 is consistent with the earlier observation with the particle set of PDG-2012 [41]. Additionally, the central values in the bands of Fig. 6.3 also supports the flavor dependence of freeze-out T in the particle set of PDG-2016+. Surely, the error bars being quite large in this case due to the uncertainty induced by the variation of the decay properties of the unconfirmed resonances is limiting us in making any quantitative estimate of flavor hierarchy. Even after including the large error bars, we can qualitatively comment that the observations favors $T_s/T_{ns} > 1$ and $V_s^3 T_s / V_{ns} T_{ns}^3 < 1$ across most of the beam energies considered in this analysis. Again, the observations with the particle set of PDG-2016+ at the highest energies available at LHC
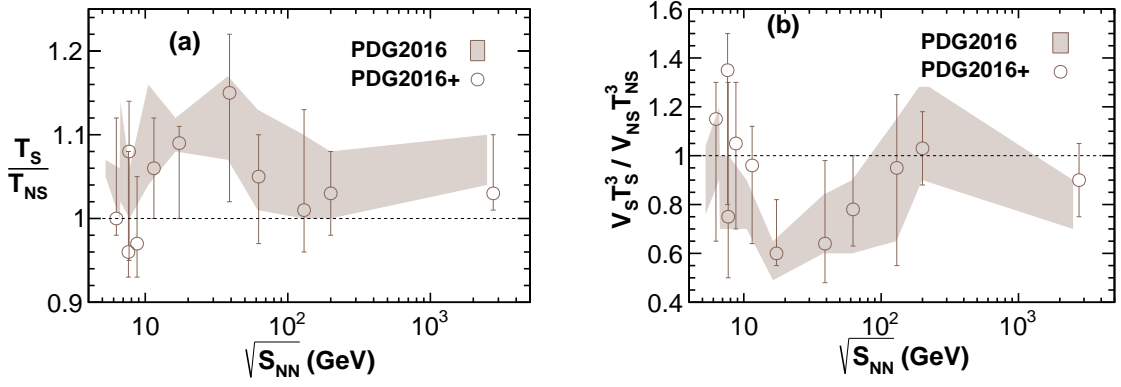
Figure 6.3: Flavor hierarchy in freeze-out T (left) and VT^3 (right) as a function of $\sqrt{s_{NN}}$ and its dependence on the hadron spectrum.

makes the flavor hierarchy nature of T and VT^3 more visible. The central value here reveals that on the addition of extra resonances in PDG-2016+ falls outside the band of PDG-2016 and closer to unity. Again, as we have noted from the earlier observations on flavor hierarchy with PDG-2012 [41], the flavor hierarchy appears more visible at the LHC energies, is also more prominent between the energy range $\sqrt{s_{NN}} \sim 10 - 100$ GeV. The quality of this flavor hierarchy structure shows a broad peak type structure in T_s/T_{ns} and whereas a trough in $V_s^3 T_s/V_{ns} T_{ns}^3$ in this beam energy range. The central values with PDG-2016+ exhibit a flip in this flavor hierarchy structure for $\sqrt{s_{NN}} < 10$ GeV. The error bars being very large in this case in not supporting any conclusive statement. In the energy range of $\sqrt{s_{NN}} \sim 10 - 100$ GeV, the monotonic nature of flavor hierarchy structure points us towards the earlier freeze-out of hadrons in the non-strange sector [41]. Another point to be noted here is that, the data from the STAR beam energy scan [66] shows a very interesting trend in mean transverse mass $\langle m_T \rangle - m$ similar to that observed in VT^3 in this energy range. This trend in STAR data is till now open for discussion and is yet to be fully understood [67, 68]. Future investigations in this direction may unveil the physics behind this trend and any common origin of this matching.

So far we have observed that the systematics of the hadron spectrum mostly affects the freeze-out temperature T. The dimensionless thermodynamic parameters μ_B/T and VT^3 shows quite stability to the addition of extra resonances into the hadron spectrum. The reduction in freeze-out T upon addition of extra resonances into the hadron spectrum can be understood in two ways. At first, on adding more resonances the ratio μ_S/μ_B obtained from

the strangeness equilibrium condition shifts towards the lower value of T [16, 17]. This brings down the temperature T only for the strange sector. In the second way, the cooling of T may be understood by the feed-down contribution of the additional resonances. The feed-down contribution to the non-strange hadrons comes both from heavier strange and non-strange hadrons, but this contribution to strange hadrons is only from the strange sector. Thus, it could mean that the first factor lowers only the strange T, whereas the second factor cools down both the strange and non-strange temperatures affecting more strongly the non-strange T. This is a favorable reason for the maintenance of flavor hierarchy on the addition of extra resonances.
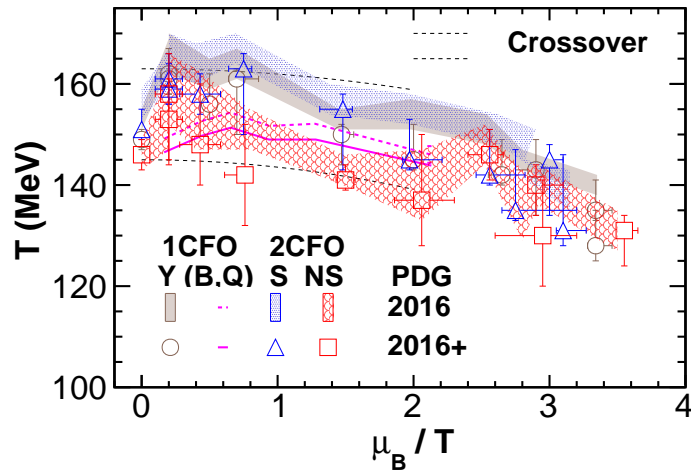
Figure 6.4: $T - \mu_B/T$ plane: Freeze-out coordinates in heavy ion collisions have been compared with the QCD crossover region as estimated in lattice QCD computations [69–73].

In the end, we have plotted all the freeze-out T as a function of μ_B/T for all the beam energies analyzed in Fig. 6.4. The two dashed lines represent the estimates of the QCD crossover transition from the hadron to the quark gluon plasma (QGP) phase from the lattice QCD approach which are shown for comparison purposes. The dashed lines corresponds to a temperature $T = 163$ MeV (Upper) and $T = 145$ MeV (lower) at $\mu_B = 0$ [69]. These respectively have curvatures of ~ 0.006 [70, 71] and ~ 0.01 [72, 73] and cover the estimates of the QCD crossover region from lattice QCD calculations. The central values of the results from PDG-2016 hadron spectrum gives freeze-out $T < 165$ MeV. This reveals a consistency between the hadronization surface estimated on the lattice and the extracted freeze-out temperature. Additional suspected resonances included in the hadron spectrum of PDG-2016+ further shifts this

$\sqrt{s_{NN}}$ (GeV)	T (MeV)		μ_B (MeV)		χ^2	
	Confirmed	All	Confirmed	All	Confirmed	All
11.5	146.05(1.65)	143.85(0.55)	310.25(3.85)	306.5(3.0)	0.14	0.12
19.6	152.12(0.12)	149.0(0.05)	194.0(0.5)	190.75(0.25)	0.63	0.13
27	51.7(0.1)	149.0(0.05)	142.2(0.2)	139.5(0.5)	0.23	0.19
39	154.35(0.05)	151.35(0.05)	101.2(0.1)	99.25(0.05)	0.19	0.21
62.4	152.65(0.06)	149.74(0.06)	67.25(0.05)	66.01(0.05)	0.14	0.26
200	149.16(0.1)	146.47(0.05)	24.69(0.1)	24.24(0.1)	0.12	0.19

Table 6.3: 1CFO parameters obtained from the data of scaled variance of net B and net Q with the hadron spectrum of PDG-2016 and PDG-2016+ respectively represented as Confirmed and All. In the brackets the errors on the parameters are given.

temperature towards the hadron phase. Till now, estimates available from lattice calculations are limited to $\mu_B/T \sim 2$. Whereas, the freeze-out parameters extracted at lower beam energies results in $\mu_B/T \sim 4$. However, these results suggest no abrupt change in curvature resulting in a smooth continuation of the hadronization surface with the increase in baryon density. Another interesting part of these types of studies may be checked by including inter-hadron interaction into HRG in terms of attractive and repulsive forces [32, 33]. Thereby, we can check either these results maintain its consistency or changes upon the addition of these extra resonances.

$\sqrt{s_{NN}}$ (GeV)	T (MeV)		μ_B (MeV)		$10^4 V$ (fm^3)		χ^2	
	Confirmed	All	Confirmed	All	Confirmed	All	Confirmed	All
6.27	132(3)	128(-3,+7)	440(5)	430(-6,+26)	1.6(2)	1.9(-7,+3)	9.5	11-14
7.62	140(2)	135(-2,+6)	390(10)	380(-12,+30)	1.4(1)	1.7(-6,+2)	17	12-19
7.7	145(2)	143(-9,+2)	405(15)	415(-40,+15)	1.1(2)	1.1(-2,+7)	14.4	14-19
8.76	151(3)	142(-2,+7)	390(15)	365(-10,+40)	0.9(1)	1.2(-4,+2)	9.1	5-22
11.5	154(3)	145(-2,+7)	305(15)	285(-12,+40)	1.0(2)	1.5(-5,+2)	7.7	9-13
17.3	153(2)	150(-6,+2)	220(5)	220(5)	1.4(1)	1.6(-2,+7)	29	24-51
39	164(3)	161(-11,+2)	115(15)	115(-22,+10)	1.1(2)	1.2(-2,+9)	7.7	10-11
62.4	162(3)	156(-3,+6)	71(10)	70(10)	1.6(3)	1.9(-5,+3)	14.6	3-20
130	166(4)	162(4)	35(12)	35(12)	1.6(3)	1.8(4)	7.7	1-10
200	166(3)	161(-3,+6)	33(10)	32(10)	1.8(2)	2.0(-6,+4)	47	8-60
2760	153(2)	149(2)	0	0	7(1)	7.5(-1.0,+2.0)	15	7-19

Table 6.2: 1CFO parameters obtained from the fits of to mean hadron yields with the hadron spectrum PDG-2016 and PDG-2016+ respectively represented as Confirmed and All. In the brackets the errors on the parameters are given.

$\sqrt{s_{NN}}$ (GeV)	T (MeV)				μ_B (MeV)				$10^4 V$ (fm^3)				χ^2	
	Confirmed		All		Confirmed		All		Confirmed		All		Confirmed	All
	S	NS	S	NS	S	NS	S	NS	S	NS	S	NS		
6.27	139(4)	131(4)	131(-3,+15)	131(-7,+3)	440(10)	450(5)	410(-15,+50)	450(10)	1.1(2)	1.5(3)	1.7(-13,+2)	1.4(-3,+6)	3	2-11
7.62	143(2)	140(4)	135(-2,+12)	140(-6,+4)	415(15)	405(10)	375(-15,+75)	405(-15,+15)	1.2(2)	1.1(3)	1.7(-7,+2)	1.1(-2,+5)	4	2-9
7.7	147(4)	136(7)	145(-11,+3)	130(-10,+11)	425(20)	390(25)	435(-55,+25)	390(-30,+20)	1.0(2)	1.5(6)	1.0(-2,+8)	2(-1.1,+1)	7	8-16
8.76	151(3)	148(4)	142(-2,+9)	146(5)	400(20)	375(20)	365(-15,+60)	365(20)	0.8(2)	1.1(3)	1.2(-6,+2)	1.1(4)	8	1-20
11.5	155(3)	140(7)	145(-2,+8)	137(-9,+13)	310(20)	295(25)	285(-40,+45)	290(-25,+30)	1.0(1)	2.0(8)	1.5(-5,+2)	2(1)	2	7-11
17.3	157(3)	143(3)	155(-12,+3)	141(-2,+3)	215(10)	212(6)	230(-40,+15)	215(10)	1.1(1)	3.0(3)	1.2(-2,+9)	3.0(-9,+8)	10	9-32
39	167(3)	151(4)	163(-13,+3)	142(-10,+10)	115(15)	120(15)	120(-25,+15)	110(30)	1.0(2)	2.0(5)	1.1(-1,+10)	2.8(-10,+8)	1	4-10
62.4	164(4)	155(8)	158(4)	148(-8,+12)	70(20)	70(20)	70(20)	70(20)	1.4(3)	2.2(8)	1.7(3)	3(-1.7,+1)	13	2-19
130	166(4)	159(7)	161(5)	158(-14,+8)	35(20)	30(20)	40(-20,+10)	35(15)	1.6(4)	2.2(8)	1.8(4)	2.2(10)	7	1-9
200	163(4)	155(8)	159(-3,+5)	153(8)	32(20)	30(20)	35(20)	30(15)	2.5(5)	2.5(7)	2.4(6)	2.6(8)	31	4-41
2760	156(3)	146(3)	151(-2,+4)	146(3)	0	0	0	0	6(1)	10(2)	8(-2,+1))	9.5(-15,+25)	6	5-12

Table 6.4: 2CFO parameters obtained from the fits of to mean hadron yields with the hadron spectrum PDG-2016 and PDG-2016+ respectively represented as Confirmed and All. In the brackets the errors on the parameters are given.

The chemical freeze-out parameters (T, μ_B, V) obtained in this analysis from the fits to mean hadron yields and conserved charge fluctuations in 1CFO picture from the hadron spectrum of PDG-2016 and PDG-2016+ are respectively tabulated in the Tables 6.2, 6.3. These results in the 2CFO scheme from the data of hadron yields is listed in Table 6.4.

6.7   Summary

We have carried out the analysis using the data of hadron yields and fluctuations in conserved charges in the framework of HRG and extracted the chemical freeze-out surface. These results are always associated with unavoidable uncertainties due to the input of the hadron spectrum. We have obtained the results within both 1CFO as well as 2CFO picture of freeze-out. The analysis has been carried out with the latest hadron spectrum available in the Particle Data Group of 2016 (PDG-2016). The missing resonances still remaining experimentally unconfirmed is included in the set PDG-2016+ in addition to the all confirmed resonances listed in PDG-2016. We have investigated the effect of the addition of these extra resonances on the estimation of the freeze-out surface. We have observed that this addition of extra resonances into the hadron spectrum mostly affects the freeze-out T and reduces it by about $\sim 5\%$ than the hadron spectrum of PDG-2016. The other two dimensionless parameters, the phase space volume factor VT^3 and baryon fugacity factor μ_B/T are almost insensitive towards the variation of the hadron spectrum. The new freeze-out temperature calculated from the updated hadron spectrum remains within the upper bound of lattice estimate of hadronization temperature.

The cooling behavior of freeze-out temperature is seen in both the analysis from the data

of hadron yields as well as conserved charge fluctuations. The calculated temperature from the data of conserved charge fluctuations are always found to be lower than the calculations on mean hadron yields data within the 1CFO picture. On the other hand, in 2CFO picture, the non-strange freeze-out temperature obtained from the data of hadron yields is found to match with that extracted from the scaled variance of net B and net Q.

The results obtained in this study with the updated hadron spectrum mimics the future perspective on these types of studies as soon as the suspected resonances will get their experimental evidences. The comparison between the fits of PDG-2016 and PDG-2016+ reveals a stable behavior of μ_B/T and VT^3 and lower value of freeze-out T on the addition of extra resonances into the hadron spectrum. These observations can be understood by the following two ways:

1. First remark can be drawn from the plot of μ_S/μ_B mostly governed by the strange sector. The addition of extra resonances brings down the freeze-out temperature. In 1CFO picture with a single freeze-out T, this ratio brings down both strange and non-strange T resulting in all total in lower value of T upon addition of extra resonances. In the 2CFO picture, it only cools down the strange sector reducing the flavor hierarchy structure. We have seen in Fig. 6.1 that the spectrum PDG-2016+ is lying in the lower edge of T of the continuum lattice QCD estimate. This suggests that in future the more updated hadron spectrum with more resonances can not further bring down the temperature through this mechanism. The continuing flavor hierarchy structure in the hadron spectrum of PDG-2016+ is also not expected to be reduced in the future upon addition of any more resonances.

2. The second contribution to the cooling of the system upon addition of extra resonances is from the feed-down contribution. The feed-down contribution of additional resonances cools down both strange and non-strange temperatures. All the resonances have their feed-down contribution to observed non-strange hadrons, whereas only heavier strange resonances have their contribution to stable strange hadrons. Thus, this feed-down mechanism cools down both strange and non-strange temperature and more strongly the non-strange temperature. This induces the flavor hierarchy structure to survive on the addition

234

of extra resonances more prominently.

The observations in this analysis confirm the flavor hierarchy nature of treating strange and non-strange hadron separately. More evidences about these flavor dependent nature of thermodynamic observables could be investigated by the inclusion of attractive and repulsive forces into the HRG model. The important consideration in this type of analysis is the choice of thermodynamic parameters to clearly visualize its flavor dependent nature.

Bibliography

[1] C. Patrignani *et al*. (Particle Data Group), Chin. Phys. **C 40**, 100001 (2016).

[2] P. Braun-Munzinger, J. Stachel, J. P. Wessels, and N. Xu, Phys. Lett. **B 365**, 1 (1996).

[3] G. D. Yen and M. I. Gorenstein, Phys. Rev. **C 59**, 2788 (1999).

[4] J. Cleymans and K. Redlich, Phys. Rev. **C 60**, 054908 (1999).

[5] F. Becattini, J. Cleymans, A. Keranen, E. Suhonen, and K. Redlich, Phys. Rev. **C 64**, 024901 (2001).

[6] A. Andronic, P. Braun-Munzinger, and J. Stachel, Nucl. Phys. **A 772**, 167 (2006).

[7] S. Chatterjee, S. Das, L. Kumar, D. Mishra, B. Mohanty, R. Sahoo, and N. Sharma, Adv. High Energy Phys. **2015**, 349013 (2015).

[8] S. Chatterjee, A. K. Dash, and B. Mohanty, (2016), arXiv:**1608.00643** [nucl-th].

[9] F. Karsch and K. Redlich, Phys. Lett. **B 695**, 136 (2011).

[10] P. Garg, D. K. Mishra, P. K. Netrakanti, B. Mohanty, A. K. Mohanty, B. K. Singh, and N. Xu, Phys. Lett. **B 726**, 691 (2013).

[11] A. Bhattacharyya, S. Das, S. K. Ghosh, R. Ray, and S. Samanta, Phys. Rev. **C 90**, 034909 (2014).

[12] P. Alba, W. Alberico, R. Bellwied, M. Bluhm, V. Mantovani Sarti, M. Nahrgang, and C. Ratti, Phys. Lett. **B 738**, 305 (2014).

[13] S. Capstick and N. Isgur, Phys. Rev. **D 34**, 2809 (1986).

[14] D. Ebert, R. N. Faustov, and V. O. Galkin, Phys. Rev. **D 79**, 114029 (2009).

[15] R. G. Edwards, N. Mathur, D. G. Richards, and S. J. Wallace (Hadron Spectrum), Phys. Rev. **D 87**, 054506 (2013).

[16] A. Bazavov *et al.*, Phys. Rev. Lett. **113**, 072001 (2014).

[17] P. Alba *et al.*, (2017), arXiv:**1702.01113** [hep-lat].

[18] W. Broniowski and W. Florkowski, Phys. Lett. **B 490**, 223 (2000).

[19] W. Broniowski, W. Florkowski, and L. Ya. Glozman, Phys. Rev. **D 70**, 117503 (2004),

[20] J. Noronha-Hostler, C. Greiner, and I. A. Shovkovy, Phys. Rev. Lett. **100**, 252301 (2008),

[21] S. Chatterjee, R. M. Godbole, and S. Gupta, Phys. Rev. **C 81**, 044907 (2010),

[22] P. M. Lo, M. Marczenko, K. Redlich, and C. Sasaki, Phys. Rev. **C 92**, 055206 (2015),

[23] E. Ruiz Arriola, W. Broniowski, E. Megias, and L. L. Salcedo (2016) pp.128-139, arXiv:**1612.07091** [hep-ph].

[24] J. Noronha-Hostler (2016) pp. 118-127, arXiv:**1612.07765** [nucl-th].

[25] V. V. Begun, V. Yu. Vovchenko, and M. I. Gorenstein, arXiv:**1701.03358**.

[26] R. V. Gavai and S. Gupta, Phys. Lett. **B 696**, 459 (2011).

[27] A. Bazavov *et al.*, Phys. Rev. Lett. **109**, 192302 (2012).

[28] S. Borsanyi, Z. Fodor, S. D. Katz, S. Krieg, C. Ratti, and K. K. Szabo, Phys. Rev. Lett. **111**, 062005 (2013).

[29] A. Bazavov et al., Phys. Rev. **D 93**, 014512 (2016).

[30] S. Gupta, X. Luo, B. Mohanty, H. G. Ritter, and N. Xu, Science **332**, 1525 (2011).

[31] R. P. Adak, S. Das, S. K. Ghosh, R. Ray, and S. Samanta, Phys. Rev. **C 96**, 014902 (2017).

[32] M. Albright, J. Kapusta, and C. Young, Phys. Rev. **C 92**, 044904 (2015).

[33] V. Vovchenko, M. I. Gorenstein, and H. Stoecker, Phys. Rev. Lett. **118**, 182301 (2017).

[34] P. Huovinen and P. Petreczky, (2017), arXiv:**1708.00879**[hep-ph].

[35] V. Vovchenko, A. Pasztor, Z. Fodor, S. D. Katz, and H. Stoecker, (2017), arXiv:**1708.02852** [hep-ph].

[36] M. Kitazawa and M. Asakawa, Phys. Rev. **C 86**, 024904 (2012), [Erratum: Phys. Rev. **C 86**, 069902(2012)].

[37] A. Adare *et al.* (PHENIX collaboration), Phys. Rev. **C 93**, 011901 (2016).

[38] L. Adamczyk *et al.* (STAR collaboration), Phys. Rev. Lett. **112**, 032302 (2014).

[39] L. Adamczyk *et al.* (STAR collaboration), Phys. Rev. Lett. **113**, 092301 (2014).

[40] R. Bellwied, S. Borsanyi, Z. Fodor, S. D. Katz, and C. Ratti, Phys. Rev. Lett. **111**, 202302 (2013).

[41] S. Chatterjee, R. M. Godbole, and S. Gupta, Phys. Lett. **B 727**, 554 (2013).

[42] K. A. Bugaev, D. R. Oliinychenko, J. Cleymans, A. I. Ivanytskyi, I. N. Mishustin, E. G. Nikonov, and V. V. Sagun, Europhys. Lett. **104**, 22002 (2013).

[43] J. M. Torres-Rincon, B. Sintes, and J. Aichelin, Phys. Rev. **C 91**, 065206 (2015).

[44] J. Beringer *et al.* (Particle Data Group), Phys. Rev. **D 86**, 010001 (2012).

[45] C. Alt *et al.* (NA49 collaboration), Phys. Rev. **C 77**, 024903 (2008).

[46] C. Alt *et al.* (NA49 collaboration), (2005), arXiv:nucl-ex/**0512033**,[nucl-ex].

[47] C. Alt *et al.* (NA49 collaboration), Phys. Rev. **C 78**, 034918 (2008).

[48] C. Alt *et al.* (NA49 collaboration), Phys. Rev. **C 78**, 044907 (2008).

[49] S. V. Afanasiev *et al.* (NA49 collaboration), Phys. Rev. **C 66**, 054902 (2002).

[50] C. Alt *et al.* (NA49 collaboration), Phys. Rev. **C 73**, 044910 (2006).

[51] C. Alt *et al*. (NA49 collaboration), Phys. Rev. Lett. **94**, 192301 (2005).

[52] S. Das (STAR collaboration), Nucl. Phys. **A 904-905**, 891c (2013).

[53] B. I. Abelev *et al*. (STAR collaboration), Phys. Rev. **C 79**, 034909 (2009).

[54] B. I. Abelev *et al*. (STAR collaboration), Phys. Rev. **C 79**, 064903 (2009)

[55] M. M. Aggarwal. *et al*. (STAR collaboration), Phys. Rev. **C 83**, 024901 (2011).

[56] C. Adler *et al*. (STAR collaboration), Phys. Rev. **C 65**, 041901 (2002).

[57] J. Adams *et al*. (STAR collaboration), Phys. Rev. Lett. **92**, 182301 (2004).

[58] K. Adcox *et al*. (PHENIX collaboration), Phys. Rev. **C 69**, 024904 (2004),

[59] K. Adcox *et al*. (PHENIX collaboration), Phys. Rev. Lett. **89**, 092302 (2002).

[60] J. Adams *et al*. (STAR collaboration), Phys. Lett. **B 612**, 181 (2005).

[61] S. S. Adler *et al*. (PHENIX collaboration), Phys. Rev. **C 69**, 034909 (2004).

[62] J. Adams *et al*. (STAR collaboration), Phys. Rev. Lett. **98**, 062301 (2007).

[63] B. Abelev *et al*. (ALICE collaboration), Phys. Rev. **C 88**, 044910 (2013).

[64] B. B. Abelev *et al*. (ALICE collaboration), Phys. Rev. Lett. **111**, 222301 (2013).

[65] B. B. Abelev *et al*. (ALICE collaboration), Phys. Lett. **B 728**, 216 (2014).

[66] L. Adamczyk *et al*. (STAR Collaboration), Phys. Rev. **C 96**, 044904 (2017).

[67] L. Van Hove, Phys. Lett. **118B**, 138 (1982).

[68] B. Mohanty, J.-e. Alam, S. Sarkar, T. K. Nayak, and B. K. Nandi, Phys. Rev. **C 68**, 021901 (2003).

[69] A. Bazavov *et al*., Phys. Rev. **D 85**, 054503 (2012).

[70] O. Kaczmarek, F. Karsch, E. Laermann, C. Miao, S. Mukherjee, P. Petreczky, C. Schmidt, W. Soeldner, and W. Unger, Phys. Rev. **D 83**, 014504 (2011).

[71] G. Endrodi, Z. Fodor, S. D. Katz, and K. K. Szabo, JHEP **04**, 001 (2011).

[72] C. Bonati, M. D'Elia, M. Mariti, M. Mesiti, F. Negro, and F. San

   lippo, Phys. Rev. **D 92**, 054503 (2015).

[73] R. Bellwied, S. Borsanyi, Z. Fodor, J. Gunther, S. D. Katz, C. Ratti, and K. K. Szabo,

   Phys. Lett. **B 751**, 559 (2015).

Chapter 7

Conclusions

Really speaking, the 7 letter word "Physics" is so vast, deep, enthusiastic and full of knowledge that a person will desperately feel proud to be a physicist.

As a big tree full of several branches, leafs, flowers and fruits looks really beautiful to see and always attracts the nature lovers. Similar is the scientific tree of physics, where the interest of a good physicist adds a new branch or leaf or flower or fruit to it. Every individual physicist has a never ignorable contribution to its existence to pay attention. This tree of physics are dreamed by all physicist to maintain its never ending growth. In this context, the effort of this thesis salutes this spirit of the scientists and tried for a little contribution to add to the growth of this tree of physics. "Let the tree of physics continue its growth".

The work presented in this thesis are related to study in the field of experimental high-energy heavy-ion collisions. This thesis contributed as a part to the ongoing scientific program at the Solenoidal Tracker At RHIC (STAR) situated at BNL, USA. At the STAR experiment, heavy-ions moving in relativistic speed are primarily collided to study the underlying physics of the medium formed. Its physics interest lies to test the predictions of QCD, to explore the QCD phase diagram, to find the signatures of Quark-Gluon-Plasma medium and to search for the QCD critical point. This exotic QGP medium is supposed to exist at the very beginning of the Universe.

With such physics goals, the STAR experiment is functioning since 19 years and has collected data in Au+Au collisions in a wide range of center of mass energies ranging from 7.7 GeV to 200 GeV. The first phase of the Beam Energy Scan program (BES-I) was commis-

sioned for the dedicated scan of the QCD phase diagram to study the phases of QCD, nature of QCD transitions and to locate the QCD critical point region. In BES-I, Au+Au collisions are recorded at $\sqrt{s_{NN}}$ = 7.7, 11.5, 19.6, 27 and 39 GeV in the years 2011-2012. In the year 2014, Au+Au collisions were taken at $\sqrt{s_{NN}} = 14.5$ GeV to fill up the μ_B (Baryon chemical potential) gap of nearly 200 MeV between the beam energies 11.5 and 19.6 GeV. The study of identified hadron production in Au+Au collisions at $\sqrt{s_{NN}}$ =14.5 GeV is one of the focus of this thesis. In addition to Gold nuclei collisions, RHIC has also explored the options of various other nuclei collisions such as p+p, d+Au, Cu+Cu, Cu+Au, Au+Au, U+U etc. The dependence of the experimental observables on the initial colliding system can be studied by varying the type and size of the nuclei. The study of the identified particle production in U+U collisions recorded at $\sqrt{s_{NN}} = 193$ GeV is also a part of this thesis. In this thesis, we have analyzed the basic properties of the medium through the measurement of the transverse momentum spectra, average transverse momentum ($\langle p_T \rangle$), particle yields, particle ratios, chemical and kinetic freeze-out parameters using information from pion, kaon, proton and their anti-particles produced in the collisions.

The measurement of pion ($\pi^{\pm}$), kaon ($K^{\pm}$) and (anti-)proton production in Au+Au collisions at $\sqrt{s_{NN}} = 14.5$ GeV has been carried out in this thesis. With the help of two major detector sub-systems of the STAR experiment named as the Time Projection Chamber (TPC) and Time-Of-Flight Detector (TOF), pions ($\pi^{\pm}$), kaons ($K^{\pm}$) and protons ($\pm$) were identified upto $p_T = 2.0$ GeV/c. In the mid-rapidity ($|y| < 0.1$), the transverse momentum (p_T) spectra of $\pi^{\pm}$, $K^{\pm}$ and $p(\bar{p})$ for Au+Au collisions at $\sqrt{s_{NN}} = 14.5$ GeV in nine different collision centrality classes 0-5%, 5-10%, 10-20%, 20-30%, 30-40%, 40-50%, 50-60%, 60-70%, 70-80% have been reported in this thesis. The yields of the particles extracted were corrected for detector efficiency and acceptance through Monte-Carlo simulation via embedding technique. The yields calculated from TPC and TOF were properly matched by correcting the yields from the TOF matching efficiency. The yield of pions are corrected for muon contaminations and weak decay contributions with the use of the Monte-Carlo simulation. The knock out protons coming from the interaction of highly energetic particles with the beam pipe and other detector material are subtracted from the raw yields of protons. After the application of all these cor-

rection factors we have obtained the final p_T spectra of $\pi^{\pm}$, $K^{\pm}$ and $p(\bar{p})$ for Au+Au collisions at $\sqrt{s_{NN}} = 14.5$ GeV. The inverse slope of the p_T spectra have been found to increase with the increase in mass of the particle from pion to kaon and kaon to proton. The p_T spectra of the particle has been integrated w.r.t. to p_T to extract the quantitative information in terms of mean p_T ($\langle p_T \rangle$) and particle yields (dN/dy) for a definite collision centrality. The dependence of $\langle p_T \rangle$, dN/dy and particle ratios were analyzed as a function of collision centrality and beam energy. The systematic uncertainty in p_T spectra, $\langle p_T \rangle$, dN/dy and particle ratios has been estimated in detail and presented in this thesis. The values of dN/dy for pions increases slightly with collision centrality suggesting an approximate scaling behavior with number of participant nucleons ($\langle N_{\text{part}} \rangle$) in Au+Au collisions at $\sqrt{s_{NN}} = 14.5$ GeV. Whereas for kaons and protons it increases from peripheral to central collisions. With increase in beam energy dN/dy was found to increase for pions, kaons and anti-protons, whereas a decrease was observed in the case of protons. This behavior can be attributed to baryon stopping. Mean p_T increases from peripheral to central collision for pions, kaons and protons indicating stronger radial flow effects in central collisions. The π^-/π^+ and K^-/K^+ ratio remains almost constant with collision centrality. A slight decrease in the ratio of $\bar{p}/p$ from peripheral to central collisions has been observed, which is a consequence of baryon stopping. The K^+/π^+ as well as K^-/π^- ratio increases with increasing collision centrality. The p/π^+ ratio increases from peripheral to central collisions, whereas there was no significant dependence on centrality for $\bar{p}/\pi^-$ ratio in Au+Au collisions at $\sqrt{s_{NN}} = 14.5$ GeV. The chemical and kinetic freeze-out parameters were extracted in Au+Au collisions at $\sqrt{s_{NN}} = 14.5$ GeV. The chemical freeze-out temperature T_{ch} showed no significant centrality dependence in Au+Au collisions at $\sqrt{s_{NN}} = 14.5$ GeV. On the other side, baryon chemical potential has been found to slightly increase with increase in collision centrality. The kinetic freeze-out temperature T_k decreases, whereas average radial flow velocity $\langle \beta \rangle$ increases with centrality in Au+Au collisions at $\sqrt{s_{NN}} = 14.5$ GeV. Thus, an anti-correlation has been observed between T_k and $\langle \beta \rangle$. All these results obtained in Au+Au collisions at $\sqrt{s_{NN}} = 14.5$ GeV were compared with the corresponding published results in Au+Au collisions at $\sqrt{s_{NN}} = 7.7, 11.5, 19.6, 27, 39, 62.4$ and 200 GeV. The results in Au+Au collisions at $\sqrt{s_{NN}} = 14.5$ GeV are further compared with models like AMPT and UrQMD.

UrQMD is a hadronic transport model, whereas AMPT includes both hadronic and partonic interactions. Previous model predictions suggest that at energies below 7.7 GeV hadronic contribution dominates whereas above 19.6 GeV partonic contribution dominates. Au+Au collisions at $\sqrt{s_{NN}} = 14.5$ GeV being an intermediate point between this borrows its interest in such model comparisons. The prediction from AMPT model were found to be in better agreement with STAR results, whereas UrQMD calculations showed poor agreement in Au+Au collisions at $\sqrt{s_{NN}} = 14.5$ GeV.

In this thesis, we have analyzed the pion, kaon and (anti-)proton production in U+U collisions at $\sqrt{s_{NN}} = 193$ GeV. Uranium is a prolate shaped nucleus in contrast to almost spherical Gold nucleus. This deformed shape of Uranium nucleus results in different types of interesting initial stage orientations between the two colliding nuclei. This initial stage geometrical orientations were predicted to affect the finally observed bulk properties of the system. Higher energy density and particle multiplicity have been predicted for U+U collisions at $\sqrt{s_{NN}} = 193$ GeV with respect to Au+Au collisions $\sqrt{s_{NN}} = 200$ GeV. In this context, we have measured the $\pi^{\pm}$, $K^{\pm}$, $p(\bar{p})$ p_T spectra in mid-rapidity ($|y| < 0.1$) in U+U collisions at $\sqrt{s_{NN}} = 193$ GeV for nine different collision centralities. Different correction factors such as energy loss correction, detector efficiency and acceptance, TOF matching efficiency, pion feed-down correction and proton background corrections were applied to the raw yields of the particles to obtained the final p_T spectra. The systematic uncertainties were also estimated. The inverse slope of the p_T spectra has been found to increase as we go from pions through kaons to protons, suggesting radial flow like effects for the system. We have extracted dN/dy, $\langle p_T \rangle$ and particle ratios from the p_T spectra of the pions, kaons and protons for the nine centrality classes. We have observed that dN/dy do not scale with the number of participant nucleons in U+U collisions at $\sqrt{s_{NN}} = 193$ GeV rather it was found to increase from peripheral to central collisions for pions, kaons and protons, anti-protons remain constant to this. This is due to contributions from soft and hard processes involving nucleon-nucleon binary collisions. The $\langle p_T \rangle$ has been found to increase from central to peripheral collisions indicating stronger radial flow effects in central collisions. We have also extracted kinetic freeze-out parameters in U+U collisions at $\sqrt{s_{NN}} = 193$ GeV through the simultaneous Blast-wave fit to the p_T spectra of pions, kaons,

and (anti)protons. All these results were compared with the corresponding published results of Au+Au collisions at $\sqrt{s_{NN}} = 200$ GeV. We observed that inspite of different geometrical shape of Uranium nucleus, the results in U+U collisions at $\sqrt{s_{NN}} = 193$ GeV were observed to be consistent with the published results in Au+Au collisions at $\sqrt{s_{NN}} = 200$ GeV within systematic uncertainty. A comparison with the calculations from the string melting version of AMPT model modified to incorporate the deformation of Uranium nucleus has also been carried out in U+U collisions at $\sqrt{s_{NN}} = 193$ GeV. AMPT model calculation with 10 mb cross-section describes the STAR results upto a good extent relative to AMPT model with 1.5 mb cross-section, in U+U collisions at $\sqrt{s_{NN}} = 193$ GeV.

As understanding freeze-out dynamics is a key theme for the thesis, we have studied in some details the models associated with this physics. The freeze-out conditions in high-energy nucleus-nucleus collisions can be extensively studied in the framework of statistical thermal models assuming a thermally localized fireball at the time of freeze-out. These thermodynamical model have successfully explained the particle multiplicity in heavy-ion collisions. In this thesis, we have extracted the chemical freeze-out parameters by implementing statistical thermal model using THERMUS package. The opportunity to test the predictive capability of statistical thermodynamic models in small system of p+p collisions has been explored. The p+p collisions at $\sqrt{s} = 17.3$, 200, 900 and 7000 GeV were analyzed in two freeze-out schemes: single freeze-out (1CFO) and double freeze-out (2CFO). In 1CFO all hadrons freeze-out at a single time whereas in 2CFO strange and non-strange hadrons freeze-out separately. The analysis has been done by employing three different ensembles : grand canonical, strangeness canonical and canonical ensemble as well. At lower energies freeze-out T_{ch} has been found to be higher than A+A collisions, whereas at higher energy it showed agreement with heavy-ion collisions. We observed the value of radius has been remarkably smaller for the p+p collisions in comparison with A+A collisions at same energy. It follows from an obvious expectation for with system size being small. Additionally, the strangeness saturation factor is found to be lower in p+p than A+A collisions even at LHC energies. This suggests significant strangeness suppression in p+p collisions relative to heavy-ion collisions.

The resonances which are theoretically predicted but not yet fully confirmed by experiments

are usually excluded from the calculations of HRG model. A study of the role of such missing resonances in two different freeze-out schemes (1CFO and 2CFO) have been presented in the thesis. We have extracted the freeze-out surface by implementing the Hadron resonance Gas (HRG) model as well as the higher moments of conserved charges (Baryon number (B) and Charge (Q)). Two particles sets were analyzed. One was PDG-2016, which included all the confirmed resonances listed the Particle Data Group, 2016. The other was PDG-2016+, which additionally included all the one-star and two-star mesons and baryons from the PDG table which are still awaiting for experimental confirmation. The freeze-out surface has been characterized with suitable choice of freeze-out parameters. In our study, the temperature T has only dimension, whereas two other dimensionless parameters μ_B/T and VT^3 were constructed. The freeze-out temperature T has been found to be mostly influenced by the systematics of the hadron spectrum, whereas μ_B/T and VT^3 were almost insensitive. A lowering of freeze-out temperature has been observed upon addition of extra resonances. The flavor hierarchy resulting in the difference of strange and non-strange T has been found to exist in PDG-2016 as well as in PDG-2016+.